Surface organometallic chemistry on Metal Organic Frameworks (MOF) : synthesis, characterization and their application in catalysis

Cherif Larabi

N° d'ordre 08 - 2011 Année 2011

THESE

Présentée

devant l'UNIVERSITE CLAUDE BERNARD - LYON 1
ECOLE DOCTORALE DE CHIMIE
SPECIALITE CHIMIE

Pour l'obtention

du DIPLOME DE DOCTORAT

(arrêté du 7 août 2006)

Présentée et soutenue publiquement le

Vendredi 13 Janvier 2011

par

M. Cherif LARABI

Surface organometallic chemistry on Metal Organic Frameworks (MOF): synthesis, characterization and their application in catalysis.

Directeur de thèse:
M. Jean-Marie Basset.
Encadrante:
Mme. Alessandra Quadrelli.

Jury :
M. Jean Marie Basset
M. Daniel Bianchi
Mme. Silvia Bordiga
M. Thierry Loiseau
Mme. Unni Olsbye
Mme. Alessandra Quadrelli

Rapporteurs :
M. Thierry Loiseau
Mme. Unni Olsbye

UNIVERSITE CLAUDE BERNARD - LYON 1

Président de l'Université	**M. le Professeur L. Collet**
Vice-président du Conseil Scientifique	M. le Professeur J.F. Mornex
Vice-président du Conseil d'Administration	M. le Professeur G. Annat
Vice-président du Conseil des Etudes et de la Vie Universitaire	M. le Professeur D. Simon
Secrétaire Général	M. G. Gay

COMPOSANTES SANTE

Faculté de Médecine Lyon Est – Claude Bernard	Directeur : M. le Professeur J. Etienne
Faculté de Médecine Lyon Sud – Charles Mérieux	Directeur : M. le Professeur F-N. Gilly
UFR d'Odontologie	Directeur : M. le Professeur D. Bourgeois
Institut des Sciences Pharmaceutiques et Biologiques	Directeur : M. le Professeur F. Locher
Institut des Sciences et Techniques de Réadaptation	Directeur : M. le Professeur Y. Matillon
Département de Biologie Humaine	Directeur : M. le Professeur P. Farge

COMPOSANTES Et UFR SCIENCES ET TECHNOLOGIE

Faculté des Sciences et Technologies	Directeur : M. le Professeur F. Gieres
Département Biologie	Directeur : M. le Professeur C. Gautier
Département Chimie Biochimie	Directeur : Mme le Professeur H. Parrot
Département GEP	Directeur : M. N. Siauve
Département Informatique	Directeur : M. le Professeur S. Akkouche
Département Mathématiques	Directeur : M. le Professeur A. Goldman
Département Mécanique	Directeur : M. le Professeur H. Ben Hadid
Département Physique	Directeur : Mme S. Fleck
Département Sciences de la Terre	Directeur : M. le Professeur P. Hantzpergue
UFR Sciences et Techniques des Activités Physiques et Sportives	Directeur : M. C. Collignon
Observatoire de Lyon	Directeur : M. B. Guiderdoni
Ecole Polytechnique Universitaire de Lyon 1	Directeur : M. le Professeur J. Lieto
Institut Universitaire de Technologie de Lyon 1	Directeur : M. le Professeur C. Coulet
Institut de Science Financière et d'Assurance	Directeur : M. le Professeur J-C. Augros
Institut Universitaire de Formation des Maîtres	Directeur : M R. Bernard

« La science ne cherche pas à énoncer des vérités éternelles ou des dogmes immuables, loin de prétendre que chaque étape est définitive et qu'elle a dit son dernier mot,..., elle cherche à cerner la vérité par approximations successives »

Bertrand Russell (1872-1970)

A Soraya

Les travaux de thèses exposés dans ce manuscrit ont été réalisés entre Octobre 2007 et Octobre 2010 au sein du laboratoire de chimie catalyse polymères et procédés (C2P2) unité mixte CNRS-CPE-Université de Lyon 1 (UMR5265). Je remercie M. Gérard Pignault, directeur de CPE Lyon, de m'avoir accueilli dans ces locaux.

Je tiens à remercier vivement Monsieur Jean-Marie BASSET, Directeur de Recherche au CNRS, de m'avoir accordé sa confiance et d'avoir su me faire profiter de son expérience et ses connaissances dans le domaine de la chimie. Je le remercie tout particulièrement pour son dynamisme, sa curiosité et sa rigueur scientifique.

Je remercie Madame Alessandra Quadrelli, Chargée de recherche au CNRS, qui a encadré mes travaux de thèse. Ses précieux conseils, sa grande disponibilité et son enthousiasme ont été d'une importance inestimable durant ces trois années. Je la remercie également de m'avoir donné la possibilité de participer à de nombreuses collaborations.

Je remercie aussi Monsieur Adriano Zechina Professeur à l'université de Turin, Italie pour m'avoir reçu dans son laboratoire et pour son aide précieuse pour la progression de ce travail.

Mes remerciements vont également à Monsieur Mats Tilset et Monsieur Karl Petter Lillerud Professeurs à l'université d'Oslo, Norvège pour m'avoir accueilli dans leurs laboratoires ainsi que pour leurs conseils. Je leur suis très reconnaissant pour leurs contributions à l'avancement de ce projet.

J'adresse mes plus vifs remerciements à Monsieur Michael Brorson Chargé de recherche, et Monsieur Frank Bartnik Johansson ingénieur de recherche à Haldor Topsøe, Danemark pour leurs aides pratiques et de m'avoir permis d'effectuer des tests catalytiques.

Je souhaite remercier Mr David farrusseng Chargé de recherches au CNRS à IRCELYON pour les differentes discussions scientifiques.

Que les membres du jury, Monsieur Daniel Bianchi Professeur à l'Université de Lyon 1 Madame Silvia Bordiga Professeur à l'Université de Turin, Monsieur Thierry Loiseau, Directeur de Recherche au CNRS. Madame Unni Olsbye Professeur à l'Université d'Oslo Norvège soient vivement remerciés de l'honneur qu'ils m'ont fait en acceptant de juger ce mémoire.

Que tous les membres du laboratoire trouvent dans ces quelques mots l'expression de ma plus profonde gratitude. Je pense en particulier Mmes Anne Boudaouin, Christine Lucas, Chloé Thieuleux et Mrs Jean Pierre Candy, Kai Szeto, Laurent Veyre. Ainsi que tous ceux qui ont participé de près ou de loin à la réalisation de ce travail.

Bien sûr, tous les post-docs, les étudiants en thèse ou en Master avec lesquels j'ai partagé toutes ou une partie de ces trois années, et qui sauront se reconnaître, soient remerciés pour leurs aide quotidienne, l'ambiance joyeuse et conviviale régnant au sein du laboratoire.

Abstract:
Metal organic frameworks (MOF) are a new class of material, which consist of metal ions or clusters coordinated to organic ligands or metal-organic complexes and result in 1D, 2D or 3D crystalline networks. The possibility of constructing new MOF has been exemplified in this thesis by development of imidazolium based MOF, a highly important ligand system in catalysis. Moreover, this work has performed post synthesis modification via surface organometallic chemistry on existing MOF: i) a known MOF, UiO-66, with relatively small pores has been functionalized with amino group and its gas adsorption capacity has been investigated, ii) the syntheses of a 3D open structure MOF, CPO-27, MOFs have been optimized and used as a precursor to produce a hydrodesulfurization catalyst after introducing active species via surface organometallic chemistry approach, whose catalytic performances have been measured.

Key words: Metal Organic Framework (MOF), microporous material, catalysis, hydrodesulfurization, adsorption, surface organometallic chemistry.

Résumé :
Les structures organométalliques poreuses (Metal Organic Framework, MOF) sont une nouvelle classe de matériaux, composées d'ions métalliques ou de clusters liés à des ligands organiques ou des complexes organométalliques dans des réseaux cristallins 1D, 2D ou 3D. Au cours de cette thèse la possibilité de construire de nouveaux MOF a été illustrée par le développement de matériaux MOF à base d'imidazolium, précurseur important pour la synthèse de catalyseurs. En outre, ce travail démontre l'utilité de la modification post-synthèse des MOFs par chimie organometallique de surface à visée catalytique : i) un MOF connu, UiO-66, avec des pores relativement petits a été fonctionnalisé avec un groupement amino et ses capacités d'adsorption de gaz ont été étudiées. ii) la synthèse de MOF a structure poreuse, CPO-27, MOF a été optimisée et utilisée comme précurseur pour produire un catalyseur d'hydrodésulfuration après l'introduction d'espèces actives, via la chimie organométallique de surface, dont les performances catalytiques ont été évaluées.

Mots clés: Metal Organic Framework (MOF), matériau microporeux, catalyse, hydrodésulfuration, adsorption, chimie organometallic de surface.

Université Lyon 1, LC2P2, Laboratoire de Chimie OrganoMétallique de Surface (LCOMS), UMR 5265, CNRS-CPE Lyon, 43 boulevard du 11 novembre 1918, F-69616 Villeurbanne Cedex, France.

Table of Contents

Abbreviation

Nomenclature of samples

Abbreviations

δ	chemical shift in NMR downfield from TMS, ppm
$\nu_{(A-B)}$, $\delta_{(A-B)}$	stretching and bending frequencies of A-B bond
Å	angstrom
AB	ammonia borane
ABDC	2-amino terephtalate
BDC	tereftalate
BET	Brunauer, Emett and Teller theory
BJH	Barret Joyner Halenda
BPDC	biphenyl dicarboxylate
*n*Bu	nbutyl, $-(CH_2)_3CH_3$
*t*Bu	tertbutyl, $-CH(CH_3)_3$
Bipym	2,2'-bipyrimidine
°C	relative temperature in Celsius degree: T = °C + 273.15
CCD	charge coupled device
COD	1,5-cyclooctadiene
COT	1,3,5-cyclooctatriene
CP	cross-polarization
Cp	cyclopentadienyl
CPO	coordination polymer of Oslo
Cy	cyclohexyl
DMDS	dimethyldisulphide
DMF	dimethylformamide
DMSO	dimethylsulfoxide
DRIFT	diffuse reflectance infrared fourier transform
DSC	differential scanning calorimetry
EDS	energy dispersive X-ray spectrometry
ee	enantiomeric excess
Et	ethyl
EtOH	ethanol
ES HRMS	electrospray high resolution mass spectrometry
FID	flame ionization detector
FWHM	full width at half maximum
GC	gas chromatography
h	hour
HDS	hydrodesulfurization
HDN	hydrodenitrogenation
HETCOR	heteronuclear correlation
HK	Horvath Kawazoe
HKUST	Hong Kong university of science and technology
HYD	hydrogenation
Hz	hertz, s^{-1}
ICP-MS	inductively coupled plasma mass spectrometry

IR	infrared
J_{A-B}	coupling constant between the atoms A and B in NMR, Hz
kcal	kilocalorie
KHMDS	potassium hexamethyldisilazane
M	molar concentration
MAS	magic angle spinning
MCM	mobile crystalline material
MCT	mercury cadmium telluride
Me	methyl, CH_3
MeCN	acetonitrile
MIL	matériaux institut lavoisier
mn	minute
MOF	metal organic framework
MPAB	methyl para-aminobenzoate
Naph	naphthalene
NHC	N-heterocyclic carbene
Np	neopentyl, $-CH_2C(CH_3)_3$
NMR	nuclear magnetic resonance
OAc	acetylacetonate
PABA	para-aminobenzoic acid
PAMBA	para-aminomethylbenzoic acid
P(CO)	CO pressure
PROX	preferential oxidation
PCy	tricyclohexylphosphine
RT	room temperature
s	second
Salen	salicylic aldehyde and ethylenediamine
SBA	santa barbara amorphous
SBU	secondary building unit
SEM	scanning electron microscopy
SOMC	surface organometallic chemistry
T	absolute temperature in Kelvin: T = °C + 273.15
TGA	thermogravimetry analysis
TEM	transmission electron microscopy
THF	tetrahydrofuran
TMS	tetramethylsilane, $Si(CH_3)_4$
WCA	weakly coordinating anion
XRD	X-Ray diffraction
ZIF	zeolitic imidazole framework
1D, 2D, 3D	one, two and three dimensional

Nomenclature of samples

Au@CPO-27-Ni-1	gold nanoparticles at CPO-27-Ni from chloro(dimethylsulfide)gold
Au@CPO-27-Ni-2	gold nanoparticles at CPO-27-Ni from methyl(trimethylphosphine)gold
CPO-27-Ni	nickel based coordination polymer of Oslo (MOF)
CPO-27-Zn	zinc based coordination polymer of Oslo (MOF)
CPO-27- Ni-Zn	bimetallic zinc and nickel based MOF
LCH-1	zinc 1,3-bis(4-carboxyphenyl)imidazolium based MOF
LCH-2	zinc 4-imidazolyl-benzoic acid based MOF
Ni-Mo6	molybdenum from $Mo(CO)_6$ at CPO-27-Ni with Mo/Ni = 0.5 method b
Ni-Mo7	molybdenum from $Mo(CO)_6$ at CPO-27-Ni with Mo/Ni = 0.75
Ni-Mo8	molybdenum from $Mo(CO)_6$ at CPO-27-Ni with Mo/Ni = 1
Ni-Cr9	chromium from $Cr(CO)_6$ at CPO-27-Ni
Ni-Mo10	molybdenum from $Mo(CO)_6$ at CPO-27-Zn
Ni-Mo11	molybdenum from $Mo(CO)_6$ at CPO-27-Zn-Ni
Ni-Mo12	molybdenum from MoO_3 at CPO-27-Ni
Ni-Mo13	molybdenum form $H_2Mo_{12}O_{40}P$ at CPO-27-Ni
UiO-66-ABDC	zirconium-amino benzene dicarboxylate based MOF
UiO-66-BDC	zirconium-benzene dicarboxylate MOF
UiO-66-BPDC	zirconium-biphenyl dicarboxylate MOF

General outline

Metal organic frameworks (MOFs) are self assembled network structures, which are generally constructed by coordination of organic ligands to inorganic cornerstones (metal ions or clusters). The high number of different inorganic and organic modules allows to prepare large variety of materials with different properties and applications in various fields, including catalysis.

The main objective of this study was to generate new well defined catalysts by post synthetic modification of the Metal Organic Framework (MOFs) via surface organometallic chemistry.

Results were described in four chapters, as follows:

Chapter I is divided into two parts, where the first one reviews well defined supported metal hydrides on classical supports obtained via surface organometallic chemistry, and their catalytic properties towards C-C cleavage and C-C bond formation. The second part contains some examples of the use of MOF in catalysis reported in the literature and focuses on creating a strategy of functionalizing MOFs with organometallic complexes, having in perspective their applications in catalysis.

Chapter II describes the design and preparation of a novel class of MOFs based on a series of ligands containing heterocyclic carbenes. Such ligands play a central role in organometallic chemistry and catalysis.

Chapter III describes the synthesis of UiO-66 MOF containing one or two phenyl rings on the linker and amino-functionalized compounds. The synthesized MOFs are used to perform surface organometallic chemistry on OH groups. Studies of their gas adsorption properties, in particular CO_2 have been carried out.

Chapter IV involves synthesis of CPO-27 MOF with permanent porosity and development of post synthesis modification via surface organometallic chemistry on this material (either on the phenyl ring or the open metal site) in order to prepare single site catalyst are described.

Chapter V offers a general conclusion of this thesis work.

Chapter I:

Bibliography

I.1. Introduction

Heterogenization of homogenous complexes:

Catalysis is essential from the smallest biological system to large scale industrial processes. Already in the early 19th century, it has been observed that the reaction rate can be significantly increased in the presence of certain substances. Only minor quantities of these substances were necessary and the reactions proceeded without loss or change of the added compounds. In 1835, Jons Jakob Berzelius introduced the concept of catalysis to describe this phenomenon.[1] Today a catalyst is defined as a substance that increases the rate of a reaction without being consumed in the process. This implies that the catalyst permits reactions to take place more efficiently or under milder conditions. Most of the commercial catalytic processes operate under heterogeneous conditions rather than the homogenous due to the robustness of the system. In heterogeneous catalysis the catalyst and the reagents are in separate phases, making the isolation of the product from the catalyst easy. This eliminates or minimizes also further work-up procedures which are often expensive and lead to large volumes of waste. Typical heterogeneous catalyst are solids or an active specie (inorganic cluster or metal organic complexes) immobilized on a solid support such as silica,[2] alumina,[3] clay,[4] zeolite,[5] … These supports have high surface area and thereby allow high dispersion of the active sites. Typical commercial heterogeneous catalysts are suffering from the presence of different active and ill defined sites due to the heterogeneity of the surface. A traditional approach to heterogenize a well defined homogenous catalyst is by tethering them on supported organic linker, but the activity and selectivity of the heterogenizied catalyst can be compromized by the support, since the surface structure and surface characteristics can affect the catalytic performance and the product distribution.[6]. However, the chemical and thermal stability can be improved compared to their parent homogenous systems.

An alternative approach to prepare molecularly well defined species on a support involves surface organometallic chemistry.[7]

I.2. Surface Organometallic Chemistry approach SOMC:

The surface organometallic chemistry, SOMC, approach to a "single-site" heterogeneous catalyst consists of grafting an organometallic or coordination compound directly onto a surface in a molecularly precise way. In fact, it has been shown that from an organometallic point of view, a surface can be considered as a repetition of ligands, like [≡SiOH] in the case of silica. The concentration and density of the ligands can be controlled by a rigorous pre-treatment step. For example, treatment of a silica under dynamic vacuum at 500 °C for 10 hours followed by two hours treatment at 700 °C leads, by successive dehydroxylation steps (Scheme I.1), to mostly isolated surface silanols at a 0.7 OH/nm² concentration.[8]

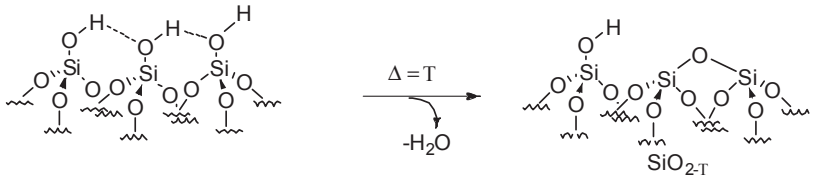

Scheme I.1: dehydroxylation process of the silica surface.

Sublimation or impregnation of a volatile metal alkyl precursor, such as $Ta(=CH^tBu)(CH_2{}^tBu)_3$, onto the partially dehydroxylated silica surface leads then to the formation of the well defined grafted organometallic species, $[(\equiv SiO)Ta(=CH^tBu)(CH_2{}^tBu)_2]$, and $[(\equiv SiO)_2Ta(=CH^tBu)(CH_2{}^tBu)]$,[9] whose relative distribution depends on the starting concentration of surface silanol groups. The quantification of the by-products released during the grafting reaction (viz. neopentane, CMe_4) gives an indication of grafting stoichiometry. The extensive characterization by several *in situ* and *ex situ* techniques (IR, EXAFS, SS MAS NMR, microanalysis, GC,…) gives a precise molecular definition of the grafted complexes, and thereby allows to define the reaction pathway as a surface organometallic chemical equation (Scheme I.2).

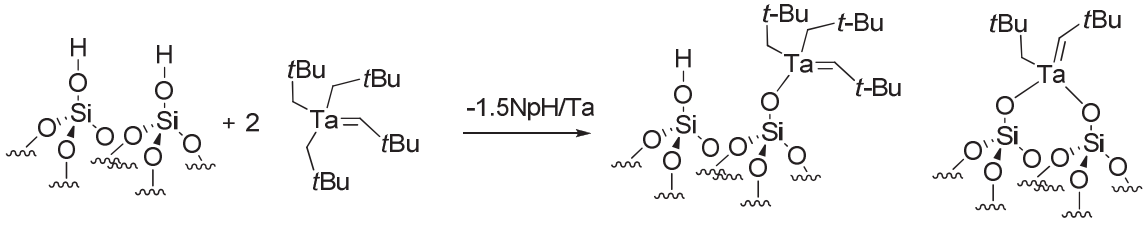

Scheme I.2: Reaction of trineopentylneopentylidene tantalum with dehydroxylated silica.

The grafting mechanism can also be understood by deuterium labeling studies or the synthesis of molecular analogues.

In analogy to the tantalum species, alkyls of group 4 metals are prepared by reacting a tetrakisnepentyl metal (zirconium, titanium and hafnium) with silica or silica-alumina dehydroxylated at 500 °C. Well defined surface organometallic species $[(\equiv SiO)M(CH_2{}^tBu)_3]$ and $[(\equiv SiO)_2M(CH_2{}^tBu)_2]$ (Scheme I.3) with M = Zr[10-12], Ti[6], Hf[13]) can be obtained.

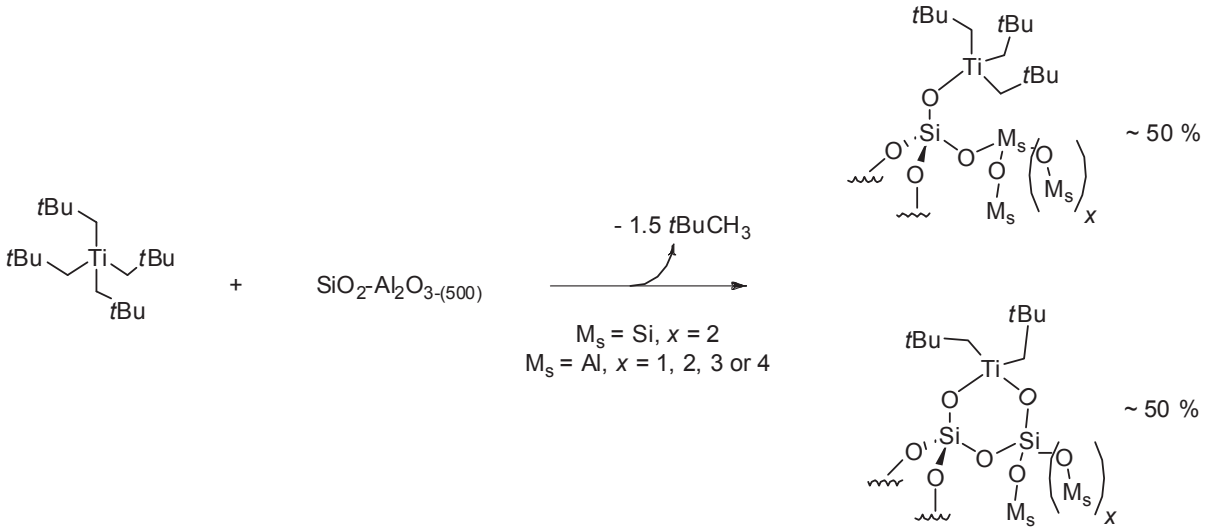

Scheme I.3: Reaction of tetraneopentyl titanium with SiO_2-$Al_2O_{3-(500)}$.

These catalysts have shown outstanding activity and selectivity toward different reactions (homologation/hydrogenolysis, polymerisation/oligomerization, alkanes and alkenes metathesis). The nature of the active sites allows a deeper mechanistic understanding of the reaction.[14]

I.3. Catalysis by surface organometallic chemistry:

The rational basis for the surface organometallic chemistry approach to a single site heterogeneous catalyst is summarized in scheme I.4. Based on the known molecular steps of the target catalytic mechanism, and in particular on the chemical nature of the active catalytic species, SOMC can be used to develop the adequate surface analogues. The optimization of the results by feedback loops or the study of unexpected catalytic results from a mechanistic and molecular view point leads to optimized systems.

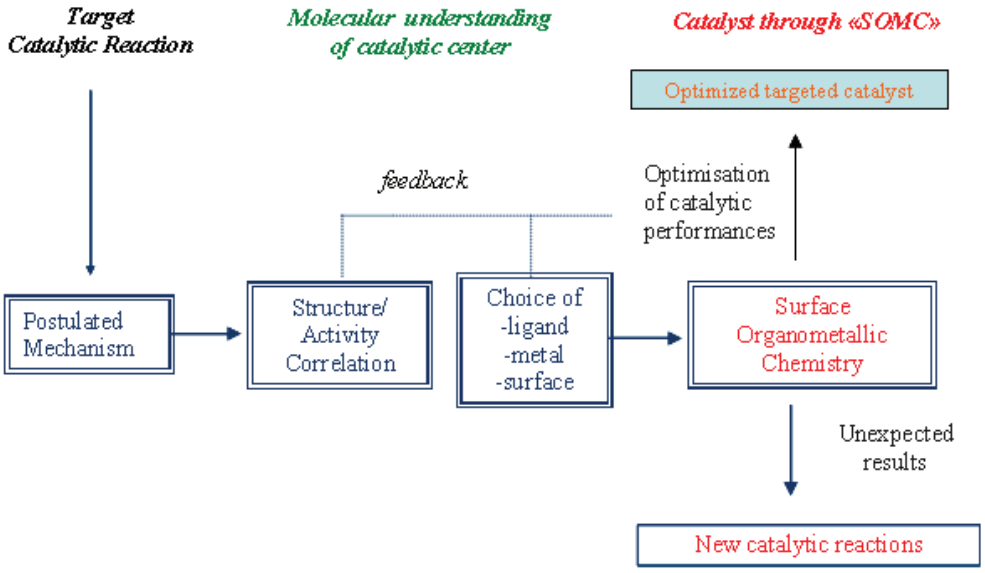

Scheme I.4: The design of well-defined single site catalyst by the surface organometallic chemistry approach.

As examples of some of SOMC successes in heterogeneous catalysis, one could mention systems such as silica-grafted olefin metathesis catalysts with TON of 231000 in 1500 min for propene,[15] the trifunctional tungsten-based catalyst for direct conversion of ethylene to propylene,[16] and tantalum-based catalytic system for the non-oxidative coupling of methane to ethane,[17] and other remarkable activity toward C-C and C-H bonds in stoichiometric activation and catalytic reactions such as alkane metathesis,[18] cross-metathesis between ethane and toluene.[19]

I.3.1. Supported hydride transition metal and their activity in C-C and C-H activation:

Important industrial processes such as Fischer-Tropsch synthesis; alkene and alkane homologation (hydrogenolysis, isomerisation, metathesis, oligomerization,…) involve C-C and C-H bonds activations. One of the most successful development of surface organomettalic chemistry, supported metal hydride, has lead to remarkable C-H, C-C catalytic activity.

I.3.1.1 Supported group 4 metal hydrides:

The silica-alumina grafted metal alkyl described above reacts under H_2 at 150 °C leads to $(\equiv SiO)_2MH_2$ and $(\equiv SiO)_3MH$ with a mixture of methane and ethane (3:1) (Scheme I.5).

Preparation of supported titanium hydride leads to the concomitant formation of M(III), which is not observed in the case of zirconium and hafnium.

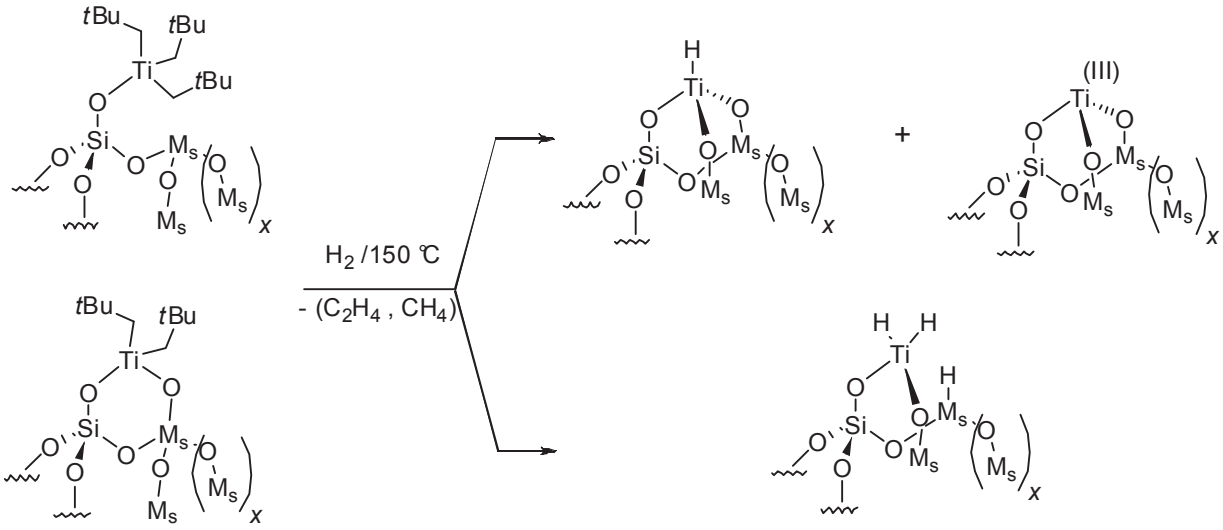

Scheme I.5: Main structures proposed for titanium hydrides supported on silica-alumina.

These species have been characterized via the combined use of several techniques such as IR spectroscopy, ^{1}H MAS, ^{13}C-CP/MAS, 2D ^{1}H-^{13}C HETCOR, and *J*-resolved solid-state NMR as well as mass balance analysis, EXAFS, and theoretical modelisation. The analogous surface species can be prepared with silica as support, while alumina gives a rather complicated system.[20, 21]

The formation of methane and ethane instead of $^{t}BuCH_3$ during the hydrogen treatment indicates that $(\equiv SiO)_{(4-x)}TiH_x$ catalyze the hydrogenolysis of alkanes.

Indeed, extensive studies of alkane hydrogenolysis were performed in batch reactor. The titanium hydrides catalyze the C-C cleavage reaction under hydrogen except ethane C-C bond, thus suggesting that the C-C bond cleavage occurs via a β-alkyl transfer of the surface metal alkyl intermediates (Scheme I.6).

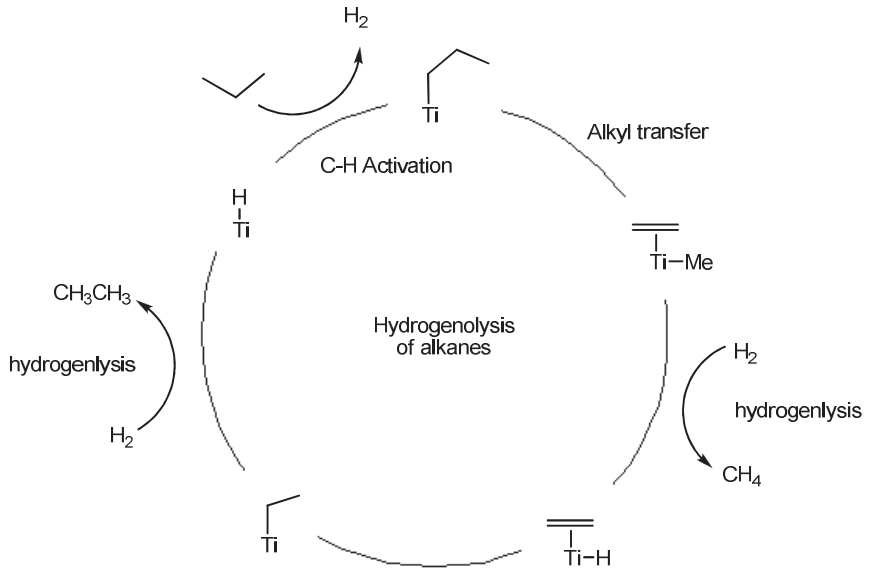

Scheme I.6: Proposed mechanism of alkane (propane) hydrogenolysis, Ti-H = $[(\equiv SiO)_{(4-x)}TiH_x]$/ x= 1 or 2.

It was shown that it is possible to polymerize ethylene or propylene to the corresponding polyolefins with a zirconium hydride supported on silica-alumina. And under hydrogen the same catalyst can also cleave C-C bonds of polyethylene or polypropylene to shorter chains, including methane as shown in Scheme I.7.[9]

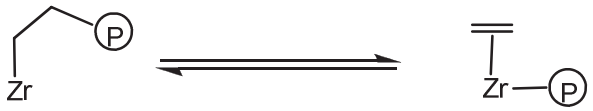

Scheme I.7: Ziegler-Natta polymerisation and depolymerisation mechanism over [Zr-H], with Zr-H = $[(\equiv SiO)_{(4-x)}ZrH_x]$/ x= 1 or 2.[9]

It was also demonstrated that silica supported zirconium dihydride catalyze the conversion of alkane to higher homologues, by β-Alkyl transfer or β-H transfer mechanism.[22, 23] These hydrides react with a wide range of alkanes and cycloalkanes, at low temperature to yield the corresponding metal alkyl complexes and H_2.[10, 12, 24]

I.3.1.2. Supported group 5 metals:

Concerning the supported group 5 metals, the most studied element is tantalum. Surface organometallic tantalum species can be obtained by a reaction of $Ta(CH_2{}^tBu)(=CH{}^tBu)$ with a silica dehydroxylated at 500 °C, resulting in a mixture of $[(\equiv SiO)Ta(CH_2{}^tBu)_2(=CH{}^tBu)]$, $[(\equiv SiO)_2Ta(CH_2{}^tBu)(=CH{}^tBu)]$ and neopentane. Treatment of

these two species under 500 torr of hydrogen at 150 °C leads to the formation of a surface tantalum (III) monohydride, $[(\equiv SiO)_2Ta^{III}H]$ as the major specie. In contrast to group 4 transition metal, only methane is detected (Scheme I.8),[25-27] suggesting that the hydrogenolysis mechanism is different.

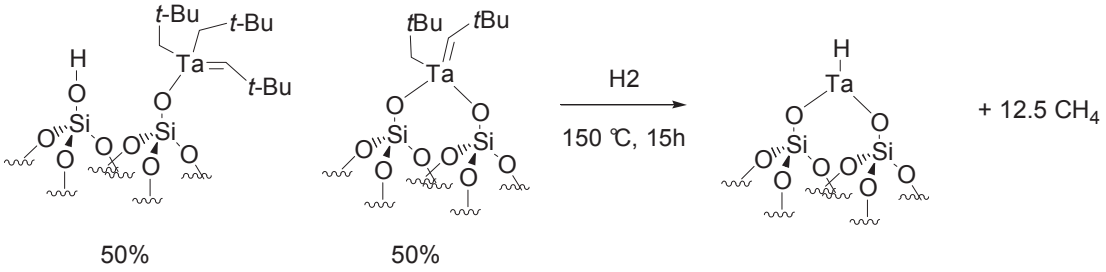

Scheme I.8: Preparation of silica supported tantalum hydride.

Extensive investigation of the hydrogenolysis reaction of acyclic alkanes shows a conversion into their lower homologues, and only CH_4 is detected at the end. Selectivities evaluation of the hydrogenolysis of 2-methylpropane at different temperature and low conversion indicates that the process does not involve only successive β-alkyl transfer as for supported group 4 metal hydrides. Moreover, the hydrogenolysis of 2,2-dimethylbutane leads to neopentane, indicating that the cleavage occurs via α-alkyl transfer.[28]

The tantalum hydride $[(\equiv SiO)_2Ta^{III}H]$ catalyzes alkane metathesis,[29] a reaction that transforms an alkane to its higher and lower homologues. The mechanism involves formation and cleavage of C-C bonds.[28, 30]

It has been also demonstrated that the silica-supported tantalum carbene complexes $[(\equiv SiO)Ta(=CH^tBu)(CH_2{}^tBu)_2]$ and $[(\equiv SiO)_2Ta(=CH^tBu)(CH_2{}^tBu)]$ are also active as precursor of alkane metathesis. Later investigations suggest that the mechanism involves i) dehydrogenation of the alkane, ii) alkene metathesis with the metallacyclobutane as important intermediate according to the Chauvin mechanism,[31] and iii) alkene hydrogenation.[32]

Silica-supported tantalum hydride $[(\equiv SiO)_2Ta\text{-}H]$ was used to explore the microscopic reversibility of ethane hydrogenolysis reaction: coupling of methane into ethane and hydrogen.[17] The reaction is postulated to proceed first via a C-H bond activation of methane, leading to a surface tantalum-methyl species and hydrogen. This tantalum-methyl undergoes dehydrogenation to a carbene-hydride. Both species are able to activate another molecule of methane by a σ-bond metathesis process, affording a methyl-methylidene key intermediate.

Migratory insertion of the methyl group onto the carbene ligand would yield tantalum-ethyl. Finally, the ethyl ligand can be displaced by methane in large excess via σ-bond metathesis, liberating ethane and leading back to a tantalum-methyl specie (Scheme I.9).[17]

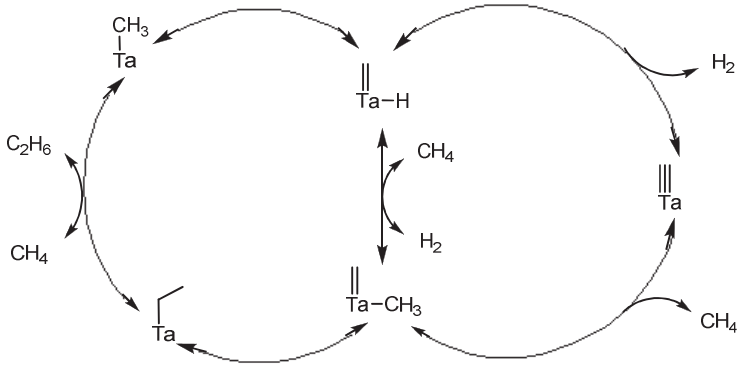

Scheme I.9: Proposed mechanism of the non-oxidative coupling reaction of methane where Ta-H is supported tantalum hydride.[17]

In conclusion, since tantalum is able to undergo oxidative addition/reductive elimination and α-alkyl (or α-H) transfer, the silica supported tantalum hydride and tantalum alkylidene catalyze C-C bond formation and cleavage, C-H activation reactions, alkane hydrogenolysis or metathesis or non-oxidative coupling of methane reactions.

I.3.1.3. Supported group 6 metals:

Supported group 6 metal alkyl (Mo, W) can be prepared as supported group 5 metal alkyl. Tungsten hydrides supported on dehydroxylated SiO_2–Al_2O_3[33-35] or Al_2O_3 [16] were prepared by thermal treatment of the grafted $[W(\equiv C^tBu)(CH_2{}^tBu)_3]$ under hydrogen at 150 °C. Tungsten hydride is less active in alkane hydrogeneloysis than tantalum hydride but more active and more stable in acyclic alkane metathesis[34] and non-oxidative coupling of methane.[36]

Moreover, this particular metal site is also active in unexpected reactions like direct conversion from ethene to propene[16] and production of 2,3- dimethylbutane from isobutane.[37]

I.4. Metal-Organic Framework (MOF):

I.4.1. Historical events:

In recent years, large progress has been made in the area of organic-inorganic hybrid compounds. The synthesis and characterization of infinite, rigid, porous, and well-defined solids, being covalently bonded in one-, two-, and three-dimensions (1D, 2D, and 3D) have been a field of rapid growth. In particular, materials constructed from inorganic units (a metal center or clusters) linked to organic or metal-organic compounds via coordination or covalent bonds and resulting in extended network.[38] This family of coordination polymers material is also known as metal-organic frameworks (MOFs).

Metal organic frameworks (MOFs) have been classified as a relatively new class of materials even though a reference dating back to 1959 can be found.[39, 40] Limited research efforts were dedicated to metal organic frameworks until an important reinitialization by Hoskins *et al.* around 1990's.[41] They postulated that unlimited number of novel materials with different topologies can be constructed by judicious combination of organic ligands and metallic centers.

Materials using this approach to construct the crystal structure have been known for a considerable time, such as compounds based on cyanide-bridged assemblies ($Zn(CN)_2$, $Cd(CN)_2$), crystallographic analyses reveal that the compounds crystallize in an extended diamond-type topology.[42] Hoskins et al. have successfully substituted both the cyanid with 4,4', 4", 4"'-tetracyanotetramethane and tetrahedral metal centers with Cu[43]. Ohba *et al*. in 1994 have reported the complete characterization of bimetallic cyano-bridged one dimensional polymer chain, $[Ni(ethyldiamine)_2]_3[Fe(CN)_6]_2 \cdot 2H_2O$. [44]

Although the concept was clearly presented in the 1990's, the quantity of work on this subject was modest until achievement of porous metal organic frameworks by Yaghi *et al*.[45, 46]

Metal organic frameworks (MOFs) have since attracted very strongly the attention of chemist, physicists, and materials scientists because of structure diversity and potential applications in catalysis,[47-50] gas storage, [51-53]and separation.[54-56]

Structurally, the construction of novel MOFs depends on the novelty of the secondary building units (SBUs) which in most cases are metal or inorganic clusters. [57] For example, rigid metal-carboxylate clusters of dinuclear, trinuclear, tetranuclear, hexanuclear, and

heptanuclear clusters have been successfully synthesized.[58-63] The ligand used in the formation of coordination polymers has to act as a bridge between SBUs. Therefore, multidentate ligands are used. The ligand can further provide important properties like rigidity and structural features. Nitrogen and oxygen donor ligands are frequently used in the formation of coordination polymers and network structures, some examples are illustrated in Figure I.1.

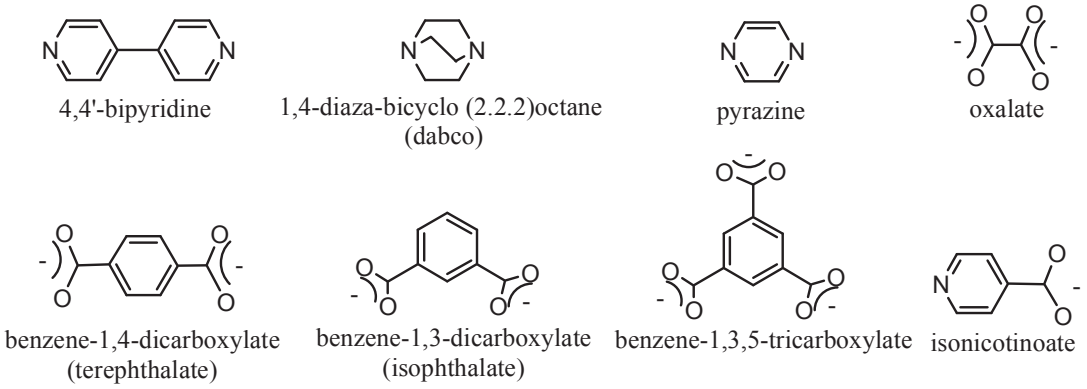

Figure I.1: Examples of some ligands which are used in constructing MOFs.

The structure, pores size, surface area, and stability of MOFs depend on geometrical consideration of the chemical attributes of the SBU's and the choice of the organic linker.

Much work on porous MOF networks has been undertaken with various polycarboxylates with zinc.[58-65] The structure contains Zn_4O tetrahedra as edges bridged by six carboxylate groups resulting in an octahedron-shaped SBU structure that forms part of a 3D primitive cubic structure with exceptionally high rigidity and porosity (Figure I.2).

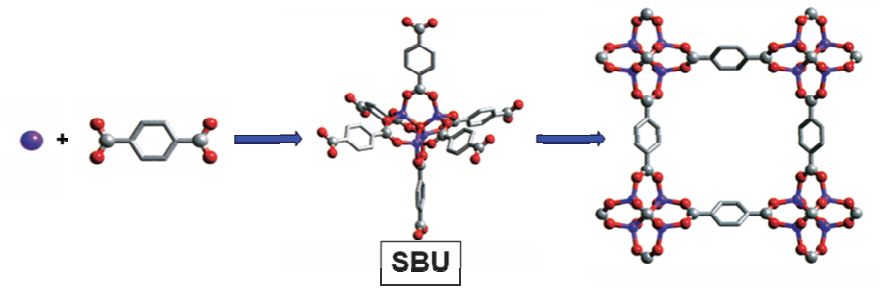

Figure I.2: Octahedral rigid metal – carboxylate clusters (SBU) connected to form a rigid extended network.[63]

By varying the type of dicarboxylate, it was shown that other structures could be obtained with similar topology but different pore sizes and functionalities (Figure I.3).

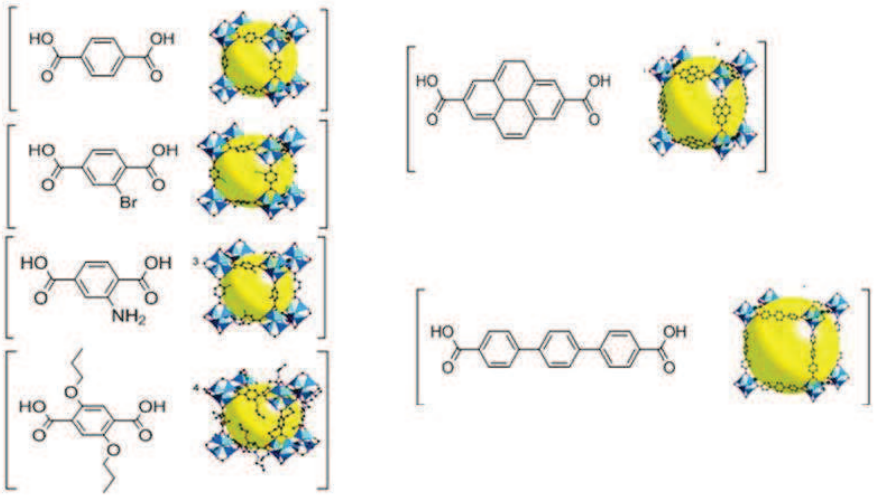

Figure I.3: MOFs with varying functionalities and pores size.[63]

I.4.2. Synthesis of Metal-organic framework:

Generally, the syntheses of MOFs are achieved using soluble salts as source of metal cornerstone such as metal nitrates, sulfates or acetates.[66] Nitrogen or oxygen containing ligands are commonly used as coordination donor.[38] Polar organic solvents, typically amine (triethylamine), amide (diethylformamide, dimethylformamide) or water are normally required. After combination of these inorganic and organic components, the metal–organic structures are formed by self-assembly from room temperature till solvothermal condition.[66]

I.4.3. Characterization and structure determination of the MOF:

MOFs are known to be highly crystalline and porous solids, with often high and accessible surface areas. X-ray diffraction on single crystal or powder is used to solve the crystal structure. Additional structural details can be obtained with neutron diffraction and electron microscopy. Nitrogen sorptions at 77 K or argon uptake at 87 K are standard techniques to determine the porosity and the surface area. However, it should be considered that the underlying model of independent, equivalent and non-infringing sorption sites might behave differently on a molecular level. Many reports have described localized rather than bulk volume adsorption phenomena on metal–organic materials.[67, 68] The nature of the adsorption sites can be revealed by neutron scattering spectroscopy.[51] Spectroscopic methods like NMR, IR, UV-Vis, Raman, XAFS and XPS can be applied to obtain information of local sites in the structure.[66] The nature of a specific site can also be determined spectroscopically by employing probe molecules.[69-71]

I.4.4. Application of Metal organic framework:

The tunability of several physical and chemical properties in metal organic frameworks, such as functionality, surface area, pore size and shape leads to the development of very large family of material with different applications.[53, 66, 72-74]

I.4.4.1. Gas adsorption:

Porous metal organic frameworks can be used in gas storage and selective adsorption. The adsorption behavior is dependent on the pore size, surface area. The adsorption capacity can be optimized by functionalization on the surface and adsorption sites.[75] At low pressure, the attraction of an adsorbate can be maximized by having a pore size similar to the adsorbate and open metal site such as CPO-27[76] and HKUST-1.[77] The pores size can be optimized by impregnation with a nonvolatile guest or concatenation such C_{60} in MOF-177.[75] At high pressures, the surface area is the determining factor for optimal adsorption. For example MOF-177 and HKUST-1 show a very high adsorption capacity for hydrogen (7.5 wt% at 77 and 70-80 bar and 3.6 wt% at 77K and 10 bar, respectively).[77, 78] However, when the temperature increases the hydrogen adsorption drops dramatically. The latter observation impedes a direct application of the existing MOF as adsorbate. However, the possibility to functionalize MOF allows further improvement of the adsorption properties.[79]

MOF-6 with a pore size of 5.9 Å has been tested in methane storage and it is able to uptake 240 cm^3/g at 298 K and 36 bar.[63]

Many reports have been dedicated to separation and purification of H_2 from CO CO_2/CH_4.[55, 80-82]

I.4.4.2. Physical properties:

Electronic, optoelectronic and magnetic properties of different categories of MOFs, IRMOF (isoreticular Metal organic framework), ZIF (Zeolitic Imidazole framework),… have been studied,[74, 83] since the combination of the organic and inorganic parts in one crystal with a well defined electronic environment may lead to enhance the properties of individual components.

Conducting and semi-conducting metal-organic frameworks are well known.[84, 85] Even problems related to the thermal expansion or contraction of semi-conductors can be solved by a judicious choice of the organic and inorganic parts of the crystal and materials with nearly zero thermal expansion can be designed.[86]

Metal organic frameworks that exhibit different luminescent properties have been reported.[74] Works describing non-linear optics are also known.[87]

I.4.4.3. Heterogeneous catalysis with MOF:

Catalysis with metal node:

One of the earliest MOF-based catalysis was reported by Fujita *et al.* in 1994 on the cyanosilylation of aldehydes by 2D square grids framework $Cd(4,4'\text{-bpy})_2(NO_3)_2$, (bpy = bipyridine). The reaction of cyanosilylation of benzaldehyde with a yield of 77% and shape selectivity was observed.[88] Corma et al. have reported a 2D, square grid MOF $[Pd(2\text{-pymo})_2]_n$ (2-Hpymo = 2-hydroxypyrimidine)[89] with activities toward alcohol oxidation, olefin hydrogenation and Suzuki C-C coupling. Albeit interesting, such reaction raises questions regarding the MOF integrity and/or the relevance of MOF defects as active sites since, to complete the catalytic cycle based on the well-known mechanism, the Pd center has to change its oxidation state which inevitably results in bond cleavage and re-orientation at the Pd environment.

Catalysis bimetallic MOF:

Bimetallic MOF containing two different metals have been developed with the aim to use one metal as the active sites and the second to assembly the structure.[90] This approach has successfully been applied for chiral olefin epoxidation by Mn-organic moiety in a Cd [91] or Zn[92] based frameworks. Szeto *et al*. reported bimetallic MOFs containing potentially catalytic C-H active sites at Pt(II) and Gd[93] or Y[94] as corner stones. Xu *et al.* reported promising catalytic oxidation of CO to CO_2 by Cu-organic based metal organic framework.[95]

Catalysis after grafting and post modification:

Metal organic framework can be turned to an active catalyst in principle through different approaches, such as direct incorporation of an active inorganic unit in the structure,[89] or by post synthesis modification and grafting of a catalytically active species on the organic ligand or secondary building unit (SBU)[96, 97] [98] as shown in Figure I.4.

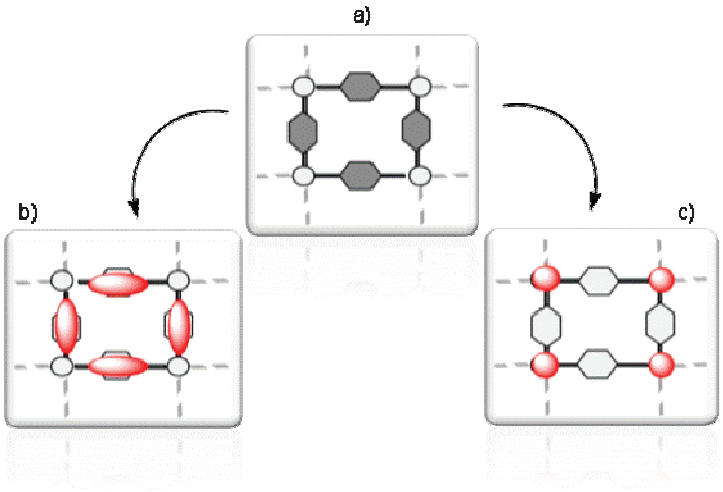

Figure I.4: Illustration of different approaches of incorporating active motif into the metal organic framework by post synthesis modification. a) Starting MOF, b) MOF with organometallic complex denoted by ellipses, c) MOF with active sites on the corner stone denoted with spheres.

Lin and co-workers have reported a homochiral MOF composed of Cd(II) ions as the cornerstone and (*R*)-6,6′-dichloro-2,2′-dihydroxy-1,1′-binaphthyl- 4,4′-bipyridine as a chiral organic building unit.[98] The ligand coordinates to Cd(II) with nitrogen, while the secondary functional group (hydroxyl) remains uncoordinated. Grafting of titanium tetraisopropoxide yielded a bigrafted titanium di-isopropoxide (Figure I.5).

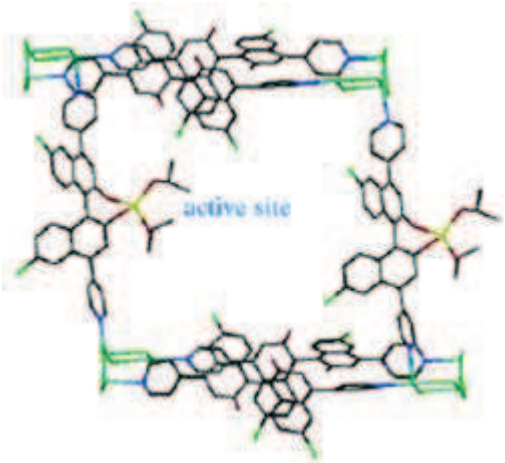

Figure I.5: Schematic representation of channel of a bipnaphtyl- MOF containing an $Ti(O^iPr)_2$ active site.[98]

This modified MOF catalyzes the addition of $ZnEt_2$ to aromatic aldehydes (Scheme I.10).

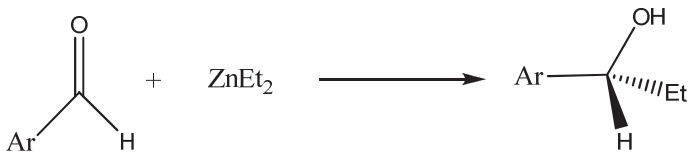

Scheme I.10: Ti(IV)-catalyzed $ZnEt_2$ addition to aromatic aldehydes.

Supplementary tests on the catalytic activity of the Ti-complexes have been performed. Similar results with respect to activity and selectivity were found in the complexes and the corresponding MOFs (Table I.1).

Table I.1: Conversion (conv) and enantiomeric excess (ee) of the $ZnEt_2$ addition to aromatic aldehydes at room temperature catalyzed by an enantiopure binaphtyl ligand in the presence of $Ti(O^iPr)_4$ homogeneous catalyst and binaphthyl MOF containing $Ti(O^iPr)_2$.[98]

Ar	Binol/$Ti(O^iPr)_4$		$Ti(O^iPr)_2$-Binol MOF	
	Conv %	ee %	Conv %	ee %
1-Naph	>99	94	>99	93
Ph	>99	88	>99	83
4-Cl-Ph	>99	86	>99	80
3-Br-Ph	>99	84	>99	80

Zhang *et al.* reported a successfully incorporation of Au(III) cation by post-synthesis modification as shown in the Scheme I.11. [99]

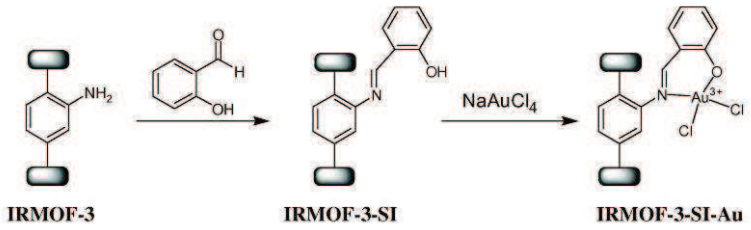

Scheme I.11: Schematic representation of the grafting of gold complex on the ligand of the IRMOF-3.[99]

This catalyst precursor shows activity in multicomponent domino coupling and cyclization of N-protected ethylaniline, aldehyde and amine, yielding the corresponding indole (Scheme I.12).

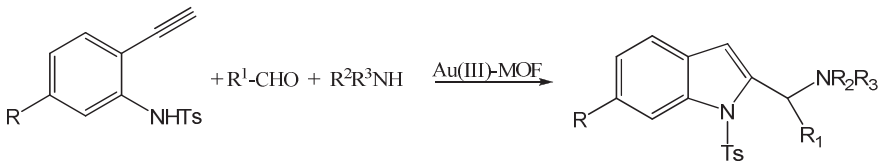

Scheme I.12: Domino three-component coupling and cyclization reaction catalyzed by Au(III)-MOF.

The catalyst has shown enhanced activity compared to soluble gold salt ($AuCl_3$), soluble gold(III) salen complex and gold supported on metal oxide (Au/ZrO_2), as shown in Figure I.6.[99]

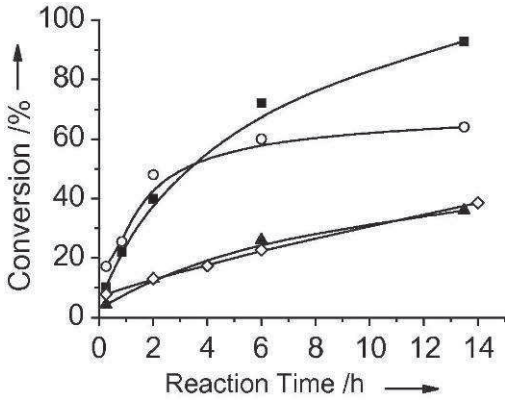

Figure I.6: Catalytic activity over Au(III)-MOF (■ , Au : 0.0008 mmol), Au/ZrO2 (▲ , Au: 0.0014 mmol), homogeneous Au(III) schiff complex (◇, Au : 0.0008 mmol), and $AuCl_3$ (O, gold: 0.025 mmol) for domino coupling and cyclization.[99]

More recently, basic metal organic frameworks have been obtained directly [100] or after post treatment.[101] These materials have shown catalytic activities in reactions such as Knoevenagel condensation.

Another approach has been also described which confine stable nanoparticles in MOF. For example Pd@MOF-5 was demonstrated to be active in selective hydrogenation of styrene to ethyl benzene [102], RuO_2@MOF-5 for oxidation of benzylalcohol to benzaldehyde with oxygen.[103]

I.5. Conclusion and goal of present work:

The structure-activity relationship achieved by surface organometallic chemistry, SOMC, approach in several cases (for example in the case of the most commonly used supports that are those of oxides) has lead to a new generation of catalysts and catalytic reactions. Nevertheless, the field still suffers from the heterogeneity of the starting material, typically amorphous oxides.

The goal of this thesis is to apply the SOMC approach to a perfectly crystalline starting material in order to obtain, after organometallic grafting, perfectly single-site heterogeneous catalysts.

Unlike previous attempts on surface organometallic chemistry on purely inorganic zeolites, whose small pore size limited the extent of grafting (mainly on cages outer rims, with application on gas sorption), this thesis will focus on crystalline large surface area organic-inorganic MOF materials.

In particular, chapter II will report progress on the synthesis of a novel imidazolium containing MOF, on route to N-heterocyclic carbene, NHC, based heterogeneous catalysis.

Chapter III reports the work on novel surface organometallic chemistry on OH residues which are present in MOF existing in literature. The chosen MOFs are UiO-66, $Zr_6(OH)_4O_4L_6(H_2O)_{18}$, (where LH_2 = terephatalic acid, 2-amino tereftalic acid or biphenyl dicarboxylic acid) which contain the OH groups on the cornerstone. Given its novelty, has also required through characterization which is also reported.

Chapter IV reports the surface organometallic chemistry performed on the linker of a known MOF. The chosen MOF is $Ni_2(dhtp)H_2O{\cdot}8H_2O$ (dhtp = dihydroxyterephtale) whose phenyl rings have been functionalized by metal carbonyls. The catalytic performances of the prepared material in hydrodesulfurisation (HDS) reaction have been also reported.
The final chapter will critically assess the results obtained and offer concluding remarks on the relevance of surface organometallic chemistry on MOF for heterogeneous catalysis.

Chapter II:

Synthesis of imidazolium dicarboxylate based ligand, organometallic complex and metal organic framework (MOF)

II.1. Introduction:

Since the first reports of N-heterocyclic carbene (NHC) metal complexes by Öfele[104] in 1968 and the isolation of a stable crystalline N-heterocyclic carbene by Arduengo in 1991,[105] NHCs and their coordination chemistry are an emerging field of research.[106]

From the chemical point of view, N-heterocyclic carbenes are neutral cycles containing divalent six electrons carbon atoms surrounded by two nitrogen atoms .They can be classified according to the Scheme II.1. It has been also demonstrated that the unsaturated carbenes of the type A, B and C show little aromaticity (Scheme II.2).[107, 108]

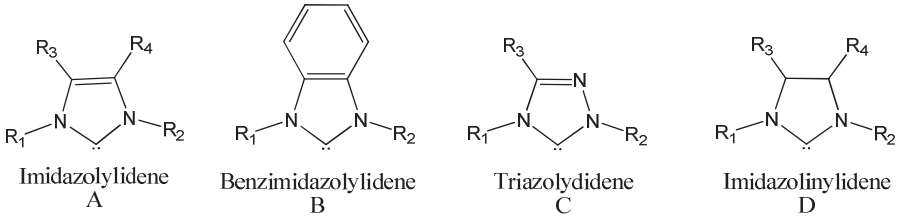

Scheme II.1: overview of different types of NHCs

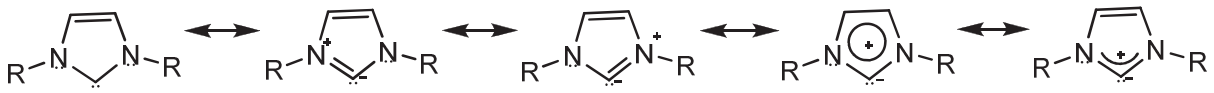

Scheme II.2: Resonance structures of imidazolyl-2-ylidenes.

After the discovery of the remarkable potential of NHC ligands in homogenous catalysis, the researchers in this field focused their attention on the development of large variety of NHC ligands.[106]

II.1.1. Synthesis of imidazolium ligands:

Six synthetic pathways of NHC ligands or their protonated precursors are known to date,[108] as shown below in the Scheme II.3. The first two methods are easy to perform, as they are one-pot reactions and do not require purification of the product. They are therefore the most applied ones.

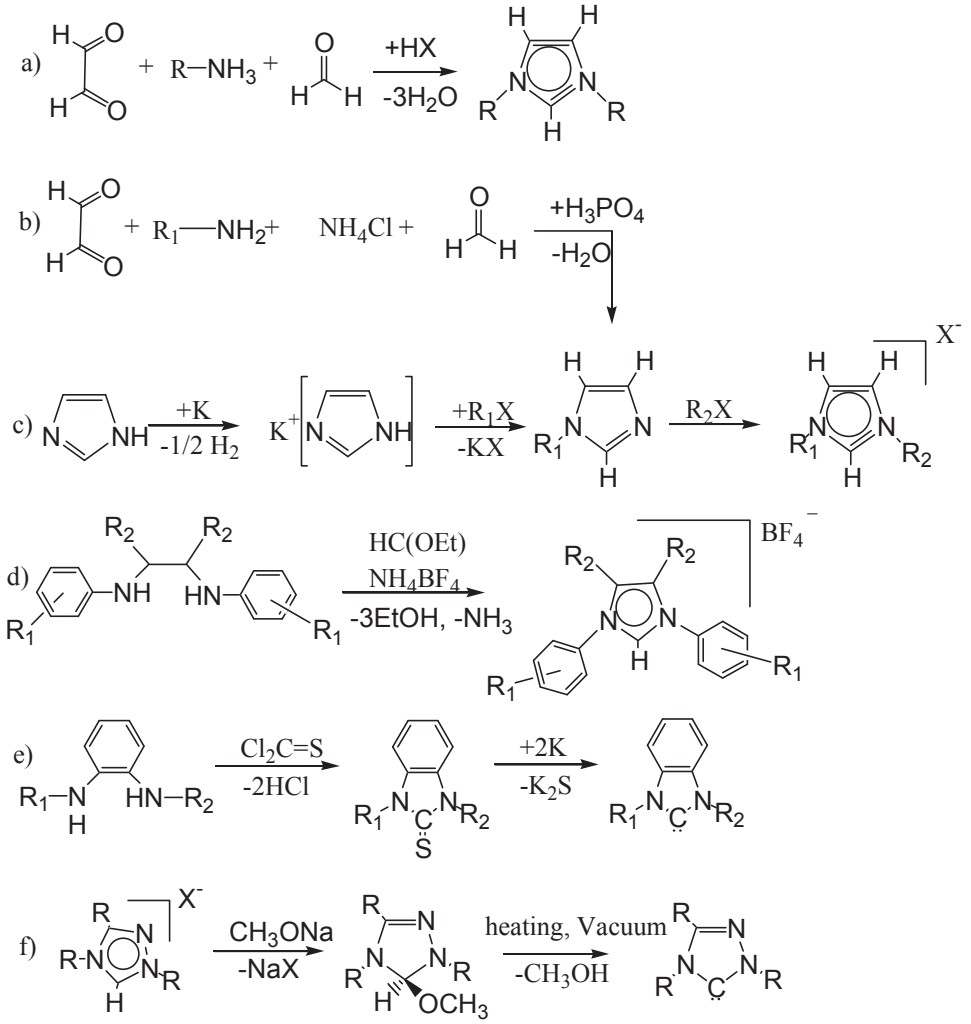

Scheme II.3: Different syntheses of NHC salts.[108]

II.1.2. Coordination chemistry of N-heterocyclic carbenes:

Generally, the free carbene ligands are not stable. Some of them were however isolated in the crystalline form and characterized by X-Ray diffraction. Because of their high chemical reactivity they were subsequently used for the preparation of various metal complexes.[107] Complexation of metals is also possible by metastable carbene species generated *in situ*.[109]

The NHC complexes can be obtained by different ways, for example deprotonation of the imidazoliuml salts with bases (KO^tBu, BuLi, KH,…)[110] or basic solid reagents (K_2CO_3, Cs_2CO_3,..).[109, 111] Insertion of CO_2 or CS_2 and consecutive elimination of carboxylates or ditiocarboxylates were reported as well.[112] Organometallic complexes with basic ligands ($Pd(OAc)_2$, $NiCp_2$,…) are also able to deprotonate imidazolium salts and exchange their ligands with such obtained carbenes.[106, 108] The other common way is to obtain a silver

complex of the carbene (using as a silver source $AgOC(CF_3)_3$, AgOAc, Ag_2O,…) and perform a transmetallation reaction.[106, 113, 114] Different synthetic methods of obtaining NHC metal complexes are summarized in Scheme II.4.

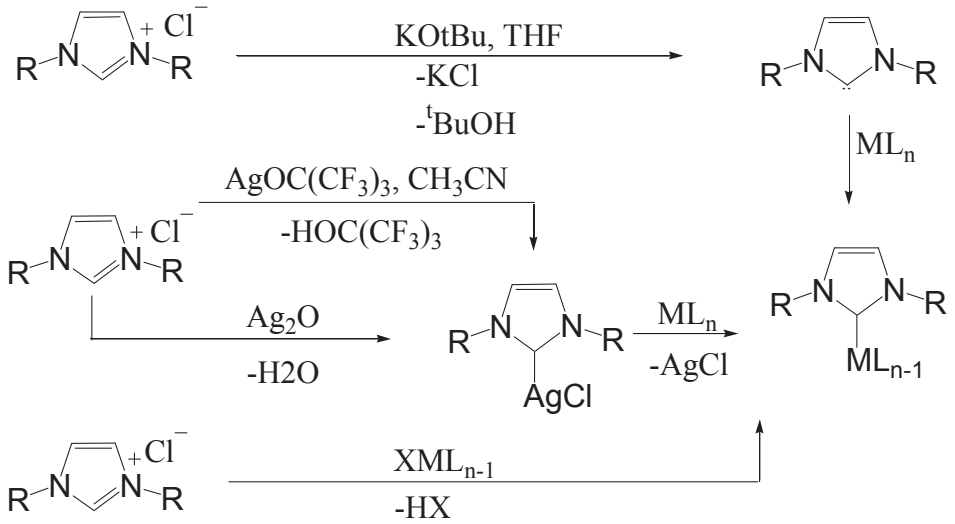

Scheme II.4: Various methaods of formation of NHC-complexes with transition metals.

Metal complexes based on carbenes were initially divided into two different families according to the type of metal carbon bond:

a) Fischer type carbenes complexes-with a σ- bond from the carbon to the metal and strong π-back donation. The carbon atom of the carbene is electrophilic.

b) Schrock type carbenes complexes - characterized by covalent bond resulting from the interaction between carbene's carbon and the metal.

Recently it was shown that all NHC carbene complexes can be rather considered as Fischer type with varying degree of π back donation, because of the presence of nitrogen atoms in the α position to the carbon of the carbene.[115-118]

Because of electron delocalization, NHC complexes can be represented graphically in different forms as shown in Scheme II.5. In practice, simplified B representation is adopted.[106]

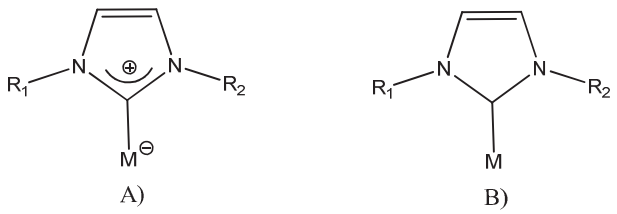

Scheme II.5: Different representations of metal-NHC bond.

As ligands, the nucleophilic NHCs are strong two-electron σ–donors with only little backbonding character, displaying similar ligand properties as trialkylphosphines.[104, 119] In comparison to metal complexes with organophosphines, their analogues with NHCs demonstrate higher chemical and thermal stability, and they were shown to possess catalytic activity in numerous reactions, the second generation of Grubbs' catalyst for olefin metathesis being a prominent example.[120, 121]

II.1.3. NHC metal complexes in catalysis:

The NHC metal complexes are widely used in catalysis because of relative simplicity in imidazolium ligands preparation, the chemical and thermal stability of the metal NHC ligand bond and their interesting properties.[122]

II.1.3.1. Homogenous catalysis:

The substitution of one neutral ligand (tricyclohexylphosphine) in the metathesis-active ruthenium alkylidene complex (complex A in the Scheme II.6) with a bulky N-heterocyclic carbene (NHC) ligand (complex B in Scheme II.6) leads to the formation of a very active catalyst with high functional group tolerance and thermal stability.[120]

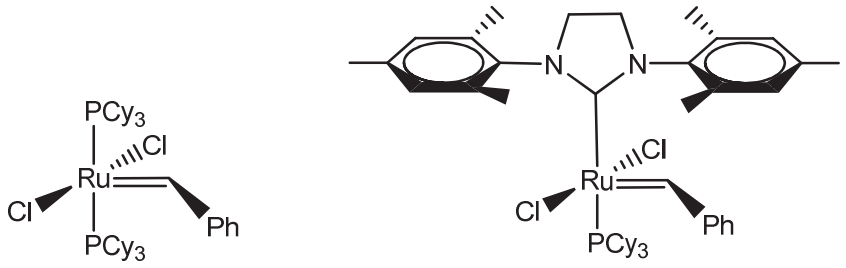

A B

Scheme II.6: First and second generation Grubbs ruthenium based metathesis catalyst.[120]

Kantchev *et al.* reviewed the palladium complexes of NHC and their application in cross coupling reaction.[106] Other examples of catalytic processes involving NHC transition metal complexes were gathered by Herrmann.[123] Chiral N-heterocyclic carbene-transition metal complexes have been also developed and used in asymmetric catalysis.[124]

II.1.3.2. Heterogeneous catalysis:

NHC metal complexes have been grafted on polymers and used for olefin metathesis leading to heterogeneous systems active in ring-closing metathesis and cross-metathesis.[125] Thieuleux *et al.* have developed another strategy based on organic inorganic hybrid materials (Scheme II.7). In this case the ligand precursors are incorporated in the structure of the silica (in the pores or in the walls) and then functionalized with organometallic complexes. Such catalysts were successfully tested in olefin metathesis [114] and C-H activation.[126]

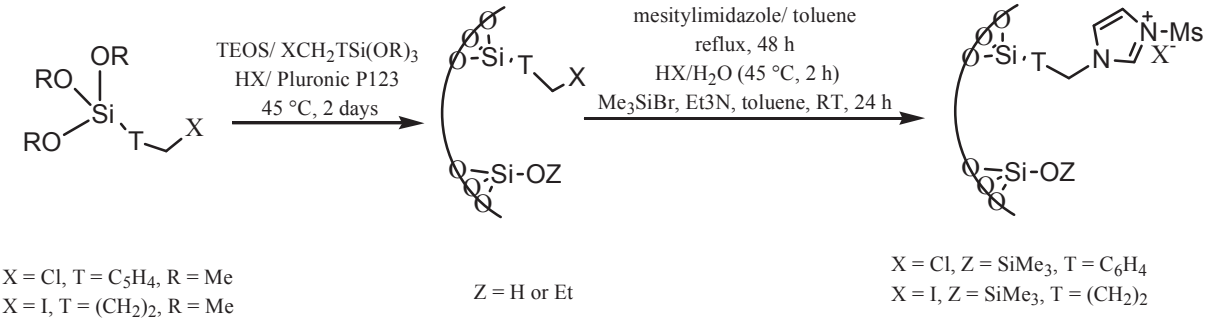

Scheme II.7: Preparation of hybride silica functionalized in the pores with imidazolium ligand.[114]

This work aims to develop novel MOFs having accessible imidazolium rings in the framework and further utilize these sites for post synthetic deprotonation to obtain single site NHC-based heterogeneous catalyst. In order to prepare a well controlled catalyst via surface organometallic chemistry on the metal organic framework, a MOF with permanent porosity and secondary functional groups on the organic linker are required.

Yaghi *et al.* have reported Zeolitic imidazolate frameworks, (ZIFs)[127, 128] characterized by their high surface area and high thermal and chemical stability, but suffer from very small pores, since the organic linker is only imidazole with no organic substituents.

In our approach the imidazolium ring contains two aromatic groups in the N, N' positions, which should confer larger pores and more stability to the ensuring MOF. Recently, a 1D NHC based metal organic framework has been described.[129, 130] During the course of this thesis, and after the experimental work was completed, a promising imidazolium based MOF have been reported by Yaghi[131] where a NHC-Pd have been successfully achieved, along the lines of our own work.

II.2. Results and discussion:

In order to obtain a robust and porous MOF, sturdy and wide organic linkers are necessary. Functionalization of the imidazolium ring with 4-carboxyphenyl subsitutents was chosen, rather than only with the carboxylates on the N, N' positions, leading to the target molecule 1,3-bis (4-carboxyphenyl)imidazolium (scheme II.8).

II.2.1. Synthesis and characterization of the imidazolium linkers:

Imidazolium salts can be manufactured by reacting glyoxal, ammonia, aldehyde, and optionally a primary amine, in the presence of a Brønsted acid. The procedures described by Liu *et al*.[132] suffered from low purity of the product and low yield. Arduengo et al.[133] reported an improved procedure. By employing a polar non protic solvent (THF or dioxane) and only catalytic amount of acetic or formic acid, a further improvement of the synthesis have been achieved. Following the modified procedure, the targeted ligand was obtained in one step with improved quality and yield (88%). The linker 1,3-bis(4-carboxyphenyl) imidazolium chloride ($\mathbf{L_2}$Cl) was obtained by reacting para amino benzoic acid ($\mathbf{L_1}$), with paraformaldehyde (0.5 eq) in the presence of formic or acetic acid (catalyst), and glyoxal in dioxane or THF followed by addition of hydrochloric acid (Scheme II.8).

By replacement of hydrochloric acid with the corresponding acid in the synthesis procedure the analogues bromide and iodide linkers were also obtained.
Since the aim of this work is to eventually obtain an organometallic derivative out of the imidazolium ring inside the MOF framework, the methylated ester of the linker $\mathbf{L_2}$ was also synthesized, $\mathbf{L_4}$, in order to serve as a soluble model of the MOF to optimize and find a successful functionalization route prior to the MOF synthesis.

The 1,3-bis (4-methyl acetate phenyl) imidazolium halides, $\mathbf{L_4}$X (X = Cl, Br, I) were hence obtained by the same procedure described above via para amino methyl benzoate, $\mathbf{L_3}$ (Scheme II.8). The hydrolysis of the $\mathbf{L_4}$ with a base (LiOH) can be used to recover the unprotected acid $\mathbf{L_2}$ but with 55% yield.

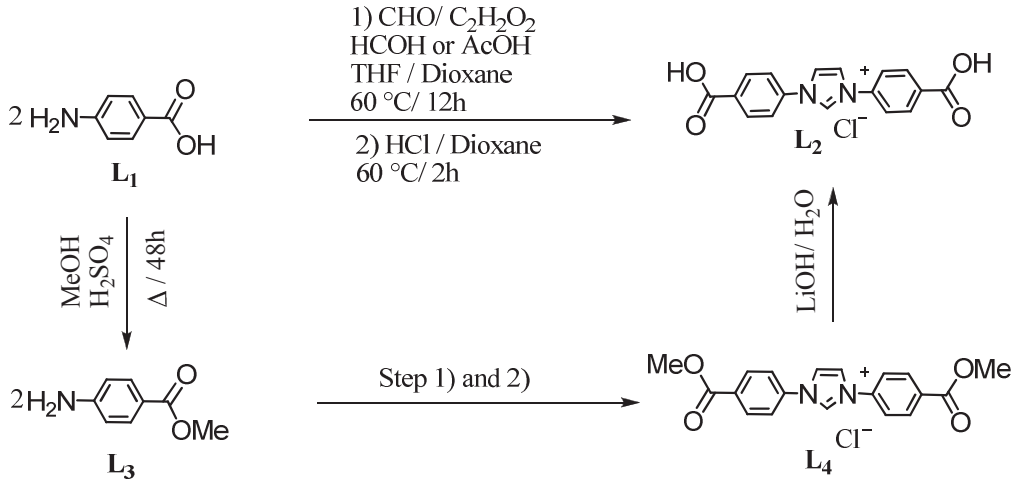

Scheme II.8: Schematic representation of the synthesis of 1,3-bis(4-carboxyphenyl)imidazolium chloride, $\mathbf{L_2}$, and 1,3-bis (4-methyl acetate phenyl) imidazolium halides, $\mathbf{L_4}$.

Tetracarboxylic linkers rather than the dicarboxylic linkers have the tendency to form a well-known paddle-wheel arrangement with metal center such as copper.[134] We have therefore synthesized the chloride, bromide and iodide salts of linker 1,3-bis (3,5-dicarboxylphenyl) imidazolium, $\mathbf{L_7}$, tailored toward MOF synthesis, and its ester analogues, 1,3 bis (3,5-bis methyl acetate phenyl) imidazolium, $\mathbf{L_8}$, for solution modeling reaction.

Ligands $\mathbf{L_7}$ and $\mathbf{L_8}$ can be obtained as depicted in scheme II.9 in analogy with the previous procedure (used for $\mathbf{L_2}$ and $\mathbf{L_4}$) starting from $\mathbf{L_5}$ (aminoisophtalic acid) with yield of 90% and 88%, respectively, for the chloride. All the products were characterized by ^{1}H, ^{13}C NMR, ES HRMS, and elemental analysis. (See experimental part).

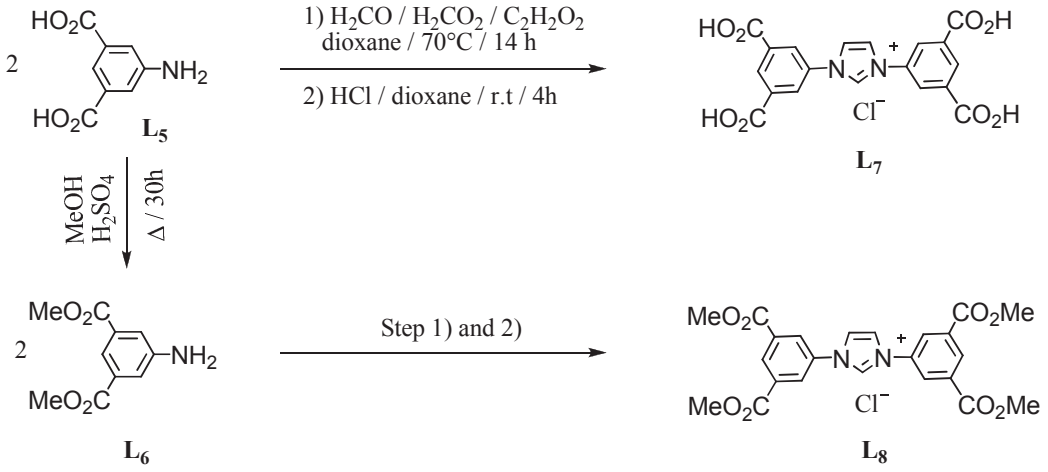

Scheme II.9: Schematic representation of the synthesis of 1,3-bis(3,5-dicarboxyphenyl)imidazolium $\mathbf{L_7}$ and 1,3-bis(3,5-bis(methoxycarbonyl)phenyl)imidazolium chlorides, $\mathbf{L_8}$.

Other counter ions (BF_4^-, $(F_3CSO_2)_2N^-$ and PF_6^-) have been tried either by substituting the acid in the procedure outlined above, or by counter ion exchange from the chloride salts, but no reaction took place.

All attempts to obtain analogues ligands via the same synthetic pathway using either dimethyl- or dichloroglyoxal failed before the final addition of hydrochloric acid.

As will be detailed later the imidazolium linkers described here resist to the deprotonation reaction, presumably because of the counter productive –I inductive effect impressed by the carboxy substituted phenyl ring on the imidazolium heterocycles.

In order to lessen this inductive effect, the linker 1,3-bis(4-carboxybenzyl)imidazolium chloride, $\mathbf{L_{11}}$, and its ester analogues $\mathbf{L_{12}}$ were also synthesiszed using the same experimental procedure as before (Scheme II.10). The three new linkers with methylene-bridge between the phenyl ring and the imidazolium unit were synthesized, in form of chloride, bromide and iodide. The structures were confirmed by NMR-spectroscopy.

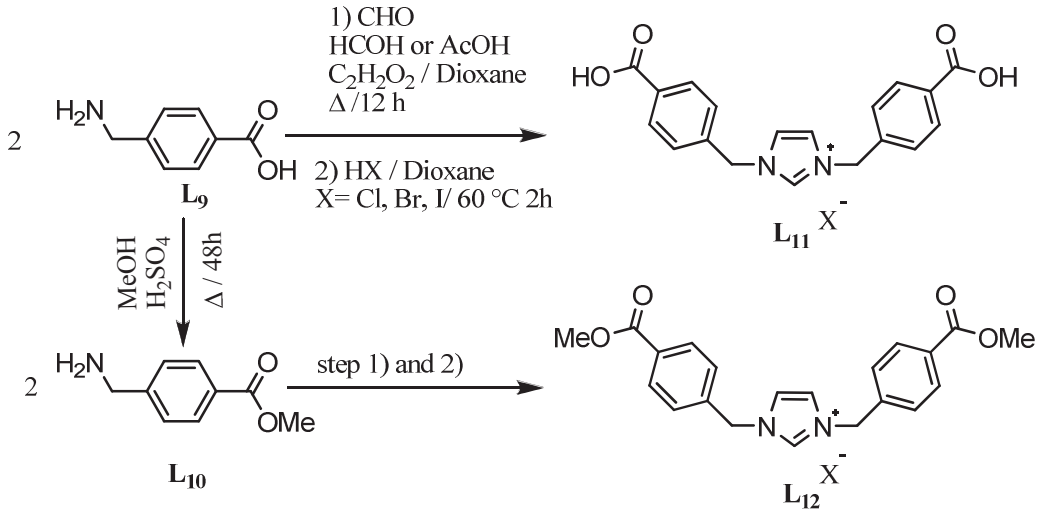

Scheme II.10: Schematic representation of the synthesis of 1,3-bis(4-carboxybenzyl)imidazolium $\mathbf{L_{11}}$ and 1,3-bis(4-(methoxycarbonyl)benzyl)imidazolium $\mathbf{L_{12}}$ halides.

The insertion of a methylene unit between the N-heterocycle and the carboxy phenyl linker is expected to change the inductive effect which should be favorable toward deprotonation steps of the imidazolium ring. At the same time, the presence of this unit should increase the flexibility of the linker, which is expected to weaken the rigidity of the putative MOF.

In order to keep a moderate –I effect, while retaining a rigid linker, the mono-substituted imidazole (4-imidazolyl-benzoic acid **L_{15}**), and its ester analogues **L_{16}** were synthesized. Imidazol ligand species with only one aromatic side chain were obtained from **L_1** and **L_3** by addition of ammonium that gives a neutral compound (Scheme II.12). These ligands were characterized by NMR-spectroscopy and elemental analysis.

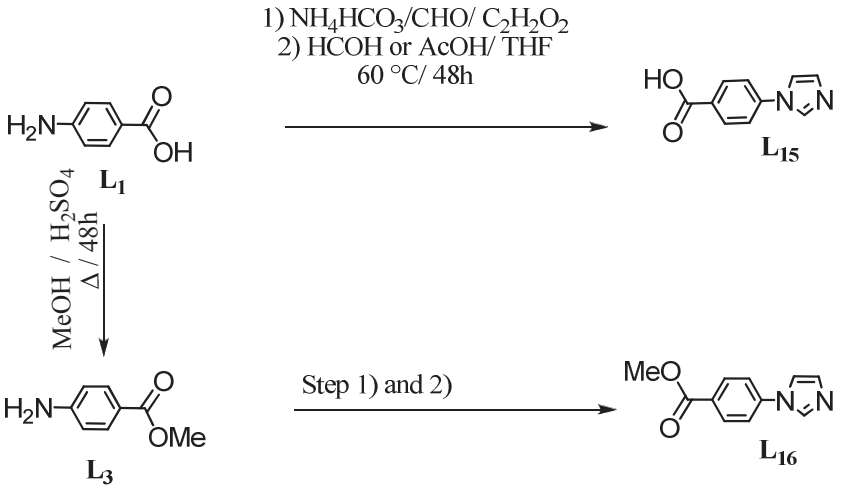

Scheme II.11: Schematic representation of the synthesis of 4-imidazolyl-benzoic acid **L_{15}** and methyl 4-imidazol benzoate **L_{16}.**

Unlike the previous cases such linkers are not expected to be precursors to NHC carbenes since the CH proton of the neutral imidazole does not display acid behavior. At the same time, N-atoms of imidazole rings are known to be good coordinating atoms. Imidazole cycles have given rise to the very large family of ZIF-type MOFs.[135]

Linker **L_{15}** should therefore constitutes a good candidate for novel MOF since carboxylate moieties and imidazole N-atoms coordinate strongly to metal center. Such bifunctional ligand applied to MOF synthesis has never been reported before.

II.2.2. Synthesis and characterization of novel MOF based on imidazolium containing ligand:

Once the desired linker is synthesized, the synthesis of novel MOF structures with desirable properties (in our case high surface area, spacious permanent porosity upon solvent removal, grafting site accessibility,…) is still a very difficult challenge to overcome.

It has been claimed that it remains in general impossible to predict the structure of even the simplest crystalline solids from knowledge of their chemical composition.[136] In

general, a high-through put method, with parallel synthesis varying the parameters known to affect the crystallization process of MOFs, efficiently leads to find the optimal synthesis conditions.

From the linker 1,3 bis (4-carboxyphenyl) imidazolium chloride, L_2Cl, a series of syntheses involving variation of different parameters such as solvent, cornerstone, temperature, time, dilution, stoichiometric ratio of linker to metal, pH (Table I.1) were carried out.

Table II.1: Different parameters varied in the 150 non-parallel synthesis of MOF with linker **L_2**Cl (100 mg).

Cornerstone	$ZrCl_4$, $Zn(NO_3)_2$, $Cd(NO_3)_2$, $Ce(NO_3)_3$, $Co(NO_3)_2$, $Cr(NO_3)_3$, $Ba(NO_3)_2$, $Cu(NO_3)_2$, $Pt(NO_3)_2$, $Mg(NO_3)_2$, $Fe(NO_3)_3$, $La(NO_3)_3$, $Y(NO_3)_3$, $Nd(NO_3)_3$.
Solvent	MeOH, THF, Toluene, DMF.
Temperature (°C)	120, 115, 110, 95, 80, 75.
Time (h)	48, 24, 12.
Dilution (ml)	15, 10, 5.
[metal]/[ligand]	2, 1.5, 1, 0.5
Other additives	NaOH, HCl.

The achievement of MOFs under the given conditions was challenging; in most cases the products were either poorly crystalline or amorphous solids. Herein, only crystalline and reproducible materials are reported.

The screening techniques used to assess whether the reaction was successful was X-Ray powder diffraction. Upon detection of a novel phase with respect to the starting reagents, the material obtained was analyzed using single crystal X-ray diffraction, microanalyses, IR, solid state NMR, BET and thermo-gravimetric analyses (TGA).

II.2.2.1. Synthesis and characterization of the novel MOF LCH-1:

A crystalline solid, **LCH-1**, was obtained when 1,3-bis(4-carboxyphenyl)imidazolium chloride, **L_2**Cl, reacted with three equivalents of $Zn(NO_3)_2 \cdot 6H_2O$ at 80 °C for 12 h followed by 24 h at 115 °C in glass vials or teflon-lined autoclaves. The two temperature step was found to be favorable to obtain a crystalline phase, while 3 days heating at 80 °C gave no precipitate. A synthesis by heating directly at 115 °C gave amorphous product.

The procedure was also successful when the bromide, $\mathbf{L_2}$Br, and iodide, $\mathbf{L_2}$I, salts of the linker were used. The three solids, corresponding to the three different counterions were first characterized by X-ray powder diffraction and thermogravimetric analysis. Figure II.1 shows the powder X-ray diffraction and TGA patterns of the corresponding MOFs, **LCH-1**-Cl, **LCH-1**-Br and **LCH-1**-I.

X-ray diffraction patterns confirm that the peaks of the free ligands have disappeared and a novel crystalline phase is formed. While the iodide derived material gives a low quality diffraction pattern, both the chloride and the bromide derived materials display very similar well-resolved sharp peaks.

The TGA curves are described by a moderate weight loss from room temperature to 350 °C, which is expected to be associated to solvent (DMF) removal in analogy to most literature reports, followed by rapid decomposition at 350 °C. The decomposition temperature of the MOFs and the corresponding linkers are similar.

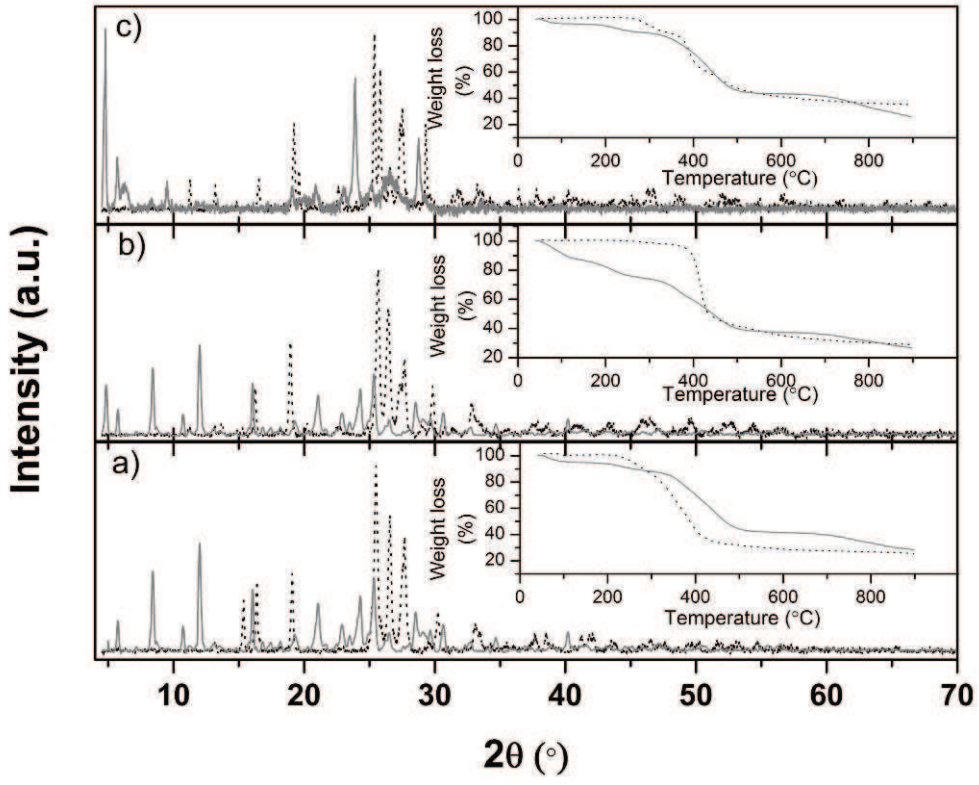

Figure II.1: X-Ray diffraction patterns and TGA profiles of linkers $\mathbf{L_2}$X (dotted lines) and corresponding material (solid lines) of a) **LCH**-1-Cl; b) **LCH**-1-Br; c) **LCH**-1-I.

The solid obtained from the chloride salts of the linker, **LCH-1**-Cl, which displays a well behaved weight loss in the TGA curve and well resolved peaks in the XRD

diffractogram, was analyzed by single crystal X-Ray diffraction. While the complete resolution of the structure is still in progress, the current level of refinement allows to understand some features of the framework arrangement. The structure is indeed a Metal Organic Framework (MOF) where each linker is coordinated to two different cornerstones (zinc atoms) with its carboxylic moieties. The cornerstones consist of single tetracoordinate zinc atom.

The local environment of zinc consists in three η^1-coordinated carboxylates. Moreover, one solvent molecule is localized on the Zn and results in a distorted tetrahedral geometry as depicted in Figure II.2.

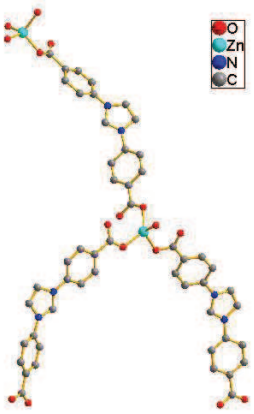

Figure II.2: Local structure representation of the cornerstone of material **LCH-1**-Cl.

The extended structure is constituted of closed ring composed of three ligands and three metal centers being interconnected by another ligand and results in a 2D structure (Figure II.3).

Unfortunately, the C-H moiety in the 2 position of the imidazolium ring, that is the carbon expected to deprotonate to give NHC ligand, points away from the pores (and inside the wall). The absence of Zn atom in the vicinity of the acidic C-H indicates that the ring is not a carbene since it would behave as a Lewis base and hence interact with the only acid present in the system which is the zinc atoms. Therefore, the linker is still under its imidazolium form. Based on elemental analyses data presented below, that discard the presence of halogen and DMF, the pores remain filled with water. The level of refinement does not allow the positioning of the solvent molecules.

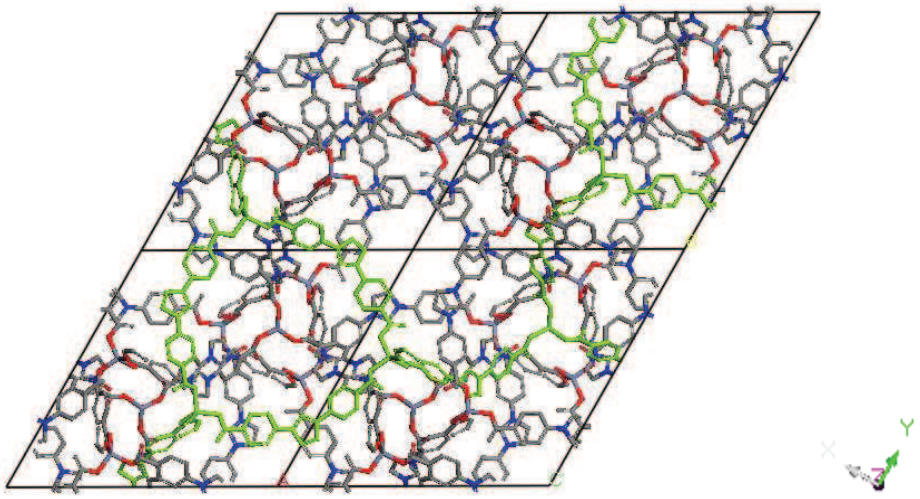

Figure II.3: 3D structure of the **LCH-1**-Cl-MOF.

The current hypothesis for the stoichiometry of the **LCH-1** MOF, taking into account the charge neutrality of the crystal, is $[Zn_2(\mathbf{L_2})_2(\mathbf{L_2}\text{-H})(OH)_2]\cdot(H_2O)_x$ where $\mathbf{L_2}$ is the 1,3 bis (4-dicarboxylatephenyl)-imidazolium linker, whose charge is overall monoanionic. Two such ligands are coordinated via both the deprotonated carboxylic groups present on the linker. The third organic linker is considered under its formally monoprotonated version, $\mathbf{L_2}$-H, hence overall neutral, for which the two coordinations to the zinc atoms to either end of the linker are different, namely: (i) coordination of the carboxylate to one zinc atom and (ii) coordination of the carbonyl moiety of the carboxylic acid group to the second zinc atom. This proposal has the advantage to offer one single coordination sphere for all the zinc atoms in the crystal, with respect to the alternative and equally formally correct $[Zn_2(\mathbf{L_2})_3(H_2O)(OH)]\cdot(H_2O)_x$. In fact, the formal localization of the protons on a linker or on an hydroxyl lignad is arbitrary since very strong hydrogen network are expected in the crystal. Furthermore, none of the hydrogen atoms could be localized in our study due to poor crystal quality.

The quantities of C, H, N, Zn, for different MOFs are similar. The halogen content of is very low in the three MOFs (1% Cl for **LCH-1-**Cl, 0.4% Br for **LCH1**-Br, and less than 0.2 for the **LCH1**-I), since the halides can easily be replaced by NO_3^-. The MOFs obtained was not influenced by the counter ion. The elemental analyses of different elements of the three MOFs (**LCH-1-**Cl, **LCH-1**-Br, **LCH-1**-I) are not in concordance with the expected from the molecular structure described above. In order to explain the discrepancies observed for the elemental analysis, one more zinc nitrate molecule can be assigned, suggesting that an

equivalent of amorphous $Zn(NO_3)_2$ salts coprecipitates with the MOF during **LHC-1** synthesis.

Table II.2: Elemental analyses of the three MOFs **LCH-1** and the calculated for (1) $Zn_2(L_2)_3(H_2O)_2$ and (2) $Zn_2(L_2)_3(H_2O)_2$ $Zn(NO_3)_2$.

	Experimental			Calculated	
	LCH-1-Cl	**LCH-1**-Br	**LCH-1**-I	Expected for (1)	Expected for (2)
% C	46.23	46.01	42.96	56.00	47.81
% H	3.63	3.76	4.03	3.70	3.14
% N	8.47	9.23	8.94	7.70	8.74
% Zn	13.00	10.11	13.89	12.00	15.31
C/Zn	19.3	24.60	16.70	25.50	17.00
N/Zn	3	4.00	3.00	3.00	2.60
C/N	6.3	5.80	5.60	8.50	6.37

The synthesized solid **LCH-1-**Cl has been characterized by ^{13}C solid state cross polarization magic angle spinning nuclear magnetic resonance (CPMAS NMR). Part a) of Figure II.4 represents the ^{13}C liquid state NMR of the imidazolium ligand in deuterated DMSO, where the different carbons are successfully attributed based on analogy to literature data. ^{13}C solid state NMR spectra of both the ligand and the corresponding MOF are presented in Figure II.4 parts b) and c), respectively. The resonances are rather broad and hence the assignment of every carbon atoms is difficult, in particular those with similar chemical shifts. Nonetheless, the main resonances of the linker are found in the solid state spectra. In the MOF **LCH-1-**Cl, the most salient features are the severe broading of the carboxylic carbon resonance and the otherwise mostly unchanged resonances of the rest of the linkers carbon atoms. Unfortunately, no conclusive comment can be made on the imidazolium CH carbon. The most pronounced displacement is C_a which is shifted by 6 ppm with respect to the starting linker due to Zn-carboxylate coordination. The materials **LCH-1-**Br, and **LCH-1-**I were analyzed by CP MAS ^{13}C NMR and similar spectra were obtained.

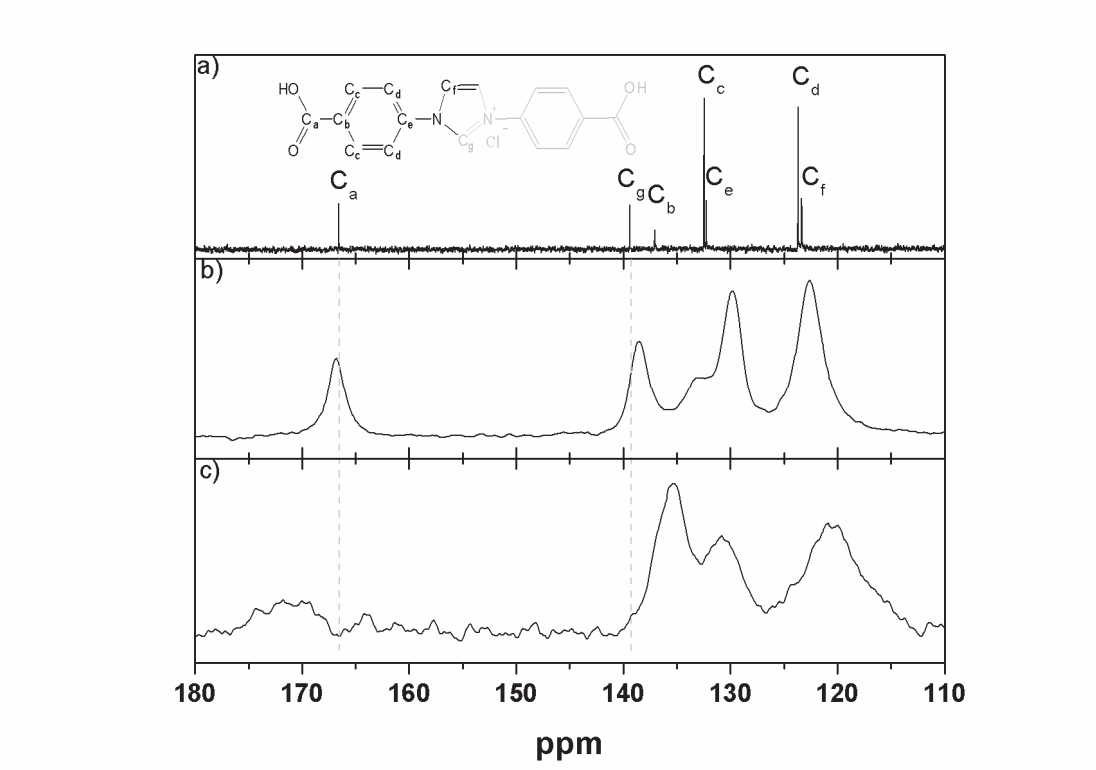

Figure II.4: NMR spectra of a) liquid state d_6-DMSO) of ligand $\mathbf{L_2}$Cl, b) and c) CP MAS solid state NMR of linker $\mathbf{L_2}$Cl and MOF **LCH-1**-Cl respectively (256 scans and d1= 32 second)

After treatment of the three solids (**LCH-1**-Cl, **LCH-1**-Br, **LCH-1**-I) under vacuum at 120 °C overnight the materials were analyzed by N_2 adsorption analyses at 77 K. The results revealed that all MOFs are characterized by very low surface area and very low porosity (Table II.3).

Table II.3: Surface are and pores volumes of different MOFs

Sample	**BET surface area (m^2/g)**	**Langmuir area (m^2/g)**	**Pores Volume (cm^3/g)**
LCH-1Cl	16	25	0.033
LCH-1Br	18	28	0.026
LCH-1I	25	32	0.022

Based on crystal structure Connolly surface of the MOF could be calculated. The MOF is composed of cavities connected by nanopores of less than 2 Å in diameter as shown in Figure II.5, thus preventing any significant accessibility to the internal surface.

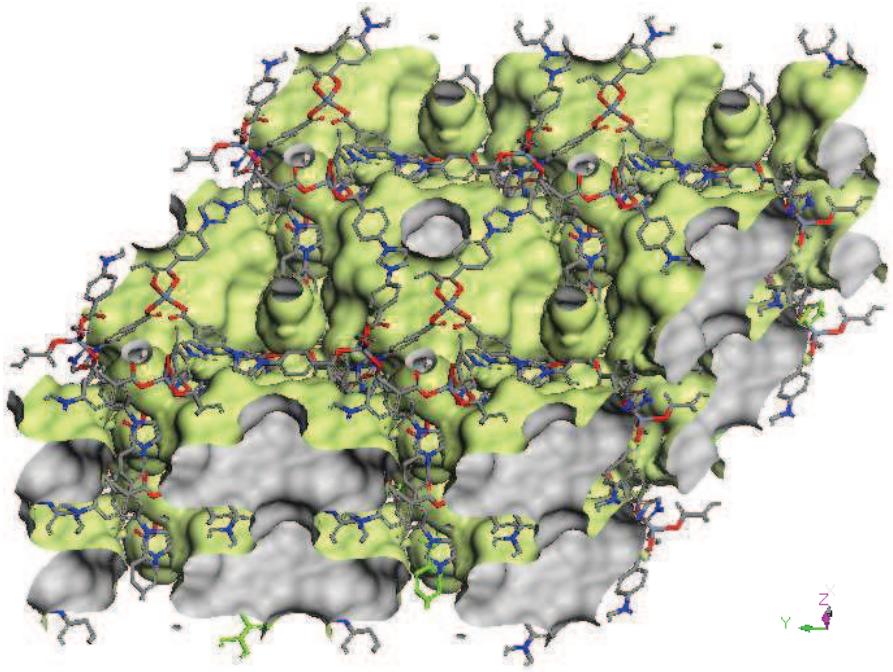

Figure II.5: Connolly surface of **LCH-1**-Cl MOF calculated with a probe radius of 1.55 Å. The green and grey faces represent the interior and exterior surface, respectively.

Because of the low surface area and porosity, a pillaring agent such as 4,4'-bipyridine was introduced in the synthesis in attempt to obtain larger cavities.[137] Only the same crystalline phase with the same porosity and surface area values was obtained.

Attempts to obtain other MOF with the tetra-carboxylate imidazolium ligands described above and different corner stones, especially copper nitrate $Cu(NO_3)_2$ have been tried. Those systems suffered from either poor crystallinity or reproducibility and are not discussed (see experimental section for an example of attempted synthesis).

In summary, by reacting the 1,3-bis(4-carboxyphenyl) imidazolium chloride linker, $\mathbf{L_2}$Cl, with a zinc salt, $Zn(NO_3)_2$, a nanoporous MOF where each linker bridge a tetracoordinated metal atom was obtained. The various analyses suggest that the imidazolium ring is not deprotonated. The very dense paking of the phase prevents any surface organometallic chemistry to take place on such MOF.

II.2.2.2. Synthesis and characterization of LCH-2:

The novel mono-substituted imidazol linker 4-imidazolyl-benzoic acid, **L_{15}**, proved to be an interesting building block for the synthesis of new MOFs.

For different syntheses, two different zinc salts ($Zn(NO_3)_2$ and $Zn(CH_3COO)_2$), and each with two different metal:linker stoichiometries (Zn/L_{15} = 1, 2 or 3) were performed in DMF at 115 °C overnight. The products were analyzed by powder X-ray diffraction and thermogravimetry analysis. The diffractograms display sharp peaks at low diffraction angles (Figure II.6). While both materials have almost superposable diffractograms up to $2\theta = 30°$, a poorly crystalline phase with broad peaks between $30° < 2\theta < 70°$ is observed for the acetate synthesis, which is absent for nitrate synthesis. No assignment has been made for this phase, but since the elemental analyses of both materials show that the have substantially same composition, both syntheses can be considered as leading to mainly same MOF structure, which is labeled **LCH-2**. The material **LCH-2** appears to be very stable, as suggested by the TGA curves, which show no substantial weight loss until 400 °C (vide infra).

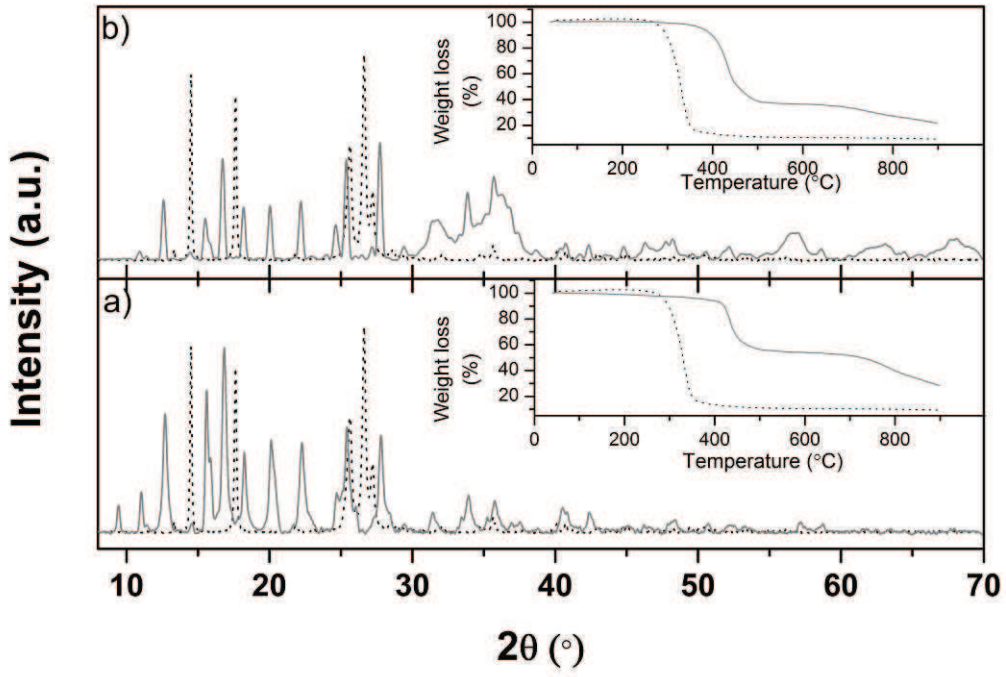

Figure II.6: X-Ray diffraction patterns and TGA profiles of the ligand, **L_{15}** (dotted lines) and corresponding material (solid line) of a) **LCH-2**-NO_3 and b) **LCH-2**-OAc.

The elemental analyses of the both **LCH-2** materials obtained for each salt $Zn(NO_3)_2$, **LCH-2-**NO_3 and $Zn(OOCH_3)_2$, **LCH-2-**OAc, are reported in Table II.3. Both samples contain approximately the same amount of the different elements (C, H, N and Zn). The experimental ratio of C/N = 5.4, which is very close to the ratio of the free linker (C/N = 10/2), indicate that

no solvent molecules (DMF), no nitrates ions from the synthesis with $Zn(NO_3)_2$ are present in the structure of **LCH-2**. The C/Zn = 16.8 corresponds to three linkers for each two zinc atoms. (Table II.4).

The possible formula of the material **LCH-2** is $Zn_2(\mathbf{L_{15}})_3X$, where X is an anion , necessary to ensure the electronic neutrality of the crystal resulting from four positive charge from the metal and three negative charge of the linker. The most likely candidate is the hydroxyl ion, since no presence of the nitrate or acetates or formiates (from the decomposition of the DMF[138]) is suggested by the elemental analyses. In addition three more water molecules can be also assigned, to optimize the agreement with elemental analyses, probably due to the hydrophilic nature of the dried compounds, to end with a formula of $Zn_2(\mathbf{L_{15}})_3(OH)(H_2O)_3$.

Table II.4: Experimental elemental analysis (C, H, N and Zn) of the **LCH-2** materials, experimental and calculated for $Zn_2(\mathbf{L_{15}})_3(OH)(H_2O)_3$.

Sample	% Zn		% C		%N		% H	
	Cal	Exp	Cal	Exp	Cal	Exp	Cal	Exp
LCH-2-NO_3	16.3	16.3	49.6	50.7	10.5	10.9	3.6	3.3
LCH-2-OAc	16.3	16.2	49.6	51.4	10.5	11.1	3.6	3.3

LCH-2-NO_3, **LCH-2**-OAc have been characterized by ^{13}C solid state CP MAS NMR spectroscopy. The spectra were identical. Part a) of Figure II.7 represents the ^{13}C liquid state NMR spectroscopy in deuterated DMSO of the imidazol linker with the proposed assignment for the carbon atoms according to the literature. ^{13}C solid state CP MAS NMR spectra of both the ligand and the corresponding MOF **LCH-2** are shown in Figure II.7 part b) and c) resepectively. The peaks are rather broad and thereby difficult to assign individually, but indicate that the ligand is present and coordinated to the zinc atoms with both carboxylic group and nitrogen atom, since a pronounced displacement is found for C_a, C_g, and C_h which are shifted by 4, 3 and 7 ppm, respectively.

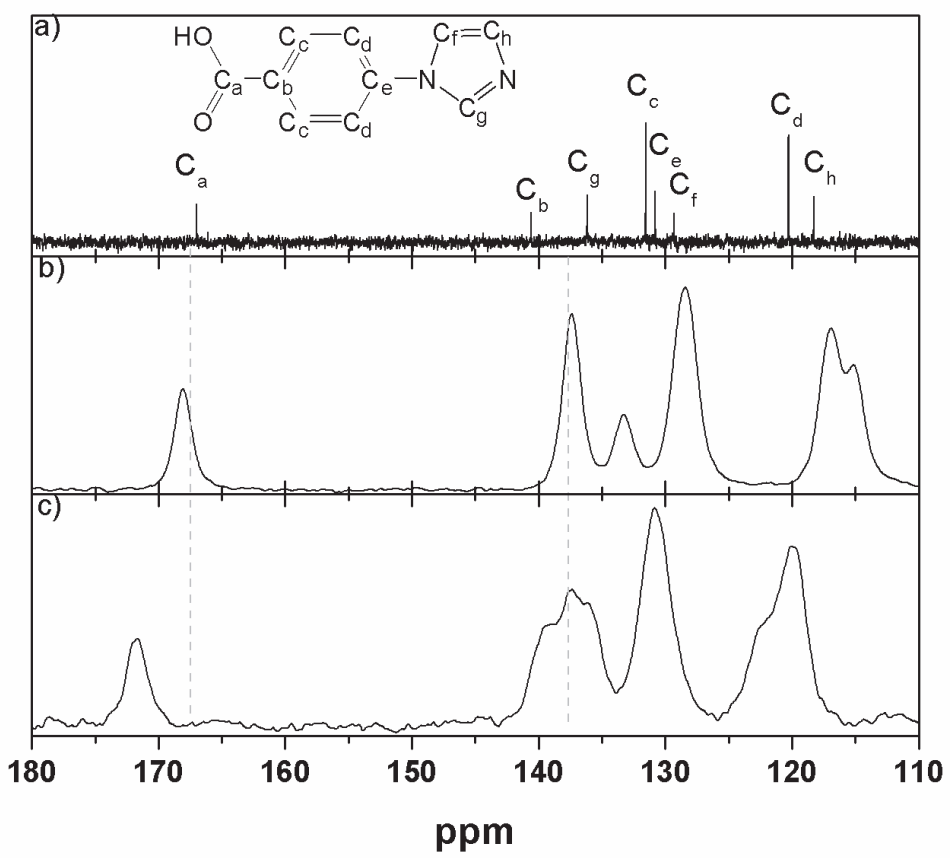

Figure II.7: ^{13}C NMR spectra of a) liquid state NMR of ligand $\mathbf{L_2}Cl$, b) and c) ^{13}C solid state NMR CP MAS of linker $\mathbf{L_2}Cl$ and **LCH-2** respectively (256 scans and d1= 16 second).

Upon mild treatment under vacuum at 135 °C overnight, the N_2 adsorption analyses at 77 K, the materials show some surface area and porosity.

Table II.5: Surface area and pores volumes of different **LCH-2** MOFs.

Sample	BET surface area (m^2/g)	Langmuir area (m^2/g)	Pores Volume (cm^3/g)
LCH-2-NO_3	52 ± 5	130 ± 10	0.093 ± 0.05
LCH-2-OAc	65 ± 5	180 ± 10	0.14± 0.05

These materials are crystalline and thermally resistant. Their low porosities and surface area make them hardly suitable for surface organometallic chemistry approach.

II.2.2.3. Deprotonation attempts of imidazolium linkers:

The imidazolium based MOF obtained above were not porous enough to allow post modification via surface organometallic chemistry. Another approach is to prepare first the organometallic complex containing the deprotonated imidazol ligand (NHC-metal complex) and then attempt the MOF synthesis using this metal organic complex as linker.

To obtain a NHC carbene from an imidazolium ring, the presence of a base is necessary. Since the deprotonated species, that is the NHC carbene, is rarely stable under such condition (few counter examples have been mentioned in the introduction), the concomitant presence of a coordinating metal complex is also required. We have attempted the *in situ* deprotonation of the linkers 1,3-bis(4-carboxyphenyl)-imidazolium chloride, $\mathbf{L_2}$Cl, with potassium hexamethyldisilazane, $C_6H_{18}Si_2N^-K^+$, KHMDS, which is a strong base in the presence of one equivalent of either Au(I) tetrahydrothiophene gold chloride, $Au(C_4H_8S)Cl$, or Ir(III) pentamethylcyclopentadienyl dichloride Cp^*IrCl_2, both having been successfully applied to similar reactions in the literature.[126, 139]. In our case, when the reaction is carried out at room temperature or below 50 °C, no deprotonation of the imidazolium ring was observed by *in situ* ^{1}H liquid state NMR spectroscopy. However, when the reaction is heated at 60 °C or above, a black precipitate is observed.

Since such route does not appear to lead to a well-defined soluble NHC-organometallic complex, we explored another deprotonation agent. Silver oxide, Ag_2O, is a good candidate to perform the desired reactions since it acts both as a base yielding a mild conjugated acid, and as a source of metal stabilizing NHC precursor, (see example of the target reaction in Scheme II.12).

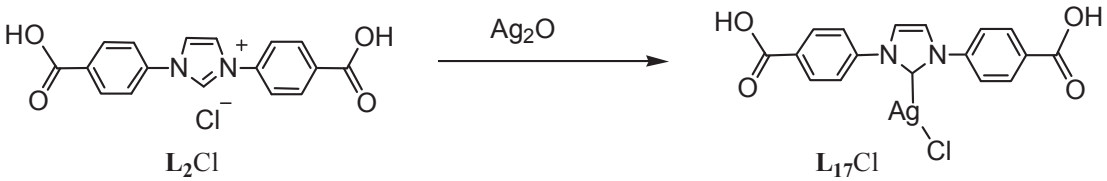

$\mathbf{L_2}$Cl $\qquad$ $\mathbf{L_{17}}$Cl

Scheme II.12: Schematic representation of the targeted Ag-NHC carbene with $\mathbf{L_2}$Cl.

Reactions under different synthetic conditions such as temperature, solvent and concentration of reactants were performed. When the experiments were carried out below 50 °C and followed by ^{1}H liquid state NMR spectroscopy, the spectra showed always the characteristic signal of imidazolium proton, suggesting that no deprotonation had taken place and hence no silver complex had been formed. However, reactions carried out above 60 °C lead to a grey precipitate, still containing considerable amount of unreacted Ag_2O. NMR

analyses showed the complete disappearance of the linker from the solution. X-Ray diffraction analyses of the powder obtained confirmed the presence of both the ligand and the silver oxide, but no new well defined phase. These results might suggest that no reaction well defined did take place between the linker and the silver oxide.

The presence of carboxylic acid groups in the linker 1,3-bis(4-carboxyphenyl)-imidazolium chloride, $\mathbf{L_2}$Cl, can prevent a selective reaction of silver towards the imidazolium proton, since both the carboxylic acid group and/ or the imidazolium ring could be deprotonated. Hence, the ester version of the linker, that is 1,3-bis(4-(methoxycarbonyl phenyl)-imidazolium chloride, $\mathbf{L_4}$Cl, was used to investigate the reaction with Ag_2O under different operating conditions (See experimental section).

As in the case of 1,3-bis(4-carboxyphenyl)-imidazolium chloride, $\mathbf{L_2}$Cl, linker, no soluble silver adduct of the NHC corresponding to the $\mathbf{L_4}$ linker was observed.

The next approach was to use an imidazolium linker containing a benzyl group between the imidazolium ring and the carboxylic functional moieties. By moving the carboxylic acid group far from the imidazolium proton could favor the targeted reaction of Ag-NHC formation as represented in scheme II.13

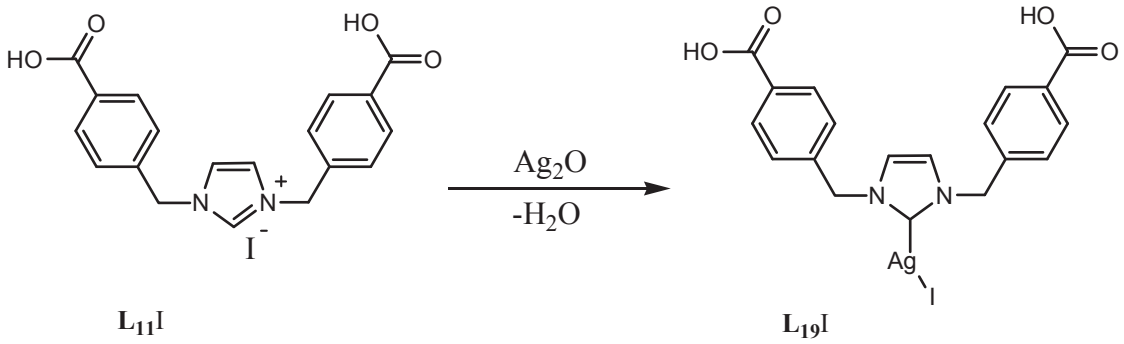

$\mathbf{L_{11}}$I $\mathbf{L_{19}}$I

Scheme II.13: Schematic representation of the targeted preparation reaction of 1,3-bis(4-carboxybenzyl)-imidazolium silver iodide.

The deprotonation reaction of 1,3-bis(4-carboxybenzyl)-imidazolium iodide, $\mathbf{L_{11}}$I, was followed by ^{1}H liquid state NMR spectroscopy. No reaction was observed below 80 °C. The kinetic of the reaction was studied at 80 °C in a Young NMR tube. Copious amount of $\mathbf{L_{11}}$I, was dissolved together with the silver oxide in DMSO.

^{1}H NMR spectra were recorded at different reaction times. After integration, taking into account the slight shifts between reactant and product signals, the reference peak at $\delta = 5.5$

ppm was set equal to an integral of 4. The other peaks preserve essentially the area except a decrease of the peak at δ = 9.4ppm, which corresponds to the isolated proton in the imidazolium ring (Figure II.8). Therefore, the desired deprotonation reaction appears to occur. Characterization of the product is underway. Attempts to build a MOF with this organometallic linker have not been made so far.

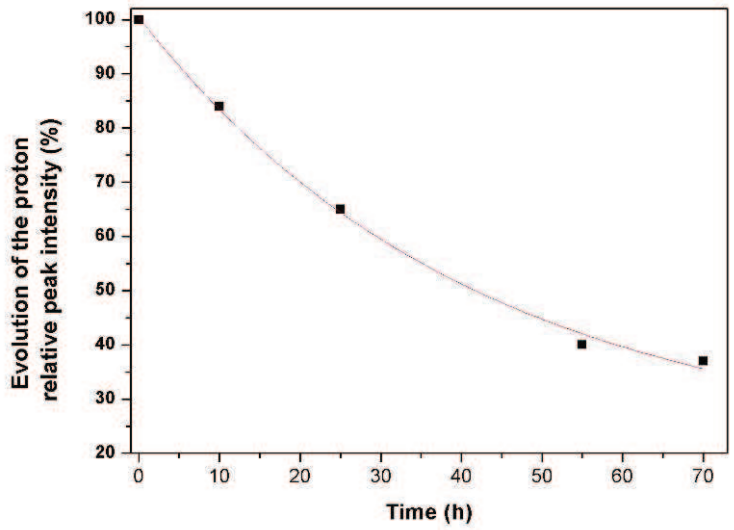

Figure II.8: Relative peak intensity of isolated proton (δ = 9.4 ppm) of L11I solution in d^6-DMSO in the presence of Ag_2O as a function of reaction time.

II.3.Conclusion:

A series of new imidazolium ligands functionalized in the N,N' positions with carboxylic acid and ester have been successfully synthesized, yielding potential ligand for MOF synthesis. Ligands with two and four carboxylate groups have been obtained. The same ligands with various counter ions (Br, I) have been prepared by ion exchange starting from 1,3-bis(4-carboxyphenyl)imidazolium chloride. Furthermore, the ligand with a methylene bridge between the imidazolium ring and the aromatic part has been prepared. Finally, an imidazol ligand, containing only one phenyl carboxylic acid was also achieved.

Using these ligands as starting materials, syntheses of several MOFs compounds were attempted. Two novel MOFs, **LCH-1** and **LCH-2**, based on 1,3-bis(4-carboxyphenyl)-imidazolium halide and 4-imidazolyl-benzoic acid ligands respectively have been synthesized. The isolated solids were characterized by NMR, XRD, TGA, and porosity measurements.

Attempts to deprotonate and coordinate the synthesized ligands to metal sites and thereby achieve a potential active NHC catalyst were successful for 1,3-bis(4-carboxybenzyl)-imidazolium iodide ligand, according to *in situ* ^{1}H NMR spectroscopy. This promising result should be further investigated and used to develop a novel family of MOFs with a NHC fonctionality.

II.4. Experimental Part:

General Procedures.

Organometallic synthesis experiments were carried out under dry and oxygen free argon atmosphere using either standard Schlenk or glove-box techniques.

High vacuum lines (10^{-5}mbar) and glove-box techniques were used for treatments of the materials.

Diethyl ether and THF were distilled over Na/benzophenone, toluene and dioxane over molten sodium, pentane over a sodium/potassium alloy, DMSO and DMF were dried on CaH_2 and distilled, ethanol and isopropanol reacted with sodium before distillation and methanol was dried using magnesium. Dichloromethane, acetonitrile, were distilled over P_2O_5. All solvents were stored under argon and molecular sieves (3 Å) before use.

Elemental analyses:

Elemental analyses were performed at the CNRS Central Analysis Department of Solaize (Lyon, France). Metal concentrations were performed using inductively coupled plasma atomic emission spectrometry (ICP-AES) apparatus (JOBIN YVON 38 Type III) in the "Laboratoire des Sciences Analytiques, Laboratoire d'Analyse Industrielle Unité CPE Lyon (LSA)" in CPE Lyon (Villeurbanne, France). ICP standards were prepared by dissolving a corresponding metal salts with purity >99.99% in volumetric flasks with up to 5% nitric acid in water.

GC analyses:

Quantification of organics was performed on a gas chromatograph HP 6890, equipped with a flame ionization detector (FID) and a HP-1 column (30 m × 0.32 mm). Light hydrocarbons analyzes were performed on a HP 5890 gas chromatograph, equipped with a flame ionization detector (FID) and a KCl/Al_2O_3 on fused silica column (50 m × 0.32 mm). Hydrogen was analysed by GC Intersmat IGC 120 MB equipped with a TCD detector and a molecular sieves (5 Å) column.

NMR analyses:

Liquid state NMR ^{1}H, and ^{13}C spectra were recorded on an AC-300 spectrometer (^{1}H 300 MHz, ^{13}C 75 MHz). Spectra were recorded using the residual peak of the deuterated solvent as internal standard. Chemical shifts are given in ppm (δ) relative to TMS (tetramethylsilane).

Solid state NMR spectra have been recorded in a Bruker DSX-300 spectrometer operating at 300.18 MHz frequency. The impeller zirconia (ZrO_2) of 4 mm is filled with the desired product and sealed with a kel-f stopper. It is then transferred into the probe Bruker CP 4 mm spectrometer allowing rotation of the rotor at a speed of 10 kHz. The time between two acquisitions is always optimized to allow complete relaxation of the protons.

X-Ray diffraction:

Powder X-ray diffraction (XRD) patterns were obtained with Siemens Bruker AXS D-5000 instrument using Cu $K\alpha_1$ radiation in bragg-bretano reflecting geometry. The sample preparation was done by grinding the material until obtaining a fine powder, followed by addition of ethanol and in the end deposition of a suspension on a glass plate. Some of the samples were also recorded with Siemens Bruker D500 instrument in the transmission Debye-Scherrer geometry in order to reduce orientation effects, gain better intensity to noise ratio.

The single crystal XRD method was used for structure determination. Sufficiently large crystals with good diffraction properties were measured on the conventional lab instrument (Siemens Bruker), which was equipped with CCD camera, Mo tube and graphite monochromator. A tiny amount of grease or glue was put on a glass fiber that was already glued onto a brass pin. The sticky fiber was then used to pick up the target crystal.

Thermogravimetric analyses:

Thermogravimetric analyses (TGA) were carried out in Mettler Toledo TGA/DSA 1 STAR System apparatus. Approximately 10 mg sample was placed in an Al_2O_3 crucible and heated in flowing of 30 ml/min of nitrogen. The heating rate was 10 °C/min, and the change in sample weight was recorded as a function of temperature.

FTIR spectroscopy:

In situ FTIR the infrared transmission (IR) spectra were collected in transmission mode on Nicolet FT-5700. The solid samples were compressed into self-supporting wafers, or by deposition of a suspension on a silicon wafer then placed in the sample holder when the spectra were recorded. The cell is equipped with KBr or CaF_2 windows.

Typically, 16 scans were made for each spectrum with a resolution of 2 cm^{-1} for the study of solids and 32 acquisitions with a resolution of 1 cm^{-1} for the study of gases.

Ex situ DRIFT spectra were recorded in diffuse reflectance mode on Nicolet FT-6700 instrument, equipped with CaF_2 windows and MCT detector. Typically, 64 acquisition scans were made for each spectrum with a resolution of 2 cm^{-1} and in Kubelka-Munka model.

Surface Area and porosity measurements:

Adsorption-desorption isotherms of nitrogen at 77 K were measured for all the materials with Micromeritics ASAP 2020 surface and porosity analyzer. Cumulative pore volume was calculated using BJH model for adsorption isotherm, pores size was determined by using Horvath Kawazu approach. The sample is thermally treated according to the thermal stability determined from TGA curves.

Syntheses of NHC linkers:

Preparation of 1,3-bis(4-carboxyphenyl)imidazolium halides L_2:

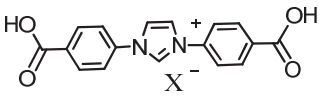

X = Cl, Br, I

In a 250 ml round-bottom flask, 5.04 g (36.8 mmol) para-aminobenzoic acid were dissolved in 90 ml THF, and 1.35 ml (18.3 mmol) of formaldehyde solution (37% in water) were added. After adding 6 ml of formic acid, the mixture was stirred at room temperature until a white suspension was obtained. 2.09 ml (18.3 mmol) of 40% aqueous glyoxal solution were added and the resulting mixture was heated to 50 °C for 5 hours. After adding 1.5 ml (18.3 mmol) of 37% aqueous solution of HCl (12 M), formation of a pink solid was observed. The mixture was heated once more to 50 °C for two hours. The resulting precipitate was filtered and washed with dichloromethane and acetone. The product was characterized by ^{1}H- and ^{13}C-NMR spectroscopy, ES HRMS.

Products with other counter-ions were obtained using the same protocol except for the acid added. The quantities added are as follows:

Product name	PABA	Formal-dehyde	Glyoxal	Formic acid	HCl 12M (37%)	HBr 5.7M (33%)	HI 7.3M (55%)
L_2Cl	5.04 g	1.35 ml	2.09 ml	6 ml	1.5 ml	-	-
L_2Br	5.04 g	1.35 ml	2.09ml	6 ml	-	3.2 ml	-
L_2I	5.04 g	1.35 ml	2.09 ml	6 ml	-	-	2.5 ml

Characterization:

L_2Cl: ^{1}H-NMR (in DMSO, 300.13MHz): [ppm] δ = 10.58 (t, 1H, HOOC-(C_6H_4)-N-(CH=CH)-C*H*-N-(C_6H_4)-COOH, ^4J=1.6Hz), δ = 8.67 (d, 2H, HOOC-(C_6H_4)-N-(C*H*=C*H*)-CH-N-(C_6H_4)-COOH, ^4J=1.5Hz), δ = 8.22 (d, 4H, HOOC-(C-(C*H*-CH)$_2$-C)-N-(CH=CH)-CH-N-(C-(CH-C*H*)$_2$-C)-COOH, ^3J=8.8Hz), δ = 8.07 (d, 4H, HOOC-(C-(CH-C*H*)$_2$-C)-N-(CH=CH)-CH-N-(C-(C*H*-CH)$_2$-C)-COOH, ^3J=8.8Hz); *H*OOC-(C_6H_4)-N-(CH=CH)-CH-N-(C_6H_4)-COO*H* not detectable

^{13}C-NMR (in DMSO, 75.47MHz): [ppm] δ = 167.7 (HOO*C*-(C_6H_4)-N-(CH=CH)-CH-N-(C_6H_4)-*C*OOH), δ = 139.2 (HOOC-(C-(CH-CH)$_2$-*C*)-N-(CH=CH)-CH-N-(*C*-(CH-CH)$_2$-C)-COOH), δ = 136.9 (HOOC-(C_6H_4)-N-(CH=CH)-*C*H-N-(C_6H_4)-COOH), δ = 133.6 (HOOC-(C_6H_4)-N-(*C*H=*C*H)-CH-N-(C_6H_4)-COOH), δ = 132.7 (HOOC-(C-(*C*H-CH)$_2$-C)-N-(CH=CH)-CH-N-(C-(CH-*C*H)$_2$-C)-COOH), δ = 123.7 (HOOC-(C-(CH-*C*H)$_2$-C)-N-(CH=CH)-CH-N-(C-(*C*H-CH)$_2$-C)-COOH), δ = 123.5 (HOOC-(*C*-(CH-CH)$_2$-C)-N-(CH=CH)-CH-N-(*C*-(CH-CH)$_2$-C)-COOH)

Note: For L_2Br and L_2I, shifts and peak intensities are almost identical.

HRMS ES $[C_{17}H_{13}N_2O_4]^+$ (309 g/mol), calculated for $[C_{17}H_{13}N_2O_4]^+$ (309 g/mol) .

Anal. Calcd for **L_2**Cl: $C_{17}H_{13}ClN_2O_4$ (344.759): C, 59.22; H, 3.80; Cl, 10.28; N, 8.12.

Found: C, 58.07; H, 3.87; Cl, 10.24; N, 7.96.

Anal. Calcd for **L_2**Br: $C_{17}H_{13}BrN_2O_4$ (389.21): C, 52.46; H, 3.36; Br, 20.52; N, 7.19.

Found: C, 52.36; H, 3.49; Br, 19.71.24; N, 7.13

Anal. Calcd for **L_2**I: $C_{17}H_{13}IN_2O_4$ (436.2): C, 46.81; H, 3.00; I, 29.09; N, 6.42.

Found: C, 47.05; H, 3.45; I, 27.24; N, 6.83

Preparation of 1,3-bis(4-carboxyphenyl)imidazolium halides L_4 :

Preparation of para amino methyl benzoate L_3:

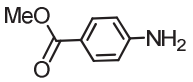

In a 500 ml round bottom flask, para amino benzoic acid (10 g, 0.073 mol) was dissolved in 150 ml of methanol, the mixture was cooled to 0 °C and sulfuric acid was added dropwise

(5.43 g, 10 ml, 0,055 mol). White precipitate was formed, after that the mixture was refluxed for 48 hours. The solvent (methanol) was removed under vacuum, 200 ml of distilled water was introduced and the pH of the solution was adjusted between 5-6. Finally, the solid was filtered and washed several times with distilled water and dried (89% yield).

^{1}H NMR (DMSO-d_6): [ppm] δ = 3.71 (s, 3H, C**H**$_3$COOC-), 5.96 (s, 2H, -N**H**$_2$), 6.54 (d, 2H, ^{3}J = 8.6 Hz, -C$_6$**H**$_4$-), 7.62 (d, 2H, ^{3}J = 8.6 Hz, -C$_6$**H**$_4$-).

^{13}C NMR (DMSO-d_6): [ppm] δ = 52.0 (**C**H$_3$COOC-), 113.5 and 131.9 (-**C**$_6$H$_4$-), 116.6 (NH2-**C**$_6$H$_4$-), 154.3 (COOCH$_3$-**C**$_6$H$_4$-), 167.2 (COOCH$_3$-).

Preparation of 1,3-bis(4-carboxyphenyl)imidazolium halides L$_4$

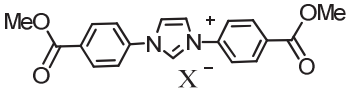

X = Cl, Br, I

In a 250 ml round bottom flask, 1.06 g (7.02 mmol) of methyl para-aminobenzoate (MPAB) were dissolved in 30 ml THF, and 0.26 ml (3.50 mmol) of formaldehyde solution (37% in water) were added. After adding 2 ml of formic acid the mixture was stirred at room temperature for 90 minutes. 0.40 ml (3.50 mmol) of 40% aqueous glyoxal solution were added and the resulting mixture was heated to 50 °C for 5 hours. 0.30 ml (3.50 mmol) of 37% aqueous solution of HCl (12 M) was added. The mixture was heated once more to 50 °C for two hours. The resulting precipitate was filtered and washed with dichloromethane and acetone. The product was characterized by ^{1}H and ^{13}C NMR spectroscopy and ES HRMS.

Products with other counter-ions were obtained using the same protocol except for the acid added. The quantities added are as follows:

Product name	MPAB	Formaldehyde	Formic acid	Glyoxal	HCl (37%)	HBr	HI (55%)
L$_4$Cl	1.06 g	0.26 ml	2 ml	0.4 ml	0.3 ml	-	-
L$_4$Br	1.06 g	0.26 ml	2 ml	0.4 ml	-	0.6 ml (33%)	-
L$_4$I	1.06 g	0.26 ml	3 ml	0.4 ml	-	-	0.73 ml

^{1}H NMR (DMSO): [ppm] δ = 3.92 [s, 6H, H$_3$COOC-(C$_6$H$_4$)-N-(CH=CH)-(CH)-N-(C$_6$H$_4$)-COOCH$_3$], 8.15 [m, 4H, H$_3$COOC-(C$_6$H$_4$)-N-(CH=CH)-(CH)-N-(C$_6$H$_4$)- COOCH$_3$] 8.25 [m, 4H, H$_3$COOC-(C$_6$H$_4$)-N-(CH=CH)-(CH)-N-(C$_6$H$_4$)- COOCH$_3$], 8.7[d, 2H, H$_3$COOC-(C$_6$H$_4$)-N-(CH=CH)-(CH)-N-(C$_6$H$_4$)- COOCH$_3$], 10.7[s, 1H, H$_3$COOC-(C$_6$H$_4$)-N-(CH=CH)-(CH)-N-(C$_6$H$_4$)- COOCH$_3$].

^{13}C NMR (DMSO): [ppm] δ = 52.6 [s, 2C, $H_3\underline{C}OOC$-(C_6H_4)-N-(CH=CH)-(CH)-N-(C_6H_4)-$COO\underline{C}H_3$], 121 [H_3COOC-(C_6H_4)-N-($\underline{C}H=\underline{C}H$)-(CH)-N-($C_6H_4$)- $COOCH_3$] 122.2, 130.7, 131, 135.6, [H_3COOC-($\underline{C}_6H_4$)-N-(CH=CH)-(CH)-N-($\underline{C}_6H_4$)- $COOCH_3$], 137.9 [H_3COOC-(C_6H_4)-N-(CH=CH)-($\underline{C}H$)-N-(C_6H_4)- $COOCH_3$]].

Note: For L4Br and L4I, shifts and peak intensities are almost identical.

HRMS ES $[C_{19}H_{17}N_2O_4]^+$ (337.1 g/mol), calculated for $[C_{19}H_{17}N_2O_4]^+$ (337.3 g/mol)

Preparation of 1,3-bis(4-carboxyphenyl)imidazolium halides(L_2) from 1,3-bis(4-carboxyphenyl)imidazolium halides (L_4):

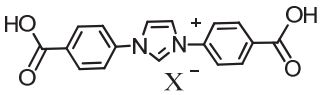

X = Cl, Br, I

The ester 1.3-dimethylbenzoate imidazolium chloride (L_4) (5.37 mmol, 2 g) was dissolved in a mixture of MeOH, THF and H_2O (20ml / 20ml / 20ml), the ester being easily soluble in MeOH + THF at 0 °C. 10 equivalents of LiOH (53.7 mmol 1.2 g) were introduced, then the mixture was stirred at 40 °C for 5h. The excess of LiOH was neutralized with acetic acid. The solvent was removed under vacuum, then 20 ml of toluene was introduced. The by- products were extracted with 3 × 20 ml of dichloromethane (several extractions were necessary), and the product was dried on $NaSO_4$. The toluene was removed under vacuum. The solid was characterized by ^{1}H , ^{13}C NMR HRMS ES(337.1). Yield = 55% (relatively low compared to direct preparation from the para amino benzoic acid).

^{1}H NMR (DMSO): [ppm] δ = 8.1 [2d, 4H, HOOC-($C_6\underline{H}_4$)-N-(CH=CH)-(CH)-N-($C_6\underline{H}_4$)-COOH] 8.2 [m, 4H, HOOC-($C_6\underline{H}_4$)-N-(CH=CH)-(CH)-N-($C_6\underline{H}_4$)- COOH], 8.7[d, 2H, HOOC-(C_6H_4)-N-($C\underline{H}=C\underline{H}$)-(CH)-N-($C_6H_4$)- COOH], 10.63[s, 1H, HOOC-(C_6H_4)-N-(CH=CH)-($C\underline{H}$)-N-(C_6H_4)- COOH], 13.3[s, 1H, $\underline{H}OOC$-(C_6H_4)-N-(CH=CH)-(CH)-N-(C_6H_4)- $COO\underline{H}$].

^{13}C NMR (DMSO): [ppm] δ = 122 [HOOC-(C_6H_4)-N-($\underline{C}H=\underline{C}H$)-(CH)-N-($C_6H_4$)- COOH] 122.2, 131, 132, 136, [HOOC-($\underline{C}_6H_4$)-N-(CH=CH)-(CH)-N-($\underline{C}_6H_4$)- COOH], 138 [HOOC-(C_6H_4)-N-(CH=CH)-($\underline{C}H$)-N-(C_6H_4)- COOH]].

Preparation of 1,3-bis(5,5′-isophtalic acid)imidazolium halides L_7:

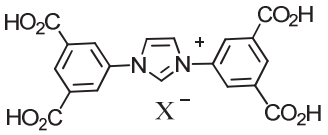

X = Cl, Br, I

In a 250 ml flask were introduced 3 g (16 mmol) of 5-aminoisophtalic acid followed by 50 ml of THF, 248 mg (8 mmol) of paraformaldehyde followed by 5 ml of acetic acid. The mixture was stirred for 2 hours at room temperature, after that glyoxal 40% (8 mmol) was added, the reaction mixture was refluxed overnight. Once at room temperature, 8 mmol of HCl were introduced resulting in an instantaneous formation of brownish solid. The mixture was refluxed for another 2 hours, finally the solid was filtered and washed with dichloromethane, and the acetone. Yield = 90%, characterization NMR ^{1}H, ^{13}C, HRMS ES.

Products with other counter-ions were obtained using the same protocol except for the acid added. The quantities added are as follows

Product name	5-aminoisophtalic acid	formaldehyde	acetic acid	Glyoxal	HCl (37%)	HBr (33%)	HI (55%)
L_7Cl	3 g	0.6 ml	5 ml	0.9 ml	1 ml	-	-
L_7Br	3 g	0.6 ml	5 ml	0.9 ml	-	1 ml	-
L_7I	3 g	0.6 ml	5 ml	0.9 ml	-		2 ml

^{1}H NMR (DMSO): [ppm] δ = 8.5 [2d, 4H, $(HOOC)_2$-($C_6\underline{H}_3$)-N-(CH=CH)-(CH)-N-($C_6\underline{H}_3$)-$(COOH)_2$], 8.6 [s,2H, $(HOOC)_2$-($C_6\underline{H}_3$)-N-(CH=CH)-(CH)-N-($C_6\underline{H}_3$)- $(COOH)_2$], 8.7 [S, 2H, $(HOOC)_2$-(C_6H_3)-N-($C\underline{H}$=$C\underline{H}$)-(CH)-N-(C_6H_3)- $(COOH)_2$, 10.6 [S, 1H, $(HOOC)_2$-(C_6H_3)-N-(CH=CH)-($C\underline{H}$)-N-(C_6H_3)- $(COOH)_2$].

^{13}C NMR (DMSO): [ppm] δ = 122 [$(HOOC)_2$-(C_6H_4)-N-($\underline{C}$H=$\underline{C}$H)-(CH)-N-(C_6H_4)-$(COOH)_2$] 126, 130, 135, 135.2 [$(HOOC)_2$-($\underline{C}_6H_3$)-N-(CH=CH)-(CH)-N-($\underline{C}_6H_3$)- $(COOH)_2$], 136 [$(HOOC)_2$-(C_6H_4)-N-(CH=CH)-($\underline{C}$H)-N-(C_6H_4)- $(COOH)_2$] 165[($HOO\underline{C}$)$_2$-(C_6H_3)-N-(CH=CH)-(CH)-N-(C_6H_3)- ($\underline{C}$OOH)$_2$

HRMS ES $[C_{19}H_{13}N_2O_8]^+$ = (397.1 g/mol), calculated for $[C_{19}H_{13}N_2O_8]^+$ (397.32 g/mol)

Preparation of 1,3-bis(4-carboxybenzyl)imidazolium halides L_{11}

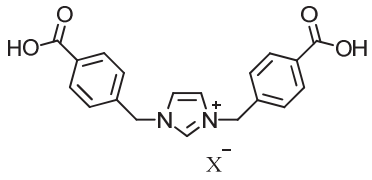

X = Cl, Br, I

In a 250 ml round bottom flask, 1 g (6.62 mmol) of para-aminomethylbenzoic (PAMBA) acid were dissolved in 20 ml THF, and 0.26 ml (3.31 mmol) of formaldehyde solution (37% in water) were added. After adding 2 ml of acetic acid the mixture was stirred at room temperature for 30 minutes. The PAMBA did not dissolve, so 10 more milliliters of THF were added. 0.40 ml (3.31 mmol) of 40% aqueous glyoxal solution were added and the resulting mixture was heated to 50°C for three and a half hours. 0.30 ml (3.31 mmol) of 37% aqueous solution of HCl (12 M) was added. The mixture was heated once more to 50 °C for two hours. The resulting precipitate was filtered and washed with dichloromethane and acetone. The product was characterized by ^{1}H ^{13}C-NMR spectroscopy.

Products with other counter-ions were obtained using the same protocol except for the acid added. The quantities added are as follows:

Product name	PAMBA	Formaldehyde	Acetic acid	Glyoxal	HCl (37%)	HBr (48%)	HI (55%)
L_{11}Cl	1 g	0.26 ml	2 ml	0.40 ml	0.30 ml	-	-
L_{11}Br	2 g	0.52 ml	4 ml	0.80 ml	-	0.75 ml	-
L_{11}I	2 g	0.52 ml	4 ml	0.80 ml	-	-	0.90 ml

Characterization:

L_{11}Cl: ^{1}H-NMR (in DMSO, 300.13MHz): [ppm] δ = 9.46 (t, 1H, HOOC-(C_6H_4)-CH_2-N-(CH=CH)-C*H*-N-CH_2-(C_6H_4)-COOH, ^{4}J not detectable), δ = 7.97 (d, 4H, HOOC-(C-(C*H*-CH)$_2$-C)-CH_2-N-(CH=CH)-CH-N-CH_2-(C-(CH-C*H*)$_2$-C)-COOH, ^{3}J=8.1Hz), δ = 7.87 (d, 2H, HOOC-(C_6H_4)-CH_2-N-(C*H*=C*H*)-CH-N-CH_2-(C_6H_4)-COOH, ^{4}J=1.5Hz), δ = 7.50 (d, 4H, HOOC-(C-(CH-C*H*)$_2$-C)-CH_2-N-(CH=CH)-CH-N-CH_2-(C-(C*H*-CH)$_2$-C)-COOH, ^{3}J=8.2Hz), δ = 5.53 (d, 4H, HOOC-(C_6H_4)-C*H*$_2$-N-(CH=CH)-CH-N-C*H*$_2$-(C_6H_4)-COOH, ^{3}J=8.2Hz); *H*OOC-(C_6H_4)-CH_2-N-(CH=CH)-CH-N-CH_2-(C_6H_4)-COO*H* not detectable

^{13}C NMR (DMSO): [ppm] δ = 54 [(HOOC-(C_6H_4)-CH_2-N-(CH=CH)-C*H*-N-CH_2-(C_6H_4)-COOH] 126, 130, 135, 135.2 (HOOC-(C_6H_4)-CH_2-N-(CH=CH)-C*H*-N-CH_2-(C_6H_4)-COOH], 136 [(HOOC-(C_6H_4)-CH_2-N-(CH=CH)-C*H*-N-CH_2-(C_6H_4)-COOH] 167(HOOC-(C_6H_4)-CH_2-

N-(CH=CH)-C*H*-N-CH_2-(C_6H_4)-COOH) (HOOC-(C_6H_4)-CH_2-N-(CH=CH)-C*H*-N-CH_2-(C_6H_4)-COOH

Preparation of 1-(4-carboxyphenyl)imidazol L_{15}:

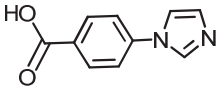

In a 250 ml round bottom flask 10 ml of AcOH (acetic acid), 2.9 ml of 37% aqueous solution of formaldehyde, and 4.4 ml of glyoxal were introduced. The mixture was heated to 70 °C. In a 100ml beaker 5 g of PABA were dissolved in 10 ml of THF. The solution was mixed with a previously prepared solution of 2.8 g of NH_4OAc, dissolved in 10 ml of AcOH and 1 ml of distilled water. The final mixture was introduced in an addition funnel and then slowly added into the round bottom flask. The solution was stirred for 12h at 70 °C. After cooling, the reaction mixture was dripped into a stirred solution of 29.4 g $NaHCO_3$ in 300 ml of water. The yellowish precipitate that formed was filtered and washed with water. The obtained product was characterized by ^{1}H-NMR spectroscopy.

Characterization:

L_{15}: ^{1}H-NMR (in DMSO, 300.13MHz): [ppm] δ = 13.06 (s, 1H, *H*OOC-(C_6H_4)-N-CH=CH-N-CH-), δ = 8.40 (t, 1H, HOOC-(C_4H_6)-N-CH=C*H*-N-CH-, ^4J=0.9Hz), δ = 8.04 (dt, 2H, HOOC-(C-(C*H*-CH)$_2$-C)-N-CH=CH-N-CH-, ^3J=8.8Hz , ^4J=2.0Hz), δ = 7.86 (t, 1H, HOOC-(C_6H_4)-N-C*H*=CH-N-CH-, ^4J=1.4Hz), δ = 7.80 (dt, 2H, HOOC-(C-(CH-C*H*)$_2$-C)-N-CH=CH-N-CH-, ^3J=8.8Hz, ^4J=1.8Hz), δ = 7.14 (HOOC-(C_6H_4)-N-CH=CH-N-C*H*-)

^{13}C-NMR (in DMSO, 75.47MHz): [ppm] δ = 167.9 (HOO*C*-(C_6H_4)-N-CH=CH-N-CH-), δ = 141.5 (HOOC-(C-(CH-CH)$_2$-*C*)-N-CH=CH-N-CH-), δ = 137.2 (HOOC-(C_6H_4)-N-CH=CH-N-*C*H-), δ = 132.5 (HOOC-(C_6H_4)-N-*C*H=CH-N-CH-), δ = 131.8 (HOOC-(C-(*C*H-CH)$_2$-C)-N-CH=CH-N-CH-), δ = 130.3 (HOOC-(C_6H_4)-N-CH=*C*H-N-CH-), δ = 121.2 (HOOC-(C-(CH-*C*H)$_2$-C)-N-CH=CH-N-CH-), δ = 119.2 (HOOC-(*C*-(CH-CH)$_2$-C)-N-CH=CH-N-CH-)

Anal. Calcd for **L_{15}**: $C_9H_9N_2O_2$ (177.18): C, 61; H, 5.12; N, 15.81.

Found: C, 63.28; H, 4.29; N, 14.47.

Syntheses of MOFs

Synthesis of LCH-1 with $Zn(NO_3)_2$:

In a test tube 60.6 mg (0.14 mmol) of 1,3-bis(4-carboxyphenyl)imidazol-3-ium chloride (**L_2**Cl) was introduced in dimethylformamide (DMF) (10 ml, 9.4 g, 128 mmol). 83.3 mg (0.28 mmol) of $Zn(NO_3)_2$ was added; (metal / linker / solvent, 3: 1: 304). The mixture was stirred for about 15 minutes at room temperature, after that the tube was sealed with a septum and placed in a pre-heated oven at 75 °C for 6h followed by 12h at 115 °C. After cooling in air to room temperature the resulting solid was characterized with powder X-Ray diffraction.

The same protocol was conducted to obtain slightly different products using linker **L_2**Br or **L_2**I. A summary of the different reactants and their quantities is given in the table below.

Product name	**L_2**Cl	**L_2**Br	**L_2**I	$Zn(NO_3)_2{\cdot}6H_2O$
LCH-1-Cl1	200 mg	-	-	517.6 mg
LCH-1-Cl1	500 mg	-	-	1.249 g
LCH-1-Br1	-	200 mg	-	458 mg
LCH-1-Br1	-	500 mg	-	1.145 g
LCH-1-I1	-	-	200 mg	409 mg
LCH-1-I1	-	-	500 mg	1.023 g

Synthesis of LCH-1Cl with $Zn(OAc)_2$:

In a 100 ml vial 200 mg (0.58 mmol) of 1,3-bis(4-carboxyphenyl)imidazolium chloride (L_2Cl) were dissolved in 40 ml of DMF (524 mmol). Under stirring, 319.2 mg (1.74 mmol) of $Zn(OAc)_2$ were added. The solution was stirred for 30 minutes at room temperature. The vial was then sealed and placed in a pre-heated furnace (75 °C) for four hours. The furnace was then set to 115 °C, and the vial was left in the furnace for another 12 hours. After cooling in air to room temperature the resulting solid was characterized by powder X-ray diffraction.

The same protocol was conducted to obtain slightly different products using linkers **L_2**Br and **L_2**I. A summary of the different reactants and their quantities is given in the table below.

Product name	**L_2**Cl	**L_2**Br	**L_2**I	$Zn(OAc)_2$
LCH-1-Cl2	200 mg	-	-	319.2 mg
LCH-1-Br2	-	200 mg	-	282.5 mg
LCH-1-I2	-	-	200 mg	252 mg

Reaction L_7 with $Cu(NO_3)_2$:

In a 100 ml vial 200 mg (0.462 mmol) **L_7**Cl were dissolved in a mixture of 16 ml of DMF, 8 ml of H_2O and 8 ml of dioxane. 0.1 ml of 37% aqueous solution of HCl was added. Under stirring, 500 mg (1.07 mmol) of $Cu(NO_3)_2 \cdot 3H_2O$ was introduced. The solution was stirred for three hours at room temperature. The vial was then sealed and placed in a pre-heated furnace (75 °C) for four hours. The furnace was then set to 115 °C, and the vial was left in the furnace for another 12 hours. After cooling in air to room temperature, the resulting product was characterized by powder X-ray diffraction.

Another product was obtained following the same protocol using the bromide of the same ligand, noted **L_7**Br. The quantities used are 200 mg (0.418 mmol) of **L_7**Br and 408 mg (1.185 mmol) of $Cu(NO_3)_2 \cdot 3H_2O$.

Synthesis of MOF-L_{11} with $Zn(NO_3)_2$

In a 100 ml vial 100 mg (0.278 mmol) of 1,3-bis(4-carboxybenzyl)imidazol-3-ium chloride (**L_{11}**Cl) were dissolved in 17.2 ml of DMF (251 mmol). Under stirring, 249 mg (0.836 mmol) of $Zn(NO_3)_2 \cdot 6H_2O$ were added. The solution was stirred for one hour at room temperature until it became clear. The vial was sealed and placed in a pre-heated furnace (75 °C) for four hours. The furnace was then set to 115 °C, and the vial was left in the furnace for another 12 hours. It was then allowed to cool down to room temperature. The resulting product was characterized by powder X-ray diffraction.

The same protocol was conducted to obtain slightly different products using linker **L_{11}**Br and **L_{11}**I. A summary of the different reactants and their quantities are given in the table below.

Product name	**L_{11}**Cl	**L_{11}**Br	**L_{11}**I	$Zn(NO_3)_2 \cdot 6H_2O$
$MOFL_{11}CL$	100 mg	-	-	249 mg
$MOFL_{11}Br$	-	100 mg	-	221 mg
$MOFL_{11}I$	-	-	100 mg	198 mg

Synthesis of LCH-2 with $Zn(NO_3)_2$

In a 100 ml vial 500 mg (2.654 mmol) of **L_{15}** were dissolved in 100 ml of DMF (1.317 mol). Under stirring, 1.579 g (5.309 mmol) of $Zn(NO_3)_2 \cdot 6H_2O$ were added (2 equivalents). The solution was stirred for two hours at room temperature until it became clear. The vial was then sealed and placed in a pre-heated furnace (75 °C) for four hours. The furnace was then set to 115 °C, and the vial was left in the furnace for another 12 hours. It was then allowed to cool

down to room temperature. The resulting product, LCH-2 was characterized by powder X-ray diffraction.

Synthesis of LCH-2 with $Zn(OAc)_2$

In a 100 ml vial 500 mg (2.654 mmol) of $\mathbf{L_{15}}$ were dissolved in 100 ml of DMF (1.317 mol). Under stirring, 974 mg (5.309 mmol) of $Zn(OAc)_2$ were added (2 equivalents). The solution was stirred for three hours at room temperature. The vial was then sealed and placed in a pre-heated furnace (75 °C) for four hours. The furnace was then set to 115 °C, and the vial was left in the furnace for another 12 hours. It was then allowed to cool down to room temperature. The resulting product was characterized by powder X-ray diffraction.

Attemps to silver carbene (deprotonation of the imidazolium ligands):

Deprotonation of L_2Cl

A 50 ml Schlenk was charged with 100 mg of $\mathbf{L_2}$Cl (0.27 mmol) and 30 ml of CH_2Cl_2 were introduced. 37.5 mg (0.161 mmol) of Ag_2O were added. The mixture was brought to reflux (50°C) for two hours. The mixture was then allowed to cool down to room temperature and was filtered on celite. During the whole reaction as well as during the cooling down, the Schlenk was covered in aluminum foil. The product was characterized by solid ^{1}H-NMR spectroscopy. Deprotonation attempts were carried out also on the $\mathbf{L_2}$Br and $\mathbf{L_2}$I linkers as well using the same protocol. The quantities used are as follows:

Product name	$\mathbf{L_2}$Cl	$\mathbf{L_2}$Br	$\mathbf{L_2}$I	Ag_2O
LCHa1	100 mg	-	-	37.3 mg
LCHa2	-	100 mg	-	33.3 mg
LCHa3	-	-	100 mg	30 mg

Variation in other parameters such as time, solvent temperature have been screened to attempt deprotonation of $\mathbf{L_2}$Cl (1,3-bis(4-carboxyphenyl)imidazol-3-ium chloride), the following table summarize different condition tested.

Entry	Linker L_2Cl n (mmol)	Linker L_2Cl m (mg)	Ag_2O n (mmol)	Ag_2O m (mg)	Solvent	T (°C)	Time (h)
1	0.29	100	0.4	95	CH_2Cl_2	R.T.	20
2	0.29	100	0.4	94	CH_2Cl_2	R.T.	24
3	0.29	100	0.4	92	CH_2Cl_2	40	18
4	0.29	100	0.4	92	CH_3CN	R.T.	24
5	0.29	100	0.4	92	CH_3CN	40	14
6	0.29	100	0.4	92	DMF	R.T.	24
7	0.29	100	0.4	94	DMF	50	14
8	0.29	100	0.4	92	DMSO-d6	30	18

Deprotonation of L_4Cl

The same procedure described above was used to try to deprotonate **L_4**Cl, 3-bis(4-methyl acetate phenyl)imidazolium chloride. The different experimental conditions are reported in the table below.

Entry	Linker L_2Cl n (mmol)	Linker L_2Cl m (mg)	Ag_2O n (mmol)	Ag_2O m (mg)	Solvent	T (°C)	Time (h)
1	0.27	100	0.17	40	CH_2Cl_2	R.T.	20
2	0.27	100	0.17	40	CH_2Cl_2	R.T.	24
3	0.27	100	0.17	40	CH_2Cl_2	40	18
4	0.27	100	0.17	40	CH_3CN	R.T.	24
5	0.27	100	0.17	40	CH_3CN	40	14
6	0.27	100	0.17	40	DMF	R.T.	24
7	0.27	100	0.17	40	DMF	50	14
8	0.27	100	0.17	40	DMSO-d6	30	18

Furthermore, the deprotonation of the imidazolium by using a base (KHMDS) in the presence of organometallic complexes have been tried.

Entry	Linker L_2Cl		KHMDS		Au(tht)Cl		(IrCp*)Cl2	
	n(mmol)	m(mg)	n(mmol)	m(mg)	n(mmol)	m(mg)	n(mmol)	m(mg)
1	0.27	100	0.3	64	0,3	103,7		
2	0.27	100	0.3	64			0,3	241

Deprotonation of L_{11}

A 50 ml Schlenk was charged with 100 mg of $L_{11}Cl$ (0.279 mmol) and 20 ml of freshly distilled THF was introduced. 38.7 mg (0.167mmol) of Ag_2O was added. The mixture was heated to 50 °C for four hours. The mixture was then allowed to cool down to room temperature and was filtered on celite. During the whole reaction as well as during the cooling down, the Schlenk was covered with aluminum foil. The product was characterized by ^{1}H-NMR spectroscopy.

A deprotonation attempt was carried out on the $L_{11}I$ linker as well. This time the reaction was conducted in a Young NMR tube. 1.2 mg of $L_{11}I$ was introduced in the tube followed by 2 ml of d_6-DMSO for NMR analysis. The ^{1}H-NMR spectrum was then recorded at t = 0 mn. 0.4 mg of Ag_2O was added in the tube. Manual stirring resulted in the dissolution of the linker in the DMSO. The mixture was then allowed to react for four hours at room temperature in the dark. The tube was heated to 80 °C. The progress of the reaction was followed by consecutive ^{1}H-NMR spectra.

Chapter III:

Synthesis and characterization of UiO-66 MOFs, their application in catalysis and gas adsorption

III.1. Introduction:

Due to the extended possibilities in variation in linkers design and central metal atoms, Metal Organic Framework (MOFs) with desirable structure and properties can in principle be constructed and tuned for a special application as catalyst or support for heterogeneous catalyst. For these aims, unsaturated metal centers[140, 141] or reactive secondary functional groups on the organic bridge have been reported.[98, 101] However, the functionalization of the organic linker with secondary functional groups is limited because these groups have a tendency to coordinate also with the metal center like in CPO-27-M (M_2dhtp(H_2O)$_2$ 8H_2O / dhtp = dihydroterephtalic acid, M = Co, Mg, Mn, Ni, Zn)[76], where the hydroxyl groups present on the phenyl ring coordinate to the metal atoms of the secondary building units, rather than remaining free for further post syntheses modification. Successful post synthetic organic functionalization of some groups such as amino and aldehyde to create other organic functionalities have been recently reported.[142-146] However, the introduction of large organic residues which reduces the pores entrance makes the materials seldom applicable for further reaction with organometallic chemistry.

To enable directly grafting of organometallic complexes, an appropriate secondary functional group is necessary. For example hydroxyl, which has been traditionally used as the grafting site in surface organometallic chemistry on amorphous oxide such as silica and alumina.[7] Only few examples of MOFs containing free and accessible hydroxyl groups in the organic linker are reported. Lin and coworkers have described the reaction via slow vapor diffusion of diethyl ether into a mixture of binol based ligand, **L1**, and $CdCl_2$ in DMF/MeOH, leads to a formation of 3D framework with large channel opening and accessible hydroxyl groups (Figure III.1). Further fictionalization has been performed on this hydroxyl groups[48] as described in chapter I.

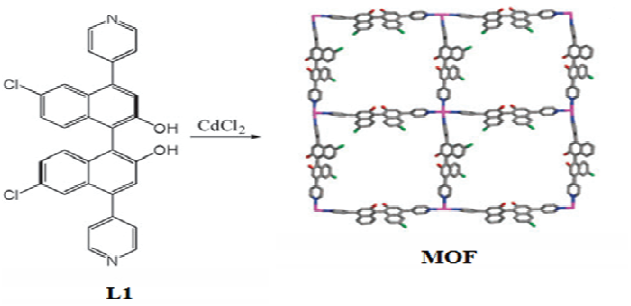

Figure III.1: Chemical structures of L1 and the crystal structure of the MOF obtained.[48]

More recently, Mulfort *et al.* have reported the formation of a crystalline product with large cavities and accessible alcohol functionalities by the reaction of tetracarboxylate linker, **L2**, with a Zn(II) source and bipyridine dihydroxyl, **L3**, (Figure III.2).[146]

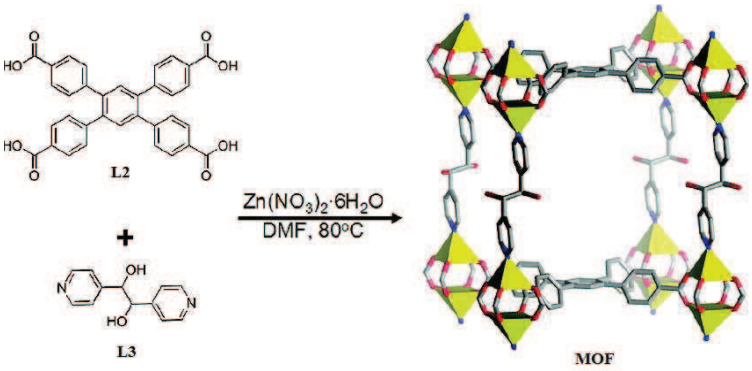

Figure III.2: Chemical structures of **L2** and **L3** and the crystal structure of the obtained MOF

Some MOFs such as MIL also displays hydroxyl groups in their corner stones.[147-149] Hafizovic *et al*. have also reported a new zirconium inorganic building block forming a three dimensional metal organic framework, UiO-66 ($[Zr_6O_4(OH)_4L_6]$ where L is the linker). Whose main characteristic are exceptional stability and available hydroxyl groups,[150] which can be used for further functionalization through surface organometallic chemistry. Hence, the focus in this chapter is on this particular MOF structure.

The general formula of UiO-66 MOF topology is $[Zr_6O_4(OH)_4L_6]$, where L is the dicarboxylate linker ; terephtalate (^-O_2C-(C_6H_4)-CO_2^-), biphenyl dicarboxylate (^-O_2C-$(C_6H_4$-$C_6H_4)$-CO_2^-) or terphenyl dicarboxylate (^-O_2C-$(C_6H_4$-C_6H_4-$C_6H_4)$-CO_2^-). The calculated surfaces areas for those structures are 1187, 3000, 4170 m²/g, respectively. The structure crystallized in a cubic system as shown in Figure III.3.

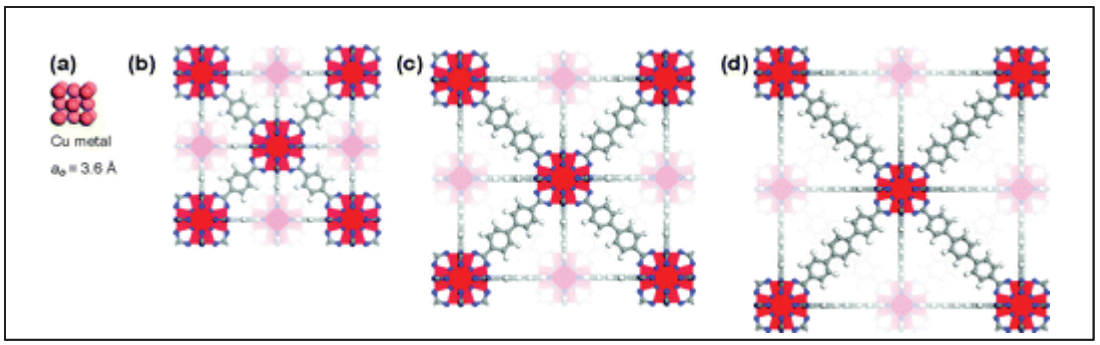

Figure III.3: (a) One unit cell of copper (b) UiO-66 with phenyl dicarboxylate linker, (c) UiO-66 with biphenyl-dicarboxylate linker, (d) UiO-66 with terphenyl dicarboxylate linker. Zirconium, oxygen, carbon, and hydrogen atoms are red, blue, gray, and white, respectively.[150]

The secondary building unit comprises $Zr_6O_4(OH)_4$ cluster in which the triangular faces of the Zr_6-octahedron are alternatively capped by μ3-O and μ3-OH groups. All polyhedron edges are bridged by carboxylates ($-CO_2$) forming a $Zr_6O_4(OH)_4(CO_2)_{12}$ cluster (Figure III.4). zirconium atom is eight-coordinated forming a square-antiprismatic coordination. One square face is formed by oxygen atoms supplied by carboxylates while the second square face is formed by oxygen atoms coming from the μ^3-O and μ^3-OH groups.[151-154]

Figure III.4 (a) shows the $Zr_6O_4(OH)_4$ inner cluster while Figure III.4 (b) shows the full $Zr_6O_4(OH)_4(CO_2)_{12}$ cluster.

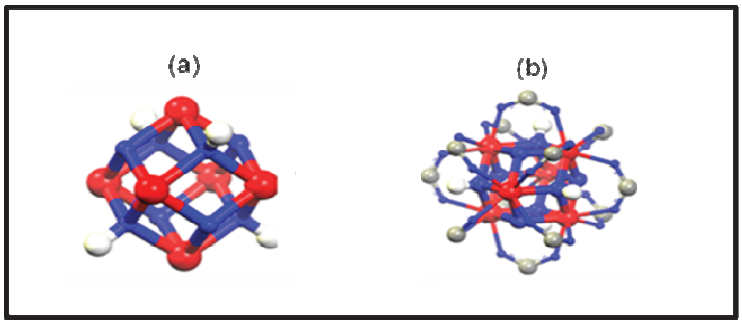

Figure III.4: Structure of SBU of UiO-66 (a) showing the inner core Zr_6 cluster drawn alone for clarity, structure (b) shows the full cluster Zirconium, oxygen, carbon, and hydrogen atoms are red, blue, gray, and white, respectively.[150]

Above 250 °C two water molecules, originated from the μ3-OH groups are released, resulting in a Zr_6O_6 inner cluster with seven-coordinated zirconium. The phenomenon is fully reversible, as demonstrated by IR and EXAFS studies.[150]

The IR spectrum of as synthesized UiO-66 (Figure III.5) is dominated by an intense and broad band centred at 3440 cm^{-1} corresponds to physisorbed water molecules. A sharp, but rather weak peak at 3675 cm^{-1} is assigned to isolated OH groups. This peak is still present after treatment under vacuum at 250 °C for 30 minutes (red curve), and disappears after treatment under high vacuum for 30 minutes at 300 °C (blue curve) The processes is reversible upon rehydration when the sample is exposed to moisture.

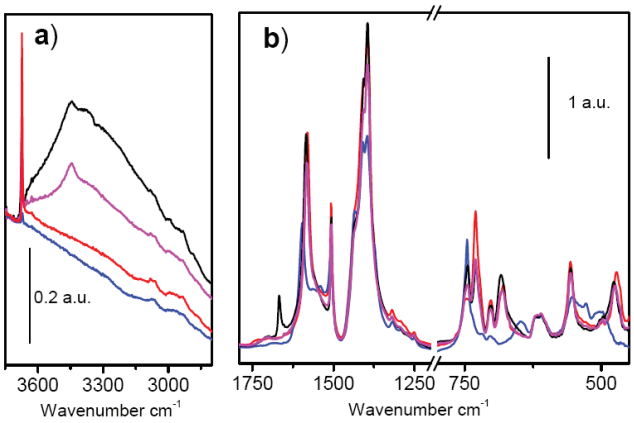

Figure III.5: IR of UiO-66: part a) OH frequency region and part b) skeletal modes region. Effect of thermal treatment in vacuo and re-hydration. Black Curve: as prepared sample; red curve outgassed at 250 °C for 30 minutes; blue curve outgassed at 300 °C for 30minutes; magenta curve effect of re-hydration.

This behavior is reminiscent of the dehydration and dehydroxylation chemistry known for the amorphous inorganic oxide systems like silica on which surface organometallic chemistry has been traditionally developed. As already stated, the goal of this chapter is to explore whether the Zr_3-OH of the UiO-66 could be good candidates for surface organometallic chemistry. Since at the time of this thesis the UiO-66 had been the object of a single communication, the characterization and large scale synthesis details therefore, were scant. This chapter also reports extensive characterization and structural development on UiO-66.

III.2. Results and discussion

III.2.1. Synthesis and characterisation of UiO-66-BDC, UiO-66-BPDC, UiO-66-ABDC MOFs:

The reproducibility of published MOF syntheses can sometimes be problematic. In our hands, the puiblished[150] 100 mg scale synthesis of UiO-66, $Zr_6(OH)_4O_4(BDC)_6$, based on solvothermal reaction of terephtalic acid, HOOC-C_6H_4-COOH (BDC-H_2), the inorganic precursor zirconium (IV) tetrachloride, $ZrCl_4$, in dimethylformamide, was reproducible. The reported synthesis and minor variations in metal: linker: solvent ratios consistently lead to white crystalline materials whose X-ray powder diffractograms matched the published ones.

Adapting the same synthesis conditions for biphenyl dicarboxylate as linker, $^-$OOC-C_6H_4-C_6H_4-COO^- (BPDC), gave a less crystalline product. Due to the low solubility of diphenyl dicarboxylic acid in DMF, it was found beneficial to first heat the mixture at 80 °C to enhance the solubility, and then increase the temperature to 100 °C, temperature at which the crystallization process starts. By this way, the product could be obtained in good yield (80%) and large scale (3g of $ZrCl_4$).

In an analogous synthesis, the novel material containing the functional 2-amino terephtalic dicarboxylate linker $^-$OOC-$C_6H_3NH_2$-COO^- (ABDC), was also synthesized. Dissolving 2-amino terephtalic acid in DMF and $ZrCl_4$ gave a clear yellow solution. The quality of the product was independent on the heating profile according to X-Ray powder diffraction pattern.

X-Ray powder diffraction pattern of different materials are shown in Figure III.6. The powder XRD patterns of UiO-66-BDC and UiO-66-BPDC are presented in part b and a respectively. Diffractogram of UiO-66-BDC is comparable to the one reported in the literature. X-Ray powder diffraction pattern of the novel material (Figure III.6 part c) UiO-66-ABDC has an identical XRD pattern as UiO-66-BDC and is therefore described by the same structure. The three materials are therefore isostructural.

Thermal stability of the pre-dried samples is shown in the inset of each part in Figure III. UiO-66-BPDC and UiO-66-BDC are thermally stable until 500 °C, while the TGA profile of UiO-66-ABDC is described by a continuous weight loss from 50 to 850 °C. Generally, the

thermal stability of MOFs lies around 350-400 °C. It has been proposed that the corner stone and the strength of the chemical bonding between the inorganic and organic parts are the key of such high thermal resistance.[150]

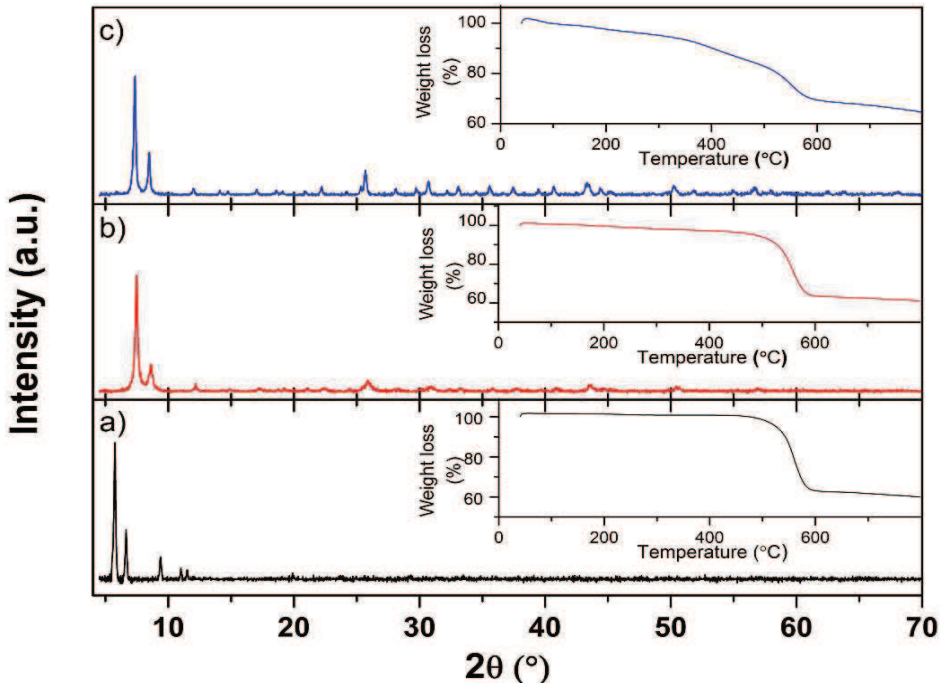

Figure III.6: X-Ray diffraction patterns and TGA profiles of a) UiO-66-BPDC; b) UiO-66-BDC; c) UiO-66-ABDC.

UiO-66BDC, UiO-66BPDC and UiO-66-ABDC can be synthesized in regular glassware since the reaction temperature is below the boiling point of DMF. Performing the synthesis in glassware allows facile monitoring the crystallization process with time. In our case, we tried to reproduce the UiO-66 MOFs and to scale up from 0.05 g to 5 g in a glass flask by first heating at 80°C for 12h and then at 110 °C for 48h. Powder X-Ray patterns shown in Figure III.7 confirm that the entire product of the three different UiO-66 MOFs described, are crystalline and present the same phase. In conclusion, this material can be prepared with relatively large quantities and with a yield of 70-80 %.

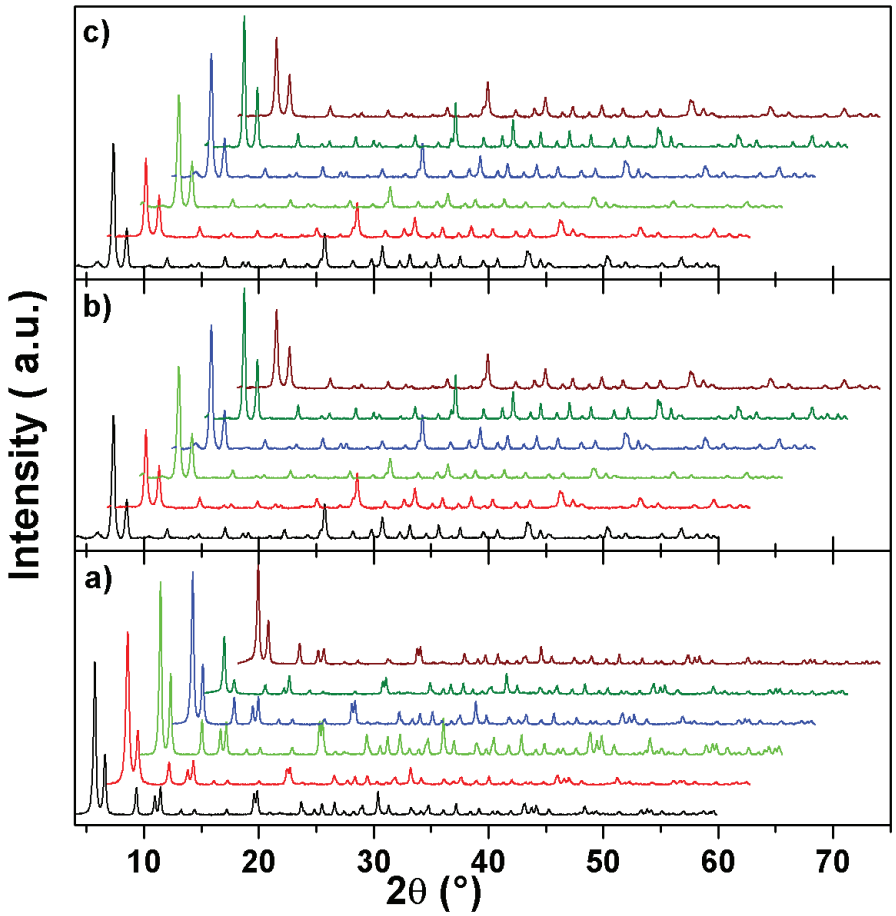

Figure III.7: XRD patterns of a) UiO-66-BPDC, b) UiO-66-BDC, c) UiO-66-ABDC MOFs in 0.5, 1, 2, 3, 4, 5 g batches.

Surface areas and pores volume of the three MOFs were measured by N_2 adsorption at 77K. Prior to the analyses, the samples have been treated by solvent exchange (methanol) followed by heat treatment at 135°C under vacuum for the UiO-66-ABDC (Zr-amino MOF), as justified by the profile of the TGA, and at 180 °C under high vacuum overnight for the two other MOFs. The adsorptions isotherms and pores sizes distribution are represented in Figure III.8 and the results are summarized in Table III.1.

The values of surface areas are comparable to the calculated surfaces.[150] The surface area and pore volume are increasing with the growth of the linker and decreasing with the presence of a secondary functional group (amine). The surface area and pore volumes were unaffected after dehydroxylation at 300 °C under high vacuum for 6h for both UiO-66-BDC and UiO-66-BPDC.

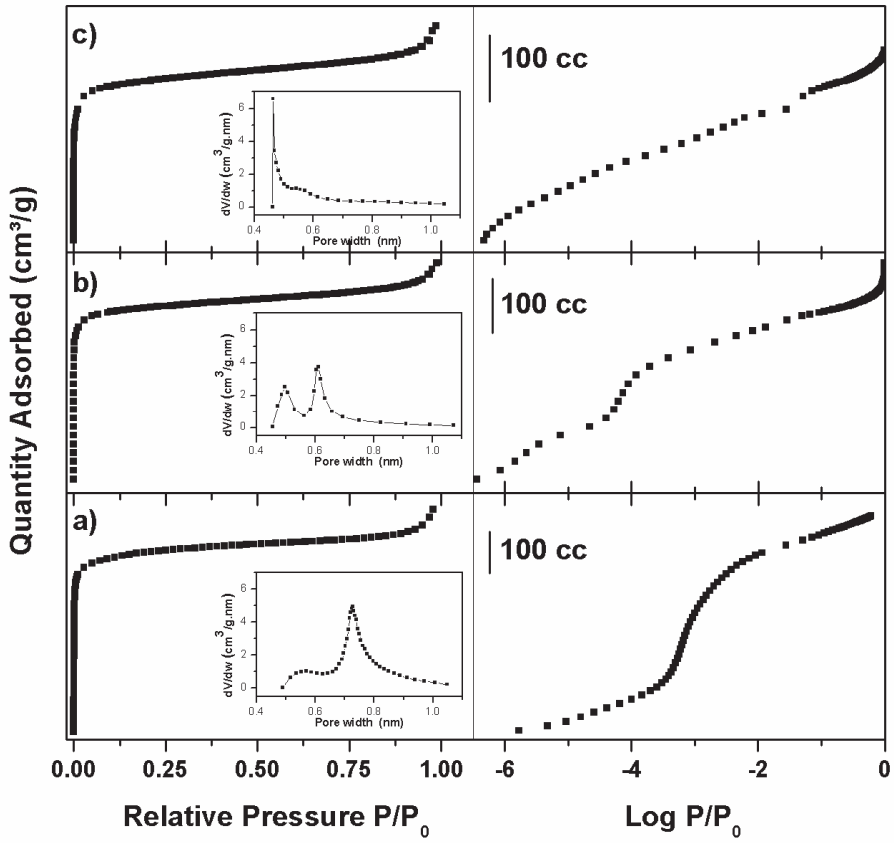

Figure III.8: Adsorption isotherms of N_2 at 77K for UiO-66-BPDC (a); UiO-66-BDC (b); UiO-66-ABDC (c). The insets represent the pores size distribution estimated from Horvath Kawazu model.

Table III.1: Results of the surfaces area and pores volume for the isostructural MOF series UiO-66 Zr-MOFs.

Sample	BET surface area (m^2/g)	Langmuir area (m^2/g)	Pores Volume (cm^3/g)
UiO-66-BDC	1090± 50	1400 ± 50	0.42± 0.05
UiO-66-ABDC	776 ± 30	1100 ± 30	0.33 ± 0.05
UiO-66-BPDC	2060 ± 100	2920 ± 100	0.85 ± 0.05

It was demonstrated that in most cases the residual DMF can be exchanged with more volatile organic solvent.[155] At the same time, the remaining un-reacted linker can also be removed, hence, leading to a porous material with higher surface area. In our case, we confirm that the pores volume and the surface areas of the three materials of the UiO-66 family increase after solvent exchange with methanol using soxhlet technique overnight.

The crystalinity of the product after treatment was checked by the powder X-ray diffraction.

The elemental analyses have been realized on samples previously extracted with methanol followed by heat treatment at 120 °C under vacuum overnight. Since the analyses were performed under air, water re-adsorption cannot be avoided.

The results are summarized in Table III.2. The expected elemental analyses based on the molecular formula determined by crystallographic analysis, are compared to the experimental results. A good agreement between the experimental and calculated values was obtained when including three molecules of water per zirconium, leading to the formula ($[Zr_6(OH)_4O_4L_6(H_2O)_{18}]$). Since the presence of residual halogen is known to be a possible source of material contamination, the three materials were tested for chlorine content (Table III.2). In the worst scenario the chlorine content is below 3%, which corresponds to less than one chlorine atom per secondary building unit, $Zr_6(\mu^3\text{-}OH)_4(\mu^3\text{-}O)_4$. Such low chlorine content indicates that the materials are reasonably free from halogen contamination.

Table III.2: Elemental analyses of UiO-66-BDC, UiO-66-ABDC, UiO-66-BPDC (C, H, Cl, N, Zr): Experimental (Exp) and calculated (Cal) for $Zr_6(OH)_4O_4L_6(H_2O)_{18}$.

Sample	**% Zr**		**% C**		**%N**		**% H**		**% Cl**	
	Exp	Cal	Exp	Cal	Exp	Cal	Exp	Cal	Exp	Cal
UiO-66-BDC	27.7	27.5	28	29	a	0	2.5	3.2	1.92	0
UiO-66-BPDC	23.6	22.4	43.8	41.3	a	0	3.3	3.6	0.24	0
UiO-66-ABDC	26.5	26.4	23.8	27	3.2	4	3.7	3.2	2.8	0

a) Analysis not performed.

The zirconium MOF UiO-66-BPDC, UiO-66-BDC, and UiO-66-ABDC have also been characterized by transmission infrared spectroscopy. The samples were prepared by deposition from a suspension of the material in toluene on a silicon wafer, a thin layer of the material remained on the surface upon drying. In the region between [4000-3500 cm^{-1}] the IR spectra are characterized by a band at 3675 cm^{-1} assigned to isolated OH groups. In the case of UiO-66-ABDC containing amino groups, two other bands at 3495 cm^{-1} and 3385 cm^{-1} characteristic of symmetric and asymmetric vibration of NH_2 respectively, are present. Peaks between [3099-2800 cm^{-1}] are attributed to C-H stretching, the bands between [1660-1240 cm^{-1}] are the signature of C=C stretching modes of the phenyl ring.

Upon treatment at 300 °C under high vacuum, the OH band starts to decrease. Perturbation of the carboxylates modes is also observed, in particular the asymmetric band decreases in intensity.

The streching bands of the OH groups in both spectra of UiO-66-BDC and UiO-66-BPDC part b) and c) respectively in Figure III.9, are fully recovered upon exposure to moisture. Apparently, the dehydroxylated MOF can easily break the OH bond of water. Thus, other molecules such as methanol or diethylether were exposed to the dehydroxylated phase with the aim to activate other O-H, O-C or C-H bonds. However, none of the mentioned molecules reacted with the material.

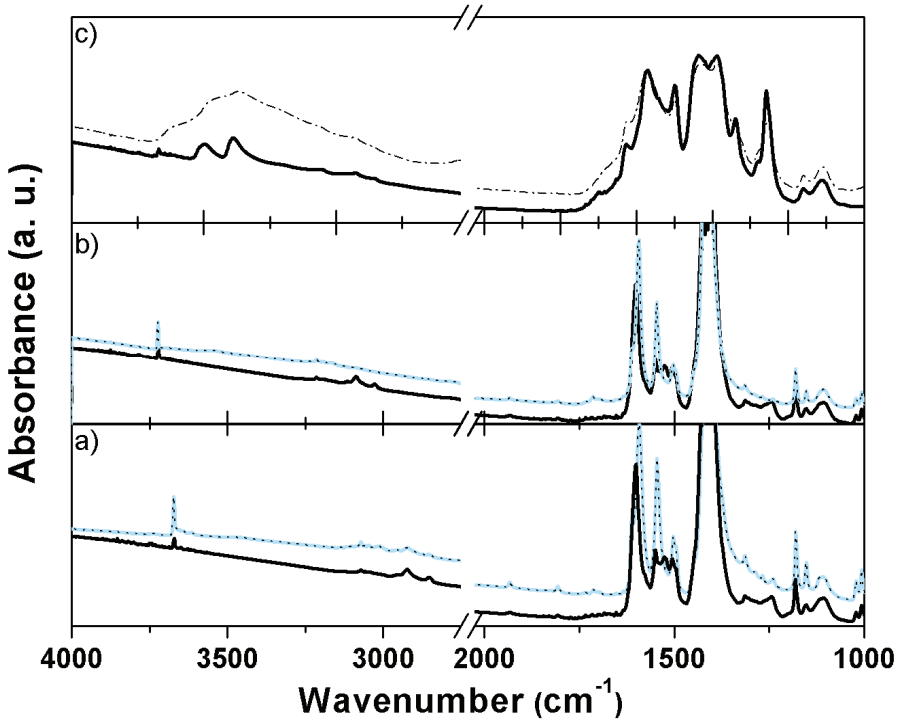

Figure III.9: FTIR spectra of a) UiO-66-BPDC; b) UiO-66-BDC. Grey line: MOF treated at 150 °C under vacuum, black line: MOF treated at 300 °C; dotted curve: MOF treated at 300 °C followed by water exposure at RT and removal of the adsorbed water excess. c) UiO-66-ABDC. Hashed line: as prepared. Black line: treated at 150 °C under vaccum.

The different zirconium MOF (UiO-66-BDC, UiO-66-ABDC, UiO-66-BPDC) have also been characterized by ^{13}C solid state CP MAS NMR spectroscopy. The spectra are superposed and compared to the corresponding linkers (Figure III.10).

As shown in Figure III.10 we can easily distinguish the displacement of different carbons for the UiO-66-BPDC (part a) and UiO-66-BDC (part b) because of the relatively high symmetry

of the ligand. The spectrum of amino terephtalic acid is described by eight less resolved and rather broad peaks. The peak positions of the linkers are similar to the corresponding MOFs.

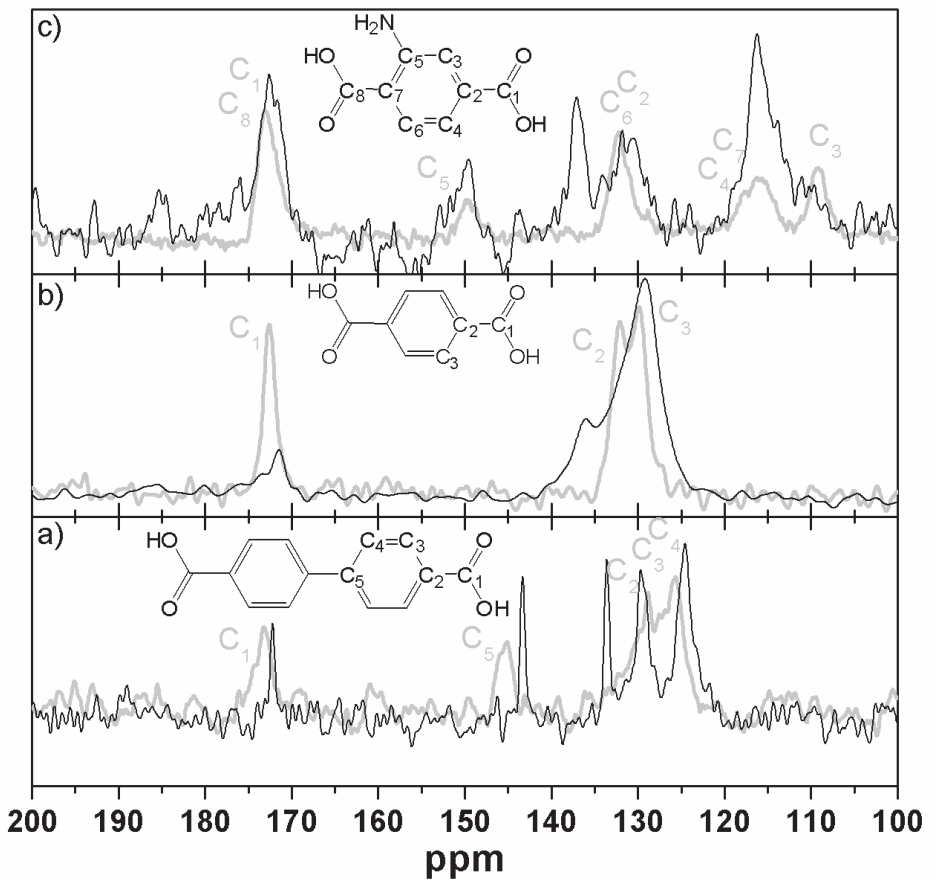

Figure III.10: NMR spectra of different MOFs, a) UiO-66-BPDC, b) UiO-66-BDC, c) UiO-66-ABDC, gray lines correspond to the ligands and black lines represent MOFs (256 scans and d1= 32 second).

III.2.2. Investigation of hydroxyl groups of the surface of UiO-66-BPDC:

As described in the literature,[150] the MOFs belonging to the UiO-66 family contain bridging hydroxyl ligands on the cornerstones, consisting under its hydrated form of Zr_6 octahedron whose eight triangular faces are capped alternatively by μ-3 bridging hydroxo and μ-3 bridging oxo. Since UiO-66 MOFs have been characterized by powder X-Ray diffraction, EXAFS, and IR, the literature description of hydroxyl moiety mostly relays on the single IR technique, since powder X-Ray diffraction is not sensitive to the light hydrogen atoms. Since the goal is to perform surface organometallic chemistry, more data linked to the OH accessibility and chemical reactivity are required.

First, the accessibility of the OH groups has been investigated by FTIR on the three materials UiO-66-BDC, UiO-66-BPDC, UiO-66-ABDC, that is $[Zr_6(\mu^3\text{-}O)_4(\mu^3\text{-}OH)_4L_6]$ with L being the terephtalate, biphenyldicarboxylate or amino terephtalate respectively. Prior to the FTIR study the materials were activated by thermal treatment at 120 °C under high vacuum (10^{-5} mbar) overnight. When heavy water is added to the pretreated sample, the ν(OH) stretching mode of the cornerstone hydroxyls at 3671 cm^{-1} (and the NH_2 stretching band for UiO-66-ABDC at 3500, 3386 cm^{-1}) are shifted to typical ν(OD) (and ν(ND_2) frequencies in the IR spectra to 2707 cm^{-1} (and 2618, 2478 cm^{-1}) respectively (Figure III.11). The observed isotopic shifts are in agreement with the calculated ones, based on the Hooke approximation formula :($\nu_{A-B} = \frac{1}{2\Pi}\sqrt{\frac{k}{\mu_{A-B}}}$)

$$\frac{\nu_{O-H}}{\nu_{O-D}} = \sqrt{\frac{\mu_{O-H}}{\mu_{O-D}}} = \sqrt{\frac{m_D(m_O + m_H)}{m_H(m_O + m_D)}} \approx 1.37$$

The protonated materials spectra are restored upon addition of regular water. In conclusion, hydroxyl moieties present on the surface of UiO-66 activated materials are chemically accessible and can be exchanged with deuterium form D_2O.

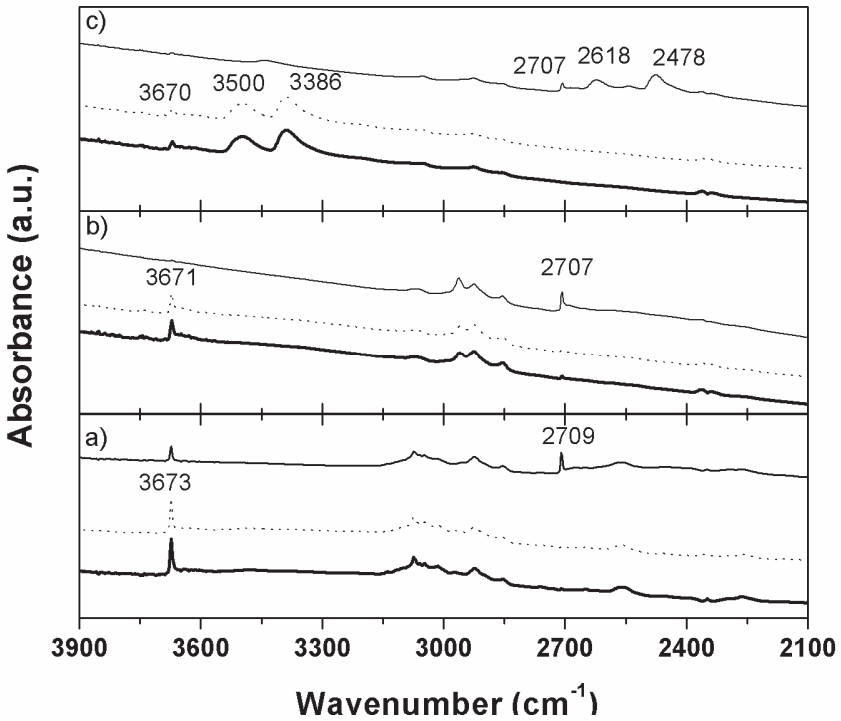

Figure III.11: FTIR spectra [3900-2100 cm^{-1}] region of a) UiO-66-BPDC, b) UiO-66-BDC, c) UiO-66-ABDC MOFs; bold line: as prepared MOFs, solid line: after dosing D_2O and removal of the excess, dotted curve: after re-dosing H_2O and removal of the excess.

A quantitave estimation of the hydroxyl content was also carried out by FTIR spectroscopy, since ^{1}H NMR approach used for silica[156] proved inappropriate given the broadening of the hydroxyl resonance and its overlap with other proton resonances of the linker under our acquisition conditions.

The response of FTIR instrument was calibrated with MCM-41 dehydroxylated at 500 °C for which the hydroxyl density of 1.4 OH/nm², that is 2.32 mmol OH/g, is known.[8] The calibration was obtained by plotting the integral of the IR spectra between 3900-3500 cm^{-1} versus hydroxyl content (Figure III.12:2). A linear relation between the amount of OH and the area of the peak was obtained:

$$Q(mmmol) = 0.0023 \times S(a.u.) \quad \text{. . . . . .(Eq.III.1)}$$

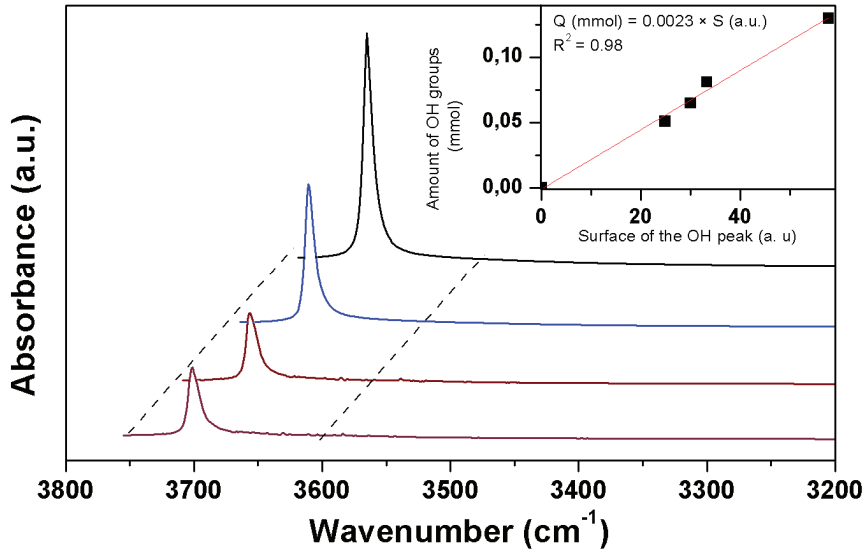

Figure III.12: FTIR spectra (hydroxyl region) of different samples of MCM-41.

A pellet of UiO-66-BPDC was prepared and treated under vacuum at 120 °C to evacuate the physisorbed water. The ν(OH) region was integrated to give 9.4 a.u. which corresponds to 0.0216 mmol of OH in the sample (10 mg of UiO-66-BPDC), or 36.72 mg OH/g through the equation (Eq.III.1). According to the molecular formula $Zr_6(OH)_4O_4(BPDC)_6$, the expected value is 32.06 OH /g. The experimental and calculated data are therefore in good agreement with an experimental overestimation of about 10%.

The amount of OH was also estimated using thermogravemetric analysis data, since UiO-66-BPDC is known to undergo a well behaved reversible reaction (Eq.III.2).

$$Zr_6(OH)_4(O)_4(BPDC)_6 \xrightarrow{T > 250\ ^\circ C} Zr_6(O)_6(BPDC)_6 + 2\,H_2O \quad \ldots\ldots\ldots \text{(Eq.III.2)}$$

It has been shown that the UiO-66-BPDC is stable until 500°C.[150] Hence, the weight loss from 250 °C until 400 °C, that is within the stability range of the MOF, is considered to be directly related to dehydroxylation of OH groups. As shown in Figure III.13 the material losses 1.4 wt%, while the calculated amount of water that can be released from dehydroxylation process is 1.7 wt% according to the molecular formula. Therefore, as in the FTIR study there is good agreement between the experimental and expected data albeit the experimental value is less than the calculated one, being about 85% of the calculated.

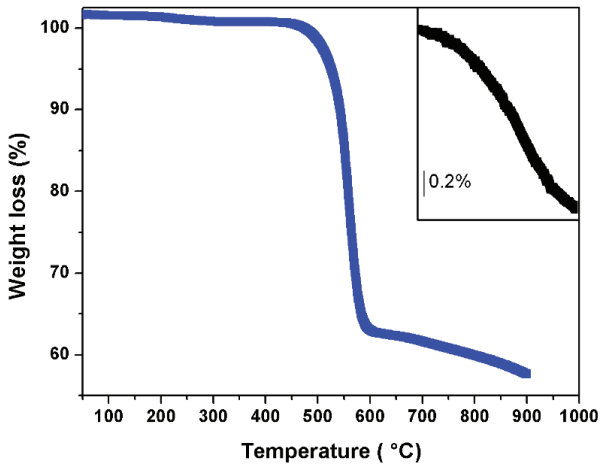

Figure III.13: TGA profile of Zr-BPDC MOF, in the inset the region between 250 °C and 400 °C.

Finally, the OH has been estimated chemically by addition of a Grignard reagent (MeMgBr) and quantification the released CH_4. Methyl magnesium bromide is known to react quantitatively with silica's surface hydroxyl to yield methane, which can be quantified by GC. Such reaction affords a dependable titration of the surface content (Eq.III.3). We attempted a similar reaction of the MOF expect the involvement of $4CH_4$/SBU (Eq.III.4)

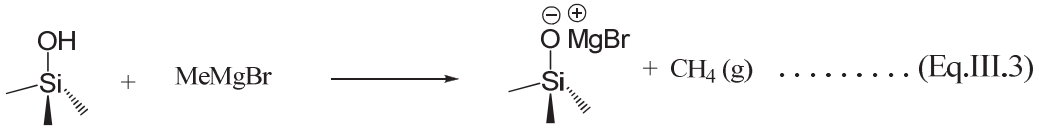

(Eq.III.3)

$$Zr_6(OH)_4(O)_4L_6 + MeMgBr \longrightarrow Zr_6(OMgBr)_4(O)_4L_6 + 4CH_4\,(g) \quad \ldots\ldots\ldots \text{(Eq.III.4)}$$

An excess of MeMgBr was added to dry ether containing UiO-66-BPDC previously mildly activated at 120 °C under inert atmosphere. The amount of CH_4 released (0.365 mmol) is in agreement with the calculated amount of OH in UiO-66-BPDC according to the formula of the MOF (0.377 mmol).

As spectroscopic confirmation that Eq.III.4 went to completion during the titration with Grignard reagent, DRIFT spectra of reaction crude was collected after the removal of the volatile. As shown in Figure III.14 all the hydroxyls group are consumed.

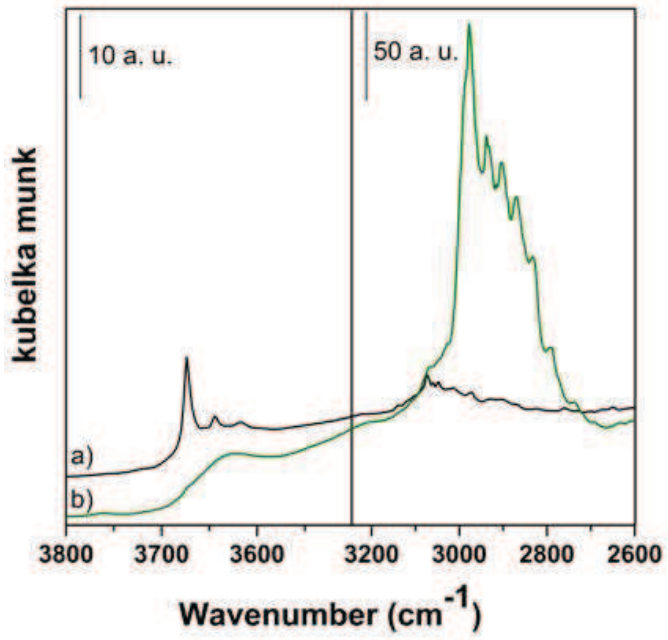

Figure III.14: DRIFT spectra of a) activated UiO-66-BPDC; b) UiO-66-BPDC after reaction with MeMgBr

In conclusion, three different quantitative measurements of the reactive OH groups accessible in UiO-66-BPDC were carried out. Each time there is a good agreement between the experimental data and expected value based on the molecular formula.

Beside accessibility, the nature of the OH residue is also with establishing. In order to study the acidity of the OH group on the surface of various solids such as inorganic oxides,[157, 158] different probe molecules such as acetonitrile, pyridine, trimethephosphine can be used. The interaction of the probe molecules with the surface can readily be followed by spectroscopic analysis and give a classification of the acidity.

Since no interaction of UiO-66-BPDC with acetonitrile was observed, a stronger base (trimethylphosphine) was used as probe.

UiO-66-BPDC was activated at 150 °C under high vacuum to remove the adsorbed water before a vapor pressure of PMe_3 was introduced in the reaction vessel. The interaction of PMe_3 with the surface of the UiO-66-BPDC MOF was followed by FTIR and NMR. After dosing Me_3P, a decrease in intensity of band characteristic of free OH was observed in the IR spectra (Figure III.15) and another band in OH region appeared which is characteristic of OH groups that interact with the probe. Simultaneously, the intensity of C-H stretching increased, due to the addition of PMe_3. This interaction resists 100 °C under vacuum, suggesting that the adsorption is strong. A rigorous treatment at 250 °C under high vacuum was needed to remove the PMe_3.

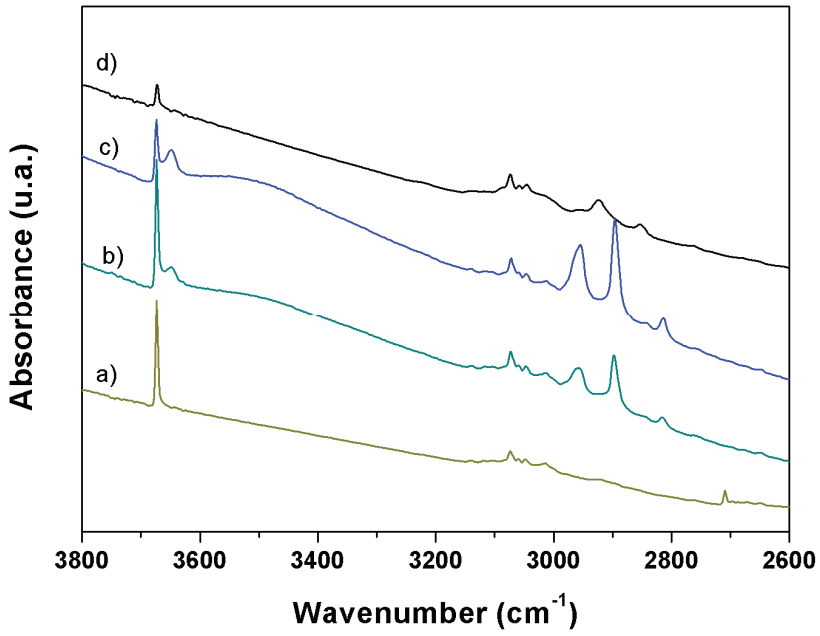

Figure III.15: *In situ* FTIR of a) starting UiO-66-BPDC activated at 120 °C under vacuum (10^{-5} mbar); b) After dosing Me_3P; c) after outgassing at 100 °C; d) after outgassing at 250 °C.

Further insight on the nature of the interaction of UiO-66-BPDC with the probe molecule PMe_3 was obtained by NMR spectroscopy analysis on activates sample, exposed to PMe_3, and treated under high vacuum at 100 °C to remove the excess of PMe_3. The NMR spectra are shown in Figure III.16. The ^{31}P spectrum contains four signals at -64, -62, -38, -35 ppm. The first two peaks are characteristic of weakly to very weakly physisorbed PMe_3.[157, 159] According to the literature, interaction of PMe_3 with a Lewis acid shifts the ^{31}P signal by

10 ppm and downfield by about 55 ppm when it interacts with the Brønsted acids.[157] The shift is also affected by the temperature[160] and the nature of the site, for example, PMe_3 on H-Y zeolite gives a signal at -40 ppm.[158] In our case, two peaks at -35 and -38 ppm were observed, suggesting that two different sites are presented in the solid. The PMe_3 can in principle interact with OH or zirconium atoms. To highlight the OH--PMe_3 interaction, 2D HetCor (^1H, ^{31}P) NMR could be used. In the ^1H spectra, two broad peaks at 7 and 8 ppm correspond to the protons of the phenyl rings. Another signal at 2 ppm attributed to the OH groups of the cornerstones was observed. When the solid was exposed to PMe_3, the relative intensity decreased and a broad peak appeared at 0.8 ppm. This peak is attributed to a shift of OH in interaction with PMe_3 and the protons of the probe. Concerning the ^{13}C NMR, the spectra of the starting MOF and the MOF with PMe_3 were identical, that is the expected carbon of the Me_3P (≈ 12 ppm[161]) was not observed.

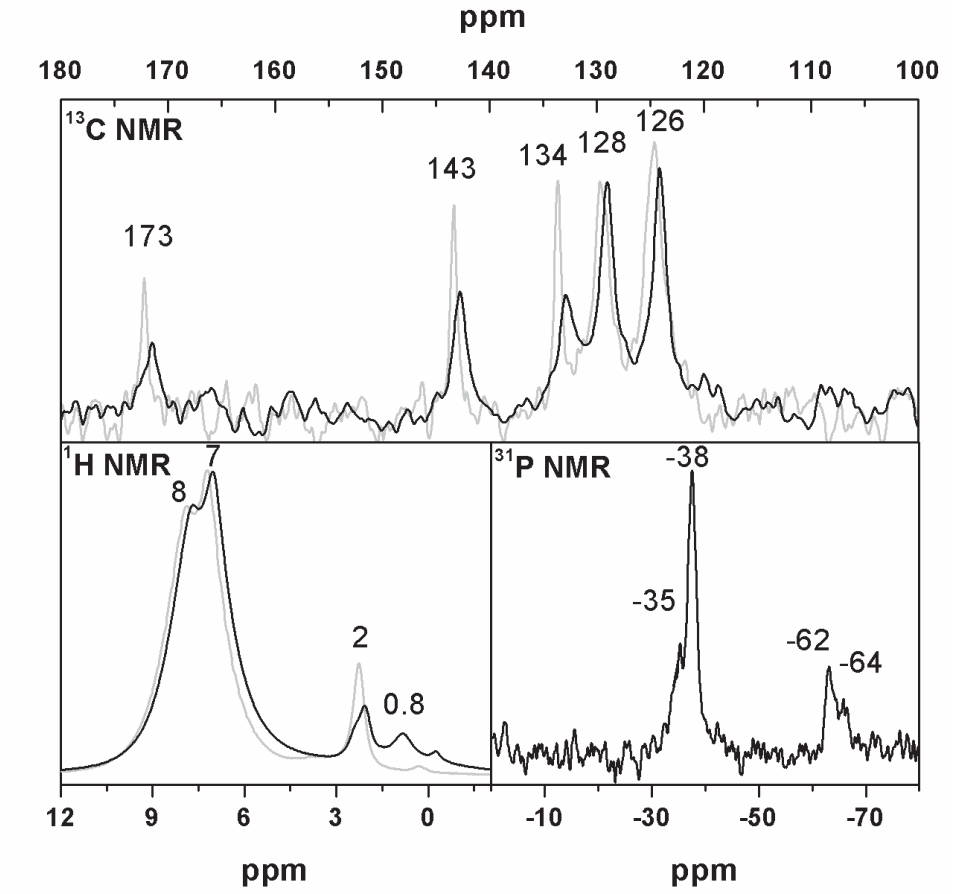

Figure III.16: ^{13}C, ^1H, ^{31}P NMR spectra of activated MOF (gray) and after treatment with PMe_3 (black).

In summary, the combined use of spectroscopic, physic-chemical and chemical titration methods, showed the quantitative, accessibility and reactivity of all hydroxyl moieties

of the MOF UiO-66-BPDC. Qualitatively, the study by IR and ^{31}P NMR spectroscopies of the interaction with PMe_3 showed weak acidic nature of the bridging OH in the $Zr_6(OH)_4(O)_4L_6$ cornerstone of UiO-66-BPDC.

III.3. Surface organometallic chemistry on UiO-66-BPDC-MOF:

III.3.1. Reactivity of the hydroxyls with organometallic complexes:

The reactivity of the OH groups present in UiO-66-BPDC was explored by exposing the activated material to reactive organometallic complexes such as $Ta[CH_2C(CH_3)_3]_3[=CHC(CH_3)_3]$, Ru(COD)(COT), Ru(COD)(Nahptalene) and PMe_3AuMe. In a typical surface organomettallic chemistry approach the reactions were first followed by FTIR and solid state NMR spectroscopies. Out of the four complexes listed above a reaction was observed only with methyl(trimethylphosphine)gold(I), PMe_3AuMe. Such result is consistent with the much smaller diameter of such linear complex with respect to the other larger complexes, therefore best suited to reach the vertex of the pyramidal-shaped nanopores of UiO-66-BPDC, where the reactive OH moiety is located.

Powder UiO-66-BPDC $Zr_6(OH)_4O_4(BPDC)_6$ (200 mg, 94 µmol) previously mildly activated at 120 °C overnight was impregnated in ethereal solution of PMe_3AuMe (110 mg, 0.382 µmol), that is containing an almost equimolar quantity of gold with respect of the variable hydroxyl (376 µmol) on the starting MOF. After stirring for few hours and removal of the volatiles under reduced pressure the resulting powder was washed with ether, dried and analyzed by IR, NMR spectroscopies and by elemental analyses.

As shown in Figure III.17, the DRIFT spectra of the material before and after impregnation shows that, upon reaction with the gold complex the ν(OH) of the material were slightly perturbed, while the appearance of new bands around 2900 cm^{-1} assigned to aliphatic ν(CH) stretching modes, showed the presence of alkyl groups.

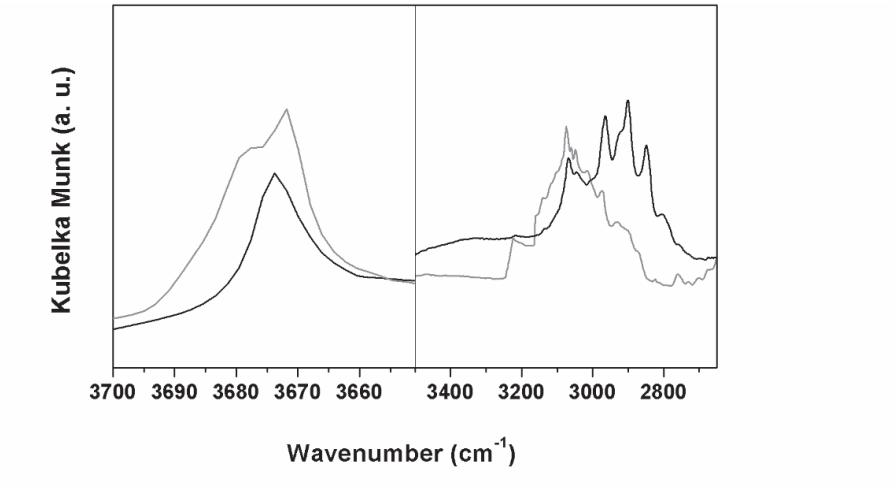

Figure III.17: DRIFT spectra in the [3700, 3650 cm^{-1}] and [3450, 2725 cm^{-1}] regions of the UiO-66-BPDC-MOF before reaction (gray spectrum) and after reaction with the gold complex (black spectrum).

^{31}P, ^{13}C and ^{1}H MAS SS NMR spectra of the sample obtained after reaction of PMe_3AuMe with UiO-66-BPDC were also recorded (Figure III.18). The ^{31}P MAS SS NMR spectrum of the final powder displayed one major resonance at +10 ppm, attributed to the gold(I)-coordinated phosphors atom, in analogy with the resonance of the organometallic precursor PMe_3AuMe, which resonates at +12 ppm in deuterated dichloromethane solution. A minor peak at -1 ppm is present which suggests some concomitant decomposition product not further investigated.

In the ^{13}C spectrum, all the resonances of the starting metal organic framework were observed. An additional weak resonance at 14 ppm was also present, attributed to the methyl groups of a coordinated trimethylphosphine, in analogy with the solution data of PMe_3AuMe. In the ^{1}H-NMR spectrum, as for the ^{13}C one, the resonances due the metal organic framework protons were observed, at 6 and 7 ppm for the phenyl groups and at 2 ppm for hydroxyl. The spectrum displayed two further resonances, at 1 ppm and 0 ppm, attributed to the trimethylphosphine ligand, possibly free and perturbed by the surface of the UiO-66-BPDC, respectively.

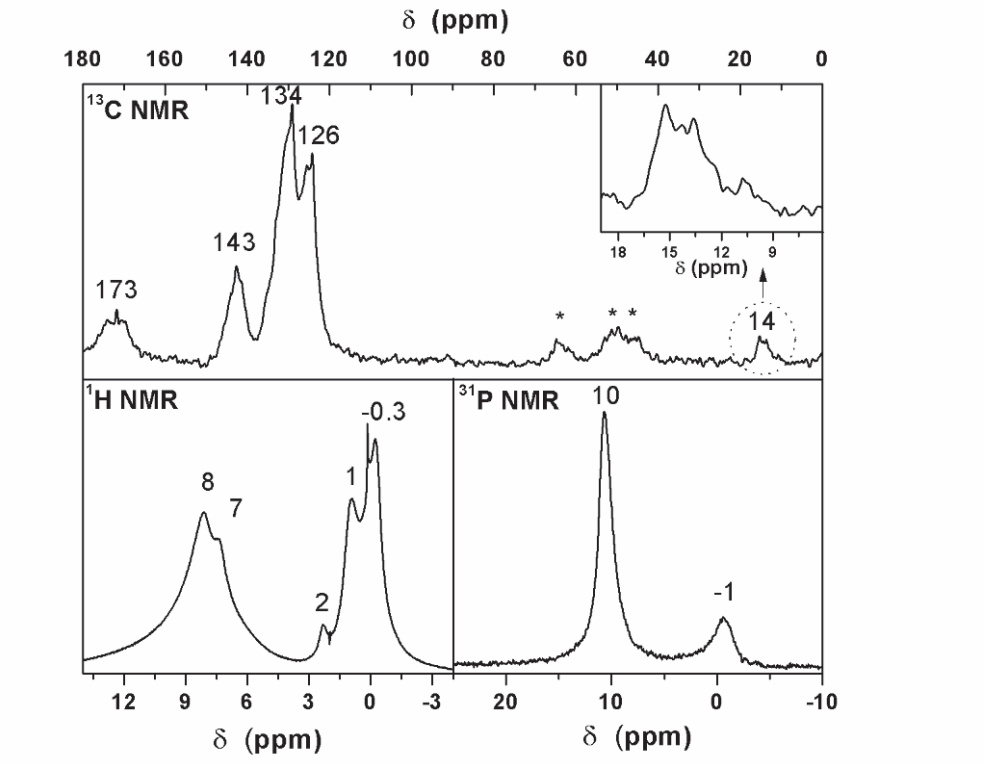

Figure III.18: ^{13}C, ^{1}H, ^{31}P solid state NMR of sample (UiO-ABDC-MOF after a reaction with gold complex).

The Zr, Au and P content determined by elemental analysis (Table III.3) indicates a final weight content of 22%, 7.6% and 1.5%, respectively, which translates to molar ratios of Zr/Au = 6 and Au/P = 0.8, in the functionalized MOF. These results suggest that only about 1 equivalent of gold(I) methyl trimethylphosphine reacts per secondary building unit, $[Zr_6(OH)_6(O)_6L_6]$, rather than 1 equivalent of gold per available starting hydroxyl, thus explaining the presence of residual ν(OH) in the IR and ^{1}H NMR spectra, respectively. The experimental Au/P = 0.8 ratio is in agreement with the data, and indicates that, in majority, the phosphoros is present as a ligand to a Au(I) center.

Finally, the grafting of the gold(I) complex on OH moiety was followed by quantitative analysis of methane release (see Eq.III.5). Gas chromatographic analysis of the volatiles obtained during the drying of the reaction mixture, showed the release of methane (18 μmol) and ethane (6 μmol), one possible explanation for the ethane detection being decomposition of the starting gold complex by homocoupling of the methyl ligands.

$$Zr_6(OH)_4(O)_4L_6 + AuMe(PMe_3) \longrightarrow Zr_6(OH)_3(O)_4L_6(OAuPMe_3) + CH_4\,(g) \quad \ldots\ldots\ldots \text{(Eq.III.5)}$$

The small quantity of the methane released (18 µmol versus 94 µmol of starting $Zr_6(OH)_4O_4L_6$ suggests that the grafting following Eq.III.5 rather than the inclusion of PMe_3AuMe in the UiO-66-BPDC cavities occurs on less than 20 % of the available cornerstone hydroxyl's of the MOF.

Table III.3: Elemental analysis results (Au, P and Zr) and gas phase analysis (CH_4 and C_2H_6) for the material obtained after a reaction of PMe_3AuMe with UiO-66-BPDC.

Phase	Solid (material)			Gas phase	
Analyte	Au	Zr	P	Methane	Ethane
Experimental	7.6[(a)]	22[(a)]	1.5[(a)]	18 ± 1[(b)]	6 ± 0.5[(b)]
calculated[(c)]	8.2[(a)]	22.8[(a)]	1.3[(a)]	94[(b)]	

(a): weight%, (b): µmol, (c): calculated for eq.III.5 yielding $Zr_6(OH)_3O_4L_6(OAuPMe_3)$.

In conclusion, PMe_3AuMe can be included into UiO-66-BPDC cavities up to 1 mol of Au per cornerstone. But only 20% of the gold was grafted on the OH moieties of the MOF.

III.3.2. Reactivity with silane:

The high temperature dehydroxylation treatment of inorganic oxides such as silica can induce the formation of highly strained cycles than can undergo reaction with organometallic or organic complexes providing a route to surface organometallic chemistry not involving starting silanols. For example, upon treatment of silica at 700 °C highly strained four member cycles have been shown to react with $MeReO_3$[162, 163] or silane[164] to yield the functionalized metallated or silanized material (Eq.III.6, Eq.III.7 respectively). While in the absence of such strained cycles the silica surface is unreactive with respect to SiH_4.

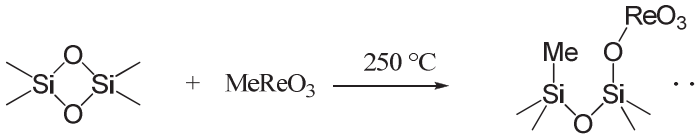

. . . . . (Eq.III.6)

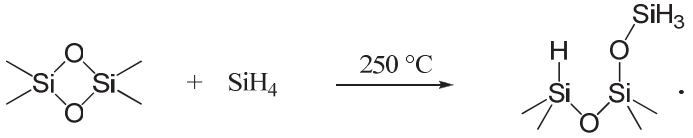

. . . . . (Eq.III.7)

As discussed above, the UiO-66 cornerstone is able to undergo dehydration step which generates a dehydroxylated form $[Zr_6(\mu^3\text{-}O)_6L_6]$. The absence of ligands on two of the eight

triangular faces of the Zr_6 octahedron, coupled with the known readiness of the dehydrated phase to split water O-H bond to regenerate the starting MOF prompted as to investigate the reactivity of such dehydroxylated phase of UiO-66 with bands less reactive than O-H bonds.

The dehydroxylated phase of the UiO-66-BPDC does not react with alkane C-H bonds. Another more reactive molecule, SiH_4 was tested. Changes on the surface of the MOF or the gas phase mixture were followed by FTIR.

A thin film deposition of the UiO-66-BPDC on silicon wafer was totally dehydroxylated at 300 °C for 5h under high vacuum (10^{-5} mbar). Then, SiH_4 (250 mmHg of 0.5% in Argon) was added to the cell. At room temperature, no change in the pressure of SiH_4 was observed and hence, no reaction with the zirconium cornerstone is expected. At 50 °C, the OH intensity started to increase as illustrated in Figure III.19, which can be explained by reaction of the zirconium cornerstone with SiH_4. However, no Si-H band was detected on the surface. The reason can be related to the low extinction coefficient of Si-H compared to O-H groups. Moreover, no appreciable drop in the gas phase (SiH_4) was observed.

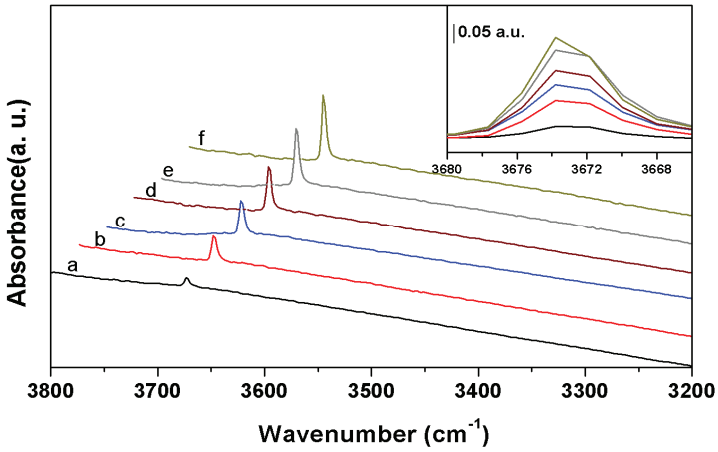

Figure III.19: *In situ* FTIR spectra in 3800-3200 cm^{-1} region of the UiO-66-BPDC-MOF in the presence of SiH_4, a) at RT, b) at 50 °C, c) at 100 °C, d) at 150 °C, e) at 200°C, f) at 300 °C. The inset represents a zoomed overlap between 3680-3666 cm^{-1} in the OH stretching region.

A substantial consumption of silane was only observed under heat treatment at 300 °C. After 2h at 300 °C the silane is completely consumed as depicted in the Figure III.20. A blank was realized where silane was heated at 300°C for 4h in the absence of UiO-66-BPDC and no reaction took place.

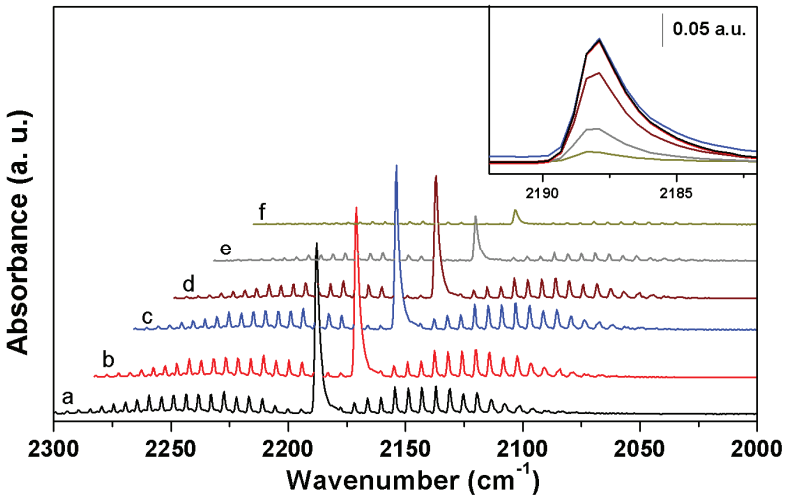

Figure III.20: *In situ* FTIR spectra of the gas phase in the 2300-2000 cm^{-1} region (SiH_4) a) at RT, b) at 50 °C, c) at 200 °C, d) at 300 °C for 30 mn, e) at 300°C for 60 mn, f) at 300 °C for 120 mn. The insert represent a zoomed overlap in the Si-H stretching band.

The sample obtained after reaction with SiH_4 was also characterized by X-Ray diffraction. According to the XRD pattern the structure of the MOF was preserved, and peaks of the compound were becoming more intense and narrow. In addition a peak at 28.2° is rising and corresponds to crystalline silicon. (Figure III.21)

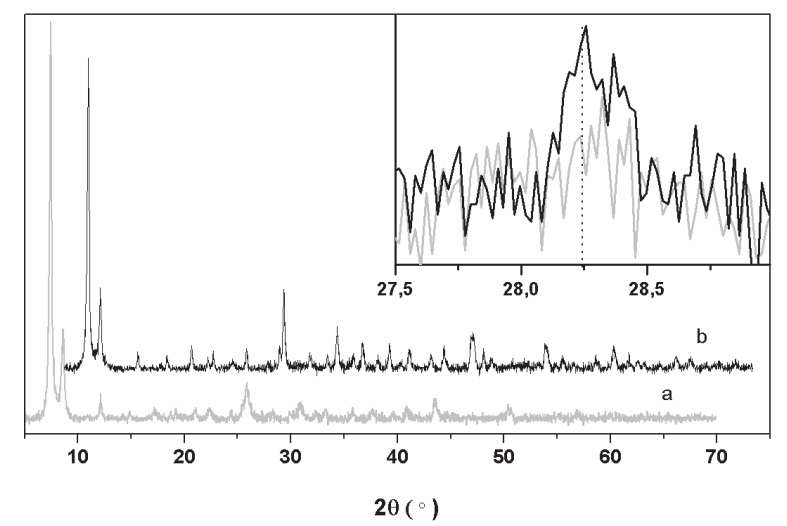

Figure III.21: XRD pattern of a) (black curve) UiO-66-BPDC-MOF as synthesized, b) (gray curve) after treatment under SiH_4 at 300 °C.

The progress of thin films transistors, solar cells, image sensors depend on the development of high quality polycrystalline silicon.[165] Such material can be obtained by

different methods like metal-induced crystallization (MIC) using different metals (Ni, Al, Cu,..),[165]vapor-liquid-solid (VLS) growth techniques, epitaxial or non epitaxial methods[166]. The preparation of nanowire using a non-epitaxial technique requires a template such as anodic aluminium oxide (AAO)[166] having an ordered 1D honeycomb nanopore. The size of the pore can be controlled from a few nanometer to several hundred nanometers.[167] Kok-Keong Lew et al[168] described a method to prepare Si nanowire in the direction of the pores. We are investigating whether the method presented here of SiH_4 polymerization within a MOF nanocavities could be promising in the context of controlled growth of silicon nanowire.

III.4. Application of UiO-66 MOF:

III.4.1. Catalytic activities of UiO-66-ABDC and UiO-66-BDC in aza-Michael reaction:

Addition of amines to α-β unsaturated carbonyls known as Michael reaction (Scheme III.1) is well used in pharmaceutical intermediates, antibiotics, and other biologically active molecules and drugs.[169] This reaction requires basic or acidic conditions.[170] UiO-66-ABDC contains amine groups with basic character, and is therefore a good candidate for the aza Michael reaction.

UiO-66-ABDC and UiO-66-BDC were tested in this reaction and, the latter MOF being used as a standard to assess the role, if any, of hydroxyl groups to catalyze this type of reaction.

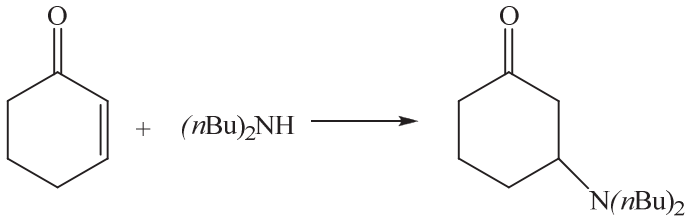

Scheme III.1: The aza-Michael reaction of cyclohexen-1-one with dibutylamine.

Dibutylamine (0.85ml) and cyclohexen-1-one (0.53 ml) were introduced in three different reactors: one without catalyst, the second with UiO-66-BDC (20 mg) and the third with UiO-66-ABDC (20 mg), the reations were carried out at room temperature for 24h.

The catalytic results are shown in the Figure III.22 where the three conversions are 39%, 42%, 47% for the blank test, (without any catalyst), UiO-66-BDC, UiO-66-BPDC respectively almost similar, indicating no real effect of the presence of the MOF.

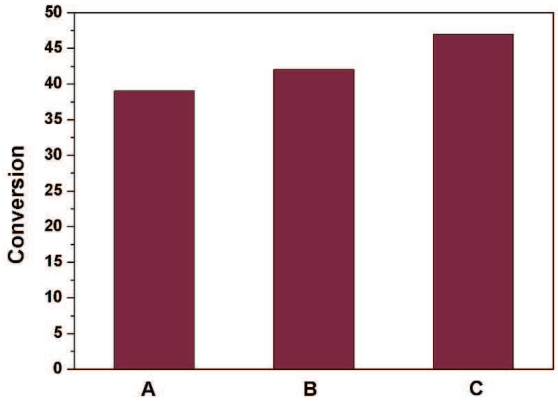

Figure III.22 : Uncatalyzed (A), catalytic activities (B) UiO-66-BDC and (C) UiO-66-BPDC in conversion of cyclohexen-1-one in aza-Michael reaction.

III.4.2. Carbon dioxide adsorption on UiO-66:

The amount of CO_2 released in the atmosphere is increasing in an alarming way, thus the capture of CO_2 excess is a desirable alternative to emission reductions.[171] However, the separation step in the capture and sequestration process is challenging.[172] Currently, the most promising method for CO_2 separation is liquid absorption using monoethanolamine (MEA). [171] Recently solid amine (amino-functionalized silica) showed interesting uptake of CO_2. [173] Our goal is to test the UiO-66-BDC and UiO-66-ABDC as adsorbents. Both materials are microporous and present high surface areas; the second one contains also a secondary functional group $–NH_2$.[150]

Two samples of isomorphic material of UiO-66 were tested in CO_2 adsorption at two different temperatures 0 °C and at 20 °C, by Baroz Aziz, and Niklas Hedin, at department of Physical Inorganic and Structural Chemistry, Arrhenius Laboratory, Stockholm University, (Sweden).

The uptake of CO_2 was analyzed using the Freundlich adsorption isotherm with two adjustable parameters. This isotherm was originally derived empirically. The Freundlich expression (Eq.III.8) relates the amount q adsorbed to the pressure, p, via the (heterogeneity) parameter n, and proportionality constant, K_f, as:

$$q = K_f p^{1/n} \quad \text{. . . . . .(Eq.III.8).}$$

The two samples exhibit physisorption of CO_2 at all pressures as indicated from the monotonic and predictable increase (with a single component Freundlich isotherm) in the adsorbed amount upon pressure increases. UiO-66-ABDC showed a significant capacity for CO_2 uptake. At the highest pressure studied (800 torr), this material took up about 3.0 mmol/g at 0 °C, that is more than two times higher than the one adsorbed by UiO-66-BDC (≈ 1 mmol/g).

The adsorbed gas is normally present at higher concentrations at low temperatures than at high, because of the exothermic nature of adsorption[174] and the two samples tested showed such typical dependencies (Figure III.23).

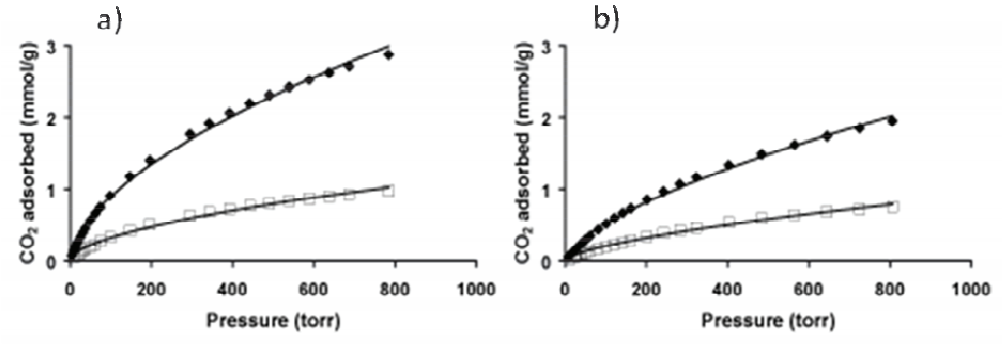

Figure III.23: Adsorption isotherms of the CO_2 as function of pressure at a) 0 °C, b) RT of Zr-ABDC-MOF (♦), and Zr-BDC-MOF (□) and corresponding Freundlich isotherms (—)

The parameterized dependencies for the uptake of CO_2 are reflected in K_f and n, and are presented in Table III.4. The tendency to the adsorption is reflected in the parameter K_f.

Even though the surface area of the UiO-66-ABDC is less than UiO-66-BDC the adsorption of CO_2 is more than two times higher suggesting that the adsorption occurs not only on the zirconium cluster but probably interact also with amine groups of the MOF showing good potential of UiO-66-ABDC as CO_2 capture.

Table III.4: Estimated parameters for the Freundlich expression model for the uptake of CO_2 on two UiO-66 MOFs.

Sample	BET (m^2/g)	T (°C)	K_f(mmol g^{-1} bar $^{-1/n}$)	n
UiO-66-ABDC	877	0	0.0606	1.71
		20	0.0260	1.54
UiO-66-BDC	1090	0	0.0242	1.78
		20	0.0105	1.55

III.5. Conclusion:

The family of isostructural MOF based on the UiO-66 structure, that is zirconium having as cornerstone octahedron where the triangular faces are bridged alternatively by hydroxyl and oxo moieties in a cubic arrangement, has proven an interesting substrate for attempting a surface organometallic chemistry approach to MOF functionalization.

The most successful parts of this work have been: (**i**) the large scale synthesis and (**ii**) the extensive and quantitative analysis of OH moieties in the UiO-66 family $Zr_6(OH)_4O_4L_6$ with L = terephtalate and biphenyl dicarboxylate (already known in the literature) and L = amino terephtalate new material described here for the first time and for which attempts to find direct applications (such aza-Michael or CO_2 adsorption) have also been done.

The UiO-66 materials are now completely characterized (for example complete texture, elemental analysis, …) and it is proven that the hydroxyl groups are fully chemically accessible. Furthermore three different titration methods have been developed based on IR, TGA, and reaction with MeMgBr, all consistently yielding a quantitative measurement of OH present in the MOF and average OH content very close to the expected one, based on the molecular formula. Such work of quantitative OH determination on a MOF has no literature precedent.

The next step in surface organometallic chemistry approach, that is the reacting with organometallic precursor, has proven more challenging. Out of the series of organometalic complexes explored $Ta[CH_2C(CH_3)_3]_3[=CHC(CH_3)_3]$, Ru(COD)(COT), Ru(COD)(nahptalene) and Me_3PAuMe, only the latter, is giving some indications that reaction with the MOF hydroxyl groups is occurring. Nevertheless, the current advancement of characterization does not allow to precisely quantify the grafted gold vs the physisorbed one, and hence showed to be considered work in progress. An extended X-Ray absorption fine structure (EXAFS) determination of the presence of Zr-O-Au bond, coupled to X-Ray diffraction (XRD) confirmation of the absence of gold nanoparticles would be beneficial to this end.

One of the probable reasons that hinder more successful surface organometallic functionalization of UiO-66 is limited size of the structure nanopores, which in fact excludes most of the organometallic complexes due to their size.

The use of reactive inorganic molecules, such as SiH_4, rather than a full metal organic complex, proved to be an interesting alternative.

By exploiting the known dehydroxylated phase of UiO-66, it was possible to polymerize gaseous of SiH_4 to crystalline silicon in the presence of MOF UiO-66-BPDC. Such novel route to silicon could be interesting in the context of controlled growth of silicon nano-objects, tailored toward electronics, photonics,…

In conclusion, surface organometallic chemistry can be achieved on MOF since these materials can be activated and reacted in a molecularly well defined way. Nevertheless, the attempt to use a functional groups present on the secondary building unit of the MOF as grafting site is probably not the best approach since in most cases such moiety could be the least accessible site of the material, therefore hindering reaction with incoming organometallic precursor, especially in MOF with small to medium nanopores.

III.6. Experimental Part:

General synthetic procedures.

(See experimental part of chapter II for physical and chemical characterization techniques).

MeMgBr (sigma-aldrich) was used as received without further purification. PMe_3 was stored under argon on molecular sieves. Dibutylamine (Fluka, 99%), cyclohexen-1-one (Fluka, 98%), toluene (Chimie-Plus, 99%) and decane (Alfa Aesar, 9%) were used as received.

Organometallic complexes $Ta[CH_2C(CH_3)_3]_3[=CHC(CH_3)_3]$,[175] Ru(COD)(COT),[176, 177] Ru(COD)(naphthalene)[123, 178] and PMe_3AuMe[179] were prepared as described in the literature.

Preparation of UiO-66-BDC, UiO-66-BPDCand UiO-66-ABDC:

Two methods for the synthesis of the MOFs: UiO-66-BDC, UiO-66-BPDC, UiO-66-ABDC were applied. The solvent (DMF) was used as received or distilled but no influence on the quality of crystals was observed.

UiO-66-BDC

Literature synthesis of UiO-66-BDC[150] was performed by dissolving 1,4-benzenedicarboxylic acid (H_2BDC) (66.5 mg, 0.4 mmol) and $ZrCl_4$ (93.2 mg 0.4 mmol) in N,N' dimethylformamide (DMF) (9.44 g, 129 mmol) at room temperature. The thus obtained mixture was sealed and placed in a pre-heated oven at 120 °C for 24 hours. Crystallization was carried out under static conditions. In the second approach, the mixture was heated at 80 °C for 12 h followed by 48 h at 110 °C. After cooling down to room temperature the resulting solid was filtered, washed with fresh DMF and dried at room temperature. Characterization included BET, TGA, XRD measurements.

UiO-66-BPDC

In a volumetric flask biphenyl-4, 4'-dicarboxylic acid ($BPDCH_2$) (2.0790g, 8.58 mmol) was dissolved in N,N' dimethylformamide (DMF) (200 ml, 188.8 g, 2.58 mol) under stirring. $ZrCl_4$ (2 g, 8.58 mmol) was added; (metal: linker: solvent = 1: 1: 300), and the mixture stirred for about 10 minutes at room temperature. After that, the flask was sealed with a septum and placed in a pre-heated oven at 80 °C for 12h then at 110 °C for 48h. Crystallization was carried out under static conditions. After cooling down to room temperature the resulting solid

was filtered, washed with fresh DMF and dried at room temperature. Characterization included BET, TGA, XRD measurements.

UiO-66-ABDC

Standard synthesis of Zr-ABDC MOF was performed by dissolving 2-amino terephtalic acid ($ABDCH_2$) (1.166 g, 6.4 mmol) in N,N' dimethylformamide (DMF) (169.9 g, 2.32 mol). $ZrCl_4$ (1.5 g, 6.4 mmol) was added with stirring at room temperature. The thus obtained mixture was sealed and placed in a pre-heated oven at 120 °C for 24 hours. In a second method, 2-amino tereftalic acid ($ABDCH_2$) (1.166 g, 6.4 mmol) was introduced to a volumetric flask, followed by N,N' dimethylformamide (DMF) (150 ml, 141.6 g, 1.94 mol). $ZrCl_4$ (1.5 g, 6.4 mmol) was added; (metal: linker: solvent = 1: 1: 300), and the mixture was stirred for about 30 minutes at room temperature. After that the flask was sealed with a septum and placed in a pre-heated oven at 80 °C for 12h then at 100 °C for 36h. Crystallization was carried out under static conditions. After cooling down to room temperature the resulting solid was filtered washed with fresh DMF and dried at room temperature. Characterization included BET, TGA, XRD measurements.

H/D exchange:

In situ FTIR spectra were obtained in transmission mode on a thin film deposited on a silicon wafer. The thin film has been prepared from a toluene suspension of 10 mg of UiO-66 MOFs. Such coated silicon wafers were activated at 120 °C under high vacuum (10^{-5} mbar) for two hours, after which vapor pressure of deuterated water was introduced to the IR cell and the excess removed. Regular water was introduced after that to check the reversibility of isotope exchange.

Calibration of the IR response towards hydroxyl groups:

The response of FTIR instrument was calibrated with MCM-41 dehydroxylated at 500 °C (1.4 OH nm², 1000m²/g, 2.32 mmol OH/g). Four pellets of silica of 22, 28, 35, and 56 mg were treated at 500 °C overnight and analysed by IR. The OH region bands were integrated in the range 3900-3500 cm^{-1} and gave following areas: 24.9, 30, 33.3, and 57.8 respectively. A linear relation between the amount of OH and the area of the peak was plotted:

$Q(mmmol) = 0.0023 \times S(a.u.)$.

A pellet of 10 mg of UiO-66-BPDC was prepared and treated under vacuum at 120 °C to evacuate the physisorbed water and its IR spectrum was taken. The OH band region was integrated and a value of 9.4 a.u. obtained. According to the formula obtained above it corresponds to 0.0216mmol of OH in the sample (10 mg), and 36.72 mg OH per 1g of UiO-66-BPDC. According to the molecular formula of UiO-66-BPDC [$Zr_6O_4(OH)_4(O_2C\text{-}C_6H_4\text{-}C_6H_4\text{-}CO_2)_6$], the theoretical weight of OH groups is $\frac{4\times17}{2120.5} = 32.06$ mg per 1g of UiO-66-BPDC.

Titration of the OH with Grignard reagent:

In a glovebox, 200 mg of activated UiO-66-BPDC (extraction with methanol and treatment at 150 °C under high vacuum overnight) was introduced in a Schlenk. Under inert atmosphere of argon 1 ml of MeMgBr (3M in diethyl ether) in 2ml of dry ether was introduced by dropping funnel and the reaction was stirred overnight. Both the evolved gases and the solvent were trapped at 77 K in a Schlenk tube connected to a large round-bottomed flask (volume of the flask, $V_{Reactor}$ = 6000 ml), allowing all the solvent to be evaporated. Samples of the gas phase from the reactor were collected through a septum with a gas-tight syringe and were analyzed by GC. The molar quantities of the different hydrocarbons evolved were estimated after a standardization of the detector of the gas chromatograph with methane and using the following formula:

$$n_{Gaz} = \frac{(V_p + V_I)\times(V_R + V_P)}{V_P \times V_I} \times \frac{k}{C_n} \cdot Area_{Gaz} \quad \text{.....(1)}$$

n_{Gaz} n(alkane) (in mol).

V_R : volume of the reactor (in ml)

V_I : injected volume (in ml)

k constant ($2.8.10^{-12}$) determined by a methane standardization

Cn number of carbon atoms in the considered alkane (= 1 for methane)

AreaAlk averaged area of the alkane GC signal on the chromatogram

V_p : volume of the sampling.

An aliquot of about 20 mg was analyzed by DRIFT technique to check if all the hydroxyl groups were neutralized.

Interaction of UiO-66-BPDC with trimethylphosphine PMe_3:

Two different experiments have been performed

For *in situ* FTIR analysis: thin film of UiO-66-BPDC deposited on silicon disk was prepared as described for H/D exchange experiment. The material was activated at 150 °C under high vacuum to remove the adsorbed water, and vapor pressure of PMe_3 was introduced into the IR cell. The interaction of PMe_3 with the surface of the UiO-66-BPDC was followed by FTIR by analyzing the region of O-H and C-H stretching modes. The sample was then treated at 100 °C, 150 °C, 200 °C, and 250 °C under vacuum to follow the desorption of PMe_3.

For CP MAS ^{1}H, ^{13}C, and ^{31}P NMR spectroscopy: In a glove-box 100 mg of UiO-66-BPDC were introduced to a glass reactor. Argon was removed on a high vacuum line and the material was exposed to a vapor pressure of PMe_3 overnight, followed by heat treatment at 50 °C under high vacuum for four hours. The final product was transferred to the glove-box, put in zirconia rotor and characterized by solid state NMR spectroscopy.

Reactivity of the hydroxyls with PMe_3AuMe:

200 mg (0.023 mmol) of activated UiO-66-BPDC MOF was impregnated with an excess of PMe_3AuMe (110 mg, 0.377 mmol, 16 equivalents) in 10 ml of ether for 4 hours at room temperature under argon. After the reaction, the released methane was quantified by GC analysis. The excess of the organometallic complex was extracted by washing three times with ether. The material was dried under high vacuum and has been characterized by DRIFT, NMR (^{1}H, ^{13}C, ^{31}P), and elemental analysis.

Reactivity of UiO-66-BDC with silane:

A thin film of the UiO-66-BDC of *ca.* 10 mg deposited on silicon wafer was totally dehydroxylated at 300 °C for 5h under high vacuum (10^{-5} mbar). 250 mmHg of 0.5% SiH_4 in argon was added to the IR cell. The changes in the gas phase (SiH_4) and the surface of UiO-66-BDC (O-H and Si-H stretching regions) were followed by FTIR at different temperatures (50, 100, 150, 200, 250, 300 °C) and in time.

Aza-Michael reaction test:

To three reactors dibutylamine (0.85 ml) with cyclohexen-1-one (0.53 ml), were introduced. The first one without any catalyst added served as a standard. To the second and the third 20

mg of activated UiO-66-ABDC (amino-terephtalic acid) and activated UiO-66-BDC (benzene dicarboxylic acid)-MOF were added, respectively. The reactions were carried out at room temperature for 24h, and analyzed by GC.

CO_2 uptake:

CO_2 uptake was determined for two samples: UiO-66-BDC UiO-66-ABDC at 0 °C and at room temperature. A Micromeritics ASAP 2020 surface area analyzer was used to measure the adsorption of CO_2 on the samples. About 50-200 mg of the adsorbent were added to the sample container in glove-box under an atmosphere of argon before the analysis. The samples were then degassed under vacuum conditions (2 μmmHg) at 150 °C for 6 hours and refilled with dry N_2 using the degassing unit of the ASAP 2020. During adsorption, the sample was kept under isothermal conditions in a temperature controlled Dewar. At 0 °C, slurry of ice and water we used to keep the temperature constant. For the room temperature measurements, water equilibrated to the room temperature was used. The temperature in the Dewar was measured by an external thermocouple. The specific volumetric uptakes were measured at conditions of standard temperature (0 °C) and pressure (1 atm) and recalculated to specific amounts (mmol/g).

Chapter IV:

Modification of CPO-27 by SOMC and a novel method to prepare enhanced unsupported HDS catalyst.

IV.1. Introduction:

Post-synthetic modification is a possible route to introduce an organometallic group in metal organic frameworks and thus tailored it toward the desired properties such as selective adsorption,[146] or catalysis.[99] While the presence of a functional group, such as hydroxyl moieties, is an uncommon feature in most MOFs reported in the literature, as discussed in the prevouis chapter, phenyl rings are ubiquitous. Nevertheless, to apply MOF as supports, the material has to display some further properties, like thermal and chemical stabilities, reproducibility at large scale and permanent porosity. Reported MOF that satisfy these criteria are relatively rare, some examples being available in the literature are isoreticular metal-organic frameworks (IRMOF-n), Lavoisier institute materials (MIL) and zeolitic imidazolium frameworks (ZIF), upon which the post synthetic modification are exemplified in chapter I. Another attractive candidate displaying such physicochemical properties suitable for post-synthetic modification is the MOF isostructural series termed CPO-27,[180] or MOF-74[181], which contains a metal cation (Ni, Zn, Mg, Mn, Co) and dihydrotereftalate (dhtp) linker.

The MOF-74 and CPO-27 structure type was initially solved by single crystal XRD, yield the common structural formula after solvent removal [M_2(dhtp)] (dhtp = 2,5 dihydroxy terephtalate, $OOCC_6H_3OO$-COO). Figure IV.1 highlights the structure of CPO-27-Ni. All oxygen atoms are coordinated to the corner stone unit. Furthermore, the corner stones are linked together as helical chains along the [001] direction. The organic linker is connecting the 1D helical chains which results in a porous honeycomb structure with 1D hexagonal channels of 11 Å in diameter along the c-axis. The channels are filled with solvent.

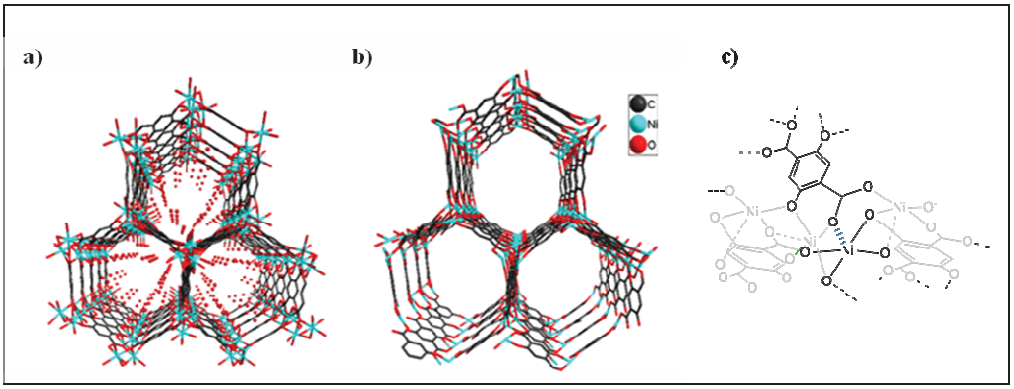

Figure IV.1: Crystal structure of CPO-27-Ni in the hydrated, $[Ni_2(dhtp)(H_2O)_2]\cdot 8H_2O$ (a), dehydrated $[Ni_2(dhtp)]$ (b) forms and molecular arrangement around $Ni_2(dhtp)$ (c)

For CPO-27-Ni, the nickel is octahedrally coordinated to six oxygen atoms, five of them being originated from the linker, while the last one is a water molecule that points towards the channel. The coordinated water molecules can be removed upon heat treatment. Removal of the coordinated water causes a transformation of the coordination sphere of Ni from octahedral to square pyramidal and generate an open site. Further investigation showed that this site can coordinate molecules such as CO, NO, N_2.[71, 182]

Temperature resolved powder X-Ray diffraction under N_2 atmosphere reveals that the long-range order of the framework is maintained to around 250 °C. The initial structure can be recovered by exposing the dehydrated sample to moisture. Thermogravimetric analysis, TGA, shows that the sample undergoes a weight loss upon heating until 200 °C. The structure starts to decompose at 350 °C, as indicated by the weight drop in the TGA curve.[76, 183] The permanent porosity of CPO-27-Ni is demonstrated by the reversible adsorption of nitrogen at 77 K.

Among the isostructural members of the series, CPO-27-Zn, has been the object of a thorough study of the phase transition between the fully hydrated $[Zn_2(dhtp)(H_2O)_2]\cdot 8H_2O$ (dhtp = 2,5 dihydroxy tereftalate) to fully dehydrated $[Zn_2(dhtp)]$ forms, and is therefore an interesting candidate for surface organometallic chemistry studies on a well defined metal organic framework.

In fact, this chapter has focused on acquiring a new spectroscopic and surface analysis data on the $M_2(dhtp)$ family, in particular for M = Zn and Ni, attempting surface organometallic by post-synthetic modification and exploring possible catalytic application.

IV.2. Results and discussion:

IV.2.1. Synthesis and characterization M_2(dhtp) (M= Ni, Zn and $Ni_{0.1}Zn_{0.9}$):

IV.2.1.1. Comparison of reported synthetic routes for M_2(dhtp):

The three different syntheses methods reported for the same MOF with the final molecular structure [M_2(dhtp)] are either based on solvothermal conditions as for route 1: for CPO-27 (M = Ni, Zn, Co, Mn),[183] and for route 2: for MOF-74 (M = Zn),[181] or at room temperature reactions, route 3.[184]

Herein, the three methods were reproduced for M = Ni and Zn and compared based on the quality of the X-Ray diffraction patterns and thermogravimetric analysis.

For all routes, a third novel material containing 10% of Ni and 90% of Zn, which will be useful for a catalytic application described at the end of the chapter has also been synthesized and characterized.

The materials obtained following the CPO-27 route are all crystalline and their X-Ray diffraction and thermogravemitric analysis patterns agree with literature data (Figure. IV.2). In particular, the TGA profiles are characterized by two distinct steps where the first one from 40 °C to 120 °C is characteristic of solvent loss. The second weight loss corresponds to the decomposition of the materials and occurs around 300 °C for CPO27-Zn and CPO-27-$Zn_{0,9}$-$Ni_{0,1}$, and around 400 °C for CPO-27-Ni.

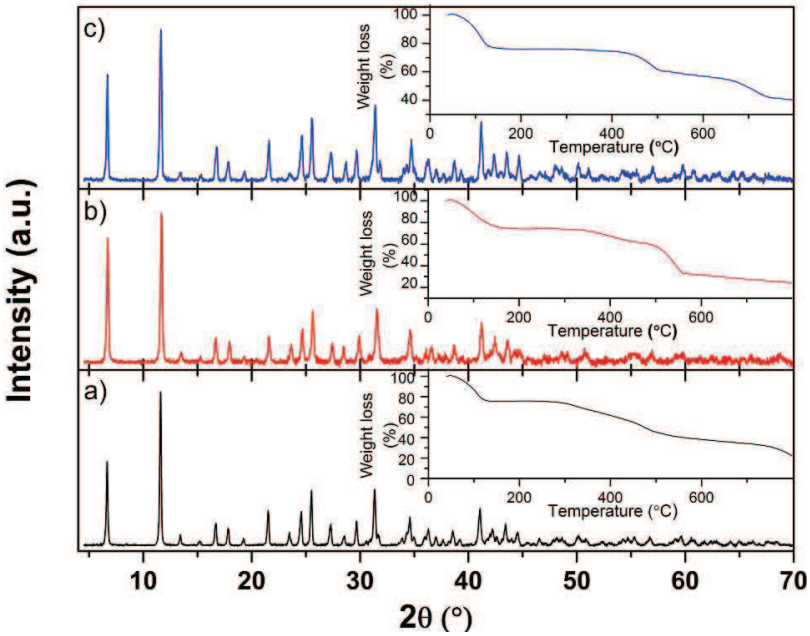

Figure IV.2: X-Ray diffraction patterns and TGA profiles of a) CPO-27-Zn; b) CPO-27-$Zn_{0.9}Ni_{0,1}$; c) CPO-74-Ni.

The materials obtained by following the MOF-74 solvothermal route[181] are also crystalline and in agreement with the reported patterns according to the X-Ray diffractograms (Figure IV.3). The TGA profiles are characterized by a continuous weight loss from the moment the solvents are released until the structure is fully decomposed, without clear weight stable region for the neatly desolvated phase [M_2(dhtp)].

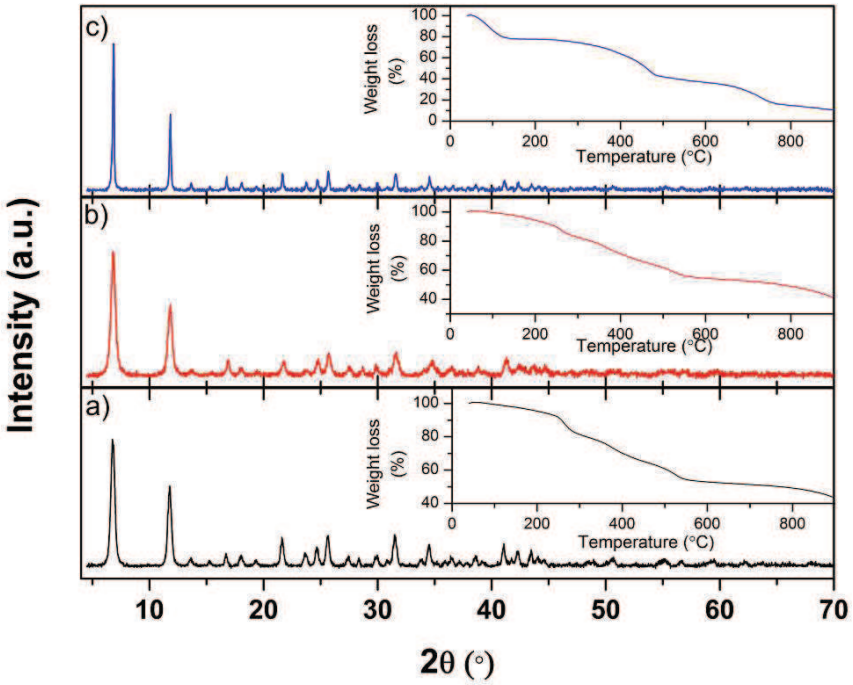

Figure IV.3: X-Ray diffraction patterns and TGA profiles of a) MOF-74-Zn; b) MOF-74-$Zn_{0.9}Ni_{0,1}$; c) MOF-74-Ni prepared under solvothermal conditions.

Likewise, the syntheses of the materials MOF-74 following the room temperature route,[184] gave crystalline materials, but with ill defined weight loss regions as shown in the inset in each part of Figure IV.4, where the TGA patterns as function of temperature are described by a continuous decrease from 40 °C to 850 °C.

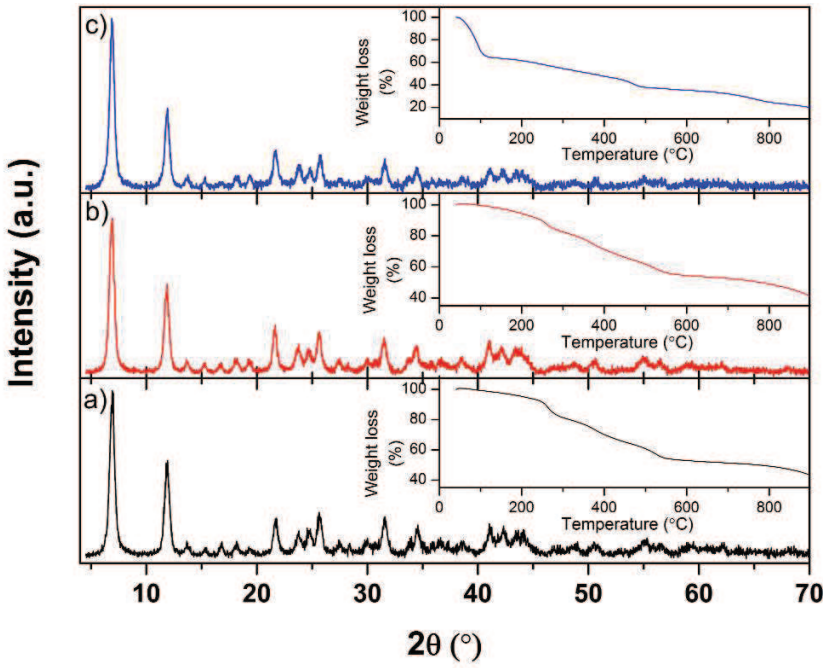

Figure IV.4: X-Ray diffraction patterns and TGA profiles of a) MOF-74-Zn; b) MOF-74-Zn0.9Ni0,1; c) MOF-74-Ni prepared at room temperature.

The results obtained from XRD and TGA suggest that CPO-27 is the most promising route to obtain the desired well defined M_2(dhtp) materials and is adopted throughout the rest of the chapter.

IV.2.1.2. Controlling the crystallite size of CPO-27 Ni during the synthesis:

In situ studies of the crystallization kinetics require advanced set-up and are generally not easily accessible. Hence, different synthesis parameters, like concentration of the reactants (by keeping the amount of reactants constant and varying the solvent content), synthesis time and temperature have been investigated and are reported in Table IV.1, in order to explore in a pragmatic way how to control the crystallite size of the final MOF. Seven samples, labeled **a÷g** have thus been obtained.

Table IV.1: The experimental parameters varied during the synthesis of CPO27-Ni to explore the effect on the final μ crystallite size.

Sample	Temperature (°C)	Time (day)	H_2O (ml)	THF (ml)
a	110	3	10	10
b	110	3	20	20
c	110	3	30	30
d	110	2	10	10
e	110	1	10	10
f	60	3	10	10
g	50	3	10	10

All the samples obtained were characterized by X-Ray diffraction. As shown in Figure IV.5, the samples are crystalline and have similar diffraction patterns.

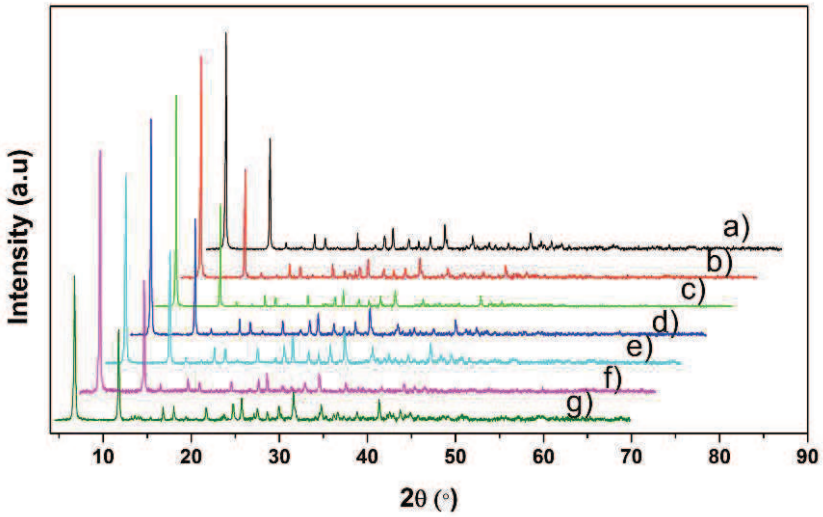

Figure IV.5 : Powder diffraction pattern of CPO-27-Ni samples **a** ÷ **g**

From the diffraction pattern the mean size of microcrystals could be evaluate, since it is related to diffraction's peak broadening by Scherrer's equation.[185]

$T = \frac{0.9 \times \lambda}{\cos\theta \times \sqrt{H^2 - H'^2}}$, where:

T - size of the particles (Å).

λ - X-Ray wavelength (Å).

θ - Bragg angle.

H - full width at half maximum (FWHM) of the measured line.

H' - full width at half maximum (FWHM) of the instrument's response.

The results are given in Table IV.2.

The crystals were also characterized by SEM technique, to observe the shape and the dispersion of the crystals and to estimate their size. The images are presented in Figure IV.6. We notice that all the different samples show almost the same shape crystallite regardless of size and have tendency to agglomerate when they are relatively small (<50 Å). The size estimate based on the SEM analysis, given in Table IV.4 result from an averaging between the large particles and small particles size. The propensity to agglomerate complicated such evaluation, especially for the small crystals, therefore yielding large error bar on these values (Table IV.2). Nevertheless, the agreement between the XRD and the SEM-based methods to evaluate the mean crystallite size is very satisfying and tends to show that these size estimations are reliable.

Table IV.2: The particle size of the different samples of CPO-27 Ni

Sample	particle diameter (Å) (from Scherrer equation)	particle diameter (Å) (SEM analysis)
a	53	40 ± 5
b	71	78 ±10
c	86	100 ± 10
d	64	52 ± 5
e	54	50 ± 5
f	74	95 ± 10
g	81	105 ± 10

From the gathered data, we conclude that when the concentration of the reagents or the temperatures of the synthesis are low, the crystals have tendency to become bigger. However, when the time of crystallization process is reduced, SEM images show the presence of amorphous product, which signifies that the reaction is not yet completed. In order to obtain the crystals best suited for catalytic applications (with small sizes but well-developed, which will cause less problems for diffusion of the reactants inside the pores) the synthetic procedure described in the literature[76] is therefore the best and will be henceforth applied.

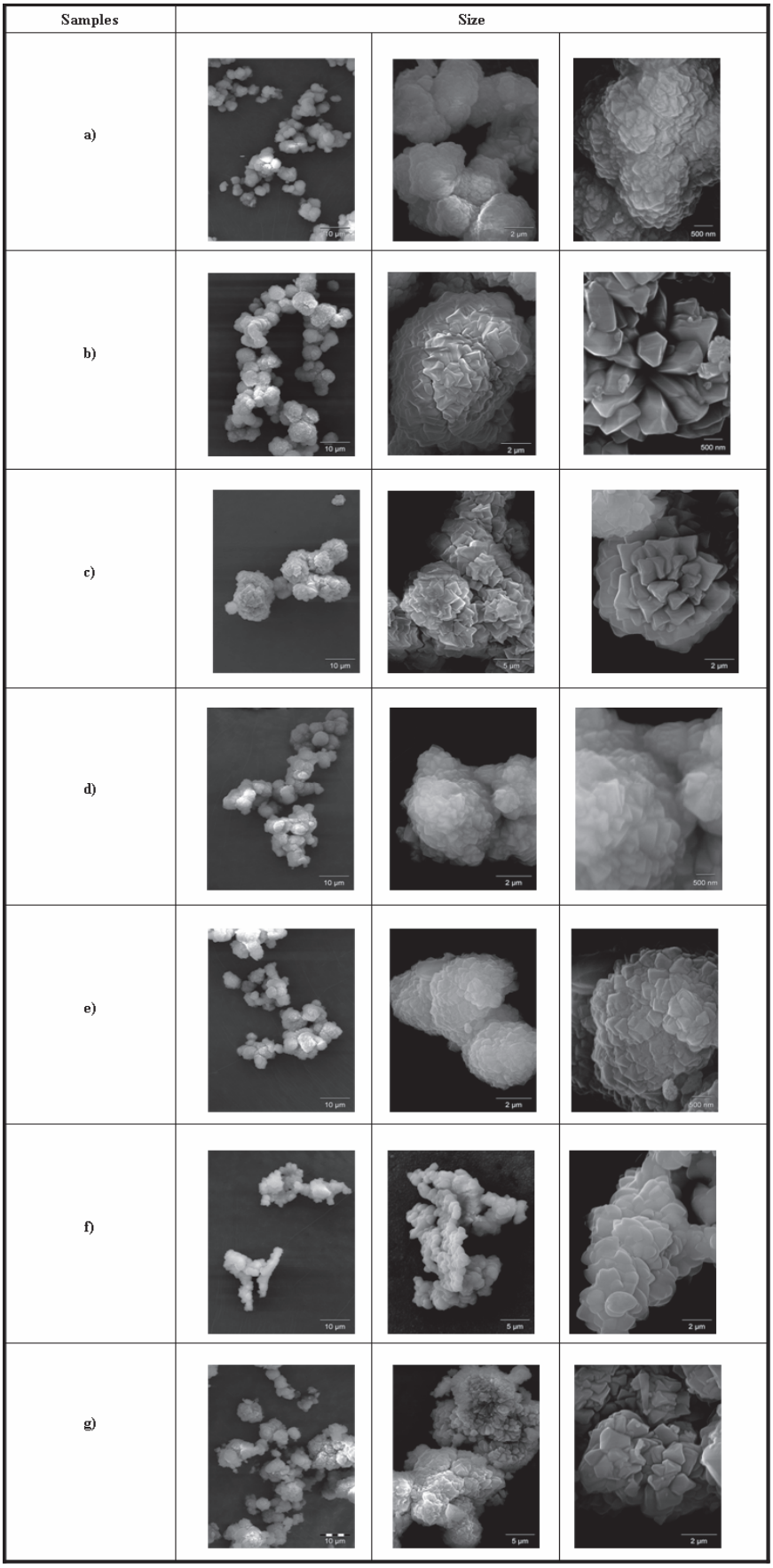

Figure IV.6: SEM images of different CPO27-Ni samples **a** ÷ **g**.

IV.2.2.1. Texture analysis of CPO-27 materials:

In the context of surface organometallic chemistry, one of the most attractive features of the COP-27 structure is the surface area and the presence of large hexagonal channels. In order to be suitable for post modification, the material must undergo a well defined activation procedure.

In the original literature synthesis of CPO-27, permanent porosity was obtained when the sample was activated under dynamic vacuum at 200 °C for 19 h in an external pre-treatment station, and then the sample was connected to the adsorption instrument and treated at 110 °C for 1 h under vacuum to obtain a fully accessible surface. A Langmuir surface area of 1316 $m^2 g^{-1}$, BET surface area of 1100 $m^2 g^{-1}$, and pore volume of 0.47 $cm^3 g^{-1}$ were found. [182]

Treatment of the CPO-27 at 150 °C under high vacuum overnight followed by 135°C for one hour on the BET setup just before the analysis was observed to be sufficient to obtain large surface areas, without loss in material crystallinity. The results are summarized in Table IV.3. It must be stressed that BET surface area is not a well defined in case of microporous materials. Therefore BET, values given in the first column of the table are valid only for comparison for MOFs from the same family. 10 Å for CPO-27-Ni, 8 Å for CPO-27-Zn and 9 Å for the bimetallic CPO-27$Ni_{0.1}Zn_{0.9}$ pores diamater were obtained. This could be due to the known interaction of molecules such as CO[71] and N_2,[182] on the available coordination site of [M_2(dhtp)] which should be stronger for Ni than for Zn. Metal interaction of N_2 molecules during the N_2 adsorption studies is also indicated by the fact that at low P/P_0 values ($4\ 10^{-7} < P/P0 < 3\ 10^{-6}$), the amount of N_2 adsorbed increases rapidly until a plateau just below 1 : 1 ratio between adsorbed N_2 molecules and available Ni^{2+} sites, suggesting that the primary adsorption occurs on Ni^{+2} sites.[182] The extent of such interaction is expected to vary with the nature of the metal center, and such variations are not fully taken into account in the measured pores volume in the three samples. As conclusion, the CPO-27-Ni MOF gives higher surface area and larger pores size compared to the two others. However, overall the three materials have all accessible and relatively large 1D channels (8 Å or above) after proper activation.

Table IV.3: Adsorption properties of CPO-27-M (M = Ni, Zn, $Ni_{0.1}Zn_{0.9}$).

Sample	BET surface area (m^2/g)	Langmuir area (m^2/g)	Pores Volume (cm^3/g)	Mean pore diameter HK (Å)
CPO-27-Ni	800 ± 40	1100 ± 50	0.43 ± 0.05	10 ± 1
CPO27-Zn	450 ± 20	600 ± 30	0.38 ± 0.05	8 ± 1
CPO-27-$Ni_{0.1}Zn_{0.9}$	600 ± 30	780 ± 35	0.40 ± 0.05	9 ± 1

IV.2.2.2. Elemental analysis:

The microanalysis results (Table IV.4) of different elements (C, H, Ni, Zn) of the CPO-27 materials are in concordance with the molecular structure determined by X-Ray diffraction and elementary analysis reported in the literature $M_2dhtp(H_2O)_{10}$ or $M_2C_8H_{22}O_{16}$[183] for the CPO-27-Ni. Concerning the other two materials, CPO-27-Zn and CPO-27-$Ni_{0.1}Zn_{0.9}$, calculated and experimental elemental composition values show minor discrepancies possibly due to the presence of another phase.[186, 187]

Table IV.4: Elementary analysis of the CPO27-M (M = Ni, Zn, $Ni_{0.1}Zn_{0.9}$) measured (Exp) and calculated for $M_2dhtp(H_2O)_{10}$ ($M_2C_8H_{22}O_{16}$) .

Sample	% Zn		% Ni		% C		%H	
	Exp	Cal	Exp	Cal	Exp	Cal	Exp	Cal
CPO27-Zn	25.48	25.90	a	0.00	25.58	19.00	3.37	4.40
CPO27-$Ni_{0.1}Zn_{0.9}$	21.23	23.40	3.00	2.30	19.36	19.00	3.78	4.40
CPO27- Ni	a	0.00	23.60	23.87	22.10	19.60	3.80	4.50

a) value not measured.

IV.2.2.3. IR and NMR spectroscopic studies on CPO-27-M (M = Ni, Zn, $Ni_{0.1}Zn_{0.9}$):

IV.2.2.3.1. Infrared spectroscopy:

The CPO-27-Ni metal organic framework under its completely dehydrated form, [Ni_2(dhtp)] has extensively been characterized by XRD, TGA, BET, IR, Uv-Vis and Raman spectroscopies.[70, 71, 180, 182, 188]

The IR investigation of the three samples of CPO27-M (Ni, Zn, $N_{0.1}Zn_{0.9}$) was indeed useful to confirm the complete activation procedure. The sample was prepared by deposition of a suspension of CPO-27 in toluene on a silicon wafer. A thin layer of the material was coated on the surface upon drying.

The evolution of the IR spectra of three samples of CPO27-M (M = Ni, Zn, $Zn_{0.9}$-$Ni_{0.1}$) were followed over solvent removal at 120 °C. The disappearance of the characteristic water stretching mode around 3400 cm^{-1} is observed. The observation of similar disappearance of water bending mode, expected around 1653 cm^{-1} is less resolved due to the overlap of the vibration modes of the MOF skeleton. In fact, beside the water related modes, the IR spectra above 1000 cm^{-1} of the three MOF methods are characterized by bands between [3099-2800 cm^{-1}] attributed to ν(CH) stretching. Bands between [1660-1240 cm^{-1}] in the signature region of ν(C=C) stretching modes of aromatic rings. Some bands of ν(C-H) deformation were also observed.

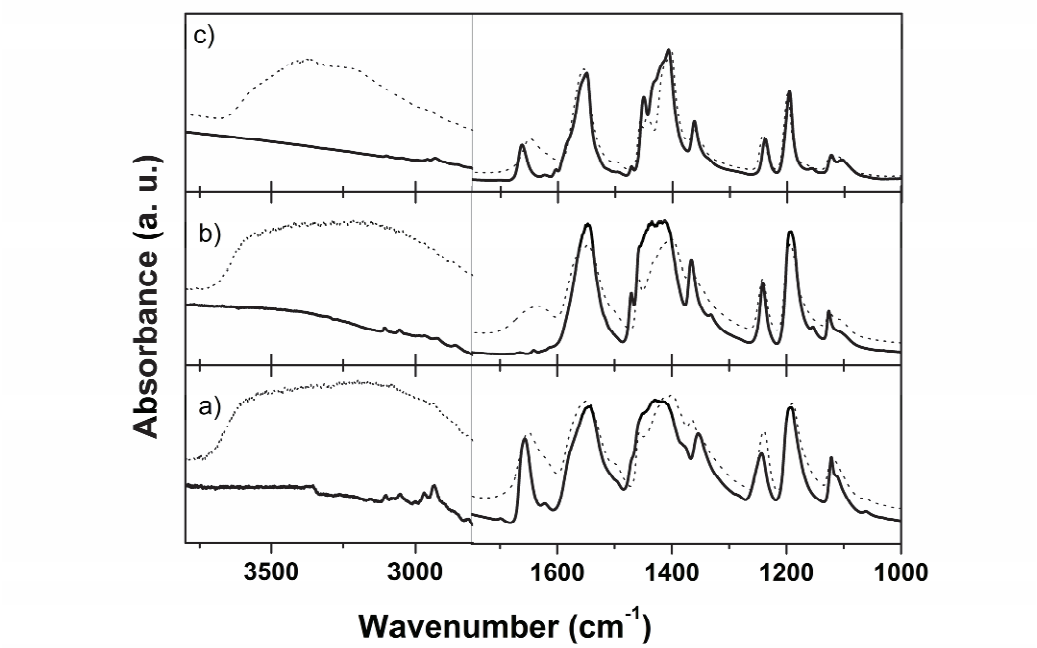

Figure IV.7: FTIR spectra of samples a) CPO-27-Zn; b) CPO-27-$Ni_{0.1}Zn_{0.9}$; c) CPO-27-Ni as prepared (dotted line) and after thermal activation (120 °C, 1h, solid line).

The interaction of CO with CPO-27-Ni was studied by IR spectroscopy and volumetric study. At room temperature and low coverage of CO, a single band at 2178 cm^{-1} is observed, whose intensity increases with CO pressure. The same band is found at liquid nitrogen temperature and it is associated with the formation of $Ni^{2+} \cdots CO$ adducts inside the CPO-27-Ni cavities.[71] The isotherm adsorption of CO on CPO-27-Ni shows coverage of 88% of the amount of nickel atoms available,[182] whose little discrepancy with respect to the expected 100% coverage can be explained by a non perfect activation of the material and/ or the presence of another phase in minor quantities.

The CO adsorption on the three different CPO-27-M materials studied (M = Ni, Zn, $Ni_{0.1}Zn_{0.9}$) was measured in a similar manner. Only CPO-27-Ni showed a strong interaction with CO as depicted in the Figure IV.8, where the peak of CO is blue-shifted by 30 cm^{-1} with respect to free CO, associated with the formation of $Ni^{2+} \cdots CO$ adducts inside CPO-27-Ni as already reported in the literature.[71] The adsorption of CO on CPO-27-Ni is easily reversible by outgassing at room temperature. By increasing the pressure of CO in the reactor, the area of the peak increases, suggesting an equilibrium between the adsorbed and the gaseous phase, confirmed by adsorption studies.

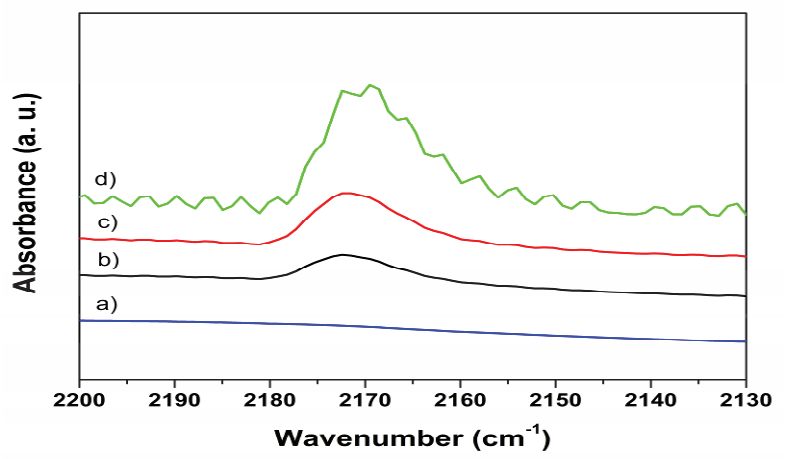

Figure IV.8: FTIR spectra of the adsorbed CO on the surface of CPO-27Ni a) activated CPO-27-Ni; b) P(CO) = 5mbar; c) P (CO) = 8mbar d) P (CO) = 15mbar

Such equilibrium phenomenon can be used to estimate the quantity of available nickel sites in the material: in analogy with the CO study mentioned above,[71] NO adsorption isotherm measurement, extrapolated from the IR spectra of the NO adsorption on CPO-27-Ni at room temperature which gives a unique band at ν(NO) = 1845 cm^{-1},[69] yielding 95% coverage on Ni sites.

The amount of CO adsorbed on CPO-27-Ni is measured at room temperature on an activated CPO-27 Ni. The adsorption isotherm has a type I profile (Figure IV.9), fitted with the Sips equation.[189]

$$N = 6.8 \times \frac{0.18 \times p^{0.6}}{0.18 \times P^{0.6} + 1}, \ldots\ldots\ldots \text{(Eq.IV.1)}$$

N: quantity adsorbed of CO mol/ g of CPO-27-Ni MOF.

P: Pressure of CO (mbar).

The adsorption profile shows that the material adsorbs large amount of CO at low pressure. Upon a gradual pressure increases, the amount of adsorbed CO is estimated to reach a plateau at 550 mbar that corresponds to 6 mmol of CO per 6.2 mmol of Ni (95% coverage), a little higher than the published 88% coverage obtained by the approach of CO coverage[71]. This number is exactly the same as the coverage obtained by NO adsorption isotherm on CPO-27-Ni already reported in the literature.[69] From IR and the adsorption study we conclude that the vacancy sites are responsible of the adsorption of CO.

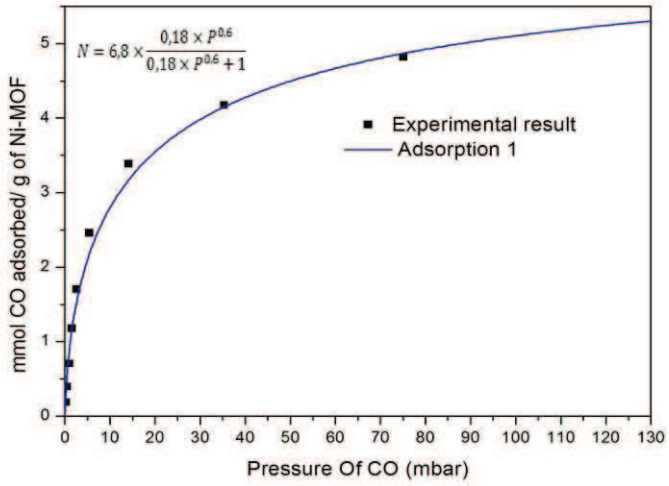

Figure IV.9: Adsorption isotherm of CO on CPO27-Ni

Deuterated acetonitrile can also be used as a probe molecule, and the study gives insight on the presence of both Lewis and Brønsted acid sites on the material.[94] Vapor pressure of CD_3CN was introduced into the IR cell containing activated CPO-27-Ni deposited on a silicon wafer, and the IR spectrum was recorded after adsorption at room temperature. The ν(C≡N) and ν(C-D) adsorption bands associated to physisorbed (2254 and 2109 cm^{-1}) and perturbed acetonitrile (2281 and 2102 cm^{-1}) are clearly observed. Upon heating at 120 °C under high vacuum, the bands at 2281 and 2102 cm^{-1} are still presented as shown in Figure IV.10. These data suggest that acetonitrile is strongly adsorbed on the Lewis sites of CPO-27-Ni. The other two materials CPO-27-Zn, CPO-27-$Ni_{0.1}Zn_{0.9}$ under same study gave no strong adsorption of acetonitrile.

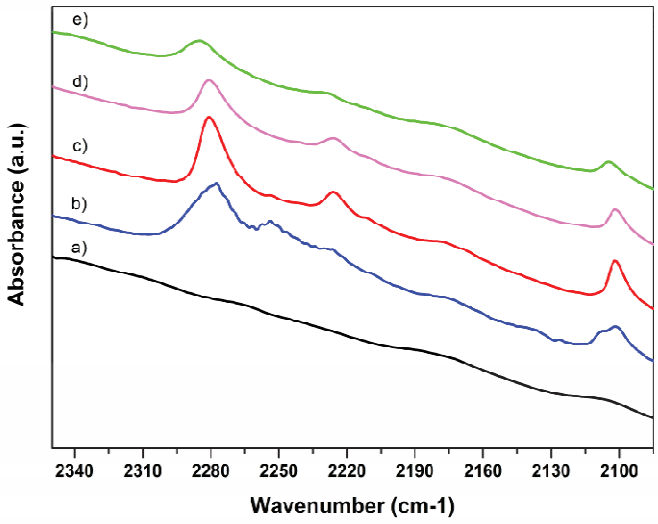

Figure IV.10: FTIR spectra of the adsorbed CD_3CNon the surface of CPO-27-Ni a) starting activated CPO-27-Ni; b) Adsorption of vapour pressure of CD_3CN; c) outgassing at room temperature of excess; d) outgassing at 120°C 1h; e) outgassing at 120°C 3h.

IV.2.2.3.2. ^{13}C CP MAS NMR spectrum of the CPO-27 materials:

The CPO-27 materials were also characterized by ^{13}C CP MAS solid state NMR. Spectra of CPO-27-Zn and CPO-27-$Ni_{0.1}Zn_{0.9}$ were recorded, however no signal was detected for the CPO-27-Ni as expected due to the presence of the paramagnetic center (Ni^{+2}). Spectra of pure ligand, CPO-27-Zn and CPO-27-$Ni_{0.1}Zn_{0.9}$ are shown in Figure IV.11, respectively. They all consist of the same sequence of peaks attributed to carboxylate (A), ipso (B), dehydroxylate ortho phenoxy (C) and orthocarboxylate (D) carbon atoms as described on the ligand's structure scheme. Comparison of spectra shows that carbon labeled A is not affected by the presence of a metal cation and resonates at the same chemical shift at 173 ppm for pure ligand and the two metal organic frameworks. On the other hand, the phenoxy carbon C in both MOFs is slightly shifted compared to the linker (~3ppm) while the other aryl carbon atoms (D and B) exhibit a more pronounced downfield shift of 8 ppm. Observed tendencies in chemical shifts could be a result of the presence of oxygen atoms with high electron affinities in the structure. Carbon A having in its surroundings two such atoms is already electron-deficient and therefore the coordination to the metal center practically does not influence the electron density around it. Carbons B and D are more sensitive to local electron density changes which is reflected in their peaks displacement. Carbon C which is bound to only one oxygen demonstrates an intermediate behavior.

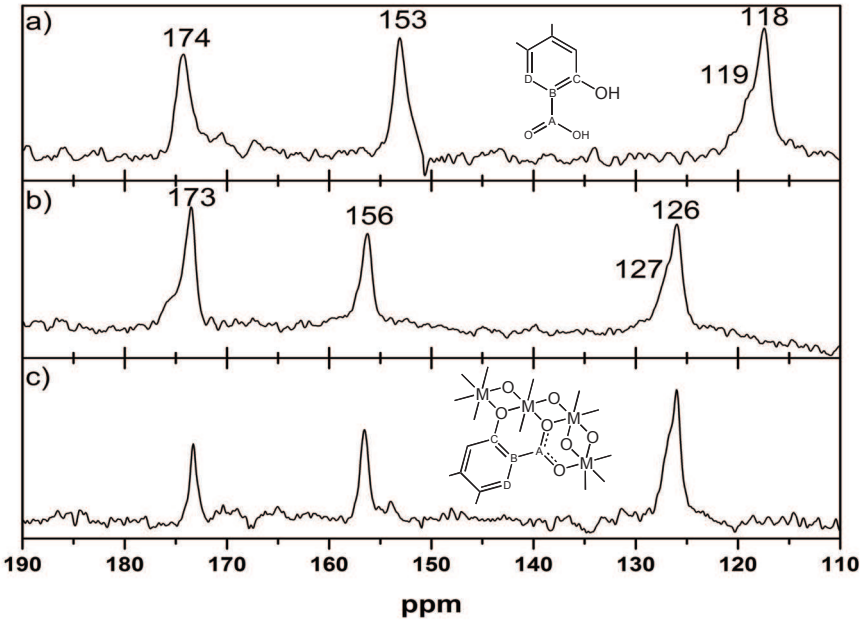

Figure IV.11: ^{13}C CP MAS solid state NMR of a) dihydroterphtalic acid; b) CPO-27-Zn; c) CPO-27- $Zn_{0.9}Ni_{0,1}$.

IV.3. Investigation of the catalytic properties of the unfunctionalized CPO-27-Ni:

IV.3.1. Acid catalysis –Meinwald rearrangement:

Epoxide derivates are widely used in organic synthesis also to produce by their rearrangement aldehydes and ketones, by the so called Meinwald rearrangement see Eq.IV.2. Many parameters have been identified as possible cause of the product distribution such as nature of the epoxide substituents, solvent and Lewis acid employed.[190, 191]

The activated CPO-27-Ni, which contains Lewis vacancy sites as demonstrated by CO and acetonitrile adsorption, was tested as catalyst for the Meinwald rearrangement. The rational for attempting such catalysis is that in CPO-27-Ni the acid site is distributed in the pore and may limit a specific migration and thereby increase the selectivity.

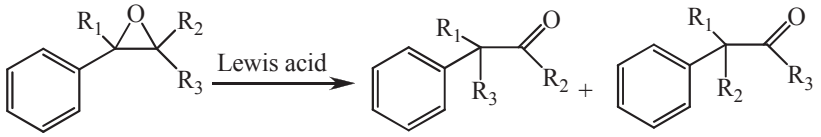

. . . . . Eq.IV.2

The experiment was performed by suspending activated CPO-27-Ni in liquid styrene epoxide at room temperature. The reaction was followed by NMR and by GC (0.1 mol of Ni/mol epoxide). No consumption of styrene epoxide was observed even after 2 days.

IV.3.2. Preferential oxidation of CO to CO_2 in CPO-27-Ni:

Metal organic frameworks with open metal sites show promising hydrogen adsorption properties.[75] CPO-27-Ni, which has indeed open metal sites, displays a fairly low hydrogen uptake, even at high pressure and low temperature, only 1.8 wt% of hydrogen can be adsorbed in the material at 77K, the storage capacity falls to about 0.3 wt% at room temperature and approximately 65 bar, which is typical for physical adsorption at ambient temperature.[183]

CPO-27-Ni displays a high affinity for CO as discussed in the previous section of the chapter, and low affinity for hydrogen. We investigated if such very marked different affinity of CO vs H_2 could be exploited in the context of preferential catalytic oxidation in the presence of H_2, also termed PROX catalysis, relevant in fuel cell technology. In fact, the hydrogen gas used in fuel cells is mainly produced from steam reforming and partial oxidation of methane.[192] Since such synthesis route always implies CO production, a thorough CO removal step is necessary before fuel cell utilization, since amount of CO as low

as 10 ppm in hydrogen stream can poison the Pt electrode and damage the cell.[193] Generally, the CO is removed by catalytic oxidation to CO_2 (Eq.IV.3). However, most of existing catalysts are also active in the reverse water gas shift reaction (Eq.IV.4), and hydrogen oxidation (Eq.IV.5).

$$CO + [OX] \longrightarrow CO_2 \quad \text{..... Eq.IV.3}$$

$$H_2 + CO_2 \longrightarrow H_2O + CO \quad \text{..... Eq.IV.4}$$

$$H_2 + [OX] \longrightarrow H_2O \quad \text{..... Eq.IV.5}$$

In the context of the purification reaction (Eq.IV.3), the other two reactions (Eq.IV.4) and (Eq.IV.5) are detrimental and therefore explain the search for a catalyst maximizing reaction (Eq.IV.3) over reactions (Eq.IV.4) and (Eq.IV.5).

Our first attempt was to try to convert the CO adsorbed in CPO-27-Ni to CO_2 by using different oxidant, such as oxygen and nitrogen oxide. Unfunctionalized CPO-27-Ni proved inactive in CO oxidation.

The reaction was followed by *in situ* gas phase IR acquired in a batch reactor containing CPO-27-Ni powder over a CO and oxidant atmosphere. No conversion of CO to CO_2 was detected in the presence of O_2 or N_2O even after heating overnight at 100 °C, 120 °C or 150 °C.

The second attempt was to introduce gold nanoparticles inside the MOF, since gold nanoparticles are known to activate molecular oxygen.[194] The CO oxidation to CO_2 is expected to be facilitated if an activated oxygen atom is close to the adsorbed CO, that is if the gold nanoparticles are close to the adsorption sites (Ni atoms in CPO-27-Ni).

Two samples, [Au@CPO-27-Ni]-1 and [Au@CPO-27-Ni]-2 were prepared from two different precursors, chloro(dimethylsulfide)gold (I) and methyl(trimethylphosphine)gold(I).

The synthesis of Au@CPO-27-Ni materials is a modified procedure of the reported ones, such as the formation of ruthenium nanoparticles Ru(0) inside MOF-5 by reduction of the previously encapsulated organometallic precursor Ru(COD)(COT) [COD = cyclooctadiene, COT = cyclooctatriene).[103] In our case, the non-sublimable gold(I) complexes were introduced in the previously activated CPO-27-Ni by wet impregnation procedure (10 mg of gold per 1 g of CPO-27). After removal of volatiles under reduced pressure, the powder was exposed to hydrogen atmosphere and heated at 100 °C, leading to Au(I) reduction to gold nanoparticles. The activities of such materials, [Au@CPO-27-Ni]-1 and [Au@CPO-27-Ni]-2

in CO oxidation were monitored by IR with the same batch reactor containing IR transparent windows described above, with 1 : 1 for O_2 : CO atmosphere. The CO consumption and a CO_2 production were observed. In order to obtain quantitative data for the conversion and for the reaction rate the integral of the CO_2 roto-vibrational bands between 2400 and 2250 cm^{-1} were monitored over time. A previous calibration of the IR signal vs CO_2 pressure (see experimental part) allowed the obtention of the conversion values (Figure IV.12).

The first sample [Au@CPO-27-Ni]-1 displayed a very low activity at room temperature. However, increasing the temperature to 100 °C the activity increased to a conversion of about 50% after 4h. The second catalyst [Au@CPO-27-Ni]-2 prepared by loading the same amount of gold but using a relatively stable gold(I) methyl complex, the catalyst is more active even at room temperature as shown in the curve in the Figure IV.12.

A possible explanation of such differences is that the gold(I) chloride complex is less stable than the gold(I) methyl on therefore decomposes fast once in contact with the MOF. The second complex is more stable and diffusion is expected to occur inside the cavities before decomposition, offering a better dispersion. One of the most salient feature of the Au@CPO-27-Ni-2 material for CO oxidation is its activity at room temperature.

Such activity is particularly relevent since the lowest temperature at which the catalysis occurs, that is the light off temperature, is a challenging parameter to minimize in the PROX catalysis.

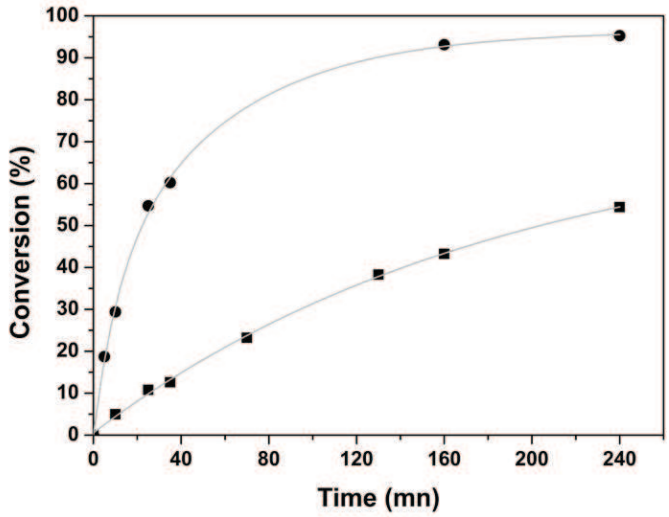

Figure IV.12: IR monitoring of CO_2 formation during the carbon monoxide oxidation over Au@CPO-27-Ni versus time squares: [Au@CPO-27-Ni]-1 at 100°C and circles: [Au@CPO-27-Ni]-2 at RT.

[Au@CPO-27-Ni]-2 was also tested as catalyst for hydrogen oxidation with the presence of O_2 (See reaction Eq.IV.4) under the same experimental conditions as described for the CO oxidation study. The IR monitoring showed no water in the gas phase, but such absence is not a direct proof of the absence of the H_2 oxidation since the eventually formed water can remain physisorbed in the solid catalyst. We therefore monitored the reaction by replacing the IR windows by a Pirani pressure gauge. When, Au@CPO-27-Ni-2 is in contact with 20 : 1 for H_2 : O_2 mixture, an overall slow pressure drop is observed indicating a slow hydrogen consumption (Eq.IV.5) Conversely, when the material Au@CPO-27-Ni-2 is in contact with 1 : 1 for CO : O_2 mixture an overall very rapid pressure increase is observed indicating fast CO_2 production (Figure IV.13).

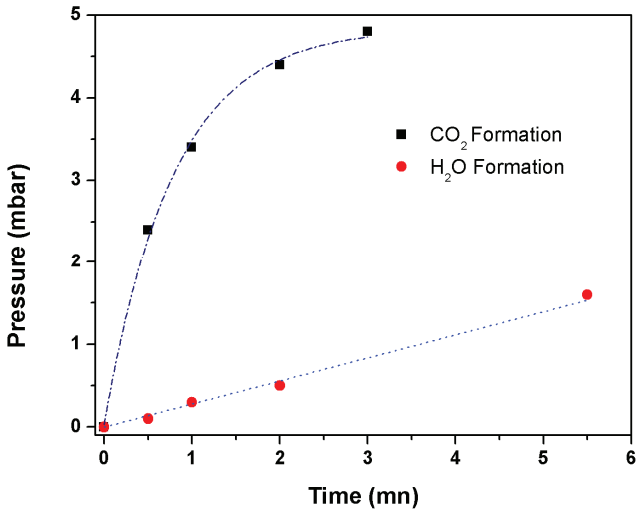

Figure IV.13: CO_2 and H_2O formation over Au@CPO-27-Ni-2 catalyst versus time.

The existence of CO and H_2O competitive adsorption phenomenon prevents a quantitative comparison of the two reaction rates. Nevertheless, the data tend to prove that the CO oxidation over Au@CPO-27-Ni-2 is much faster than H_2 oxidation suggesting that Au@CPO-27-Ni could be a good PROX catalyst.

After catalysis the crystallinity of the catalyst was checked by powder X-Ray diffraction analysis as shown in the Figure IV.14 part 1), indicating that the original CPO-27-Ni three dimensional structure is preserved. The transmission electronic microscopy of the Au@CPO-27-Ni-2 material after the catalysis is shown in Figure IV.14 part 2. No gold nanoparticles can be observed on the micrograph suggesting that the nanoparticles, are smaller than 2 nm in diameter.

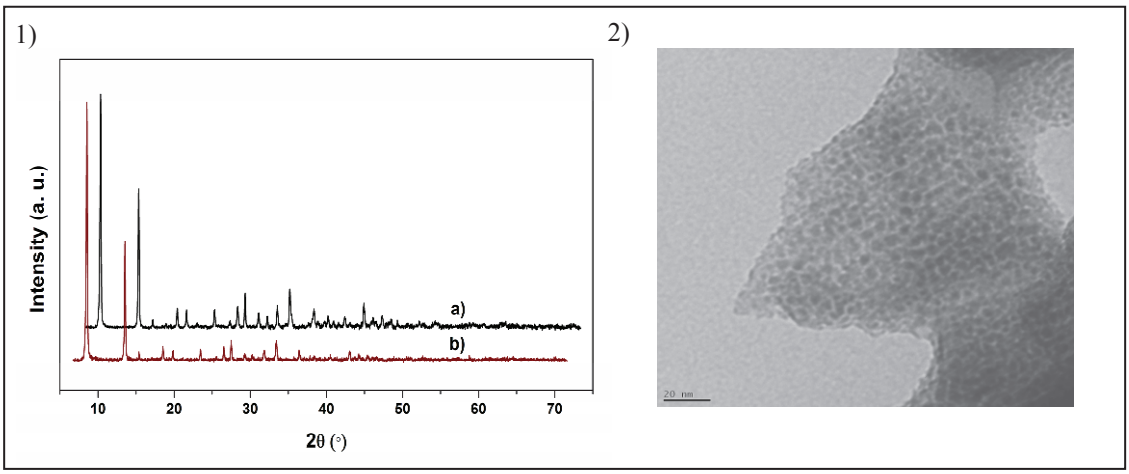

Figure IV.14: 1) X-Ray diffraction of CPO-27-Ni MOF a) as synthesized b) after impregnation of gold nanoparticles and catalysis (Au@CPO-27-Ni-2). 2) TEM picture of Au@CPO-27-Ni-2 after catalytic tests.

IV.3.3. H_2 release from ammonia borane activated by CPO-27-Ni at low temperature:

Hydrogen could be considered as a viable energy vector for the future. Nevertheless, it is suffering from the complexity linked to its storage and transportation.

Ammonia-borane (BH_3NH_3), AB is a solid with high hydrogen content (about 20 wt %), and has been considered as an interesting material for chemical hydrogen storage [195] since it could theoretically shuttle between the ammonia borane and its dehydrated version in the presence of a suitable catalyst (Eq.IV.6).

The current challenges with use of the ammonia borane as hydrogen vector are linked with: (i) the kinetics associated with the hydrogen release, (ii) the limited reversibility of reaction (Eq.IV.6) due to, for example polymerization processes (Eq.IV.7) and (iii) the overlap of further dehydrogenation steps (Eq.IV.8 and Eq.IV.9) which end up to the completely inert NB material.

$$H_3N.BH_3 \overset{T_1/Cat}{\rightleftharpoons} NH_2{-}BH_2 + H_2 \quad \text{Eq.IV.6}$$

$$n\,(NH_2{-}BH_2) \longrightarrow (NH_2{-}BH_2)_n + H_2 \quad \text{Eq.IV.7}$$

$$(NH_2{-}BH_2)_n \xrightarrow[Cat]{T_2} (NH{=}BH)_n + H_2 \quad \text{Eq.IV.8}$$

$$(NH{=}BH)_n \xrightarrow[Cat]{T_3} (N{\equiv}B)_n + H_2 \quad \text{Eq.IV.9}$$

With respect to pure ammonia borane, the presence of supports such as mesoporous silica SBA-15 have been shown to reduce to the range of 350 – 410 K the T_1 temperature at which hydrogen sarts to be released (Eq.IV.6), thus showing potential in the context of improving hydrogen chemical storage by ammonia borane, although the process is complicated by the

release of several byproducts.[196, 197] We have investigated if activated CPO-27-Ni could play a similar role low temperature of hydrogen release from ammonia borane, since its presumably use open site of Ni atoms.

The decomposition of ammonia borane, AB, has been studied by differential scanning calorimetry (DSC), thermogravimetry (TGA) and temperature programmed desorption coupled with GC. The results have been compared with the similar data acquired from a mechanical mixture between ammonia borane and mesoporous SBA-15 previously dehydroxylated at 500 °C, AB@SBA-15_{500}, and with ammonia borane mixed with previously activated CPO-27-Ni. The two components of the latter samples have been mixed in 1:1 molar ratio AB : Ni that is *ca.* 1 : 5 of AB : MOF weight ratio. The same 1 : 5 weight ratio has been kept to prepare the AB@SBA-15_{500} sample.

The thermogravimetric analysis (TGA) curve reported in Figure IV.15 part a) shows that the decomposition of a pure ammonia borane, AB, occurs in two steps, the first one starts at about 115 °C, and the second at around 130 °C. The first weight loss is about 12 ± 3%, the overall weight loss is about 33%. The released quantity is higher than the expected maximum value for hydrogen loss (i.e. 20%, calculated on 3 eq H_2/AB), suggesting that extra by-product(s) were being released. If the first weight loss of 3% release was only hydrogen, it would correspond to *ca.* 2 H_2/AB, indicating that reaction Eq.IV.6 is not the only one occurring at this temperature. The DSC analysis of the same sample indicated that the first step observed in the TGA analysis (115 °C) corresponds to an endothermic and an exothermic heat exchange, while the second step observed in the TGA does not give rise to significant heat exchange. Such behavior is consistent with previous literature reports. [198]

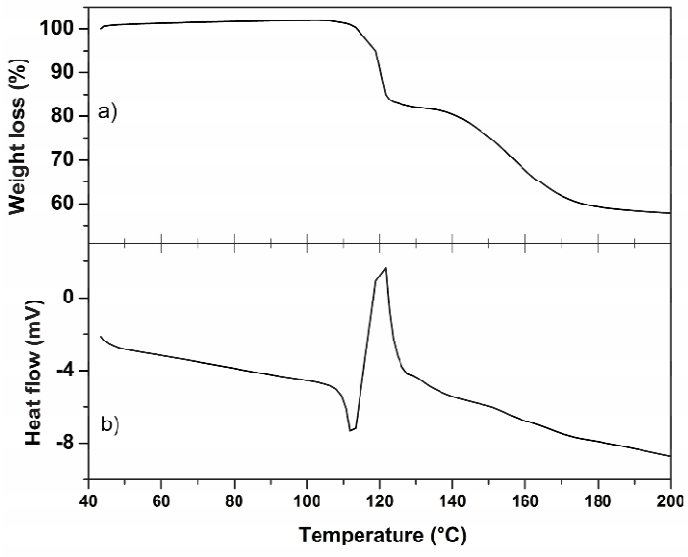

Figure IV.15: (a) TGA and (b) DSC curves of pure ammonia borane, AB, sample.

The same analyses techniques were applied for the AB@SBA-15 and AB@CPO-27-Ni see Figure IV.16 and Figure IV.17 respectively. The results proved unsatisfactory: the quantity of H_2 released was too light with respect to the inorganic matrices, yielding a large error associated with the weighing which inhibits a quantitative analysis of the TGA data. Nevertheless, the same tend is observed for the amorphous inorganic oxide and for the metal organic framework, namely both AB@SB-15_{500} and AB@CPO-27-Ni display as first main phenomenon in the TGA a weight loss starting at 85 °C, which correlates with an endothermic signal in the DSC curve.

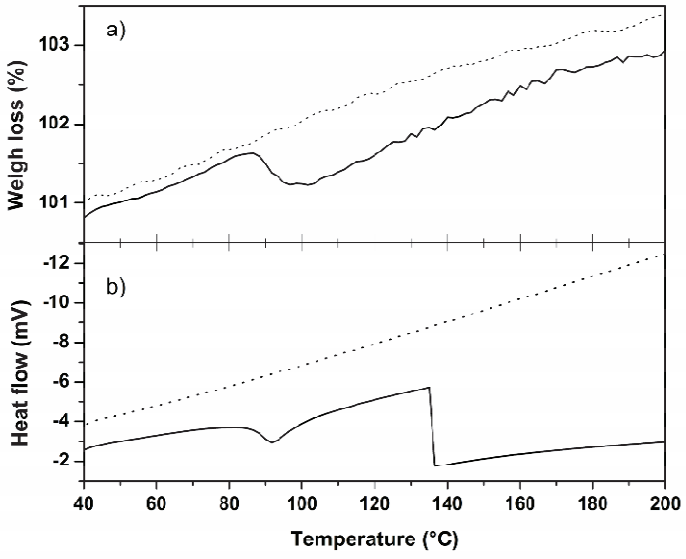

Figure IV.16: TGA (a); (b) DSC curves of SBA-15 (dotted lines) and AB@SBA15(solid lines)**.**

The AB@CPO-27-Ni also shows two further steps at 115 °C and 135 °C respectively assigned to decomposition of pure ammonia borane, AB, and adsorbed water in CPO-27-Ni cavities by comparison with pure AB data and CPO-27-Ni data (Figure IV.17).

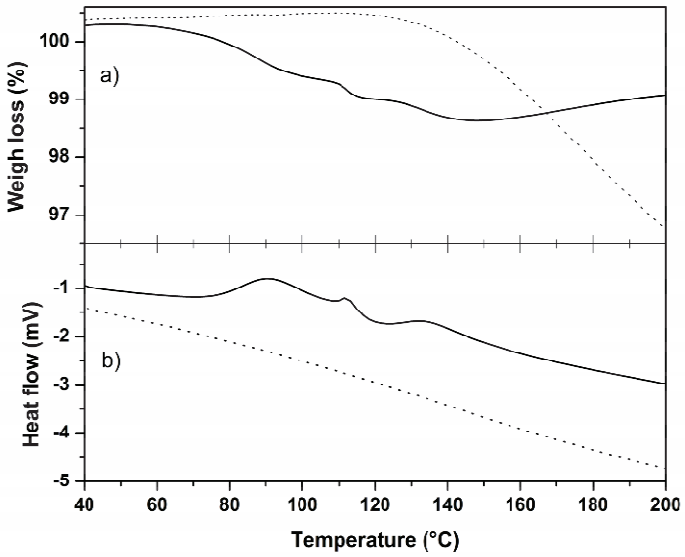

Figure IV.17: a: TGA; b: DSC curves of CPO-27 Ni MOF and AB@CPO-27-Ni

The temperature programmed desorption (TPD) of the different samples confirmed such data. The results for the cumulated H_2 release at different temperatures for the three samples: pure AB, AB@CPO-27-Ni, and AB@SBA-15 are reported in Figure IV.18.
The plot, shows that hydrogen starts to be released a significantly lower temperature with respect to pure AB when it is mixed with either CPO-27-Ni or SBA-15 (40 °C).

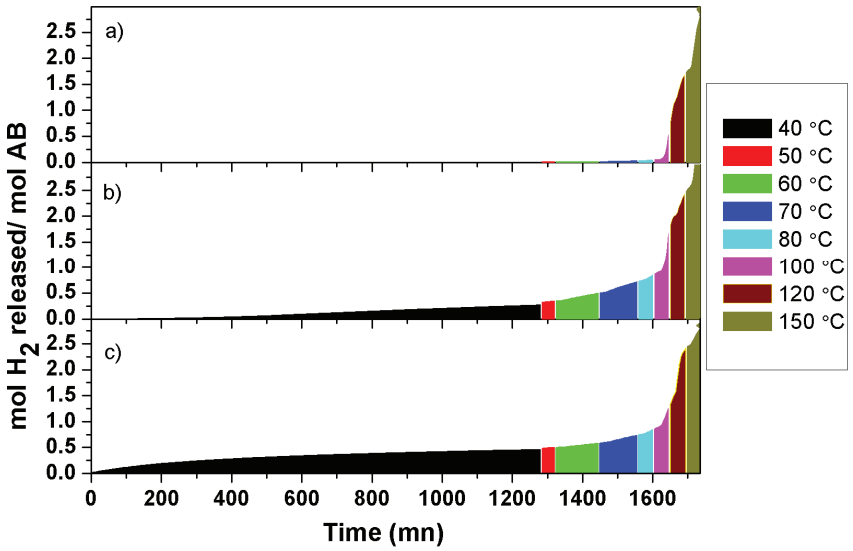

Figure IV.18: TPD of a: amonia borane; b: AB @CPO27-Ni ; c: AB@SBA-15

In summary CPO-27-Ni appears to have the same beneficial effect as SBA-15 in lowering the temperature of hydrogen release from AB to about 85 °C. No molecular explanation for such phenomenon is given at the moment, better understanding of the process as well as its reversibility could be offered by further *in situ* IR studies.

IV.4. Surface organometallic chemistry on CPO-27-Ni metal organic framework:

IV.4.1. Attempt to chemisorb Ru(0) cyclooctadiene on CPO-27-Ni:

Ru(0) catalyst such as Ru(COD)(COT) (COD = 1,5-cyclooctadiene, COT = 1,3,5-cyclooctatriene) are efficient catalysts in many reactions such as intermolecular hydroacylation of 1,3-dienes with aromatic and heteroaromatic,[199] co-dimerization of terminal acetylenes with 1,3-dienes,[200] carbon-carbon bond formation,[201] dimerization of styrene.[202]

It was shown that Ru(COD)(COT) can be encapsulated inside MOF-5 nanocavities by simple diffusion.[103] However, the physisorbed Ru(0) complex remains stable and subsequent treatement under hydrogen gives large Ru(0) nanoparticles, possibly on the external surface of MOF-5. We attempted to coordinate the Ru(0) organometallic complex on the surface of the CPO-27-Ni in order to obtain a well localized and anchored metal center. The reaction attempted was ligand exchange reaction carried out by wet impregnation technique in pentane between the phenyl ring of the metal organic framework CPO-27-Ni and the ligands of the ruthenium complexes. Neither Ru(COD)(COT) nor Ru(COD)(naphtalene) gave cyclooctatriene release during the reaction.

Likewise, the solid state NMR spectroscopy of the the material after impregnation and the removal of volatile showed simple complex infiltration, without chemical grafting. Similarly, when the reaction was performed with Ru(COD)(naphtalene) in acetonitrile which can lead to the *in situ* formation of $Ru(COD)(MeCN)_3$,[203] no grafting reaction with the phenyl ring was observe.

IV.4.2. Attempt to functionalize Ni(II) centers of CPO-27-Ni:

Metal organic frameworks (MOFs) have been successfully used to control radical polymerizations in nano confined conditions, which can be used for precision in polymer synthesis and specific polymer confinement and distribution.[204] To extend such approach to metal organic catalysis, we investigated whether open metal site of CPO-27-Ni could be transformed in a catalytically active center for polymerization by surface organometallic chemistry. As shown by Cossee and Arlman for group 4 metals catalyst,[205] the propagation requires the coordination of alkene to the vacant site, and then migration of the existing chain (R) (i.e., coordination-insertion, Scheme IV.1)

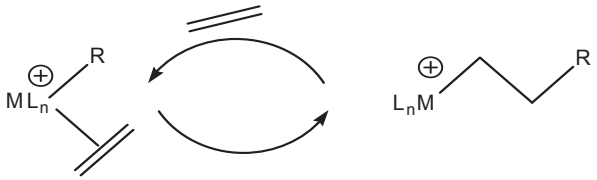

Scheme IV. 1: Cossee-Arlman mechanism for polymerisation propagation (coordination-insertion).

Three routes can be identified in order to generate the active catalyst center, all involving a cocatalyst (Schem IV.2).[206, 207]

(A) Abstraction of an alkyl anion from $[L_nMR_2]$ to give $[LnMR]^+[WCA\ ]^-$ (WCA = weakly coordinating anion), (B) abstraction of an anionic ligand X from $[L_nMRX]$ followed by its replacement with WCA to give $[LnMR]^+[WCA]^-$, (C) combined alkylation and abstraction steps to generate the coordinatively unsaturated species.

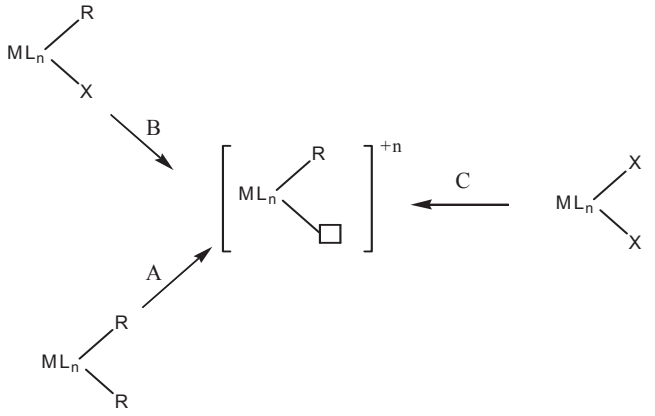

Scheme IV.2: Formation of a cationic active catalyst by three different routes: (A) alkyl abstraction; (B) X abstraction; (C) abstraction and alkylation.

In our case, the activated CPO-27-Ni MOF contains a vacancy site on the Ni(II). To complete the active site, an alkylation or hydrogenolysis process is necessary. This was attempted by heating the CPO-27-Ni under hydrogen, or by reacting with alkylating agent such as $AlMe_3$, $SnMe_4$, $SnEt_4$, tBu$_3$SnH.

The reactions were followed by IR, or CP MAS solid state NMR spectroscopies. In the latter case the CPO27-Zn was used for the NMR analysis to allow the acquisition.

However, all reactions with hydrogen treatment at elevated temperature, as well as the use of different alkylating agents have resulted into uncontrolled decomposition of the structure. Moreover, the post-treated solids are inactive in polymerization reactions.

The success of the shell higher olefin process (SHOP) heavily relies on the presence of the so called W. Keim's ligands around the active Ni(II) site, an example of such ligand being the diphenylphosphine acetic acid, Ph_2PCH_2COOH.[208] We attempted to introduce such diphenylphosphine in CPO-27-Ni to investigate whether it could coordinate on the Ni(II) open metal site. The reaction was followed by solid state ^{31}P NMR spectroscopy. No coordinated phosphoros was observed indicating that pores of the CPO-27-Ni, of about (~11 Å) in diameter, when perfectly dehydrated, are too much close to the dimensions of the ligand (~8 Å) to allow inclusion inside the pores.

The lack of specific interaction sites on the metal of the MOF limits their applicability as catalysts. The post-functionalization of MOFs frameworks is a possible strategy to obtain a catalytically active material. Importantly, due to the crystalline nature, high surface area and the porosity of CPO-27-Ni, the post modified material can still be well-defined. The reaction of organometallic complexes is monitored using different spectroscopic techniques, IR, NMR and mass balance analysis, TEM, EDS,

IV.4.3. Chemical grafting of $M(CO)_6$ (M=Cr, Mo) on CPO-27-Ni:

Metal hexacarbonyl $M(CO)_6$ (M = Mo, Cr) are known to undergo ligand exchange with phenyl rings to yield three-legged piano-stool complexes of general formula $(arene)M(CO)_3$. Such reaction has already been used on phenyl rings embedded in walls of inorganic materials such as hybrid materials containing $[O_{1.5}Si\text{-}C_6H_6\text{-}SiO_{1.5}]$[209] residues and with metal organic framework with terephtalate linker (MOF-5)[210] and UiO-66.[211] In all the reports the grafting reactions have been carried out on a milligram scale since the focus of those studies was mainly spectroscopy. But when a surface organometallic chemistry modification of a material is attempted, the goal is to generate an active functional material for subsequent use such as catalysis, thus requiring large scale syntheses. We therefore combined similar *in situ* investigation with novel large scale grafting of $Mo(CO)_6$ on CPO-27-Ni, en route to a hydrodesulfurization catalytic described in the last part of the chapter. The grafting, reaction is expected to occur on some of the linker of the CPO-27-Ni. In order to establish such coverage rate five different starting Mo : Ni_2(dhtp) ratio (namely, 0.2, 0.4, 0.6, 0.8, and 1.0) for the grafting reaction on CPO-27-Ni were studied for a common large scale procedure. The impregnation procedure was carried out on 600 mg batches of previously activated CPO-27-Ni MOF material in a self-contained double-vessel reactor. The self

contained double vessel allowed several consecutive sublimation/ heating/ desorption cycles. Further details are reported in the experimental section.

After five cycles, the reactor containing the functionalized CPO-27-Ni material was disconnected from the vessel containing leftover unreacted molybdenum(0) hexacarbonyl, and heated under vacuum to remove physisorbed $Mo(CO)_6$.

The molybdenum and nickel content in the five samples thus recovered were determined by inductively coupled plasma atomic absorption spectrometry.

As shown in Figure IV.19, this study demonstrated that all available starting molybdenum can be quantitatively grafted on CPO-27-Ni reaching a plateau at around 10 % w of molybdenum, suggesting that the maximum molybdenum content that can be loaded is about 50% molar functionalization of the arenes rings available in Ni_2(dhtp).

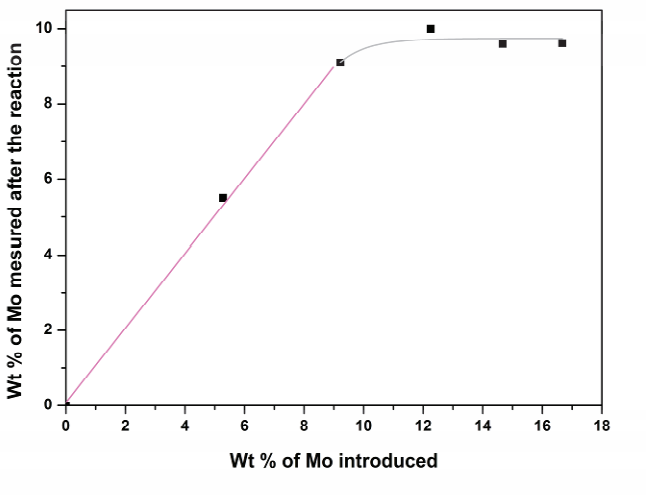

Figure V.19: Quantity of Mo present in the functionalized CPO-27-Ni-Mo material (determined by ICP-AAS) versus the initial quantity of $Mo(CO)_6$ sublimed on the material.

The estimation of the CO released during the grafting procedure was obtained by repeating the low loading reactions (that is 20% mol, 40% mol, and 60% mol) for wich a quantitative molybdenum grafting has been proven) in a reactor equipped with IR windows for *in situ* measurement of the CO released. (Quantification by gas chromatography was tried but the amount of CO presented in the gas phase is below the detection limit).

A previous calibration of the IR instrument response in function of the CO pressure over activated CPO-27-Ni, is complicated by the equilibrium between the adsorbed and gas phase CO due to the presence of open metal site on CPO-27 and requires the use of the Sips equation described earlier (Eq.IV.1), to allow the quantitative determination of the released CO moles (Table IV.5).

Table IV.5: The amount of CO to the amount of Mo grafted.

Quantity Of Mo grafted	Amount Of CO expected	Amount Of CO estimated
(20±1)%	3CO/Mo	(3,1±0,5)CO/Mo
(36 ±1) %	3CO/Mo	(2,9±0,5)CO/Mo
(50 ±1) %	3CO/Mo	(3,1±0,5)CO/Mo

For the three samples three moles of CO per mol of molybdenum grafted were measured in the gas phase (Table.IV.5) in agreement with the expected stoichiometry for the grafting (Eq.IV.10).

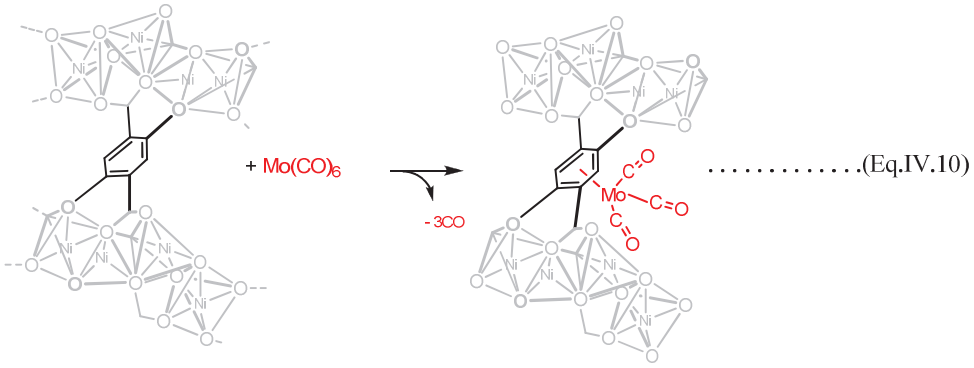

.....(Eq.IV.10)

The five different samples obtained earlier were also analyzed by DRIFT and the resulted spectra are shown in Figure IV.20.

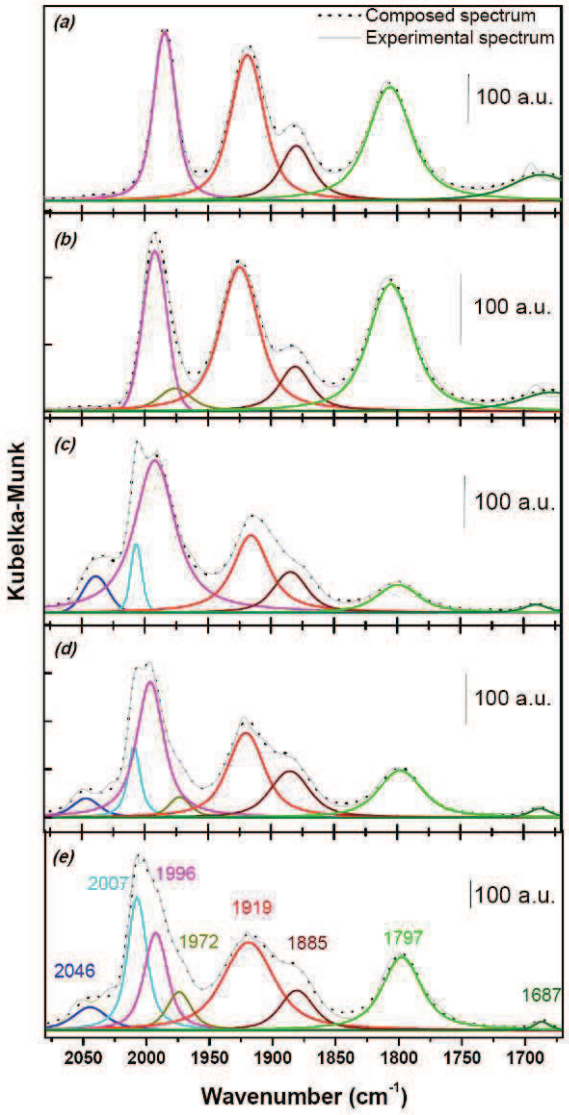

Figure IV.20: FTIR of carbonyl region [2075-1600 cm^{-1}] of the materials obtained by subliming $Mo(CO)_6$ on $Ni(dhtp)_2$ with starting Mo to dhtp ratio of : (a) 20%, (b) 40%, (c) 60%, (d) 80%, (e) 100%. The solid line is the experimental spectrum and the dash line is the composed one from the deconvolution.

The spectra appear complex but the assignment is rather straightforward and confirms the well-behaved large scale impregnation of $Mo(CO)_6$ on CPO-27-Ni.

In fact, the modes at highest wavenumber (2046 and 2007 cm^{-1}) are associated with physisorbed excess starting material and can be found only for the high loading samples. In the well behaved low loading samples only five bands are observed.

A computational study has been performed on $[\eta^6\text{-}C_6H_4(COONa)_2]Cr(CO)_3$ model system.[212] It has very well explained the effect of the Ni atom in CPO-27-Ni (modelled by Na cations in DFT calculation) on the IR modes of the (arene)$Mo(CO)_3$ moiety, the three

legged piano stool model complex can exist in two conformations staggred and eclipsed (Figure IV.21).

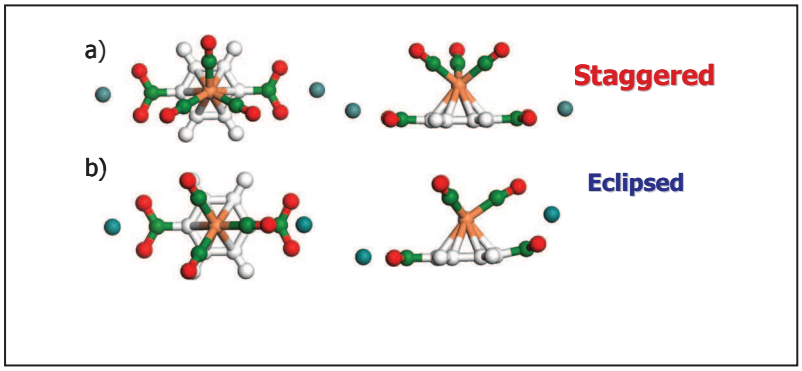

Figure IV.21: The representation of the two possible conformations staggered, eclipsed and the interaction between CO and the cation in the eclipsed conformer.

The calculated vibration energy ν(CO) of the staggred conformer consist in a doublet, while the eclipsed conformers yields a triplet due to the symmetry removal and interaction of one CO ligand with the cation.

In our material the five IR bands observed in the IR spectra of the well defined samples at 20 and 40 %w loading are therefore fully explained by attributing doublet to [dhtp]$Mo(CO)_3$ in the staggrred conformation and the remaining triplet to the same molecular species under its eclipsed conformation (Eq.IV.11).

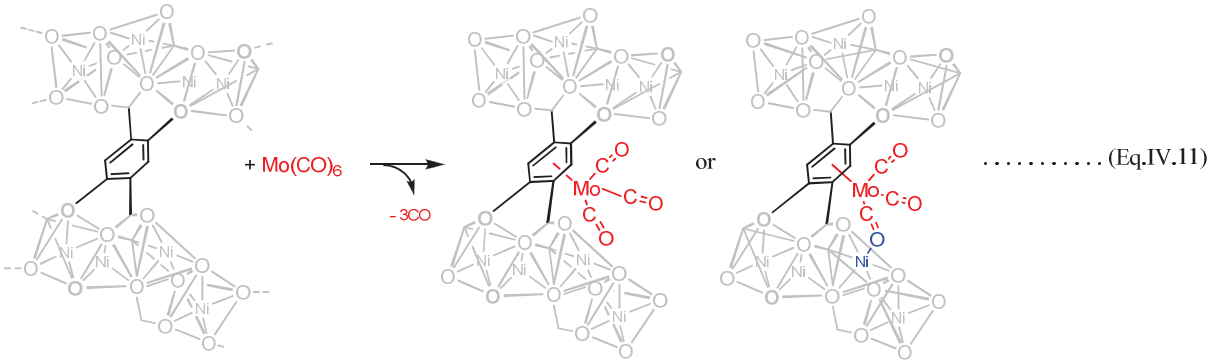

..... (Eq.IV.11)

Further *in situ* IR exstensive experiments have shown that [arene]$Mo(CO)_3$ species in the CPO-27-Ni was reversible in the presence of CO to yield $Mo(CO)_6$ (Figure IV.23), suggesting that the formation of (arene)$Mo(CO)_3$ complex from the precursor $M(CO)_6$ was an equilibrium reaction with the reverse formation of $M(CO)_6$. In order to increase the grafting the CO released during the reaction has to be evacuated.

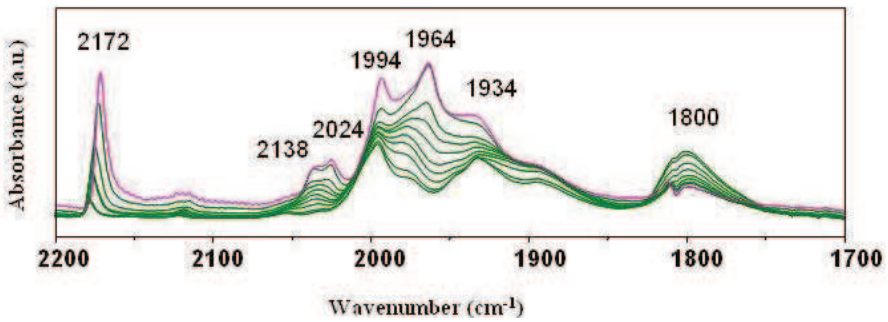

Figure IV.22: The evolution of carbonyl stretching bands of grafted [arene]$Mo(CO)_3$ in the presence of different pressures of CO in the IR cell, note that 2172 cm^{-1} corresponds to the CO in interaction with open metal site of Ni.

In conclusion we have achieved a fully stoichiometric large scale synthesis of material $[Ni_2(dhtp)][Mo(CO)_3]_x$/ x = 0.1, 0.2, 0.4, 0.5. It is interesting to notice that when the grafting is carried out on small scale for spectroscopy study only, the spectra are less well resolved and complicated the dependent changes appear to take place, as can be seen in Figure IV.22.

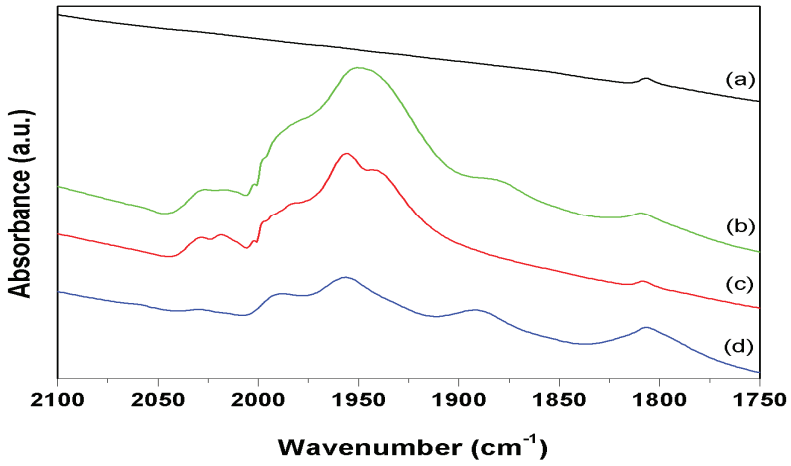

Figure IV.23: *In situ* FTIR spectra [1750-2100 cm^{-1}] of the reaction CPO-27 Ni $Mo(CO)_6$; (a): activated Ni-MOF; (b): after sublimation of hexacarbonyl; (c): after chemisorption at 120 °C; (d): after desorption of the excess at 120°C under vacuum

Finally the textural properties of the material obtained by 40% loading (BET = 200 m^2/g, pores volume = 0.1 cm^{-3}/g) show that the material still porous and can be used for catalysis.

IV.5. Catalysis on $[Ni_2(dhtp)][Mo(CO)_3]_{0.5}$:

IV.5.1. Ethylene to propylene conversion:

Olefin metathesis was discovered fifty years ago by Anderson and Merckling.[213] Nine years later, Banks and Bailey reported "a disproportionation reaction in which olefins are

converted to homologues of shorter and longer carbon chains...” In 1967, Calderon and co-workers named this metal-catalyzed redistribution of carbon-carbon double bonds as olefin metathesis. Olefin metathesis currently represents a powerful transformation in chemical synthesis.[120]

Neill *et al.* have described a direct transformation of ethylene to propylene on an olefin metathesis catalyst prepared from $Mo(CO)_6$ on Al_2O_3.[214] The $Mo(CO)_6$ in CPO-27-Ni prepared as described above was tested in this type of reaction. 100 mg (0.32 mmol) of activated MOF was functionalized to the maximum loading with the molybdenum hexacarbonyl which corresponds to 50% of phenyl ring coverage (0.16 mmol of $Mo(CO)_6$). The sample was placed in a reactor and 50 equivalents of ethylene were introduced. The reaction was carried out at three different temperatures (80, 150, 180 °C). The conversion of ethylene to propylene is shown in Figure IV.24. The activity is very low even at relatively high temperatures. The low activity can be explained by the difference in acidity of the support (CPO-27 Ni is less acid than alumina).

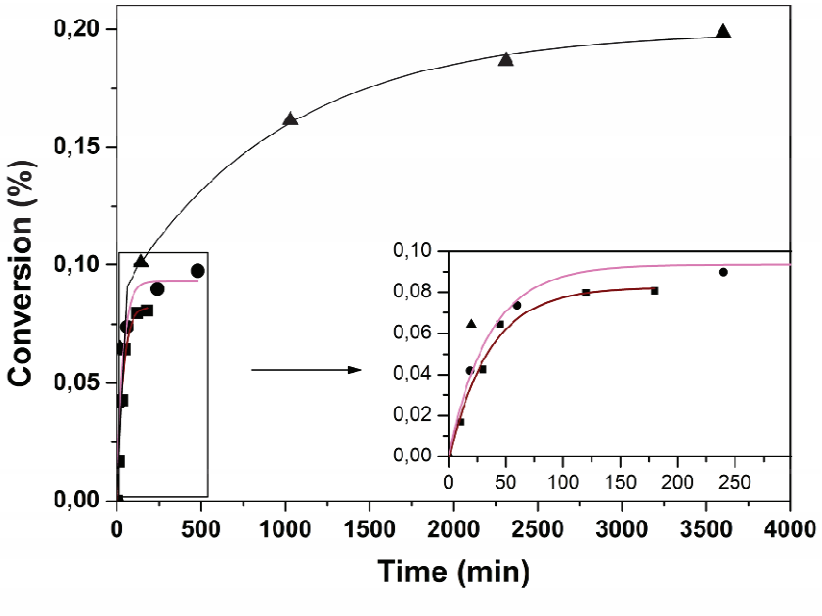

Figure IV.24: Conversion of ethene to propene over $[Ni_2(dhtp)][Mo(CO)_3]_{0.5}$ at different temperatures 120 °C (squares), 150 °C (circles), 180 °C (triangles).

The sample after catalytic test was characterized by powder XRD, the 3D structure of the material was preserved according to diffractograms (Figure IV.25).

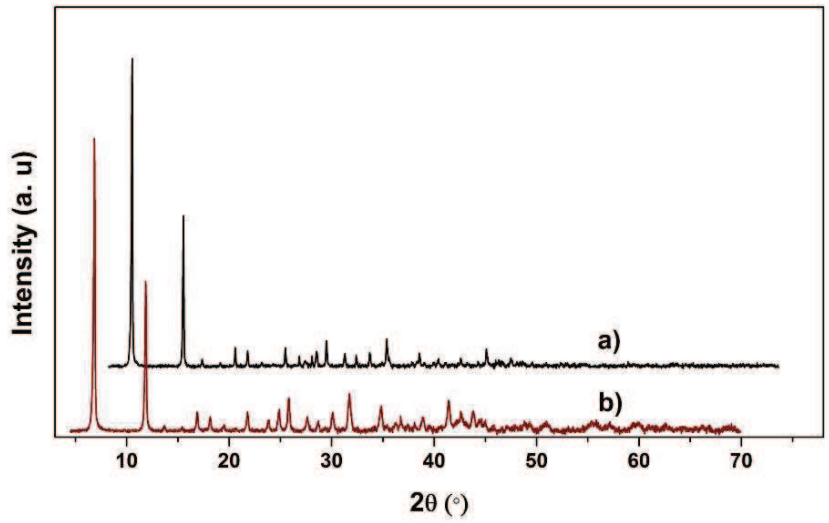

Figure IV.25: Comparaison of XRD pattern a) before, b) after catalysis

IV.5.2. Hydrodesulfurization catalysis:

Hydrodesulfuration is a chemical process involving removal of sulphur in crude oil fractions at refineries. The commercial catalyst is generally supported molybdenum sulfide promoted by nickel or cobalt, prepared *in situ* from metal oxides. During the preparation of the catalyst, many species are present on the support, and according to the "Co-Mo-S model",[215] the active parts are only the edges of the Co(Ni)MoS nano-crystallites. 70-80 wt% of a HDS catalyst is support material (Al_2O_3), without any catalytic activity, but necessary to ensure dispersion and mechanical stability. On the other hand the catalytic activity of the unsupported Co(Ni)MoS prepared from the same precursors ($CoMoO_4$ or $NiMoO_4$) is only 10-20 % of the supported system. The reason is that the unsupported catalyst gives large metal sulfide particles, which result in lower edges sites per amount of the Co(Ni)MoS.

In the quest for an efficient unsupported HDS catalyst, which would avoid the large use of inactive alumina, while still presenting a good catalytic activity, we decided to test the metal organic framework containing the molybdenum and nickel metals prepared above, $[Ni_2(dhtp)][Mo(CO)_3]_x$ (x = 0, 0.2, 0.4, 0.6) since the nanocrystallite size and regularity could be beneficial for the preparation of catalytically active phases.

The passage from the starting MOF to the active phase requires a sulfidation steps. Since this process consists in high temperature treatment under H_2S, the MOF structure will be broken down, therefore our approach is a yet unreported test on the influence of a MOF cristallinity on an ultimately amorphous catalyst.

The sulfidation was carried out by exposure in n-heptane stream pelletized materials to a dimethyl disulphide (DMDS) which is an *in situ* source of H_2S.

The sulfidations were carried out *in situ*, directly in catalytic reaction prior to the catalytic tests and the temperature used (350 °C) was the same as the one to be used during the catalysis.

Due to the complexity of natural oil in terms of hydrocarbon matrix and the various sulfur compounds present, the use of real oil in screening experiments is to be avoided. Real oil was modeled here by a mixture containing dibenzothiophene, indole, and naphtalene, these two latter components being added to mimic real HDS process where nitrogen and aromatic compounds are co-converted with sulfur compounds. Dimethyldisulfide was also present in the model feed in order to keep the catalyst in a fully sulfided state. The activity of the catalyst in hydrodesulfurization (HDS), hydrodenitrogenation (HDN), and hydrogenation (HYD) reactions (Eq.IV.12, IV.13 and IV.14 respectively) were tested.

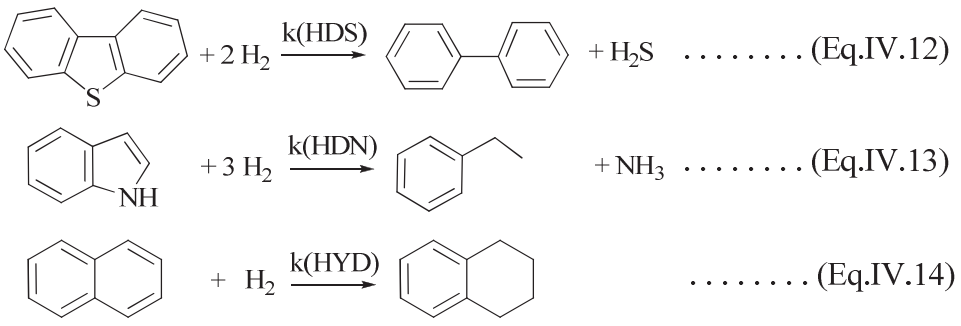

Four sample of $[Ni_2(dhtp)][Mo(CO)_3]_x$ that is with different molybdenum loading (0, 5.5, 9.1, 10 %w, which correspond to x = 0, 0.2, 0.4, 0.5 were tested in HDS catalysis after *in situ* sulfidation. Their HDS activities are shown in Figure IV.26, where k (HDS) is the activity of the catalyst compared to the standard supported commercial one (k (HDS) = 100). The activity is calculated on the measured conversion by on line calibrated GC-MS analyses and converted to the corresponding relative pseudo first order rate constant.

We observe that the HDS activity increases with the molybdenum content. The catalyst containing 10 %w of Molybdenum (half of the commercial catalyst) shows the maximum activity which is 31 %w of the commercial one.

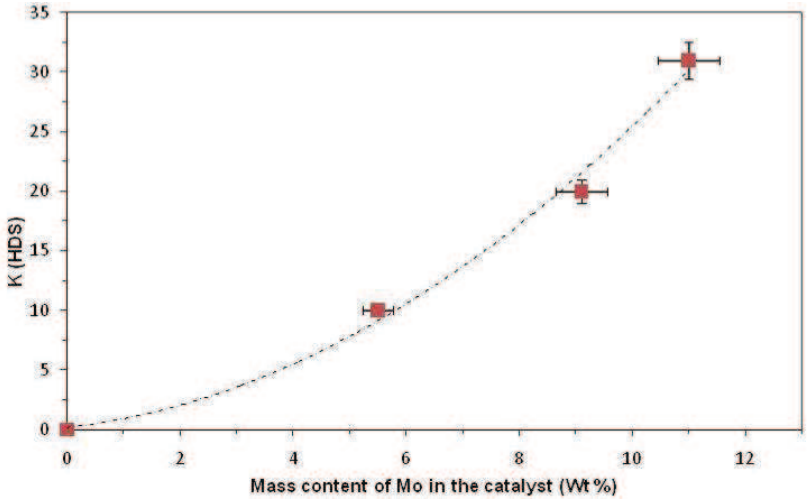

Figure IV.26: Activity of the catalysts in HDS reaction versus the Molybdenum content

The catalytic activity of $[Ni_2(dhtp)][Mo(CO)_3]_{0.5}$ after activation (sulfidation) was also determined for hydrodenitrogenation (HDN), and hydrogenation (HYD) reactions , the activities are reported in table IV.6 along with the analogous data for the standard benchmark catalyst and the unsupported precursor $NiMoO_4$.

Table IV.6: Relative pseudo first order rate constants for HDS, HDN, and HYD reactions catalyzed by benchmark supported industrial catalyst, sulfided unsupported $NiMo_4$, and sulfided $[Ni_2(dhtp)][Mo(CO)_3]_{0.5}$. The values are reported in percentage with respect to the commercial catalyst.

Precursor	Mo $\%_w$	% K(HDS)	% K(HDN)	% K(HYD)
Benchmark catalyst $NiMo/Al_2O_3$	20	100	100	100
Unsupported $NiMo_4$	44	14	48	31
$Ni_2(dhtp)/Mo(60\%)$	10	30	75	57

The MOF based unsupported catalyst reaches 30% of the industrial rate, when compared to unsupported catalyst like the one obtained by sulfidation of $NiMo_4$ the MOF-derived catalyst performs almost twice as well while containing four times less molybdenum, indicating that, while not competitive with supported industrial catalyst, the MOF precursor is better than benchmark unsupported bulk catalyst.

The spent catalysts were analysed by transmission electron microscopy (TEM) and energy dispersive X-ray spectrometry (EDS) (Figure IV.27). The samples showed the presence of Ni, Mo and S in consistency with the Ni_3S_2 and MoS_2 structures identified in both samples by powder XRD (Figure IV.28). The TEM micrographs displayed the diagnostic

D[000] = 2.71 Å (hexagonal pattern) and D[002] = 6.15 Å (intersheet distance of the MoS_2 phase.

Combined HRTEM and EDS shows the presence of MoS_2 shell structures containing approximately 5 $\%_w$ Ni. The MoS_2 structures were found by TEM to be typically 5-20 nm sized slabs having a thickness/height of 1-5 nm. An additional unidentified species with lattice plane distance d = 0.32 nm was found in high magnification TEM images. The thickness/height corresponds to about 1-5 MoS_2 layers stacked in the (002) direction. This data is significant to explain the difference in activity with respect to the other two catalytic systems since alumina supported MOS_2 crystallites in industrial catalyst can be reduced down to 1-layer thikness, while MoS_2 crystallites obtained from $NiMo_4$ sulfidation are typically of the order of 10 layers-thick, as also indicated by the FWHM parameter of the 14° peak in the XRD (Figure IV.28).

The agglomeration of MoS_2 slabs appeared to be in coexistence with Ni_3S_2 crystals as revealed from high magnification TEM images (Figure IV.27), and from the XRD patterns (Figure IV.28), the presence of Ni3S2 is expected based on the very large Ni : Mo ratio present in the starting $[Ni_2(dhtp)][Mo(CO)_3]_{0.5}$, while in the active phase Ni : Mo ~ 0.05 ratio are desired.

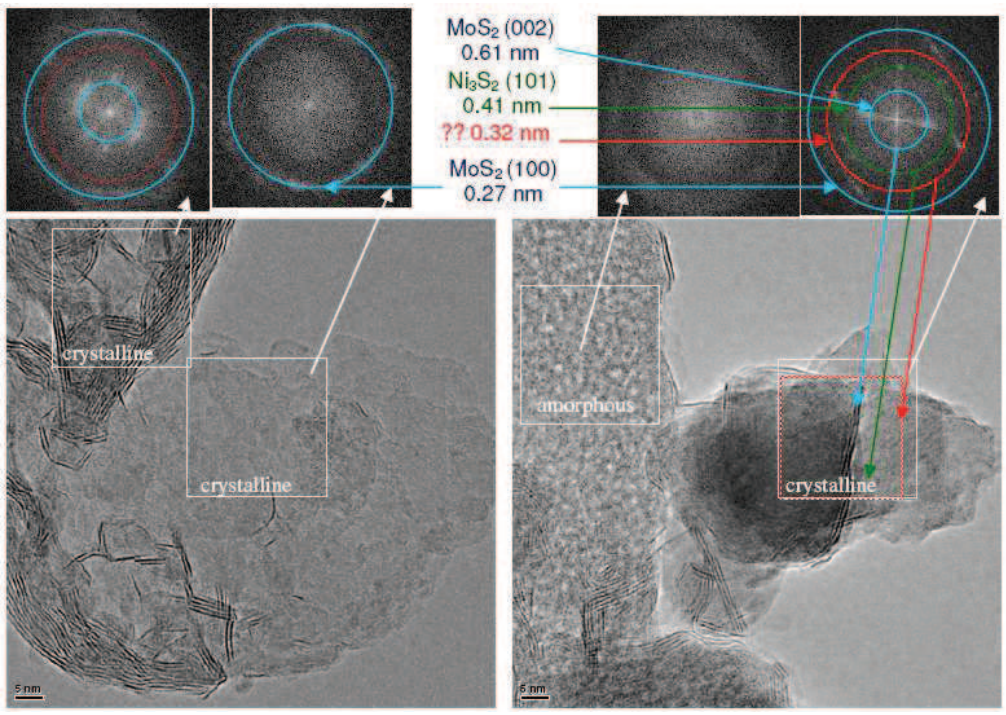

Figure IV.27: Images at different magnifications showing two different morphologies crystalline consists of bended MoS_2 layers, and amorphous formed by Ni_3S_2.

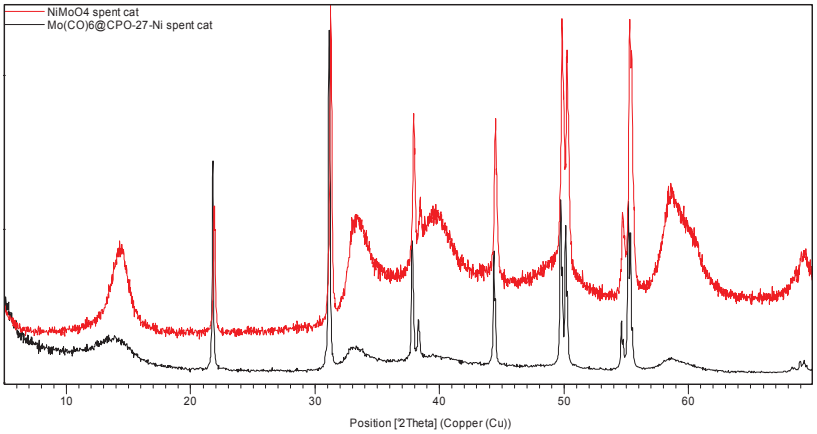

Figure IV.28: powder X-ray diffraction of spent catalyst after HDS test, obtained for $[N_2(dhtp)][Mo(CO)_3]_{0.5}$ (black line) and $NiMo_4$ (red line).

Unfortunatly the large excess of Ni_3S_2 could not be minimized by using $[Ni_{0.1}Zn_{0.9}]_2(dhtp)]$ as starting MOF. Since the HDS activity of the precursor containing 9 $\%_w$ of molybdenum and it was very low (*vide infra*).

In summary, the $Mo(CO)_6$ incorporated by by surface organometallic chemistry in activated $[Ni_2(dhtp)]$ yield after sulfidation an active HDS catalyst better than most unsupported catalyst, probably due to the small size of MoS_2 crystallites that are obtained. However, the MOF based catalyst performs worse than the standard supported catalyst because of *inter alia* the low maximum molybdenum content that can be reached by SOMC (*viz.* $1Mo(CO)_3$/ 2dhtp that is 10 $\%_w$ of Mo in the material at the best).

Since the grafting of the molybdenum on the phenyl ring via surface organmetallic chemistry approach revealed the limitation of loading, another method was adopted leading to an increase in maximum molybdenum in $[Ni_2(dhtp)]$. Contrary to the previous method where the reaction is happening only under the vapor pressure of $Mo(CO)_6$, the reaction was carried out by increasing the $Mo(CO)_6$ pressure in the in the reactor by mixing the activated CPO-27-Ni MOF and $Mo(CO)_6$ in autoclave at 120 °C. Three samples Ni-Mo-6, Ni-Mo-7, and Ni-Mo-8 were obtained by exposing 1 eq, 1.5 eq and 2 eq of $Mo(CO)_6$ with respect to arene ring in $[Ni_2(dhtp)]$ to yield materials containing almost complete molybdenum inclusion (Table IV.7), no molecular formula can be offered. IR data not shown here display very complex and previously unobserved bands confirming that this method does not yield well characterized materials. Nevertheless, their high molybdenum loading make them interesting for catalysis studies.

Table IV.7: Elemental analysis of Ni and Mo in the high loading samples.

ID of sample	Elementary analysis		
	Mo(Wt %)	Ni(Wt %)	Mo/Ni
Ni-Mo-6	19	21.6	0.9
Ni-Mo-7	22	19.7	1.3
Ni-Mo-8	28.5	16	1.8

The samples Ni-Mo-6, Ni-Mo-7, and Ni-Mo-8 were tested in the HDS catalysis and the results are shown in Figure IV.29. The activity is increasing compared to the previous catalysts. The sample containing 19 Wt % of Mo shows a promising activity about 73 % with respect to benchmark commercial catalyst. However, when the loading increases the activity drops again.

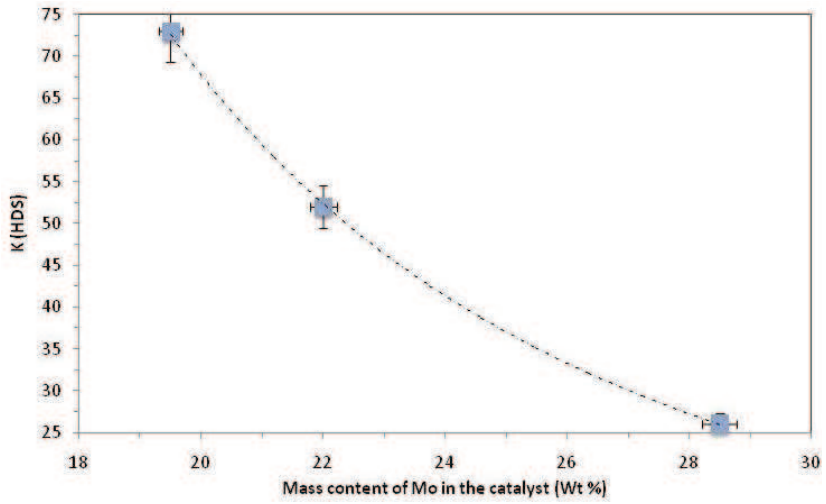

Figure IV.29: Activity of the catalysts in HDS reaction versus the Molybdenum content

Finally, in order to demonstrate the importance of both the molybdenum and the nickel atoms in the HDS catalyst, other precatalysts have been prepared. The first with CPO-27-Ni [Ni_2(dhtp)] and $Cr(CO)_6$[216] and the second with CPO-27-Zn [(Zn_2(dhtp)] and $Mo(CO)_6$. Other samples were also prepared by impregnating the CPO-27-Ni MOF (Ni_2(dhtp)) with other sources of Mo such as MoO_3 and $H_2Mo_{12}O_{40}P$. Another approach to decrease the amount of Ni_3S_2 in the catalyst was to introduce the $Mo(CO)_6$ in the bimetallic MOF ($Zn_{0.9}$-$Ni_{0.1}$MOF). The samples were characterized by EDS, TEM, SEM and XRD Cr_2NiS_4, Ni_3S_2, MoS_2 phases have been identified. The activities of different catalysts are reported in Table IV.8.

Table IV. 8 : The catalytic results of the miscellaneous HDS catalyst obtained from CPO-27 precursors.

Sample	Description	Mo Content (Wt %)	K (HDS)
Ni-Cr-9	Cr@CPO-27Ni	~ 0	1
Ni-Mo-10	Mo@CPO27-Zn	10	2
Ni-Mo-11	Mo@$Zn_{0.9}Ni_{0,1}$-MOF	9	1.8
Ni-Mo-12	MoO_3@CPO-27-Ni	23	21.6
Ni-Mo-13	$H_2Mo_{12}O_{40}P$@CPO-27Ni	20	30.9

The best activity was obtained for a pre-catalyst containing $H_2Mo_{12}O_{40}P$, which is interesting in the context of catalyst cost. In fact, while the MOF cost is not necessarily an issue, especially for terephtalate based material, such linker being very cheap, $Mo(CO)_6$ is very expensive and a cheaper molybdenum source is necessary. For the other samples the catalytic activities were very low, indicating that the presence of the both molybdenum and nickel gives better activity, in agreement with the expected "Ni-Mo-S" model.
All this HDS catalytic studies have been performed in collaboration with Michael Brorson's group at Haldor Topsøe.

In conclusion, unlike all the previous reports on MOF as catalyst, where the MOF is considered intact throughout the catalytic reaction[217] we have reported herein the first application of MOF crystal structure to yield a nanocatalyst, specifically a 4-layer-high Ni-doped MoS_2 amorphous crystallites, that compares very well with previous unsupported HDS catalysts. The starting MOF structure, albeit, being sacrificed during the activation process, after application of surface organometallic chemistry to graft the second metal, appears to play three positive roles with respect to catalyst formation: (1) ensure a regular co-dispersion of the two active metals Ni and Mo inside the pre-catalyst through its starting high crystallinity and surface area, (2) allow the retention of such regularity upon elimination of the carbonaceous struts by combustion of its organic-based linker, and (3) induce the small size, hence high dispersion of the active phase, by possibly providing finite quantities of organized NiMo in the starting MOF nanocrystals.

IV.6. Conclusion:

This chapter has investigated the known [Ni_2(dhtp)] MOF (dhtp = 2,5 dihydroxo terephtalate, chosen for its large scale synthesis, high surface area, accessible 1D channels (≈11 Å at best) and permanent porosity, for post-synthesis modification via surface organometallic chemistry en route to catalytic applications.
After screening the different literature synthesis routes of CPO-27 or MOF 74 materials, and showing that the procedure described by Dietzel *et al*.[180] gives better products, the control over crystal size was obtained by the variation in synthesis parameters such as temperature, concentration and time.

From a post-synthesis modification view point, CPO-27-Ni displays two possible target site for modification, the Ni(II) pyramidal open site and the phenyl ring of the linker.
The open metal site was tested as acid catalyst (Meinwald rearrangement), as potential coordination site for Keim phosphine, as reaction substrate for reducing agents, as promoting center for H_2-release from ammonia borane and as selective CO oxidation catalyst in presence of gold nanoparticles.

While most of the attempts proved unsuccessful, probably due to the limited size of MOF channels with respect to reagents, or incrementally better than other supports, such as SBA-15 in lowering the temperature of H_2 release from ammonia borane. The gold loaded CPO-27-Ni shows a very promising activity in PROX catalysis, suggesting a synergic effect between the SBU Ni capacity to selectively coordinate the CO and the MOF nanocavities to confine gold nanoparticles during oxidation catalysis.

The post modification via surface organometallic chemistry on the linker, albeit unproductive for large substrate such as Ru(COD)(COT) and Ru(COD)(naphthalene), was achieved from $Mo(CO)_6$. While such grafting had already been reported for spectroscopic investigation, that is on small scales, the large scale well-behaved grafting was achieved. In particular, the combination of microanalysis and IR spectroscopy studies indicated that upon close-vessel chemical vapour deposition, it is possible to obtain the well-defined surface organometallic species [Ni_2(dhtp)][$Mo(CO)_3$]$_x$. The highest Mo loading is about one Mo for two phenyl rings, leading to a material with average stoichiometry [Ni_2(dhtp)][$Mo(CO)_3$]$_{0.5}$. FTIR indicated that the carbonyl ligands can also be in interaction with adjacent Lewis acid Ni sites.

Such material, although almost inactive catalyst for converting ethylene to propylene, proved a very interesting precursor for unsupported HDS catalysis. While it performs worse than the benchmark industrial alumina-supported catalyst (i.e. 30 % of HDS activity), the MOF precatalyst was active than most of the unsupported HDS catalyst.
It was demonstrated that molybdenum encapsulated in MOF cavities was useful to obtain, after sulfidation, small (less then 5 layer thick) MoS_2 crystallites doped with $5\%_W$ in Ni, thus explaining the good activity.

Nevertheless, this result is still of limited practical interest since the material is too expensive and its activity is lower than the industrial one.

IV.7. Experimental part:

General synthetic procedures.

(See experimental part of chapter II for physical and chemical characterization techniques).

Organometallic syntheses and reactions were conducted under strict inert atmosphere or vacuum. Sealed tube reactors and break-seal techniques were used throughout. Hydrogen was dried and deoxygenated over a purificating system (BASF R3-11 + 4 Å molecular sieves) prior to use. N_2O (LINDE 5.0) was degassed by freeze-pump-thaw technique before use. Infrared follow-up of reactions was performed using surface organometallic chemistry techniques on a vacuum line connected to a diffusion pump.

2,5-dihydroxyterephtalic acid (dhtp), zinc nitrate tetrahydrate $Zn(NO_3)_2{\cdot}4H_2O$, zinc acetate dehydrate $Zn(OAc)_2{\cdot}2H_2O$, nickel acetate tetrahydrate $Ni(OAc)_2{\cdot}4H_2O$, molybdenum hexacarbonyl $Mo(CO)_6$ and chromium hexacarbonyl $Cr(CO)_6$ were purchased from Sigma-Aldrich and used as received without further purification.

$Ta[CH_2C(CH_3)_3]_3[=CHC(CH_3)_3]$,[175] Ru(COD)(COT),[176, 177] Ru(COD)(nahptalene)[123, 178] and Me_3PAuMe[179] diphenylphosphine acetic acid, Ph_2PCH_2COOH[208] were prepared as reported.

TPD reactor: TPD was carried out in a continuous flow fixed bed reactor at atmospheric pressure and variable step temperatures from 40 °C to 150 °C. The catalysts were placed in a stainless steel tube reactor located in a furnace. The Argon flow was controlled by a mass flow controller (Brooks Instrument) and sent through the reactor at a flow rate of 3 $ml.min^{-1}$. The outlet gases were analyzed with online VARIAN-Micro GC (CP4900) equipped with 4 columns and TCD detector. The column Molecular sieve 5Å (Ar as carrier gas) was used to quantify H_2.

HDS catalytic test reactor: A fixed-bed reactor was used for HDS catalytic tests. Before catalytic tests, the pre-catalyst was sulfided *in situ* (flow containing dimethyldisulfide dissolved in *n*-heptane was contacted with the catalyst precursor for 4 hours at 350 °C). Test conditions have been employed: Feed flow = 0.3 ml/min, H_2 flow = 250 Nml/min (Nml = normal ml = volume at 1 bar and 25 °C), pressure = 50 bar, temperature = 350 °C, catalyst amount (0.3 g. 600-850 μm granulate sieve) was mixed with micro glass beads (200 μm diameter) and the mixture was loaded into the vertical ca. 8 mm inner diameter tubular reactor

around the tip of a thermo couple pocket. Both below and above the catalyst bed layers of micro glass beads were placed in order to secure steady mass transport.

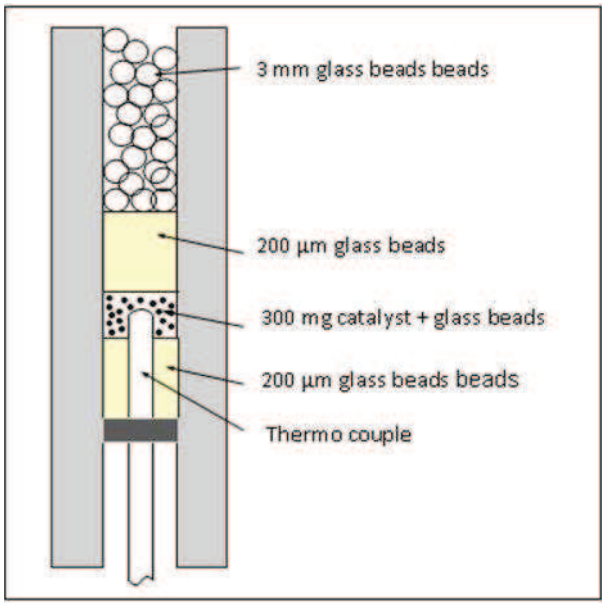

Schematic representaion of the reactor used for HDS catalytic tests.

Solvothermal synthesis of $M_2(dhtp)(DMF)_2{\cdot}(H_2O)_2$ (M = Ni, Zn, $Ni_{0.1}Zn_{0.9}$) (MOF-74):

A solid mixture of 2,5-dihydroxyterephtalic acid (50 mg, 0.252 mmol) and zinc nitrate tetrahydrate (139 mg, 0.534 mmol), was dissolved in DMF (5.0 ml), 2-propanol (0.2 ml), and water (0.2 ml). The mixture was placed in teflon-lined autoclave, and heated at 105 °C for 20 h, yielding a yellow crystalline product. After that the solid was washed with DMF and ethanol and dried in air (65 mg, yield of $Zn_2(dhtp)(DMF)_2{\cdot}(H_2O)_2$.[181]

The same procedure was performed for the synthesis of $Ni_2(dhtp)(DMF)_2{\cdot}(H_2O)_2$ $Ni_{0.2}Zn_{1.8}(dhtp)(DMF)_2{\cdot}(H_2O)_2$. The reaction of 2,5-dihydroxyterephtalic acid (50 mg, 0.252 mmol) and nickel acetate tetrahydrate (133 mg, 0.534 mmol) gave 60 mg of $Ni_2(dhtp)(DMF)_2{\cdot}(H_2O)_2$ (yield). The reaction of 2,5-dihydroxyterephtalic acid (50 mg, 0.252 mmol), zinc nitrate tetrahydrate (125 mg, 0.481 mmol) and nickel acetate tetrahydrate (13 mg, 0.053 mmol) gave 70 mg of $Ni_{0.2}Zn_{1.8}(dhtp)(DMF)_2{\cdot}(H_2O)_2$ (yield).

Room temperature synthesis of $M_2(dhtp)(DMF)_2{\cdot}(H_2O)_2$ (M = Ni, Zn, $Ni_{0.1}Zn_{0.9}$) MOF74:

For the synthesis of $Zn_2(dhtp)(DMF)_2{\cdot}(H_2O)_2$ MOF, 2,5-dihydroxyterephtalic acid (200 mg, 1 mmol) and zinc acetate dehydrate $Zn(OAc)_2{\cdot}2H_2O$ (574 mg, 2.61 mmol) were each dissolved in 20 ml of dimethylformamide (DMF). The two solutions were mixed, and stirred at room

temperature for 18 h. The product were centrifuged, and washed with 3× 20 ml of DMF. It was then washed with 2×20 ml of methanol (145 mg yield).[184]

The same procedure was performed for the synthesis of $Ni_2(dhtp)(DMF)_2$ $(H_2O)_2$ MOF by reaction of 2,5-dihydroxyterephtalic acid (200 mg, 1.00 mmol) and nickel(II) acetate tetrahydrate (647 mg, 2.60 mmol). 180 mg, yield.

$Ni_{0.2}Zn_{1.8}(dhtp)(DMF)_2$ $(H_2O)_2$ MOF was obtained following the same procedure by reaction of 2,5-dihydroxyterephtalic acid (200 mg, 1 mmol), zinc acetate dehydrate $Zn(OAc)_2.2H_2O$, (514.6 mg, 2.34 mmol) and nickel(II) acetate tetrahydrate (64.7 mg, 0.26 mmol). 170 mg, yield.

Synthesis of $M_2(dhtp)(H_2O)_2{\cdot}8H_2O$ (CPO-27-M) (M = Ni, Zn, $Ni_{0.1}Zn_{0.9}$):

$[Ni_2(dhtp)(H_2O)_2]{\cdot}8H_2O$ (CPO-27-Ni): A solution of 2,5-dihydroxyterephtalic acid (2.972 g, 15 mmol) in THF (50 ml) and a solution of nickel(II) acetate tetrahydrate (7.466 g, 30 mmol) in water (50 ml) were combined in a teflon-lined insert of 200 ml volume. The insert was transferred into an autoclave, sealed, and reacted for 3 days at 110 °C in a pre-heated furnace. Filtration yields 5.9 g of a yellowish fine crystalline product which was washed three times with water (50–100 ml).[180]

$[Zn_2(dhtp)(H_2O)_2]{\cdot}8H_2O$ (CPO-27-Zn): 2,5-dihydroxyterephtalic acid (149 mg, 0.75 mmol) was dissolved in THF (10 ml) in a teflon-lined autoclave of 40 ml volume. To this solution a sodium hydroxide solution (1 ml, 1 mol/l) and a solution of $Zn(NO_3)_2{\cdot}6H_2O$ (446 mg, 1.50 mmol) in water (5 ml) were added under stirring. The autoclave was sealed and heated for three days at 110 °C. The product was collected by filtration as a light-yellow substance. 0.3 g yield.

$[Ni_{0.2}Zn_{1.8}$ (dhtp)$(H_2O)2]{\cdot}8H_2O$ (CPO-27-$Ni_{0.1}Zn_{0.9}$): A solution of 2,5-dihydroxyterephtalic acid (1 g, 5 mmol) in THF (20 ml), a solution of nickel(II) acetate tetrahydrate (249 mg, 1 mmol) in water (10 ml) and a solution of zinc acetate dehydrate (1.98 g, 9 mmol) in water (10 ml), were combined in a teflon-lined insert of 100 ml volume. The insert was transferred into an autoclave, sealed, and reacted for three days at 110 °C in a pre-heated furnace. Filtration yields 2.2 g.

Controlling the crystallite size of CPO-27 Ni during the synthesis:

Seven samples of $[Ni_2(dhtp)(H_2O)_2]{\cdot}8H_2O$ (CPO-27-Ni), labeled **a÷g**, have been prepared by modifying some parameters in the procedure described by Dietzel *et al.* [180] including

concentration of the reactants, synthesis time and temperature. The obtained samples have been characterized by powder XRD and SEM microscopy.

CO adsorption on Ni_2(dhtp) (CPO-27-Ni):

The CO adsorption on [Ni_2(dhtp)] was followed by FTIR and the amount of the CO adsorbed was determined by adsorption study at different pressures.

The thin film has been prepared from a toluene suspension of 10 mg of CPO-27-Ni. Such coated silicon wafer was activated at 120 °C under high vacuum (10^{-5} mbar) for two hours. After which different pressures of CO were introduced to the cell, and IR spectra were recorded.

In a glovebox, 500 mg of an activated CPO-27-Ni (treated at 120 °C under high vacuum (10^{-5} mbar) overnight) were introduced in a glass reactor. The reactor was connected to a vacuum line containing a Pirani gauge pressure. Argon was evacuated and the volume of reactor was measured by pressure difference using helium. Different known pressures of CO were introduced in the reactor in order to estimate the amount of CO adsorbed by CPO-27-Ni. The pressure difference between the theorical pressure (pressure when CO is not adsorbed by the material) and the indicated pressure by Pirani gauge corresponded to the quantity CO adsorbed. This amount of CO adsorbed was plotted versus CO pressure and a Langmuir type curve was obtained. This curve fitted with the Sips equation.

$$N = 6.8 \times \frac{0.18 \times p^{0.6}}{0.18 \times P^{0.6} + 1},$$

N: quantity adsorbed of CO mol/ g of CPO-27-Ni MOF.

P: Pressure of CO (mbar).

Oxidation of CO to CO_2 in CPO-27-Ni:

Preparation of the catalyst Au@CPO-27-Ni-2: In a glass reactor, 1 g of pretreated CPO-27-Ni (150°C under vacuum (10^{-5} mbar) overnight) and 14 mg of gold(I) complex ($(CH_3)_3PAuCH_3$) were introduced in glove box. The argon was evacuated and a vapor pressure of methanol was introduced to the solid mixture, to increase the diffusion of the gold complex inside MOF cavities. After 72h methanol was removed and the gold complex was reduced under 500 torr of hydrogen at 100 °C for 2h. After removing all the volatiles under vacuum the catalyst is stored under argon.

The CO to CO_2 oxidation reaction was followed by FTIR

To estimate the amount of gases (CO, CO_2) in the reactor during the reaction by FTIR technique, the IR detector was calibrated toward CO and CO_2. For different known pressures of a gas the signal was recorded and the area was integrated and plotted versus the pressure.

CO calibration: The peaks were integrated between 2220 and 2140 cm^{-1} and the variation of the pressures (mbar) was proportional to the surface with a coefficient of 29.03.

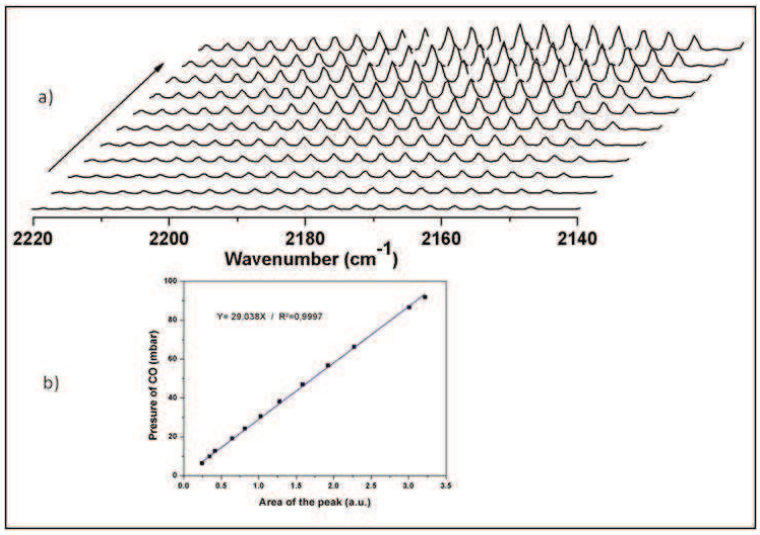

CO_2 calibration: The peaks were integrated between 2400 and 2250 cm^{-1} and the variation of the pressures (mbar) is proportional to the surface with a coefficient of 2.05

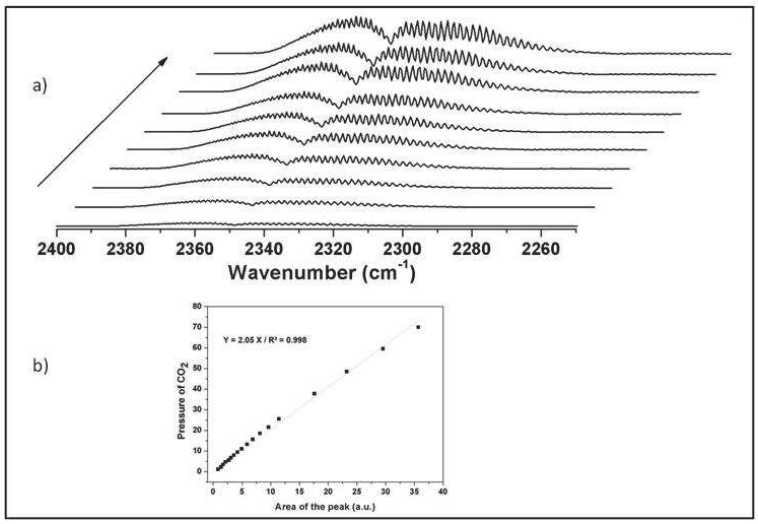

Catalytic tests for direct oxidation of CO: in the IR cell (350 ml) 500 mg of the catalyst was introduced followed by 20 mbar of CO and 200 mbar of O_2. The formation of CO_2 was followed by FTIR at room.

Catalytic tests for oxidation of CO:

In the reactor the oxidation of CO in the presence of O_2 can be followed by volumetric study, since the formation of CO_2 released, increases the pressure in the reactor.

Example:

Oxidation of CO to CO_2: 500 mg of the catalyst was introduced in a glass reactor. After that 8.9 mbar of CO was added and followed by 179.2 mbar of O_2. The variation of the pressure was measured and the results obtained are summarized in the following table

Pressure (mbar)	43	44.2	44.7	45.2	45.4
Time (mn)	0	0.5	1	2	3

The reaction rate was calculated by the slop of the curve (pressure (mbar) versus time) at the origin.

Catalytic tests for oxidation of H_2:

The reaction of H_2 with O_2 leads to the formation of water which remains adsorbed on the surface of the CPO-27 Ni. The consumption of H_2 was estimated by the pressure decrease.

Example:

Oxidation of H_2 to H_2O: in the reactor the catalyst was first regenerated under high vacuum at 80°C for 15 mn after the test in CO oxidation (see above). To the reactor 2.5 mbar of O_2 was added followed by 223.2 mbar oh H_2. The variation of the pressure was measured and the results obtained are summarized in the following table

Pressure (mbar)	169.8	169.5	169.3	169.1	168.8	168.5	167.3
Time (mn)	0	0.5	1.167	2	3	4	7

The reaction rate was calculated by the slop of the curve (pressure (mbar) versus time) at the origin.

Preparation of the supported ammonia borane samples:

Thermo gravimetric Analysis and Differential scanning calorimetry:

The samples were prepared by mixing the compounds under inert atmosphere in the glovebox.

Pure ammonia borane AB (4.6 ± 1.0 mg) stored as received from Aldrich in the glove box was analyzed by TGA and DSC. No particular air-exclusion techniques were used to transfer the sample in the equipment. A ramp of 5°C was used.

SBA-15 was prepared from $Si(OEt)_4$ according to literature procedure.[218] The SBA-15 was dehydroxylated at 500°C under vacuum (10^{-5} mbar) overnight, , and stored in the glove box ($SBA\text{-}15_{500}$, BET = 800m^2/g, 1.4 [≡SiOH]/ nm²). A sample of $SBA\text{-}15_{500}$ (4.6 mg) was analyzed by TGA and DSC between 40 to 200 °C.

A pure sample of CPO-27-Ni was activated overnight at 120°C under vacuum (10^{-5}mbar) and stored in the glove box. 12.6 mg of CPO-27-Ni were weighted and introduced in the calorimeter under air.

$AB@SBA\text{-}15_{500}$: a mechanical mixture of 40 of AB and 200 mg of $SBA\text{-}15_{500}$ (molar ratio AB/[≡SiOH] ca. 4) was prepared inside the glovebox. A sample of 6.7 mg was used for TGA and DSC analyses.

AB@CPO27 MOF: a mechanical mixture of 40 mg of AB and 200 mg of activated CPO-27-Ni MOF (molar ratio AB/Ni 1:1) and stored in glove box. A sample (18.4 mg) was taken from the batch prepared and analyzed by TGA and DSC analyses.

Temperature programmed desorption:

Inside the glove box, pure ammonia borane (32 mg), AB@SBA-15 (200 mg) and AB@CPO-27-Ni (200mg) were transferred to a dynamic reactor and analyzed by TPD.

Grafting of $Mo(CO)_6$ on MOF:

Surface organometallic grafting approach (method A) for loading molybdenum hexacarbonyl: In the glove box, the ochre starting material CPO-27-Ni was loaded in glass reactor containing a stirring bar. $Mo(CO)_6$ was loaded in another glass reactor. The two reactors were connected, and argon was evacuated after cooling the Mo-containing by liquid nitrogen bath. By removal of the liquid nitrogen, the hexacarbonyl diffused to the MOF-containing part. The MOF powder was stirred and heated at 120 °C for 3 hours. After cooling back at room temperature, the volatiles were condensed back in Mo –containing part, the sublimation-reaction-desorption cycle was repeated four times, and each time the quantity of

desorbed white crystallites diminished. By the end of the reaction the excess of white crystallites (unreacted $Mo(CO)_6$) are removed at 120°C under vacuum. The procedure was reproduced for each loading. Samples were characterized by XRD, BET and elemental analysis.

Gas released: the estimation of the amount of CO released during the reaction was experimentally measured by IR.

The adsorption of CO by CPO-27 Ni MOF was shown to follow the sips equation

$$N(\text{mmol/g} - \text{NiMOF}) = 6.8 \times \frac{0{,}18 \times P^{0,6}}{0{,}18 \times P^{0,6} + 1} \quad \text{(Eq.IV.1)}$$

The response of the IR instrument was calibrated toward different CO pressures (described above). P (mbar) = 29.03 × S (a.u.) (Eq.IV.15)

During the surface functionalization of the phenyl rings of $Ni_2(dhtp)$ with 20, 40, 60% molybdenum carbonyl, the gas phases were monitored by IR. The spectra obtained were integrated between 2142 and 2250 cm^{-1}

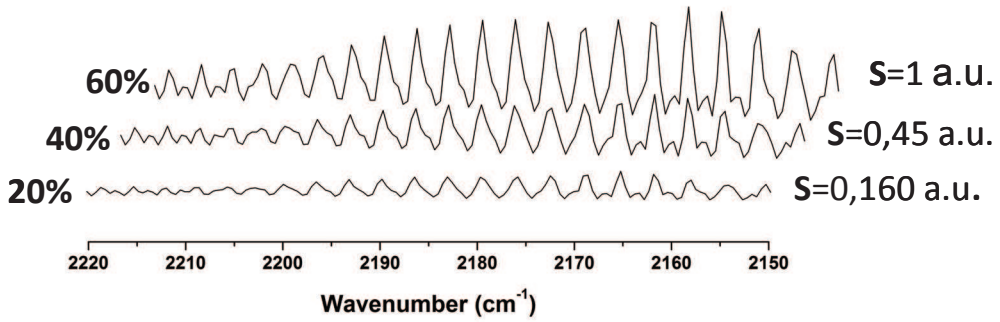

FTIR spectra of the CO released during the reactions.

$$N_{total} = N_{GP} + N_{Abs}$$

$$\begin{cases} N_{Gp} = \dfrac{PV}{RT} \Rightarrow N_{GP} = \dfrac{kV}{RT} S = 0.4 \times S(\text{mmol}). \\ P = kS \end{cases}$$

$$N_{Abs} = 6.8 \frac{0.18 \times P^{0.6}}{0.18 \times P^{0.6} + 1} \Rightarrow N_{Abs} = \frac{9.24 \times S^{0.6}}{1.36 \times S^{0.6} + 1} (\text{mmol/g})$$

The integrated surfaces for 20%, 40%, 60% loading of Mo were 0.16, 0.45, 1, respectively. The total quantity of CO released were estimated by introducing the surface of the peaks in both equations (Eq.IV.1, Eq.IV.15) and the amount of CO obtained,

Non well-defined loading (method B) of Molybdenum hexacarbonyl: In the glove-box, CPO-27 Ni-MOF and $Mo(CO)_6$ were introduced in one single Schlenk. Using liquid nitrogen

to minimize the vapor of $Mo(CO)_6$ argon was removed under vacuum. Ultrasonic bath was applied for 10mn to mix the reactants, and then put in the preheated oven at 120 °C. The reaction was cooled to room temperature and re-heated. About six cycles of heating and cooling were necessary to consume all the molybdenum and no residual $Mo(CO)_6$ was visible on the wall of the reactor. Otherwise the molybdenum hexacorbonyl was clearly seen in the reactors even after one week of continuously heating. The final product turned from light green to brown. The procedure was repeated for each loading.

Ethylene conversion with Catalyst with $[Ni_2(dhtp)][Mo(CO)_3]_{0.5}$:

100 mg (0.32mmol) of activated MOF was functionalized to the maximum loading of molybdenum hexacarbonyl which corresponded to 50% of phenyl ring (0.16 mmol of $Mo(CO)_6$. The sample was placed in a reactor and 50 equivalents of ethylene were added. The reaction was carried out at three different temperatures (80, 150, 180 °C). The conversion of ethylene and the formation of propylene were followed by GC.

HDS catalysis with Catalysts $[Ni_2(dhtp)][Mo(CO)_3]_x$ (X = 0, 0.1, 0.2, 0.4, 0.5, 1, 1.5, 2):

The test was based on a model compound, i.e. 3 % dibenzothiophene (DBT), 0.5 % indole, 1 % naphtalene, 2.5 % dimethyldisulfide (DMDS), 0.5 % *n*-nonane and the rest being *n*-heptane solvent. In addition to the representative sulfur compound (DBT) the feed also contained a representative nitrogen compound (indole) and an aromatic compound (naphthalene).

A TK-250 Topsøe's commercial catalyst was used under the same conditions as reference. Each catalyst test involved first an activation/sulfidation step in which the catalyst for 4 hours was exposed to only DMDS in *n*-heptane. The experimental feed described above was introduced. After a 4 hour stabilization period, every 60 mn a sample was analyzed by GC. A total of eight GC analyses of the product stream have been performed.

Chapter V:

General Conclusions

Numerous fields of science have found metal-organic frameworks (MOFs) attractive materials for various applications, including catalysis, due to their highly tunable properties and extensive possibilities of designing and modifying their crystal structures. The synthesis of MOFs is a complicated process which depends on a lot of parameters such as temperature, the nature and the quantity of the solvent, the nature and the ratio between cornerstones and the ligand etc. By judicious choice of a combination of all these variables, metal organic framework (MOF) with desirable characteristics should be possible to obtain.

As clearly visible by the amount of recent publications on MOFs and their applications in various disciplines, the development of this field of chemistry and materials research is very significant.

The objective of the present work was to apply the surface organometallic chemistry (SOMC) approach either to novel MOF or to existing materials by post-synthesis modification in order to develop single-site heterogeneous organometallic catalysts.

Metal Organic Frameworks (MOFs) from scratch

The first experiments of the thesis consisted on synthesizing new imidazolium dicarboxylic acid ligands and their characterizations *en route* to MOF containing N-heterocyclic carbene, a very important ligand in catalysis. New MOFs based on these imidazolium ligands have been designed, prepared and investigated by XRD, TGA, BET, elemental analysis and solid state NMR. However, because of their relatively low surface area and pore size, the obtained materials were not suitable for post modification and catalysis.

The strategy consisting in designing MOF with novel ligands for organometallic synthesis appears challenging. Because of the synthesis of multifunctional organic linker and the resulted MOF must satisfy following condition: reachable and reactive sites to allow firstly post-synthesis modification (deprotonation and coordination of the active metal center in the case of the linker with the inner imidazolium ring in our case) and secondly the accessibility of the generated active site for different reactants.

Post synthesis modification on the cornerstone of UiO-66 MOFs

The use of existing MOF known to have potentially reactive sites at the cornerstone is a second possible strategy to graft organometallic complexes via surface organometallic chemistry on MOF.

An attractive material is UiO-66 MOF family, which is a series of isostructural materials characterized *inter alia* by *i)* a very robust structure with large surface area and accessible pores and by *ii)* bridging hydroxyl groups, that can be as grating center for surface organometallic chemistry. Before the SOMC post-modification work, improved protocols for large scale syntheses of the three dimensional structures have been developed. Furthermore, a novel zirconium MOF with an amine as secondary functional group on the linker was also obtained. The adsorptive properties of carbon dioxide on zirconium MOF with and without a secondary amino group have been tested and the results indicate that adsorption of CO_2 is mainly due to the high surface area, porosity and the presence of amino group on the linker.

The MOF were modified through reactions on the bridging hydroxyl groups of the Zr_6 octahedra of the cornerstone. The hydroxyl ligands were accessible only to small molecules like D_2O and MeMgBr – which allowed quantitative chemical titration of the available OH- but showed little to no reactivity with larger organometallic substrates such as $AuMe(PMe_3)$ or $Ta(=CH\text{-}^tBu)(CH_2\text{-}^tBu)_3$. Nevertheless, the cornerstone could be modified with the purely inorganic molecule SiH_4; such grafting was followed by silane polymerization. This result, still under investigation, is a promising lead for the controlled growth of silicon nanowires in confined crystalline structure.

Post synthesis modification on the linker of CPO-27 MOFs

In the third strategy for SOMC applied to a MOF explored in this thesis, modification was attempted on the linker rather than on a cornerstone. Most of the existing MOF displaying high surface area and both thermal and chemical stability upon solvent removal (most adequate for catalysis), are characterized by the absence of accessible highly reactive site on the linker. Conversely, most of the existing MOFs have the phenyl ring, which is the unique site to perform post-synthesis modification.

The chosen starting MOFs was the well characterized isostructural family CPO-27 (named MOF-74 in earlier reports) built around the benzene-2,5-dihydroxo-1,4-dicarboxylate, or dihydroxyterephatalate (dhtp) linker. Before the post-synthesis modification, different synthetic procedures were screened and scaled-up syntheses were developed. The variation in synthesis parameters such as temperature or concentration of reactants or time was shown to affect the crystal size of the crystallites.

These MOFs present interesting physical and chemical properties, particularly the CPO-27-Ni one, i.e. a high surface area and an accessible metal site. This MOF has found before SOMC modification to favor hydrogen release from ammonia borane at 40 °C

(whereas the same process takes place at 100 °C in the absence of MOF). Encapsulation of gold nanoparticles inside the cavities of MOF proved also an interesting route since it allowed fast CO oxidation to CO_2 by oxygen while only slow hydrogen oxidation was catalyzed, which is relevant in the context of PROX catalysis.

The surface organometallic chemistry approach on CPO-27-Ni lead to a well defined surface specie ($[Ni_2(dhtp)]Mo(CO)_3$) prepared by grafting of $Mo(CO)_6$ on the phenyl rings of the CPO-27-Ni. A coverage rate study of this grafting reaction was performed, showing quantitative molybdenum uptake up to 50% of the phenyl rings. Catalytic tests have been performed on this material: while the direct conversion of ethene to propene cannot be catalyzed by $[Ni_2dhtp][Mo(CO)_3]_{0.5}$, the material is among the best unsupported precatalysts for hydrodesulphurization (HDS) of thiophene, albeit it does not reach the industrial supported precatalysts activity. Noteworthy, in this approach the structure of the starting MOF is destroyed during the sulfidation process necessary to obtain the active phase. The nickel metal is present in too large excess with respect to the molybdenum for the desired final Ni-doped MoS_2. Nevertheless, the crystalline structure imparts a good codispersion of the two metals in the final catalyst and the small size of the starting MOF nanocrystallites lead to less that 5- layer thick MoS_2 slabs. These two characteristics are probably in part responsible for the good catalytic performance observed.

Despite this success in HDS, SOMC application to CPO-27 modification for heterogeneous catalysis remains weak due to the limited organometallic chemistry which can be performed on the phenyl ring of the dihydroxyterephatlic linker. More generally, SOMC at a MOF linker appears as a possible route for MOF post-synthesis modification but it is a limited by the scarcity of moieties commonly encountered in MOFs other than phenyl ring.

In conclusion

This work has dealt with the important and difficult subject which is catalysis using post-synthesis modified metal organic frameworks. The possibility to design the material at the atomic scale and therefore tune its structure-application relationship, by a judicious choice of the cornerstone and the linker, gives enormous advantages over classical heterogeneous systems. Nevertheless, there exist difficulties that still need to be overcome, because these materials can suffer from low porosity, low chemical and thermal stability and so on, and a predictive approach on their synthesis or on their modification by surface organometallic chemistry does not exist. The thesis' results presented above were thus devoted to bridging the persisting gap between ideal approach and its realization.

References

References

[1] G. C. Bond, *Heterogeneous Catalysis: Principles and Applications. 2nd Ed*, **1987**.

[2] B. M. Reddy, P. Saikia, P. Bharali, L. Katta, G. Thrimurthulu, *Catal. Today* **2009**, *141*, 109.

[3] A. E. Castro Luna, M. E. Iriarte, *Appl. Catal.,* **2008**, *343*, 10.

[4] V. Ramaswamy, S. Malwadkar, S. Chilukuri, *Appl. Catal.* **2008**, *84*, 21.

[5] S. H. Brown, *Handb. Green Chem.* **2009**, *2*, 1.

[6] C. Larabi, N. Merle, S. Norsic, M. Taoufik, A. Baudouin, C. Lucas, J. Thivolle-Cazat, A. de Mallmann, J.-M. Basset, *Organometallics* **2009**, *28*, 5647.

[7] J.-M. Basset, A. Baudouin, F. Bayard, J.-P. Candy, C. Coperet, A. De Mallmann, G. Godard, E. Kuntz, F. Lefebvre, C. Lucas, S. Norsic, K. Pelzer, A. Quadrelli, C. Santini, D. Soulivong, F. Stoffelbach, M. Taoufik, C. Thieuleux, J. Thivolle-Cazat, L. Veyre, *Mod. Surf. Organomet. Chem.* **2009**, 23.

[8] F. Bini, C. Rosier, R. P. Saint-Arroman, E. Neumann, C. Dablemont, A. de Mallmann, F. Lefebvre, G. P. Niccolai, J. M. Basset, M. Crocker, J. K. Buijink, *Organometallics* **2006**, *25*, 3743.

[9] V. Dufaud, J.-M. Basset, *Angew. Chem., Int. Ed* **1998**, *37*, 806.

[10] F. Quignard, A. Choplin, J. M. Basset, *J. Chem. Soc., Chem. Commun.* **1991**, 1589.

[11] F. Quignard, C. Lecuyer, C. Bougault, F. Lefebvre, A. Choplin, D. Olivier, J. M. Basset, *Inorg. Chem.* **1992**, *31*, 928.

[12] C. Thieuleux, E. A. Quadrelli, J.-M. Basset, J. Doebler, J. Sauer, *Chem. Commun.* **2004**, 1729.

[13] G. Tosin, M. Delgado, A. Baudouin, C. C. Santini, F. Bayard, J.-M. Basset, *Organometallics*, *29*, 1312.

[14] J.-M. Basset, A. Baudouin, F. Bayard, J.-P. Candy, C. Coperet, A. De Mallmann, G. Godard, E. Kuntz, F. Lefebvre, C. Lucas, S. Norsic, K. Pelzer, A. Quadrelli, C. Santini, D. Soulivong, F. Stoffelbach, M. Taoufik, C. Thieuleux, J. Thivolle-Cazat, L. Veyre, *Mod. Surf. Organomet. Chem.* **2009**, 75.

[15] F. Blanc, J. Thivolle-Cazat, J. M. Basset, C. Coperet, A. S. Hock, Z. J. Tonzetich, R. R. Schrock, *J. Am. Chem. Soc.* **2007**, *129*, 1044.

[16] M. Taoufik, E. Le Roux, J. Thivolle-Cazat, J. M. Basset, *Angew. Chem. Int. Ed.* **2007**, *46*, 7202.

[17] D. Soulivong, S. Norsic, M. Taoufik, C. Coperet, J. Thivolle-Cazat, S. Chakka, J.-M. Basset, *J. Am. Chem. Soc.* **2008**, *130*, 5044.

[18] J. M. Basset, C. Coperet, D. Soulivong, M. Taoufik, J. T. Cazat, *Acc. Chem. Res.*, *43*, 323.

[19] M. Taoufik, E. Schwab, M. Schultz, D. Vanoppen, M. Walter, J. Thivolle-Cazat, J. M. Basset, *Chem. Commun* **2004**, 1434.

[20] J. Joubert, F. Delbecq, P. Sautet, E. Le Roux, M. Taoufik, C. Thieuleux, F. Blanc, C. Coperet, J. Thivolle-Cazat, J. M. Basset, *J. Am. Chem. Soc.* **2006**, *128*, 9157.

[21] J. Joubert, F. Delbecq, C. Thieuleux, M. Taoufik, F. Blanc, C. Coperet, J. Thivolle-Cazat, J. M. Basset, P. Sautet, *Organometallics* **2007**, *26*, 3329.

[22] C. Thieuleux, A. Maraval, L. Veyre, C. Coperet, D. Soulivong, J.-M. Basset, G. J. Sunley, *Angew. Chem., Int. Ed* **2007**, *46*, 2288.

[23] C. Coperet, *Chem. Rev.*, *110*, 656.

[24] C. Lecuyer, F. Quignard, A. Choplin, D. Olivier, J. M. Basset, *Angew. Chem.* **1991**, *103*, 1692.

[25] V. Vidal, A. Theolier, J. Thivolle-Cazat, J.-M. Basset, J. Corker, *J. Am. Chem. Soc.* **1996**, *118*, 4595.

[26] S. Soignier, M. Taoufik, E. Le Roux, G. Saggio, C. Dablemont, A. Baudouin, F. Lefebvre, A. De Mallmann, J. Thivolle-Cazat, J.-M. Basset, G. Sunley, B. M. Maunders, *Organometallics* **2006**, *25*, 1569.

[27] E. L. Le Roux, M. Chabanas, A. Baudouin, A. de Mallmann, C. Coperet, E. A. Quadrelli, J. Thivolle-Cazat, J.-M. Basset, W. Lukens, A. Lesage, L. Emsley, G. J. Sunley, *J. Am. Chem. Soc.* **2004**, *126*, 13391.

[28] M. Chabanas, V. Vidal, C. Coperet, J. Thivolle-Cazat, J.-M. Basset, *Angew. Chem., Int. Ed* **2000**, *39*, 1962.

[29] V. Vidal, A. Theolier, J. Thivolle-Cazat, J.-M. Basset, *Science* **1997**, *276*, 99.

[30] C. Coperet, O. Maury, J. Thivolle-Cazat, J.-M. Basset, *Angew. Chem., Int. Ed* **2001**, *40*, 2331.

[31] J. L. Herisson, Y. Chauvin, *Makromol. Chem.* **1971**, *141*, 161.

[32] O. Maury, L. Lefort, V. Vidal, J. Thivolle-Cazat, J.-M. Basset, *Organometallics*, ACS ASAP.

[33] E. Le Roux, M. Taoufik, M. Chabanas, D. Alcor, A. Baudouin, C. Coperet, J. Thivolle-Cazat, J. M. Basset, A. Lesage, S. Hediger, L. Emsley, *Organometallics* **2005**, *24*, 4274.

[34] E. Le Roux, M. Taoufik, C. Coperet, A. de Mallmann, J. Thivolle-Cazat, J. M. Basset, B. M. Maunders, G. J. Sunley, *Angew. Chem. Int. Ed.* **2005**, *44*, 6755.

[35] E. Le Roux, M. Taoufik, A. Baudouin, C. Coperet, J. Thivolle-Cazat, J. M. Basset, B. M. Maunders, G. J. Sunley, *Adv. Synth. Catal.* **2007**, *349*, 231.

[36] K. C. Szeto, S. Norsic, L. Hardou, E. Le Roux, S. Chakka, J. Thivolle-Cazat, A. Baudouin, C. Papaioannou, J. M. Basset, M. Taoufik, *Chem. Commun*, *46*, 3985.

[37] N. Merle, F. Stoffelbach, M. Taoufik, E. Le Roux, J. Thivolle-Cazat, J. M. Basset, *Chem. Commun* **2009**, 2523.

[38] C. Janiak, *Dalton Trans.* **2003**, 2781.

[39] Y. Kinoshita, I. Matsubara, Y. Saito, *Bull. Chem. Soc. Jpn.* **1959**, *32*, 1216.

[40] A. J. Saraceno, B. P. Block, *Inorg. Chem.* **1964**, *3*, 1699.

[41] B. F. Hoskins, R. Robson, *J. Am. Chem. Soc.* **1989**, *111*, 5962.

[42] J. C. Bailar, Jr., *Preparative Inorg. Reactions* **1964**, *1*, 1.

[43] B. F. Hoskins, R. Robson, *J. Am. Chem. Soc.* **1990**, *112*, 1546.

[44] M. Ohba, N. Maruono, H. Okawa, T. Enoki, J. M. Latour, *J. Am. Chem. Soc.* **1994**, *116*, 11566.

[45] O. M. Yaghi, M. O'Keeffe, N. W. Ockwig, H. K. Chae, M. Eddaoudi, J. Kim, *Nature* **2003**, *423*, 705.

[46] A. P. Cote, A. I. Benin, N. W. Ockwig, M. O'Keeffe, A. J. Matzger, O. M. Yaghi, *Science* **2005**, *310*, 1166.

[47] J. S. Seo, D. Whang, H. Lee, S. I. Jun, J. Oh, Y. J. Jeon, K. Kim, *Nature* **2000**, *404*, 982.

[48] L. Q. Ma, C. Abney, W. B. Lin, *Chem. Soc. Rev.* **2009**, *38*, 1248.

[49] A. Corma, H. Garcia, F. X. Llabres i Xamena, *Chem. Rev.*, *110*, 4606.

[50] J. Lee, O. K. Farha, J. Roberts, K. A. Scheidt, S. T. Nguyen, J. T. Hupp, *Chem. Soc. Rev.* **2009**, *38*, 1450.

[51] N. L. Rosi, J. Eckert, M. Eddaoudi, D. T. Vodak, J. Kim, M. O'Keeffe, O. M. Yaghi, *Science* **2003**, *300*, 1127.

[52] J. L. C. Rowsell, O. M. Yaghi, *J. Am. Chem. Soc.* **2006**, *128*, 1304.

[53] L. J. Murray, M. Dinca, J. R. Long, *Chem. Soc. Rev.* **2009**, *38*, 1294.

[54] A. Demessence, J. R. Long, *Chem. Eur. J.*, *16*, 5902.

[55] Y. F. Chen, J. Y. Lee, R. Babarao, J. Li, J. W. Jiang, *J. Phys. Chem. C*, *114*, 6602.

[56] R. Adams, C. Carson, J. Ward, R. Tannenbaum, W. Koros, *Microporous Mesoporous Mater.*, *131*, 13.

[57] Z. Shi, G. H. Li, L. Wang, L. Gao, X. B. Chen, J. Hua, S. H. Feng, *Cryst. Growth Des.* **2004**, *4*, 25.

[58] H. L. Li, C. E. Davis, T. L. Groy, D. G. Kelley, O. M. Yaghi, *J. Am. Chem. Soc.* **1998**, *120*, 2186.

[59] H. Li, M. Eddaoudi, M. O'Keeffe, O. M. Yaghi, *Nature* **1999**, *402*, 276.

[60] H. Li, M. Eddaoudi, T. L. Groy, O. M. Yaghi, *J. Am. Chem. Soc.* **1998**, *120*, 8571.

[61] J. Kim, B. L. Chen, T. M. Reineke, H. L. Li, M. Eddaoudi, D. B. Moler, M. O'Keeffe, O. M. Yaghi, *J. Am. Chem. Soc.* **2001**, *123*, 8239.

[62] D. T. Vodak, M. E. Braun, J. Kim, M. Eddaoudi, O. M. Yaghi, *Chem. Commun* **2001**, 2534.

[63] M. Eddaoudi, J. Kim, N. Rosi, D. Vodak, J. Wachter, M. O'Keeffe, O. M. Yaghi, *Science* **2002**, *295*, 469.

[64] C. J. Doonan, W. Morris, H. Furukawa, O. M. Yaghi, *J. Am. Chem. Soc.* **2009**, *131*, 9492.

[65] D. J. Tranchemontagne, J. L. Mendoza-Cortes, M. O'Keeffe, O. M. Yaghi, *Chem. Soc. Rev.* **2009**, *38*, 1257.

[66] A. U. Czaja, N. Trukhan, U. Muller, *Chem. Soc. Rev.* **2009**, *38*, 1284.

[67] G. Ferey, *Science* **2005**, *310*, 1119.

[68] T. Duren, Y. S. Bae, R. Q. Snurr, *Chem. Soc. Rev.* **2009**, *38*, 1237.

[69] F. Bonino, S. Chavan, J. G. Vitillo, E. Groppo, G. Agostini, C. Lamberti, P. D. C. Dietzel, C. Prestipino, S. Bordiga, *Chem. Mater.* **2008**, *20*, 4957.

[70] P. D. C. Dietzel, R. E. Johnsen, H. Fjellvaag, S. Bordiga, E. Groppo, S. Chavan, R. Blom, *Chem. Commun.* **2008**, 5125.

[71] S. Chavan, J. G. Vitillo, E. Groppo, F. Bonino, C. Lamberti, P. D. C. Dietzel, S. Bordiga, *J. Phys. Chem. C* **2009**, *113*, 3292.

[72] A. M. Spokoyny, D. Kim, A. Sumrein, C. A. Mirkin, *Chem. Soc. Rev.* **2009**, *38*, 1218.

[73] T. Uemura, Y. Ono, K. Kitagawa, S. Kitagawa, *Macromol.* **2008**, *41*, 87.

[74] M. D. Allendorf, C. A. Bauer, R. K. Bhakta, R. J. T. Houk, *Chem. Soc. Rev.* **2009**, *38*, 1330.

[75] J. L. C. Rowsell, O. M. Yaghi, *Angew. Chem. Int. Ed.* **2005**, *44*, 4670.

[76] P. D. C. Dietzel, Y. Morita, R. Blom, H. Fjellvaag, *Angew. Chem., Int. Ed* **2005**, *44*, 6354.

[77] B. Xiao, P. S. Wheatley, X. B. Zhao, A. J. Fletcher, S. Fox, A. G. Rossi, I. L. Megson, S. Bordiga, L. Regli, K. M. Thomas, R. E. Morris, *J. Am. Chem. Soc.* **2007**, *129*, 1203.

[78] A. G. Wong-Foy, A. J. Matzger, O. M. Yaghi, *J. Am. Chem. Soc.* **2006**, *128*, 3494.

[79] C. Zlotea, R. Campesi, F. Cuevas, E. Leroy, P. Dibandjo, C. Volkringer, T. Loiseau, G. Ferey, M. Latroche, *J. Am. Chem. Soc.*, *132*, 2991.

[80] Y. Li, F. Liang, H. Bux, W. Yang, J. Caro, *J. Membr. Sci.*, *354*, 48.

[81] J.-R. Li, R. J. Kuppler, H.-C. Zhou, *Chem. Soc. Rev.* **2009**, *38*, 1477.

[82] J. Gascon, F. Kapteijn, *Angew. Chem. Int. Ed.*, *49*, 1530.

[83] M. Kurmoo, *Chem. Soc. Rev.* **2009**, *38*, 1353.

[84] M. A. Fox, D. A. Chandler, *Adv. Mater.* **1991**, *3*, 381.

[85] C. G. Silva, A. Corma, H. Garcia, *J. Mater. Chem.*, *20*, 3141.

[86] J. Li, W. H. Bi, W. Ki, X. Y. Huang, S. Reddy, *J. Am. Chem. Soc.* **2007**, *129*, 14140.

[87] Y. Liu, G. Li, X. Li, Y. Cui, *Angew. Chem. Int. Ed.* **2007**, *46*, 6301.

[88] M. Fujita, Y. J. Kwon, S. Washizu, K. Ogura, *J. Am. Chem. Soc.* **1994**, *116*, 1151.

[89] F. Xamena, A. Abad, A. Corma, H. Garcia, *J. Catal.* **2007**, *250*, 294.

[90] S. Kitagawa, S. Noro, T. Nakamura, *Chem. Commun* **2006**, 701.

[91] S.-H. Cho, B. Ma, S. T. Nguyen, J. T. Hupp, T. E. Albrecht-Schmitt, *Chem. Commun.* **2006**, 2563.

[92] F. Song, C. Wang, J. M. Falkowski, L. Ma, W. Lin, *J. Am. Chem. Soc.*, *132*, 15390.

[93] K. C. Szeto, C. Prestipino, C. Lamberti, A. Zecchina, S. Bordiga, M. Bjorgen, M. Tilset, K. P. Lillerud, *Chem. Mater.* **2007**, *19*, 211.

[94] K. C. Szeto, K. P. Lillerud, M. Tilset, M. Bjorgen, C. Prestipino, A. Zecchina, C. Lamberti, S. Bordiga, *J. Phys. Chem. B* **2006**, *110*, 21509.

[95] R.-Q. Zou, H. Sakurai, S. Han, R.-Q. Zhong, Q. Xu, *J. Am. Chem. Soc.* **2007**, *129*, 8402.

[96] T. Ahnfeldt, D. Gunzelmann, T. Loiseau, D. Hirsemann, J. Senker, G. Ferey, N. Stock, *Inorg. Chem.* **2009**, *48*, 3057.

[97] M. Savonnet, S. Aguado, U. Ravon, D. Bazer-Bachi, V. Lecocq, N. Bats, C. Pinel, D. Farrusseng, *Green Chem.* **2009**, *11*, 1729.

[98] C. D. Wu, A. Hu, L. Zhang, W. B. Lin, *J. Am. Chem. Soc.* **2005**, *127*, 8940.

[99] X. Zhang, F. Xamena, A. Corma, *J. Catal.* **2009**, *265*, 155.

[100] J. Gascon, U. Aktay, M. D. Hernandez-Alonso, G. P. M. van Klink, F. Kapteijn, *J. Catal.* **2009**, *261*, 75.

[101] S. Hasegawa, S. Horike, R. Matsuda, S. Furukawa, K. Mochizuki, Y. Kinoshita, S. Kitagawa, *J. Am. Chem. Soc.* **2007**, *129*, 2607.

[102] M. Sabo, A. Henschel, H. Froede, E. Klemm, S. Kaskel, *J. Mater. Chem.* **2007**, *17*, 3827.

[103] F. Schroeder, D. Esken, M. Cokoja, M. W. E. van den Berg, O. I. Lebedev, G. Van Tendeloo, B. Walaszek, G. Buntkowsky, H.-H. Limbach, B. Chaudret, R. A. Fischer, *J. Am. Chem. Soc.* **2008**, *130*, 6119.

[104] K. Oefele, *J. Organometal. Chem.* **1968**, *12*, P42.

[105] A. J. Arduengo, III, R. L. Harlow, M. Kline, *J. Am. Chem. Soc.* **1991**, *113*, 361.

[106] B. Kantchev Eric Assen, J. O'Brien Christopher, G. Organ Michael, *Angew. Chem., Int. Ed* **2007**, *46*, 2768.

[107] F. E. Hahn, *Angew. Chem., Int. Ed* **2006**, *45*, 1348.

[108] W. A. Herrmann, *Angew. Chem., Int. Ed* **2002**, *41*, 1290.

[109] J. C. Garrison, W. J. Youngs, *Chem. Rev.* **2005**, *105*, 3978.

[110] D. Bourissou, O. Guerret, F. P. Gabbai, G. Bertrand, *Chem. Rev.* **2000**, *100*, 39.

[111] D. S. McGuinness, K. J. Cavell, *Organometallics* **2000**, *19*, 741.

[112] L. Delaude, A. Demonceau, J. Wouters, *Eur. J. Inorg. Chem.* **2009**, 1882.

[113] K. M. Hindi, T. J. Siciliano, S. Durmus, M. J. Panzner, D. A. Medvetz, D. V. Reddy, L. A. Hogue, C. E. Hovis, J. K. Hilliard, R. J. Mallet, C. A. Tessier, C. L. Cannon, W. J. Youngs, *J. Med. Chem.* **2008**, *51*, 1577.

[114] I. Karame, M. Boualleg, J.-M. Camus, T. K. Maishal, J. Alauzun, J.-M. Basset, C. Coperet, R. J. P. Corriu, E. Jeanneau, A. Mehdi, C. Reye, L. Veyre, C. Thieuleux, *Chem. Eur. J.* **2009**, *15*, 11820.

[115] R. R. Schrock, *J. Chem. Soc., Dalton Trans.* **2001**, 2541.

[116] X. L. Hu, I. Castro-Rodriguez, K. Olsen, K. Meyer, *Organometallics* **2004**, *23*, 755.

[117] J. W. Herndon, *Coord. Chem. Rev.* **2004**, *248*, 3.

[118] R. H. Crabtree, *J. Organometal. Chem.* **2005**, *690*, 5451.

[119] K. Oefele, W. A. Herrmann, D. Mihalios, M. Elison, E. Herdtweck, W. Scherer, J. Mink, *J. Organomet. Chem.* **1993**, *459*, 177.

[120] C. Vougioukalakis Georgios, H. Grubbs Robert, *Chem. Rev*, *110*, 1746.

[121] T. Weskamp, F. J. Kohl, W. Hieringer, D. Gleich, W. A. Herrmann, *Angew. Chem., Int. Ed* **1999**, *38*, 2416.

[122] R. F. R. Jazzar, S. A. Macgregor, M. F. Mahon, S. P. Richards, M. K. Whittlesey, *J. Am. Chem. Soc.* **2002**, *124*, 4944.

[123] F. Heinemann, J. Klodwig, F. Knoch, M. Wuendisch, U. Zenneck, *Chem. Ber.* **1997**, *130*, 123.

[124] M. C. Perry, K. Burgess, *Tetrahedron: Asymmetry* **2003**, *14*, 951.

[125] S. C. Schurer, S. Gessler, N. Buschmann, S. Blechert, *Angew. Chem., Int. Ed* **2000**, *39*, 3898.

[126] K. Maishal Tarun, J. Alauzun, J.-M. Basset, C. Coperet, J. P. Corriu Robert, E. Jeanneau, A. Mehdi, C. Reye, L. Veyre, C. Thieuleux, *Angew. Chem., Int. Ed* **2008**, *47*, 8654.

[127] R. Banerjee, A. Phan, B. Wang, C. Knobler, H. Furukawa, M. O'Keeffe, O. M. Yaghi, *Science* **2008**, *319*, 939.

[128] B. Wang, A. P. Cote, H. Furukawa, M. O'Keeffe, O. M. Yaghi, *Nature* **2008**, *453*, 207.

[129] J. Chun, I. G. Jung, H. J. Kim, M. Park, M. S. Lah, S. U. Son, *Inorg. Chem.* **2009**, *48*, 6353.

[130] R. S. Crees, M. L. Cole, L. R. Hanton, C. J. Sumby, *Inorg. Chem.*, *49*, 1712.

[131] K. Oisaki, Q. W. Li, H. Furukawa, A. U. Czaja, O. M. Yaghi, *J. Am. Chem. Soc.*, *132*, 9262.

[132] J. Liu, J. Chen, J. Zhao, Y. Zhao, L. Li, H. Zhang, *Synthesis* **2003**, 2661.

[133] A. J. Arduengo, III, F. P. Gentry, Jr., P. K. Taverkere, H. E. Simmons, III, (E. I. Du Pont de Nemours & Co., USA). Application: US
US, **2001**, p. 7 pp.

[134] H. Wu, J. M. Simmons, Y. Liu, C. M. Brown, X. S. Wang, S. Ma, V. K. Peterson, P. D. Southon, C. J. Kepert, H. C. Zhou, T. Yildirim, W. Zhou, *Chem. Eur. J.*, *16*, 5205.

[135] R. Banerjee, A. Phan, B. Wang, C. Knobler, H. Furukawa, M. O'Keeffe, M. Yaghi Omar, *Science* **2008**, *319*, 939.

[136] J. Maddox, *Nature* **1988**, *335*, 201.

[137] E. D. Bloch, D. Britt, C. Lee, C. J. Doonan, F. J. Uribe-Romo, H. Furukawa, J. R. Long, O. M. Yaghi, *J. Am. Chem. Soc.*, ACS ASAP.

[138] J. Muzart, *Tetrahedron* **2009**, *65*, 8313.

[139] H. G. Raubenheimer, S. Cronje, *Chem. Soc. Rev.* **2008**, *37*, 1998.

[140] K. L. Mulfort, J. T. Hupp, *J. Am. Chem. Soc.* **2007**, *129*, 9604.

[141] M. Dinca, J. R. Long, *Angew. Chem., Int. Ed* **2008**, *47*, 6766.

[142] Z. Wang, S. M. Cohen, *J. Am. Chem. Soc.* **2007**, *129*, 12368.

[143] Y.-F. Song, L. Cronin, *Angew. Chem., Int. Ed* **2008**, *47*, 4635.

[144] Y. Goto, H. Sato, S. Shinkai, K. Sada, *J. Am. Chem. Soc.* **2008**, *130*, 14354.

[145] W. Morris, C. J. Doonan, H. Furukawa, R. Banerjee, O. M. Yaghi, *J. Am. Chem. Soc.* **2008**, *130*, 12626.

[146] K. L. Mulfort, O. K. Farha, C. L. Stern, A. A. Sarjeant, J. T. Hupp, *J. Am. Chem. Soc.* **2009**, *131*, 3866.

[147] S. Surble, C. Serre, C. Mellot-Draznieks, F. Millange, G. Ferey, *Chem. Commun* **2006**, 284.

[148] A. Boutin, M.-A. Springuel-Huet, A. Nossov, A. Gedeon, T. Loiseau, C. Volkringer, G. Ferey, F.-X. Coudert, A. H. Fuchs, *Angew. Chem., Int. Ed* **2009**, *48*, 8314.

[149] C. Volkringer, T. Loiseau, N. Guillou, G. Ferey, E. Elkaim, *Solid State Sci.* **2009**, *11*, 1507.

[150] J. Hafizovic Cavka, S. Jakobsen, U. Olsbye, N. Guillou, C. Lamberti, S. Bordiga, K. P. Lillerud, *J. Am. Chem. Soc.* **2008**, *130*, 13850.

[151] U. Thewalt, K. Doppert, W. Lasser, *J. Organometal. Chem.* **1986**, *308*, 303.

[152] G. Trimmel, B. Moraru, S. Gross, V. Di Noto, U. Schubert, *Macromol. Symp.* **2001**, *175*, 357.

[153] G. Kickelbick, U. Schubert, *J. Chem. Soc.-Dalton Trans.* **1999**, 1301.

[154] M. Puchberger, F. R. Kogler, M. Jupa, S. Gross, H. Fric, G. Kickelbick, U. Schubert, *Eur. J. Inorg. Chem.* **2006**, 3283.

[155] X. Lin, J. Jia, X. Zhao, K. M. Thomas, A. J. Blake, G. S. Walker, N. R. Champness, P. Hubberstey, M. Schroeder, *Angew. Chem., Int. Ed* **2006**, *45*, 7358.

[156] N. Millot, C. C. Santini, F. Lefebvre, J. M. Basset, *Cr Chim* **2004**, *7*, 725.

[157] L. Merat, R. A. S. San Gil, S. R. Guerra, L. C. Dieguez, S. Caldarelli, J. G. Eon, F. Ziarelli, H. Pizzala, *J. Mol. Catal. A: Chem* **2007**, *272*, 298.

[158] P. J. Chu, A. Demallmann, J. H. Lunsford, *J. Phys. Chem.* **1991**, *95*, 7362.

[159] M. Taoufik, A. de Mallmann, E. Prouzet, G. Saggio, J. Thivolle-Cazat, J. M. Basset, *Organometallics* **2001**, *20*, 5518.

[160] J. H. Lunsford, P. N. Tutunjian, P. J. Chu, E. B. Yeh, D. J. Zalewski, *J. Phys. Chem.* **1989**, *93*, 2590.

[161] G. Saggio, A. de Mallmann, B. Maunders, M. Taoufik, J. Thivolle-Cazat, J. M. Basset, *Organometallics* **2002**, *21*, 5167.

[162] S. L. Scott, J. M. Basset, *J. Am. Chem. Soc.* **1994**, *116*, 12069.

[163] A. W. Moses, C. Raab, R. C. Nelson, H. D. Leifeste, N. A. Ramsahye, S. Chattopadhyay, J. Eckert, B. F. Chmelka, S. L. Scott, *J. Am. Chem. Soc.* **2007**, *129*, 8912.

[164] P. Avenier, A. Lesage, M. Taoufik, A. Baudouin, A. De Mallmann, S. Fiddy, M. Vautier, L. Veyre, J. M. Basset, L. Emsley, E. A. Quadrelli, *J. Am. Chem. Soc.* **2007**, *129*, 176.

[165] D. Dimova-Malinovska, O. Angelov, M. Kamenova, M. Sendova-Vassileva, A. Vaseashta, *J. Mater. Sci.-Mater. Electron.* **2003**, *14*, 747.

[166] T. Shimizu, S. Senz, S. Shingubara, U. Gosele, *Appl. Phys. A: Mater. Sci. Process.* **2007**, *87*, 607.

[167] H. Masuda, K. Fukuda, *Science* **1995**, *268*, 1466.

[168] A. H. Carim, K. K. Lew, J. M. Redwing, *Adv. Mater.* **2001**, *13*, 1489.

[169] Y. Wang, Y. Q. Yuan, S. R. Guo, *Molecules* **2009**, *14*, 4779.

[170] A. Kall, D. Bandyopadhyay, B. K. Banik, *Synth. Commun.*, *40*, 1730.

[171] D. Aaron, C. Tsouris, *Sep. Sci. Technol.* **2005**, *40*, 321.

[172] R. Steeneveldt, B. Berger, T. A. Torp, *Chem. Eng. Res. Des.* **2006**, *84*, 739.

[173] J. C. Hicks, J. H. Drese, D. J. Fauth, M. L. Gray, G. G. Qi, C. W. Jones, *J. Am. Chem. Soc.* **2008**, *130*, 2902.

[174] D. M. Ruthven, *Principles of Adsorption and Adsorption Processes*, **1984**.

[175] R. R. Schrock, J. D. Fellmann, *J. Am. Chem. Soc.* **1978**, *100*, 3359.

[176] P. Pertici, G. Vitulli, M. Paci, L. Porri, *J. Chem. Soc., Dalton Trans.* **1980**, 1961.

[177] K. Itoh, H. Nagashima, T. Ohshima, N. Oshima, H. Nishiyama, *J. Organomet. Chem.* **1984**, *272*, 179.

[178] G. Bodes, F. Heinemann, U. Zenneck, *Chem. Ber.* **1997**, *130*, 1321.

[179] A. Shiotani, H. Schmidbaur, *Chem. Ber.* **1971**, *104*, 2838.

[180] P. D. C. Dietzel, Y. Morita, R. Blom, H. Fjellvag, *Angew. Chem. Int. Ed.* **2005**, *44*, 6354.

[181] N. L. Rosi, J. Kim, M. Eddaoudi, B. Chen, M. O'Keeffe, O. M. Yaghi, *J. Am. Chem. Soc.* **2005**, *127*, 1504.

[182] S. Chavan, F. Bonino, J. G. Vitillo, E. Groppo, C. Lamberti, P. D. C. Dietzel, A. Zecchina, S. Bordiga, *Phys. Chem. Chem. Phys.* **2009**, *11*, 9811.

[183] P. D. C. Dietzel, B. Panella, M. Hirscher, R. Blom, H. Fjellvag, *Chem. Commun.* **2006**, 959.

[184] D. J. Tranchemontagne, J. R. Hunt, O. M. Yaghi, *Tetrahedron* **2008**, *64*, 8553.

[185] A. L. Patterson, *Phys. Rev.* **1939**, *56*, 978.

[186] P. C. Dietzel, R. Blom, H. Fjellvag, *Z. Anorg. Allg. Chem.* **2009**, *635*, 1953.

[187] P. D. C. Dietzel, R. Blom, H. Fjellvaag, *Eur. J. Inorg. Chem.* **2008**, 3624.

[188] P. D. C. Dietzel, R. E. Johnsen, R. Blom, H. Fjellvag, *Chem. Eur. J.* **2008**, *14*, 2389.

[189] R. Sips, *J. Chem. Phys.* **1948**, *16*, 490.

[190] M. W. C. Robinson, K. S. Pillinger, A. E. Graham, *Tetrahedron Lett.* **2006**, *47*, 5919.

[191] I. Karame, M. L. Tommasino, M. Lemaire, *Tetrahedron Lett.* **2003**, *44*, 7687.

[192] S. Takenaka, T. Shimizu, K. Otsuka, *Int. J. Hydrogen Energy* **2004**, *29*, 1065.

[193] A. Parinyaswan, S. Pongstabodee, A. Luengnaruemitchai, *Int. J. Hydrogen Energy* **2006**, *31*, 1942.

[194] J. J. Bravo-Suarez, K. K. Bando, J. Lu, T. Fujitani, S. T. Oyama, *J. Catal.* **2008**, *255*, 114.

[195] F. H. Stephens, V. Pons, R. T. Baker, *Dalton Trans.* **2007**, 2613.

[196] F. Baitalow, J. Baumann, G. Wolf, K. Jaenicke-Rossler, G. Leitner, *Thermochim. Acta* **2002**, *391*, 159.

[197] A. Gutowska, L. Li, Y. Shin, C. M. Wang, X. S. Li, J. C. Linehan, R. S. Smith, B. D. Kay, B. Schmid, W. Shaw, M. Gutowski, T. Autrey, *Angew. Chem., Int. Ed* **2005**, *44*, 3578.

[198] R. Benzouaa, U. B. Demirci, R. Chiriac, F. Toche, P. Miele, *Thermochim. Acta*, *509*, 81.

[199] T. Kondo, N. Hiraishi, Y. Morisaki, K. Wada, Y. Watanabe, T.-a. Mitsudo, *Organometallics* **1998**, *17*, 2131.

[200] T. Mitsudo, Y. Hori, Y. Watanabe, *J. Organomet. Chem.* **1987**, *334*, 157.

[201] T.-a. Mitsudo, Y. Ura, T. Kondo, *Proc. Jpn. Acad., Ser. B* **2007**, *83*, 65.

[202] T. Kondo, D. Takagi, H. Tsujita, Y. Ura, K. Wada, T.-a. Mitsudo, *Angew. Chem., Int. Ed* **2007**, *46*, 5958.

[203] M. A. Bennett, A. K. Smith, *J. Chem. Soc., Dalton Trans.* **1974**, 233.

[204] T. Uemura, N. Yanai, S. Kitagawa, *Chem. Soc. Rev.* **2009**, *38*, 1228.

[205] P. Cossee, *J. Catal.* **1964**, *3*, 80.

[206] G. J. P. Britovsek, V. C. Gibson, D. F. Wass, *Angew. Chem., Int. Ed* **1999**, *38*, 428.

[207] E. Y.-X. Chen, T. J. Marks, *Chem. Rev.* **2000**, *100*, 1391.

[208] U. Mueller, W. Keim, C. Krueger, P. Betz, *Angew. Chem.* **1989**, *101*, 1066.

[209] T. Kamegawa, T. Sakai, M. Matsuoka, M. Anpo, *J. Am. Chem. Soc.* **2005**, *127*, 16784.

[210] S. S. Kaye, J. R. Long, *J. Am. Chem. Soc.* **2008**, *130*, 806.

[211] S. Chavan, J. G. Vitillo, M. J. Uddin, F. Bonino, C. Lamberti, E. Groppo, K. P. Lillerud, S. Bordiga, *Chem. Mater.*, *22*, 4602.

[212] J. G. Vitillo, E. Groppo, S. Bordiga, S. Chavan, G. Ricchiardi, A. Zecchina, *Inorg. Chem.* **2009**, *48*, 5439.

[213] W. L. Truett, D. R. Johnson, I. M. Robinson, B. A. Montague, *J. Am. Chem. Soc.* **1960**, *82*, 2337.

[214] P. P. O'Neill, J. J. Rooney, *J. Am. Chem. Soc.* **1972**, *94*, 4383.

[215] H. Topsoe, *Appl. Catal.,* **2007**, *322*, 3.

[216] A. Thiollier, P. Afanasiev, P. Delichere, M. Vrinat, *J. Catal.* **2001**, *197*, 58.

[217] F. Gandara, E. Gutierrez Puebla, M. Iglesias, D. M. Proserpio, N. Snejko, M. Angeles Monge, *Chem. Mater.* **2009**, *21*, 655.

[218] D. Y. Zhao, Q. S. Huo, J. L. Feng, B. F. Chmelka, G. D. Stucky, *J. Am. Chem. Soc.* **1998**, *120*, 6024.

Abstract:
Metal organic frameworks (MOF) are a new class of material, which consist of metal ions or clusters coordinated to organic ligands or metal-organic complexes and result in 1D, 2D or 3D crystalline networks. The possibility of constructing new MOF has been exemplified in this thesis by development of imidazolium based MOF, a highly important ligand system in catalysis. Moreover, this work has performed post synthesis modification via surface organometallic chemistry on existing MOF: i) a known MOF, UiO-66, with relatively small pores has been functionalized with amino group and its gas adsorption capacity has been investigated, ii) the syntheses of a 3D open structure MOF, CPO-27, MOFs have been optimized and used as a precursor to produce a hydrodesulfurization catalyst after introducing active species via surface organometallic chemistry approach, whose catalytic performances have been measured.

Key words: Metal Organic Framework (MOF), microporous material, catalysis, hydrodesulfurization, adsorption, surface organometallic chemistry.

Résumé :
Les structures organométalliques poreuses (Metal Organic Framework, MOF) sont une nouvelle classe de matériaux, composées d'ions métalliques ou de clusters liés à des ligands organiques ou des complexes organométalliques dans des réseaux cristallins 1D, 2D ou 3D. Au cours de cette thèse la possibilité de construire de nouveaux MOF a été illustrée par le développement de matériaux MOF à base d'imidazolium, précurseur important pour la synthèse de catalyseurs. En outre, ce travail démontre l'utilité de la modification post-synthèse des MOFs par chimie organometallique de surface à visée catalytique : i) un MOF connu, UiO-66, avec des pores relativement petits a été fonctionnalisé avec un groupement amino et ses capacités d'adsorption de gaz ont été étudiées. ii) la synthèse de MOF a structure poreuse, CPO-27, MOF a été optimisée et utilisée comme précurseur pour produire un catalyseur d'hydrodésulfuration après l'introduction d'espèces actives, via la chimie organométallique de surface, dont les performances catalytiques ont été évaluées.

Mots clés: Metal Organic Framework (MOF), matériau microporeux, catalyse, hydrodésulfuration, adsorption, chimie organometallic de surface.

Université Lyon 1, LC2P2, Laboratoire de Chimie OrganoMétallique de Surface (LCOMS), UMR 5265, CNRS-CPE Lyon, 43 boulevard du 11 novembre 1918, F-69616 Villeurbanne Cedex, France.